UNIVERSIDADE FEDERAL DE GOIÁS
INSTITUTO DE FÍSICA
PROGRAMA DE PÓS-GRADUAÇÃO EM FÍSICA

UNIVERSITÉ GRENOBLE ALPES
ÉCOLE DOCTORALE I-MEP²
DOCTORAT EN MATERIAUX, MECANIQUE, GENIE CIVIL, ELECTROCHIMIE

CAMILA TSUCHIDA NOGUEIRA

Development and investigation of lanthanide-doped oxide nanocrystals for nanothermometry

Desenvolvimento e investigação de nanocristais de óxidos dopados com lantanídeos para nanotermometria

GOIÂNIA
2024

UNIVERSIDADE FEDERAL DE GOIÁS
INSTITUTO DE FÍSICA

TERMO DE CIÊNCIA E DE AUTORIZAÇÃO (TECA) PARA DISPONIBILIZAR VERSÕES ELETRÔNICAS DE TESES

E DISSERTAÇÕES NA BIBLIOTECA DIGITAL DA UFG

Na qualidade de titular dos direitos de autor, autorizo a Universidade Federal de Goiás (UFG) a disponibilizar, gratuitamente, por meio da Biblioteca Digital de Teses e Dissertações (BDTD/UFG), regulamentada pela Resolução CEPEC nº 832/2007, sem ressarcimento dos direitos autorais, de acordo com a Lei 9.610/98, o documento conforme permissões assinaladas abaixo, para fins de leitura, impressão e/ou download, a título de divulgação da produção científica brasileira, a partir desta data.

O conteúdo das Teses e Dissertações disponibilizado na BDTD/UFG é de responsabilidade exclusiva do autor. Ao encaminhar o produto final, o autor(a) e o(a) orientador(a) firmam o compromisso de que o trabalho não contém nenhuma violação de quaisquer direitos autorais ou outro direito de terceiros.

1. Identificação do material bibliográfico

[ ] Dissertação [X] Tese [ ] Outro*:_____________

*No caso de mestrado/doutorado profissional, indique o formato do Trabalho de Conclusão de Curso, permitido no documento de área, correspondente ao programa de pós-graduação, orientado pela legislação vigente da CAPES.

Exemplos: Estudo de caso ou Revisão sistemática ou outros formatos.

2. Nome completo do autor

Camila Tsuchida Nogueira

3. Título do trabalho

Development and investigation of lanthanide-doped oxide nanocrystals for nanothermometry

4. Informações de acesso ao documento (este campo deve ser preenchido pelo orientador)

Concorda com a liberação total do documento [X] SIM [ ] NÃO[1]

[1] Neste caso o documento será embargado por até um ano a partir da data de defesa. Após esse período, a possível disponibilização ocorrerá apenas mediante:
a) consulta ao(à) autor(a) e ao(à) orientador(a);
b) novo Termo de Ciência e de Autorização (TECA) assinado e inserido no arquivo da tese ou dissertação.
O documento não será disponibilizado durante o período de embargo.
Casos de embargo:
- Solicitação de registro de patente;
- Submissão de artigo em revista científica;
- Publicação como capítulo de livro;
- Publicação da dissertação/tese em livro.

Obs. Este termo deverá ser assinado no SEI pelo orientador e pelo autor.

---

sei! assinatura eletrônica

Documento assinado eletronicamente por **Camila Tsuchida Nogueira**, **Discente**, em 05/12/2024, às 08:41, conforme horário oficial de Brasília, com fundamento no § 3º do art. 4º do Decreto nº 10.543, de 13 de novembro de 2020.

Documento assinado eletronicamente por **Jesiel Freitas Carvalho**, **Professor do Magistério Superior**, em 05/12/2024, às 12:00, conforme horário oficial de Brasília, com fundamento no § 3º do art. 4º do Decreto nº 10.543, de 13 de novembro de 2020 .

A autenticidade deste documento pode ser conferida no site https://sei.ufg.br/sei/controlador_externo.php?acao=documento_conferir&id_orgao_acesso_externo=0, informando o código verificador **5016911** e o código CRC **1F078BEA**.

Referência: Processo nº 23070.055533/2024-86 SEI nº 5016911

CAMILA TSUCHIDA NOGUEIRA

Development and investigation of lanthanide-doped oxide nanocrystals for nanothermometry

Desenvolvimento e investigação de nanocristais de óxidos dopados com lantanídeos para nanotermometria

Thesis presented to Programa de Pós-Graduação em Física of Instituto de Física of Universidade Federal de Goiás for the degree of Doctor in Physics in co-tutelle with École Doctorale I-MEP^2 of Université Grenoble Alpes for the degree of Doctor in Materials, Mechanics, Civil Engineering and Electrochemistry.
Concentration field: Physics & Materials, Mechanics, Civil Engineering and Electrochemistry.
Research line: Physics of Materials

Advisors: Profº Dr. Jesiel Freitas Carvalho, and Dr. Alain Ibanez
Co-advisors: Profº Dr. Lauro June Queiroz Maia, and Dr. Géraldine Dantelle.

GOIÂNIA
2024

Ficha de identificação da obra elaborada pelo autor, através do
Programa de Geração Automática do Sistema de Bibliotecas da UFG.

Nogueira, Camila Tsuchida
Development and investigation of lanthanide-doped oxide nanocrystals for nanothermometry [manuscrito] / Camila Tsuchida Nogueira. - 2024.
23, 169 f.: il.

Orientador: Prof. Dr. Jesiel Freitas Carvalho; co-orientador Dr. Alain Ibanez; co-orientador Dr. Lauro June Queiroz Maia.
Tese (Doutorado) - Universidade Federal de Goiás, Instituto de Física (IF), Programa de Pós-Graduação em Física, Goiânia, 2024.
Bibliografia. Apêndice.
Inclui siglas, abreviaturas, símbolos, gráfico, tabelas, lista de figuras, lista de tabelas.

1. photoluminescence. 2. nanothermometry. 3. oxides. 4. thermal sensitivity. 5. nanocrystals. I. Carvalho, Jesiel Freitas, orient. II. Título.

CDU 53

UNIVERSIDADE FEDERAL DE GOIÁS

INSTITUTO DE FÍSICA

ATA DE DEFESA DE TESE

Ata Nº 77 da sessão de Defesa de Tese de Camila Tsuchida Nogueira que confere o título de Doutora em Física, na área de concentração em Física.

Aos 14 dias do mês de novembro de 2024, a partir das 12h00min, no Laboratório de Mídias do Instituto de Física da UFG, realizou-se a sessão pública de Defesa de Tese intitulada “Development and investigation of lanthanide-doped oxide nanocrystals for nanothermometry”, realizada em regime de cotutela com a Universidade Grenoble Alpes (UGA) - França. Os trabalhos foram instalados pelo Orientador no Brasil, Professor Doutor Jesiel Freitas Carvalho (IF/UFG) com a participação dos demais membros da Banca Examinadora: Orientador na França, Professor Doutor Alain Ibanez (Institut Neel/CNRS/Grenoble/França), membro titular externo, cuja participação ocorreu por meio de videoconferência; Coorientador no Brasil, Professor Doutor Lauro June Queiroz Maia (IF/UFG), membro titular interno; Coorientadora na França, Professora Doutora Geraldine Dantelle (Institut Neel/CNRS/Grenoble/França), membro titular externo, cuja participação ocorreu por meio de videoconferência; Professora Doutora Corine Gerardin (Institut Charles Gehardt/CNRS/França), membro titular externo, cuja participação ocorreu por meio de videoconferência; Professor Doutor Luís António Ferreira Martins Dias Carlos (Dep. Física/Universidade de Aveiro/Portugal), membro titular externo, cuja participação ocorreu por meio de videoconferência; Professor Doutor Jérôme Chauvin (Université Grenoble Alpes/Grenoble/França), membro titular externo, cuja participação ocorreu por meio de videoconferência; Professor Doutor Eudes Borges de Araújo (DFQ/UNESP), membro titular externo; Professora Doutora Danielle Cangussu de Castro Gomes (IQ/UFG), membro titular externo; e Professora Doutora Rogéria Rocha Gonçalves (FFCLRP/USP), membro titular externo, cuja participação ocorreu por meio de videoconferência. Durante a arguição, os membros da banca não fizeram sugestão de alteração do título do trabalho. A Banca Examinadora reuniu-se em sessão secreta a fim de concluir o julgamento da Tese, tendo sido a candidata aprovada pelos seus membros. Proclamados os resultados pelo Professor Doutor Jesiel Freitas Carvalho, Presidente da Banca Examinadora, foram encerrados os trabalhos e, para constar, lavrou-se a presente ata que é assinada pelos Membros da Banca Examinadora, aos 14 dias do mês de novembro de 2024.

TÍTULO SUGERIDO PELA BANCA

Documento assinado eletronicamente por **Jesiel Freitas Carvalho**, **Professor do Magistério Superior**, em 14/11/2024, às 16:29, conforme horário oficial de Brasília, com fundamento no § 3º do art. 4º do Decreto nº 10.543, de 13 de novembro de 2020 .

Documento assinado eletronicamente por **Danielle Cangussu De Castro Gomes**, **Professora do Magistério Superior**, em 14/11/2024, às 16:40, conforme horário oficial de Brasília, com fundamento no § 3º do art. 4º do Decreto nº 10.543, de 13 de novembro de 2020 .

Documento assinado eletronicamente por **Eudes Borges de Araújo**, **Usuário Externo**, em 14/11/2024, às 16:42, conforme horário oficial de Brasília, com fundamento no § 3º do art. 4º do Decreto nº 10.543, de 13 de novembro de 2020.

Documento assinado eletronicamente por **Lauro June Queiroz Maia**, **Professor do Magistério Superior**, em 14/11/2024, às 16:45, conforme horário oficial de Brasília, com fundamento no § 3º do art. 4º do Decreto nº 10.543, de 13 de novembro de 2020 .

A autenticidade deste documento pode ser conferida no site https://sei.ufg.br/sei/controlador_externo.php?acao=documento_conferir&id_orgao_acesso_externo=0, informando o código verificador **4943208** e o código CRC **8DF40F32**.

Referência: Processo nº 23070.055533/2024-86 SEI nº 4943208

Acknowledgments

My four-year PhD journey has finally come to an end! I didn't get this far on my own, so I'd like to dedicate this section to thanking a few people properly. Here we go!

First of all, my biggest thanks go to my family. Starting with my mother, **Satie**, she was the person who supported my education the most, and I can't thank her enough. She taught me to write and read at home when I was just 4 years old, bought me books whenever I asked (specifically a collection of 11 math books) and always worked hard to ensure that I had access to the best education. What's more, if I've managed to write this entire thesis in English, it's all down to her. She used to study English with me when I was very young and then paid for an English course and encouraged me to keep going until the end, even when my timetable was a nightmare to follow. So, Mom, thank you. To my father, **Dorisvaldo**, who always showed me that the right path in life is to study. To my siblings **Thalita** and **Fabio**, my grandparents **Tieko**, **Keiji,** and **Terezinha**, my aunt **Emi** and my uncle **Adolfo**, who always believed in my potential, even though they had no idea what this work was! However, this is for you too.

My sincerest gratitude goes to my husband, **Pedro**. He is certainly the person who knows best what this journey has been like. Thank you for saying "*I do*" and joining me on an adventure in the French Alps for 18 months so that I could develop part of this thesis. Thank you for sharing the freezing days with me, for preparing breakfast so that I could sleep a few extra minutes before work, for being so enthusiastic about doing new things, for the trips we took together, for the boring conversations I made you listen to about the PhD and for standing by me so patiently, no matter what. Also, thank you for welcoming our dog **Caramel** home. This cute little wiener has been my supporting pet and a great companion during the writing period. Thank you.

My deepest thanks go to my "team" of supervisors. First of all, **Jesiel**, who was my supervisor during my master's degree and once again agreed to be with me during my doctorate. Thank you for trusting me to undertake this work and for everything you did to turn it into a reality. Soon after I started my doctorate, **Lauro** joined as my co-supervisor. Thank you for the discussions, for the suggestions you gave me during our time in Campinas in 2023 (NanoAndes workshop) and for giving me the best letter of recommendation I've ever received when I applied for the LANEF scholarship. Speaking of which, when the opportunity arose to go to France, Géraldine and Alain agreed to host me in France for the co-tutored PhD, and I really appreciated that. Thanks to **Géraldine** for preparing me for the interview to get the LANEF grant. **Alain**, thank you for everything you've done since our first contact. For hosting me at your home at the beginning of my stay in France, for helping me with the bureaucratic issues, for all the discussions and experiments in the lab, for the jokes, for correcting my texts and preparing me for all kinds of presentations, and for all the advice. *J'espère avoir réussi à être une étudiante mémorable.* To all of you, thanks.

I would like to give a very special thanks to **Majed**, my lab partner in Grenoble. Thank you for being so enthusiastic in the lab, regardless of the results of the experiments. We went crazy together several times, especially when the SEM was down (OMG), and we needed it so much! I enjoyed all the random conversations while we were waiting for the autoclave to stabilize or when we were doing lots of centrifugations to rinse the nanomaterials. It was wonderful working with you and having the opportunity to train you. I'm very proud of you and I'm sure you have a bright future ahead of you. Thanks also to Majed's supervisor, **Xavier**, who is not my official supervisor, but I consider him one. Thank you for the ideas, meetings, discussions and your interest in this research. I feel lucky to have this partnership, which was crucial in this work (Chapter II is there as proof).

Behind the good results, of course there is a wonderful technician staff. In Brazil, I would like to thank **Tatiane** for the TEM images. She is the best undoubtedly. **Nathany**, for the Raman analysis. **Paulo**, for the STEM images. **Vinicius**, for all the analysis management. **Alisson**, for the photoluminescence measurements at the beginning and, especially, the discussion about science we always have. Our talks were very inspiring for me. In France, thanks to **Olivier Leynaud** for teaching me the Le Bail fit method, how to operate the diffractometer, and all the times I asked him for help. **Rémy**, for dealing with the autoclave problems whenever we had one. **Mathieu**, for the TG/DTA analysis and the discussions. **Sebastien**, for training me to operate the FE-SEM equipment. Finally, **Corinne Felix**, thank you. We got to make outstanding photoluminescence measurements as a function of the temperature because of her! Corinne prepared all the experimental set up and always adjusted it according to the needs of this work. So, thank you all.

My friends were also important in this process, especially in keeping me sane. I would like to kindly thank **Luiz**, the best friend the master's gave me for life. He was the pioneering nanothermometry student in our group and taught me a lot about this area when I started my PhD. But my biggest thanks go to him for our video calls full of gossip and conversations about life, and for the wonderful time we spent at the NanoAndes school (which was unforgettable). **Marília**, who has been my friend for an incredible 20 years and is also on the PhD road. Thank you for being this amazing friend with whom I feel comfortable sharing everything in endless talks. **Giovanna** and **Tahyne**, who inspired me to join the running lifestyle and also helped me not to quit the gym during the winter in France, even though they were so far away from me. Thank you for the non-research conversations. After all, we need to take a breath outside of science too! **Raissa**, my dear friend who has moved to Italy for good, but still cheers me up with her nonsense talks from time to time. Thanks to all of you, my friends.

Lastly, thanks to all the funding agencies, especially **CAPES** in Brazil and **LANEF** in France, and the laboratories Institut Néel, LabMic, and CRTI, for supporting this work somehow.

Once my favorite math teacher, **Reinaldo**, said "I wish you success. I know you will have it". Today I am sure he was right.

Enjoy the reading!

Abstract

Temperature sensing with accuracy and good spectral resolution is highly sought in research and industry, especially in biomedicine and microelectronics, where conventional thermal probes are unsuitable for remote measurements below 10 μm. In biology, thermal monitoring can indicate inflammatory areas, diseases, and tumors. Previous studies suggest temperature monitoring is promising for early diagnosis and assisting disease treatments, such as hyperthermia for cancer treatment. In this regard, luminescent nanoprobes made of inorganic materials doped with rare-earth ions have emerged as an effective means to measure local temperature precisely and remotely.

The thermal readout is obtained by tracking the Luminescence Intensity Ratio (LIR) between two photoluminescence (PL) emission lines, which evolves with temperature. A calibration curve between LIR and temperature can then be extracted from experimental data in the laboratory. Nonetheless, developing adequate luminescent nanothermometers for biological applications continues to be a major hurdle. These thermal sensors must be small, stable and well-dispersed in physiological solutions, non-toxic, and exhibit strong PL emissions within the biological windows (BWs) — the wavelength ranges where light penetrates tissues deeply.

This work focuses on oxides doped with rare-earth ions for nanothermometry in future biological applications, comprising the synthesis, characterization, and analysis of thermal sensing performance using PL emissions in the BWs of $Y_3Al_5O_{12}$ (YAG), Y_2O_3, and $Y_4Al_2O_9$ (YAM) co-doped with Nd^{3+} and Yb^{3+}. The first two host matrices were synthesized via the modified Pechini method for co-doping engineering to optimize the concentrations of Nd^{3+} and Yb^{3+} for ideal PL emission. To obtain well-dispersed individual nanocrystals (NCs), YAG: Nd^{3+}- Yb^{3+} and Y_2O_3: Nd^{3+}-Yb^{3+} were synthesized by the solvothermal route and the two-step urea-based route, respectively, with conditions systematically optimized to fulfill the requirements of this thesis. The third host matrix, YAM, was also studied using the modified Pechini synthesis to investigate its thermal response when single-doped with Nd^{3+} and co-doped with Nd^{3+} and Yb^{3+}. Lastly, a new synthesis method for YAM was explored.

The findings showed that YAG: Nd^{3+}-Yb^{3+} exhibited great potential, particularly after applying a silica coating around the NCs synthesized by the solvothermal route. This coating allowed annealing at 850°C to enhance the PL emission without agglomerating the NCs. The resulting YAG: Nd^{3+}-Yb^{3+}@SiO_2 nanoparticles (NPs) had a final size of 87 ± 20 nm, a relative thermal sensitivity (Sr) of $0.60\%.K^{-1}$, and thermal resolution (δT) of 0.2 K at physiological temperature. Y_2O_3: Nd^{3+}-Yb^{3+} NCs of 22 ± 10 nm had Sr of ~ $0.50\%.K^{-1}$, but $\delta T \sim 0.4$ K due to a lower signal-to-noise ratio. YAM, when single-doped with Nd^{3+}, revealed competitive thermal response with Sr = $0.50\%.K^{-1}$ and $\delta T = 0.3$ K at body temperature. However, co-doping YAM with both Nd^{3+} and Yb3+ ions hampers the thermal sensing efficiency to less than $0.40\%.K^{-1}$ of Sr at physiological temperature, with δT fluctuating between 0.2 and 0.7 K across the temperature range.

Thus, this study paves the way for improving the synthesis and applications of the oxides in nanothermometry and highlights promising prospects of Nd^{3+}-Yb^{3+} co-doped YAG nanothermometers thanks to their decreased size, good thermal sensing features, and intense PL emission within the BWs.

Keywords: photoluminescence, nanothermometry, oxides, thermal sensitivity, nanocrystals.

Résumé

La détection de la température avec précision et une bonne résolution spectrale est très demandée dans la recherche et l'industrie, notamment en biomédecine et microélectronique, où les sondes thermiques classiques sont inadéquates pour les mesures à distance en dessous de 10 μm. En biologie, la surveillance thermique peut révéler des zones inflammatoires, des maladies et des tumeurs. Des études antérieures montrent que la surveillance de la température est prometteuse pour le diagnostic précoce et l'aide aux traitements, comme l'hyperthermie pour le traitement du cancer. À cet égard, les nanosondes luminescentes de matériaux inorganiques dopés avec des ions de terres rares sont un moyen efficace de mesurer la température locale de manière précise et à distance.

La lecture thermique est obtenue en suivant le rapport d'intensité de luminescence (LIR) entre deux bandes d'émission de photoluminescence (PL), en fonction de la température. Une courbe de calibration reliant le LIR et la température peut être extraite des données expérimentales en laboratoire. Cependant, le développement de nanothermomètres luminescents adaptés aux applications biologiques reste un défi. Ces capteurs doivent être petits, stables, bien dispersés dans les solutions physiologiques, non toxiques, et présenter de fortes émissions PL dans les fenêtres biologiques (BWs), qui sont les gammes de longueurs d'onde où la lumière pénètre profondément dans les tissus.

Cette étude se concentre sur les oxydes dopés avec des ions de terres rares pour la nanothermométrie dans des applications biologiques futures. Elle comprend la synthèse, la caractérisation et l'analyse de la performance thermique en utilisant les émissions PL dans les BWs de $Y_3Al_5O_{12}$ (YAG), Y_2O_3 et $Y_4Al_2O_9$ (YAM) co-dopés avec Nd^{3+} et Yb^{3+}. Les deux premières matrices ont été synthétisées via la méthode Pechini modifiée afin d'optimiser les concentrations de Nd^{3+} et de Yb^{3+} pour une émission PL idéale. Pour obtenir des nanocristaux (NCs) individuels bien dispersés, YAG: Nd^{3+}-Yb^{3+} et Y_2O_3: Nd^{3+}-Yb^{3+} ont été synthétisés par la voie solvothermale et la voie en deux étapes à base d'urée, respectivement, avec des conditions optimisées. La troisième matrice, YAM, a également été étudiée avec la méthode Pechini modifiée pour évaluer sa réponse thermique en étant dopée avec Nd^{3+} seul et co-dopé avec Nd^{3+} et Yb^{3+}. Enfin, une nouvelle méthode de synthèse du YAM a été explorée.

Les résultats ont montré que YAG: Nd^{3+}-Yb^{3+} avait un fort potentiel, surtout l'application d'un revêtement de silice autour des NC synthétisées par la méthode solvothermale. Cette couche a permis un recuit protégé à 850°C pour améliorer l'émission PL sans agglomération. Les nanoparticules (NPs) YAG:Nd^{3+}-Yb^{3+}@SiO_2 obtenues avaient une taille de 87 ± 20 nm, une sensibilité thermique relative (Sr) de 0,60 %.K^{-1}, et une résolution thermique (δT) de 0,16 K. Les NCs de Y_2O_3: Nd^{3+}- Yb^{3+} de 22 ± 10 nm avaient une Sr de ~ 0,50 %.K^{-1}, mais une δT de ~ 0,4 K en raison d'un rapport signal-bruit plus faible. YAM, dopé avec Nd^{3+} seul, a montré une réponse thermique compétitive avec Sr = 0,50 %.K^{-1} et δT = 0,3 K à température corporelle. Toutefois, le co-dopage de YAM avec Nd^{3+} et Yb^{3+} réduit l'efficacité thermique à moins de 0,40%.K^{-1} de Sr à température physiologique, avec δT fluctuant entre 0,2 et 0,7 K.

Ainsi, cette étude ouvre la voie à l'amélioration de la synthèse et des applications des oxydes en nanothermométrie et met en avant le potentiel des nanothermomètres YAG co-dopé Nd^{3+}-Yb^{3+} pour leurs petites tailles et leurs bonnes caractéristiques thermiques.

Mots-clés : photoluminescence, nanothermométrie, oxydes, sensibilité thermique, nanocristaux.

Resumo

O controle de temperatura com precisão e boa resolução espectral altamente demandado na pesquisa e na indústria principalmente nas áreas de biomedicina e microeletrônica, em que os sensores térmicos convencionais são inadequados para medidas abaixo de 10 µm. No ramo da biologia, o monitoramento térmico pode indicar a presença de áreas inflamatórias, doenças e tumores. Estudos anteriores sugerem que monitorar a temperature pode ser promissor para o diagnóstico precoce e no tratamento de doenças, como a hipertermia para o tratamento do câncer. Portanto, nanosondas térmicas feitas de materiais inorgânicos dopados com íons terras-raras surgiram como um meio efetico de medir a temperatura local de forma precisa e remota.

A medição térmica é feita a partir da razão entre duas linhas de emissão de fotoluminescência (PL), aqui denominada de Razão de Intensidade de Luminescência (LIR), que evolui com a temperatura. Uma curva de calibração que relaciona LIR e a temperatura pode ser então extraída de dados experimentais no laboratório. No entanto, o desenvolvimento de nanotermômetros luminescentes apropriados para aplicações biológicas continua sendo um grande obstáculo. Esses sensores térmicos devem ser pequenos em tamanho, estáveis e bem dispersos em soluções fisiológicas, possuir baixa toxicidade, apresentar uma excelente resposta térmica e ter emissões intensas de PL dentro das janelas biológicas (BWs) — as faixas de comprimento de onda em que a luz penetra mais profundamente nos tecidos biológicos.

Este trabalho relata o desenvolvimento de óxidos dopados com íons terras raras visando à nanotermometria para futuras aplicações biológicas. Ele abrangeu a síntese, a caracterização e a análise do desempenho térmico usando emissões de PL nas BWs de $Y_3Al_5O_{12}$ (YAG), Y_2O_3 e $Y_4Al_2O_9$ (YAM) co-dopados com Nd^{3+} e Yb^{3+}. Inicialmente, as duas primeiras matrizes hospedeiras foram sintetizadas por meio do método Pechini modificado para engenharia de co-dopagem para determinar a concentração ideal de Nd^{3+} e Yb^{3+} a fim de obter uma emissão de PL otimizada dos íons terras raras. Em seguida, para obter nano cristais individuais (NCs) bem dispersos, YAG: Nd^{3+}-Yb^{3+} e Y_2O_3: Nd^{3+}-Yb^{3+} foram sintetizados pelo método solvotermal e pela rota de duas etapas à base de ureia, respectivamente, com condições sistematicamente otimizadas para atender aos requisitos deste projeto. A terceira matriz hospedeira, YAM, foi estudada com base na síntese de Pechini modificada para investigar sua resposta térmica quando dopada com

Nd^{3+} e co-dopada com Nd^{3+} e Yb^{3+}. Por fim, um novo método de síntese do YAM foi explorado.

Os resultados deste trabalho mostraram que o YAG: Nd^{3+}-Yb^{3+} apresentou um potencial significativo, especialmente depois que uma fina camada de sílica foi depositada em torno dos NCs sintetizados em condições solvotermais. Esse revestimento permitiu um tratamento térmico protegido a 850°C para melhorar a PL, sem causar aglomeração dos NCs. Em temperatura fisiológica, as nanopartículas (NPs) de YAG: Nd^{3+}-Yb^{3+}@SiO_2 apresentaram tamanho final de 87 ± 20 nm, sensibilidade térmica relativa (Sr) de 0,60%.K^{-1} e excelente resolução térmica (δT) de 0,2 K. Em comparação, os NCs de Y_2O_3: Nd^{3+} - Yb^{3+} de 22 ± 10 nm apresentaram Sr de cerca de 0,50%.K^{-1}, mas δT ~ 0,4 K devido a uma relação sinal/ruído mais baixa. Por sua vez, o YAM revelou uma resposta térmica competitiva quando dopado com Nd^{3+}, apresentando Sr = 0,50%.K^{-1} e δT = 0,3 K na temperatura corporal. Por outro lado, devido à complexa estrutura cristalina desse óxido, a inserção de Nd^{3+} e Yb^{3+} prejudica o desempenho térmico para Sr abaixo de 0,40%.K^{-1} com δT variando entre 0,2 K e 0,7 K no intervalo de temperaturas.

Portanto, este estudo abre caminho para melhorar a síntese e as aplicações dos óxidos em nanotermometrua e destaca as perspectivas promissoras dos nanotermômetros de YAG co-dopado com Nd^{3+} e Yb^{3+}, graças ao seu tamanho reduzido, boas características de detecção térmica e intensa emissão de PL dentro das janelas biológicas.

Palavras-chave: fotoluminescência, nanotermometria, óxidos, sensibilidade térmica, nano cristais.

Contents

Abstract .... **iv**

Résumé .... **vi**

Resumo .... **viii**

List of figures .... **xiii**

List of tables .... **xx**

List of abbreviations and symbols .... **xxii**

Introduction **1**

Chapter I: Introduction **4**

1.1 General concepts of Nanothermometry 4

1.1.1. Thermal sensing by LIR approach 5

1.1.2. Luminescent nanocrystals for LIR nanothermometry 10

1.1.2.1. Basic requirements of luminescent materials for biological applications 10

1.1.2.2. Selection of the rare-earth ions 12

1.1.2.3. Selection of the nanocrystalline inorganic host matrices 16

1.1.2.4. Implementation of luminescent nanothermometers in biomedicine 19

1.2. Preparation of nanocrystals: general concepts and mechanisms 23

1.2.1. Modified Pechini method 23

1.2.2. Synthesis from solution 24

1.2.3. Coating with amorphous silica 27

1.3. Objectives 28

Chapter II: Enhancement of photoluminescence emission and thermal sensing properties of YAG: Nd^{3+} - Yb^{3+} nanocrystals for nanothermometry **30**

2.1. Introduction 30

2.2. Experimental protocol 31

2.2.1. Materials syntheses 31

2.2.1.1. Modified Pechini method 31

2.2.1.2. Solvothermal method 32

2.2.1.3. Silica-coating of YAG nanocrystals via the biphasic method 34

2.2.2. Characterization techniques 35

2.3. Results and discussion 39

2.3.1. Co-doping engineering for an optimal photoluminescence emission of YAG: Nd^{3+} - Yb^{3+} nanocrystals 39

2.3.2. Preparation of individual core-shell YAG: Nd^{3+}-Yb^{3+} @ SiO_2 nanoparticles 47

2.3.2.1. Optimization of the solvothermal synthesis of YAG nanocrystals 47

2.3.2.2. Silica-coating of YAG: Nd^{3+}-Yb^{3+} nanocrystals and protected annealing 54

2.3.3. Nanothermometry of YAG: Nd^{3+}-Yb^{3+} nanocrystals 63

2.4. General Remarks and perspectives 69

Chapter III: Synthesis and characterization of yttria nanocrystals co-doped with Nd^{3+} and Yb^{3+} for nanothermometry 71

3.1 Introduction 71

3.2 Experimental protocol 72

3.2.1. Materials syntheses 72

3.2.1.1. Modified Pechini method 72

3.2.1.2. Two-step urea-based route 72

3.2.2. Characterization techniques 73

3.3 Results and discussion 73

3.3.1. Calcination tests of the samples obtained by the modified Pechini method 73

3.3.2. Co-doping engineering to achieve an optimal photoluminescence emission intensity of Y_2O_3: Nd^{3+}-Yb^{3+} NCs 77

3.3.3. Synthesis of Y_2O_3 nanocrystals by the two-step urea-based process: optimization of the experimental protocol 84

3.3.3.1. Size control of $Y(OH)CO_3.H_2O$ 85

3.3.3.2. Calcination tests of $Y(OH)CO_3.H_2O$ nanoparticles to yield Y_2O_3 nanocrystals89

3.3.3.3. Structural characterization and photoluminescence measurement of Y_2O_3: Nd^{3+}-Yb^{3+} nanocrystals 93

3.3.4. Nanothermometry of Y_2O_3: Nd^{3+}-Yb^{3+} nanocrystals 97

3.4 General remarks and perspectives 101

Chapter IV: A study of YAM: Nd^{3+} and YAM: Nd^{3+}-Yb^{3+} as luminescent nanothermometers 103

4.1 Introduction 103

4.2 Experimental protocol 104

4.2.1. Materials syntheses 104

4.2.1.1. Modified Pechini method 104

4.2.1.2. Two-step urea-based route.. 105

4.2.2. Characterization techniques.. 105

4.3 Results and discussion 106

4.3.1. YAM synthesized by the modified Pechini method: synthesis and nanothermometry analysis 106

4.3.1.1. Nd^{3+} single-doped YAM nanocrystals 106

4.3.1.2. Effect of Yb^{3+} co-doping 115

4.3.2. The two-step urea-based route: an alternative way of synthesizing YAM nanocrystals 121

4.4 General remarks and perspectives 127

Conclusions & Future outlooks 129

Bibliography.. 135

Appendix: Supplementary Information 163

List of figures

Figure 1. Types of variations in PL emission spectrum after a temperature change in **(a)** band-shape, **(b)** intensity, **(c)** bandwidth, **(d)** spectral shift, **(e)** lifetime, and **(f)** polarization [15]. 5

Figure 2. Simple energy-level scheme showing the dynamic between two thermally coupled states after light irradiation (Created by the author). 6

Figure 3. Simple energy-level scheme to illustrate the energy transfer of one emitter to the other in dual-center emission materials (Created by the author). 9

Figure 4. Absorption spectrum of human skin, displaying the BWs. The green stars represent endogenous autofluorescence, and the arrows are related to the degree of light scattering. In BW-IIb, the reduced light scattering provides a higher spatial resolution compared to the other BWs [36]. 11

Figure 5. (a) Energy level diagram of Nd^{3+}; **(b)** Energy level diagram of Yb^{3+}, **(c)** Scheme showing the dynamics of Nd^{3+} - Yb^{3+}, with indication of energy transfer of $Nd^{3+} \rightarrow Yb^{3+}$, back energy transfer of $Yb^{3+} \rightarrow Nd^{3+}$ and diffusion (migration) energy of Yb^{3+} - Yb^{3+} (Created by the author). 14

Figure 6. YAG crystal structure. This scheme was reproduced in the software Vesta based on the ICSD CIF 17663. 18

Figure 7. YAM crystal structure. This scheme was reproduced in the software Vesta based on the ICSD CIF 230984. 18

Figure 8. Y_2O_3 crystal structure. This scheme was reproduced in the software Vesta based on the ICSD CIF 26190. 19

Figure 9. (a) Fluorescence image showing the presence of LaF_3:Nd^{3+}@ LaF_3: Yb^{3+} NPs in the mouse body; **(b)** Picture of the mouse during the experiments; **(c)** Scheme illustrating the procedure for thermal sensing; **(d)** Thermal infrared images before and **(e)** in the end of the heating; **(f)** Evolution of measured temperature with calibration curve (gray points) and infrared thermal camera (orange squares) in time [70]. 22

Figure 10. Chemical reaction involved in the modified Pechini method (Created by the author). 24

Figure 11. LaMer's diagram, displaying the nucleation and growth steps of the synthesis from solution[114]. 26

Figure 12. Flowchart of the modified Pechini synthesis (Created by the author). 32

Figure 13. Dehydration of yttrium acetate tetrahydrate in a glass oven connected to a vacuum line, in the presence of P_2O_5 (Created by the author). 33

Figure 14. Flowchart describing the solvothermal route for YAG synthesis (Created by the author). 34

Figure 15. Flowchart illustrating the process of silica coating YAG nanocrystals through the biphasic method (Created by the author). 35

Figure 16. (a) Experimental set up for thermometry measurements of powder. **(b)** A close view showing the sample inside a sample-holder, placed in the LINKAM device. **(c)** The foam box built to insulate the thermometry measurements in solution. **(d)** The view from inside the foam box, showing the set up made with a hot plate, the cuvette placed inside the black mounting, the laser diode, and the optical fiber to collect the emission signal to the detector (Created by the author). 38

Figure 17. XRD patterns of YAG co-doped with different % mol Yb^{3+} when Nd^{3+} concentration is fixed at **(a)** 0.25, **(b)** 0.50, and **(c)** 0.75% mol. **(d)** HR-XRD (black curve) with calculated Le Bail fit (pink circles) of YAG: 0.75% mol Nd^{3+}, 0.50% mol Yb^{3+} NCs. 40

Figure 18. FE- SEM image of YAG: 0.75% mol Nd^{3+}, 0.50% mol Yb^{3+} obtained by the modified Pechini method. 41

Figure 19. (a) DR spectrum and **(b)** determination of the optical bandgap energy of YAG: 0.75% mol Nd^{3+}, 1.00% mol Yb^{3+}. 42

Figure 20. PL emission spectra of YAG for different % mol Yb^{3+} considering Nd^{3+} concentration fixed at **(a)** 0.25, **(b)** 0.50, and **(c)** 0.75% mol. 43

Figure 21. Energy level diagram of YAG co-doped with Nd^{3+} and Yb^{3+}. The numbers indicate the energy values in cm^{-1}, and the acronyms in the parenthesis designate each Stark level (Created by the author). 44

Figure 22. Integrated intensities at 1030 nm (I_{1030}) and 1063 nm (I_{1063}) as a function of % mol Yb^{3+} when Nd^{3+} concentration is fixed at **(a)** 0.25, **(b)**0.50, and **(c)** 0.75% mol. All the graphs are on the same scale for a better comparison. 46

Figure 23. (a) Comparison of integrated intensity at 1030 nm (Yb^{3+}) for all samples. The red arrows indicate the four samples with higher Yb^{3+} PL emission. **(b)** The emissivity of Nd^{3+} of the samples that presented highest Yb^{3+} PL intensities. The red arrow points out to the composition that gave highest Nd^{3+} emission among the four samples previously selected. 47

Figure 24. Mechanism to obtain YAG by the solvothermal method. R means C_3H_7 (Created by the author). 48

Figure 25. HR-XRD of YAG NCs synthesized with different % in volume of DEG. All diffractograms were indexed as YAG and no spurious phase was detected. The samples were co-doped with 0.75% mol Nd^{3+} and 0.50% mol Yb^{3+}. 49

Figure 26. TEM images of YAG NCs prepared with **(a)** 0.00, **(b)** 0.50, **(c)** 1.00, **(d)** 2.00, and **(e)** 3.00% in volume of DEG. **(f)** HR-TEM of YAG NC (0.00% volume DEG). All samples were co-doped with 0.75% mol Nd^{3+} and 0.50% mol Yb^{3+} 52

Figure 27. FTIR spectrum of YAG: 0.75% mol Nd^{3+}, 0.50% mol Yb^{3+} synthesized by the solvothermal method. ν: stretching, δ: bending, ω: wagging. 53

Figure 28. **(a)** FE-SEM, and **(b)** STEM images of YAG: 0.75% mol Nd^{3+}, 0.50% mol Yb^{3+}@SiO_2 NPs. **(c)** Hydrodynamic size, and **(d)** autocorrelation function when these core-shell NPs are suspended in water. 56

Figure 29. **(a)** TG/DSC and **(b)** mass spectrometry of YAG: 0.75% mol Nd^{3+}, 0.50% mol Yb^{3+}@SiO_2 NPs. 57

Figure 30. FE-SEM images of YAG: 0.75% mol Nd^{3+}, 0.50% molYb^{3+}@SiO_2 NPs annealed at **(a)** 700°C, **(b)** 850°C, **(c)** 1000°C, and **(d)** 1100°C for 1h. 58

Figure 31. FTIR of YAG: 0.75% mol Nd^{3+}, 0.50% mol Yb^{3+}@SiO_2 NPs before and after heat treatments. The temperature written inside the parenthesis refers to the annealing temperature. ν: stretching, δ: bending. 59

Figure 32. **(a)** PL spectra of nude YAG NCs compared to YAG@SiO_2 NPs annealed at 700°C, 850°C, 1000°C, and 1100°C for 1h. **(b)** Integrated PL emissions at 1063 nm and 1030 nm of Nd^{3+} and Yb^{3+}, respectively, for the different annealing temperatures compared to nude YAG. All the samples were co-doped with 0.75% mol $Nd^{3+}$and 0.50% mol Yb^{3+}. 61

Figure 33. **(a)** FE-SEM, and **(b)** STEM images of YAG: 0.75% mol Nd^{3+}, 0.50% mol Yb^{3+}@SiO_2 NPs with thin shell (17 ± 2 nm). **(c)** PL spectra of nude YAG NCs compared to YAG@SiO_2 NPs annealed at 850°C with thick shell (21 ± 4 nm) and thin shell (17 ± 2 nm). **(d)** Integrated PL emissions at 1063 nm and 1030 nm of Nd^{3+} and Yb^{3+}, respectively, for different shell thickness compared to nude YAG. All the samples were co-doped with 0.75% mol $Nd^{3+}$and 0.50% mol Yb^{3+}. 62

Figure 34. **(a)** PL emission spectra of powdered YAG: 0.75% mol Nd^{3+}, 0.50% mol Yb^{3+}@SiO_2 before and after dripping H_2O. **(b)** PL emission spectra of powdered YAG: 0.75% mol Nd^{3+}, 0.50% mol Yb^{3+}@SiO_2 before and after dripping D_2O. 63

Figure 35. **(a)** PL(T) and **(b)** calibration curve of YAG synthesized by modified Pechini method. **(c)** PL(T) and **(d)** calibration curve of YAG@SiO_2 (solvothermal route + protected annealing) in powder. **(e)** PL(T) and **(f)** calibration curve of YAG@SiO_2 dispersed in water. The samples were co-doped with 0.75% mol Nd^{3+} and 0.50% mol Yb^{3+}. 65

Figure 36. Number of PL spectra at 309.3 ± 0.1 K versus δLIR........ 66

Figure 37. **(a)** Sr and **(b)** δT of YAG: 0.75% mol Nd^{3+}, 0.50% mol Yb^{3+} NCs synthesized by the modified Pechini method in powder and YAG: 0.75% mol Nd^{3+}, 0.50% mol Yb^{3+} @ SiO_2 NPs in powder and solution. 68

Figure 38. Recording of LIR over 11 heating-cooling cycles of **(a)** YAG: 0.75% mol Nd^{3+}, 0.50% mol Yb^{3+} NCs obtained by the modified Pechini method and **(b)** YAG: 0.75% mol Nd^{3+}, 0.50% mol Yb^{3+} @ SiO_2 NPs in powder. The repeatability is ≥ 98.0% or both cases. 68

Figure 39. **(a)** HR-XRD pattern (orange circles) with calculated Le Bail fit (solid black line), and **(b)** TEM with an inset of HR-TEM of Y_2O_3 heat-treated at 900°C/10 min**.** **(c)** HR-XRD (green circles) with calculated Le Bail fit (solid black line), and **(d)** TEM with an inset of HR-TEM of Y_2O_3 heat-treated at 450°C/12 h and 1000°C/1h. The sizes were measured with the ImageJ software........ 75

Figure 40. **(a)** FTIR, and **(b)** PL emission spectra of Y_2O_3 after calcining the *puff* at 900°C/10 minutes, and at 1000°C/1h preceded by an intermediate treatment at 450°C/12h. Both samples were co-doped with 1.00% mol Nd^{3+} and 0.50% mol Yb^{3+}. 77

Figure 41. X-ray diffractograms of Nd^{3+}- Yb^{3+} co-doped Y_2O_3 for different % mol Yb^{3+} when Nd^{3+} concentration fixed at **(a)** 0.25, **(b)** 0.50, and **(c)** 1.00% mol........ 79

Figure 42.(a) DR spectrum and **(b)** determination of the optical bandgap energy of Y_2O_3: 1.00% mol Nd^{3+}, 1.00% mol Yb^{3+}........ 80

Figure 43. PL emission spectra of yttrium oxide for different % mol Yb^{3+} considering Nd^{3+} concentration fixed at **(a)** 0.25, **(b)** 0.50, and **(c)** 1.00% mol. 81

Figure 44. Energy level diagram of yttrium oxide co-doped with Nd^{3+} and Yb^{3+}. The numbers indicate the energy values in cm^{-1}, and the acronyms in the parenthesis designate each Stark level (Created by the author). 82

Figure 45. Integrated intensities at 1030 nm (I_{1030}) and 1056 nm (I_{1063}) as a function of % mol Yb^{3+} when Nd^{3+} concentration is fixed at **(a)** 0.25, **(b)** 0.50, and **(c)** 1.00% mol in Y_2O_3. All the graphs are on the same scale for a better comparison. 83

Figure 46.(a) Comparison of integrated intensity at 1030 nm (Yb^{3+}) for Y_2O_3: Nd^{3+}-Yb^{3+} samples. The red arrows indicate the four samples with higher Yb^{3+} emission. **(b)** The emissivity of $Nd^{3+}$of the samples that presented highest Yb^{3+} PL intensities. The red arrow points out to the composition that gave highest Nd^{3+} emission among the four samples previously selected. 84

Figure 47.(a) XRD pattern and **(b)** FE-SEM image of $Y(OH)CO_3.H_2O$ NPs synthesized by using 83% in volume of 1,4-butanediol and 0.2 mol.L^{-1} of urea.............................. 88

Figure 48. Thermal analysis along with mass spectrometry of $Y(OH)CO_3.H_2O$ NPs under oxygen atmosphere. The mass spectrometry of H_2O and CO_2 is given in arbitrary units. 90

Figure 49. Diffractograms of Y_2O_3 after calcining $Y(OH)CO_3.H_2O$ NPs under different conditions. The XRD peaks were compared with the reference PDF 00-041-1105. 91

Figure 50. TEM images of Y_2O_3 NCs after calcination at **(a)** 700°C/5 minutes, **(b)** 700°C/120 minutes, **(c)** 800°C/5 minutes, **(d)** 800°C/120 minutes, considering a slow heating rate of 1°C.min^{-1}; **(e)** 900°C/1h with a 10 times faster heating rate, that is, equal to 10°C.min^{-1}. 92

Figure 51. X-ray diffractograms of Y_2O_3 after calcination of $Y(OH)CO_3.H_2O$ NPs with NaCl under different conditions. The symbol * indicates the presence of sodium yttrium chloride oxide, identified based on the reference PDF 04-010-9094. 93

Figure 52. (a) HR-XRD pattern (pink circles) with calculated Le Bail fit (black solid line), and **(b)** TEM images of Y_2O_3: 1.00% mol Nd^{3+}, 0.50% mol Yb^{3+} synthesized via the two-step urea-based route. 94

Figure 53. (a) Hydrodynamic sizes and **(b)** autocorrelation function of Y_2O_3: 1.00% mol Nd^{3+}, 0.50% mol Yb^{3+} NCs after annealing at 700°C/5 minutes (blue curves) and 550°C/20 min with NaCl (pink curves). 95

Figure 54. FTIR spectra of $Y(OH)CO_3.H_2O$ NPs and Y_2O_3 NCs synthesized via the two-step urea-based route. 96

Figure 55. PL emission spectra of Y_2O_3 NCs synthesized by the two-step urea-based route (550°C/20 min with NaCl) and the modified Pechini method. The same co-doping concentration of 1.00% mol Nd^{3+} and 0.50% mol Yb^{3+} was applied to both samples... 97

Figure 56. (a) PL(T) and **(b)** calibration curve of Y_2O_3 synthesized by modified Pechini method. **(c)** PL(T) and **(d)** calibration curve of Y_2O_3 synthesized by the two-step urea-based route. Both samples were co-doped with 1.00% mol Nd^{3+} and 0.50% mol Yb^{3+}. 99

Figure 57.(a) Sr and **(b)** δT values of Y_2O_3: 1.00% mol Nd^{3+}, 0.50% mol Yb^{3+} NCs as a function of the temperature for both synthesis procedures employed in this work...... 100

Figure 58. Measurements of LIR over 11 heating- cooling cycles of Y_2O_3: 1.00% mol Nd^{3+} , 0.50% mol Yb^{3+} obtained by **(a)** the modified Pechini method and **(b)** the two-step urea-based route. The repeatability is 99.4% for both cases. 101

Figure 59. (a) HR-XRD of YAM doped with different concentrations of % mol Nd^{3+}. **(b)** Evolution of the cell parameters *a*, *b*, and *c*, and **(c)** coherence length (Lc) with the Nd^{3+}concentration. **(d)** TEM image of YAM: 0.83% mol Nd^{3+}................................. 108

Figure 60. (a) Raman and **(b)** FTIR spectra of YAM doped with 0.83% mol Nd^{3+}. .. 109

Figure 61. (a) PL emission spectra of YAM doped with different concentrations of % mol Nd^{3+}, **(b)** Simple energy-level diagram of Nd^{3+} in YAM, and **(c)** Integrated area of PL spectrum of YAM: Nd^{3+} as a function of % mol Nd^{3+}. 110

Figure 62. (a) PL emission spectrum as a function of temperature of YAM: 0.83% $Nd^{3+}$and **(b)** Calibration curves obtained of LIR formed by the peaks at 1049 nm and 1080 nm, 1084 nm, and 1100 nm over the thermal range. The errors associated with ln (LIR) are in the order of 10^{-3} and thus, the error bars became too small to be displayed in the figure.. 112

Figure 63.(a) Sr and **(b)** δT of YAM: 0.83% mol Nd^{3+} as a function of temperature. Both thermal parameters were calculated for the LIR of I_{1049}/I_{1080}, I_{1049}/I_{1084}, and I_{1049}/I_{1100}. 114

Figure 64. Measurement of LIR over 11 heating- cooling cycles of YAM: 0.83% mol Nd^{3+} for LIR equal to **(a)** I_{1049}/I_{1080}, **(b)** I_{1049}/I_{1084}, and **(c)** I_{1049}/I_{1100}.......................... 115

Figure 65. (a) HR-XRD of YAM doped with 0.83% mol Nd^{3+} and different concentrations of % mol Yb^{3+},**(b)** Evolution of cell parameters *a*, *b*, and *c* and **(c)** coherence length (Lc) with the Yb^{3+} concentration, **(d)** FE-SEM image of YAM: 0.83% mol Nd^{3+}, 0.17% mol Yb^{3+}. 117

Figure 66.(a) PL emission spectra of YAM co-doped with 0.83% mol Nd^{3+} and different concentrations of % mol Yb^{3+}, **(b)** Simplified energy level scheme of Nd^{3+} and Yb^{3+}, **(c)** Integrated PL area as a function of % mol Yb^{3+}.. 119

Figure 67. (a) PL(T) spectra of YAM: 0.83% mol Nd^{3+} and 0.17% mol Yb^{3+}, **(b)** LIR vs temperature for ratios I_{1049}/ I_{1029} and I_{1049}/I_{976}. The error bars of LIR are in the order of 10^{-3}, which are too small to show up in the figure. 120

Figure 68. (a) Sr and **(b)** δT of YAM: 0.83% mol Nd^{3+}, 0.17% mol Yb^{3+} for LIR of I_{1049}/I_{1029} (pink symbols) and I_{1049}/I_{976} (dark green symbols)..................................... 121

Figure 69. **(a)** XRD, and FE-SEM images of the amorphous as-obtained product for **(b)** 0, **(c)** 50, and **(d)** 80% in vol. of 1,4-butanediol as co-solvent. 124

Figure 70.(a) HR-XRD, **(b)** TEM, **(c)** size distribution of NCs based on TEM, and **(d)** HR-TEM of YAM: 0.83% mol Nd^{3+} synthesized by the two-step urea-based route... 125

Figure 71. FTIR spectra of as-obtained sample (blue curve) and after calcination at 1000°C/1h (red curve). 126

Figure 72. PL emission spectra of YAM: 0.83% mol Nd^{3+} synthesized by the modified Pechini method compared to the one obtained through the two-step urea-based route. 127

Figure 73. PL emission spectra of YAG: 0.75% mol Nd^{3+}, 0.50% mol Yb^{3+}, Y_2O_3: 1.00% mol Nd^{3+}, 0.50% mol Yb^{3+}, and YAM: 0.83% mol Nd^{3+}, 0.17% mol Yb^{3+}. All three oxides were synthesized via the modified Pechini method, and the corresponding spectra were acquired under the same conditions. 130

Figure S1. HR-XRD patterns with Le Bail fit of YAG NCs synthesized via the solvothermal method using **(a)** 0.00, **(b)** 0.50, **(c)** 1.00, **(d)** 2.00, and **(e)** 3.00% vol. DEG. 163

Figure S2. Size distribution of YAG NCs synthesized via the solvothermal method using **(a)** 0.00, **(b)** 0.50, **(c)** 1.00, **(d)** 2.00, and **(e)** 3.00% vol. DEG. This calculation was performed considering above 150 NCs from different TEM images. 164

Figure S3. HR-XRD of YAG: 0.75% mol Nd^{3+}, 0.50% mol Yb^{3+} synthesized via the solvothermal method before and after annealing. 165

Figure S4. HR-XRD patterns with calculated Le Bail fit of YAM when doped with **(a)** 0.33, **(b)** 0.50, **(c)** 0.67, **(d)** 0.83, **(e)** 1.00, and **(f)** 1.50% mol Nd^{3+}. 166

Figure S5. HR-XRD patterns with calculated Le Bail fit of YAM when doped with 0.83% mol $Nd^{3+}$and **(a)** 0.17, **(b)** 0.50, **(c)** 0.67, **(d)** 1.00, and **(e)** 1.50% mol Yb^{3+}. 168

List of tables

Table 1. Summary of Nd^{3+}-doped and Nd^{3+}-Yb^{3+} co-doped NPs with corresponding thermal performance published in the literature. The selection of these works was restricted to the excitation wavelength (λ_{exc}) in the BW-I.. 15

Table 2. Nd^{3+} and Yb^{3+} concentrations of YAG samples in % mol relative to all metals (yttrium and aluminum) with corresponding chemical formula.................................. 39

Table 3. Cell parameters and Lc of YAG: 0.75% mol Nd^{3+}, 0.50% mol Yb^{3+} NCs synthesized by the modified Pechin method. 40

Table 4. Cell parameters and refinement parameters according to the Le Bail fit of YAG: Nd^{3+}-Yb^{3+} synthesized by the solvothermal method. The co-doping concentration used was 0.75% mol Nd^{3+} and 0.50% mol Yb^{3+}... 50

Table 5. Summary of Lc, NC size, degree of polydispersity, and hydrodynamic size of YAG: 0.75% mol Nd^{3+}, 0.50% mol Yb^{3+} NCs.. 52

Table 6. Cell parameters, Lc, and refinement parameter according to the Le Bail fit of Y_2O_3: 1.00% mol Nd^{3+}, 0.50% mol Yb^{3+}. 75

Table 7. Nd^{3+} and Yb^{3+} concentrations of Y_2O_3 in % mol in relation to yttrium with corresponding chemical formulas.. 78

Table 8. Summary of the conditions for the synthesis of $Y(OH)CO_3.H_2O$: nature of the organic co-solvent, its percentage in volume relative to water, urea amount, size of NPs measured with FE-SEM images, and PDI. 88

Table 9. Conditions tested to obtain Y_2O_3 from heat treatment of $Y(OH)CO_3.H_2O$ under O_2 atmosphere in a tubular furnace. 90

Table 10. Concentration of Nd^{3+} in % mol in relation to all metals, and the corresponding chemical formulas.. 106

Table 11. Calibration curves, energy difference between TCLs extracted from the calibration curves (ΔE_{calc}) and from the PL emission spectrum (ΔE_{exp}) for each LIR. R^2 is the statistical value attesting a good fitting of the points. 112

Table 12. Concentration of Yb^{3+} in % mol in relation to all metals and the corresponding chemical formulas. The content of Nd^{3+} was set constant at 0.83% mol for all compounds. 116

Table 13. Conditions tested to synthesize YAM through the two-step urea-based process. 122

Table 14. Cell parameters and coherence length estimated through the Le Bail fit of HR-XRD of YAM: 0.83% mol Nd^{3+} synthesized by the two-step urea-based route.......... 125

Table S1. Cell parameters and coherence length of YAG: 0.75% mol Nd^{3+}, 0.50% mol Yb^{3+} synthesized via the solvothermal method before and after annealing. 165
Table S2. Cell parameters and coherence length of YAM doped with different concentrations of Nd^{3+}.. 167
Table S3. Cell parameters and coherence length of YAM doped with 0.83% mol Nd^{3+} and different concentrations of Yb^{3+}. 169

List of abbreviations and symbols

Abbreviations

BW	Biological Window	
CTAB	Cetyltrimethylammonium bromide	
DEG	Diethylene glycol	
DLS	Dynamic Light Scattering	
DR	Diffuse Reflectance	
DSC	Differential Scanning Calorimetry	
DTA	Differential Thermal Analysis	
Eg	Optical bandgap energy	(eV)
FE-SEM	Field Emission Scanning Electron Microscopy	
FTIR	Fourier Transform Infrared spectroscopy	
HR-XRD	High-resolution X-ray Diffraction	
HR-TEM	High-resolution Transmission Electron Microscopy	
k_B	Boltzmann constant	(cm^{-1}. K^{-1})
Lc	Coherence length	(nm)
LIR	Luminescence Intensity Ratio	
Ln^{3+}	Lanthanide	
NIR	Near Infrared	
NC	Nanocrystal	
NP	Nanoparticle	
PEG	Polyethylene Glycol	
PL	Photoluminescence	
PL(T)	Photoluminescence as a function of temperature	

PDI	Polydispersity Index	
Ref.	Reference	
Sr	Relative thermal sensitivity	(%.K^{-1})
STEM	Scanning-Transmission Electron Microscopy	
T	Temperature	(°C or K)
TCLs	Thermally Coupled Levels	
TEM	Transmission Electron Microscopy	
TEOS	Tetraethyl orthosilicate	
TG	Thermogravimetry	
VIS	Visible	
XRD	X-Ray Diffraction	
YAG	$Y_3Al_5O_{12}$	
YAM	$Y_4Al_2O_9$	

Symbols

δT	Thermal resolution	(K)
ΔE	Energy gap	(cm^{-1})
λ	Wavelength	(nm)
σ	Standard deviation	
$\hbar$	Reduced Planck constant	
$\tilde{\nu}$	Wavenumber	(cm^{-1})

Introduction

Temperature is a fundamental physical parameter that profoundly impacts not only industrial processes and research, but also living organisms, since it directly influences the biochemical reactions occurring within the cells. Because temperature variations are closely intertwined with vital cellular processes, the precise measurement of local temperature is essential and can be facilitated by advanced remote sensing techniques. Such measurements can enhance our comprehension of the cellular processes, revolutionize disease diagnosis and treatment of cancerous tumors, and pinpoint inflammatory areas. In light of these considerations, luminescent nanothermometers emerge as a promising and innovative tool to fulfill this crucial task.

For such an objective, oxides doped with rare-earth ions have good prospects as this type of inorganic material is chemically stable, non-toxic, and can be easily synthesized. The rare-earth ions chosen were Nd^{3+} and Yb^{3+} once they operate well within the biological windows (BWs), the wavelength ranges in which the scattering and absorption of the light by skin components are reduced. According to the previous thesis led by Itália Vallerini Barbosa[1] in our group, $Y_3Al_5O_{12}$ (YAG) and Y_2O_3 co-doped with Nd^{3+} and Yb^{3+} were the oxides that stood out in nanothermometry. Nonetheless, some optimizations were still required to pursue this work in the development of luminescent nanothermometers: 1) to obtain nanocrystals (NCs) with high crystal quality and small size associated with a narrow size distribution through the improvement of synthesis conditions, 2) amplification of the photoluminescence (PL) emission of the doping ions, 3) optimization of the experimental conditions regarding the measurements of PL emission as a function of the temperature. Hence, this thesis focuses on producing individual NCs of YAG and Y_2O_3, with optimal concentrations of Nd^{3+} and Yb^{3+}, for luminescence nanothermometry. Two synthesis methods were employed: the modified Pechini method to conduct several syntheses to determine the ideal co-doping concentration, and synthesis from solution under solvothermal conditions to obtain non-agglomerated NCs. Our team has great experience in synthesizing YAG NCs by using a solvothermal route, as already reported in former theses of Alexandra Cantarano[2] and Itália Vallerini Barbosa[1], but a two-step urea-based route was applied to obtain Y_2O_3 NCs. In parallel, $Y_4Al_2O_9$ (YAM) was proposed as a third host matrix to be studied for nanothermometry. In this case, experiments of YAM single-doped with Nd^{3+} and co-doped with Nd^{3+} and Yb^{3+} were conducted.

Chapter I of this thesis concerns the background of luminescence nanothermometry, explaining how the PL emission can be used to measure the temperature, and elucidates the main challenges associated with the practical implementation of light-emitting nanothermometers in the biomedicine field. As the development of such a project is a multifaceted endeavor, early-stage optimizations are essential prerequisites before embarking on biological assays. Therefore, the appropriate selection of yttrium aluminate oxides (YAG and YAM) and yttrium oxide as host matrices, along with Nd^{3+} and Yb^{3+} as doping elements to produce nanothermometers, has been described. In addition, the main concepts of synthesis methods for their fabrication (the modified Pechini method and synthesis from solution) are highlighted.

Chapter II unveils the preparation and structural characterization of YAG NCs co-doped with Nd^{3+} and Yb^{3+}, with an emphasis on controlling phase purity, crystallinity, size, and morphology. Initially, several samples were synthesized, with different concentrations of Nd^{3+} and Yb^{3+}, for further selection of which composition would bring up an optimized PL emission intensity of both luminescent ions (co-doping engineering). To achieve this goal, the modified Pechini method was employed, as this technique allows the synthesis of many samples in a rapid, simple, and cost-effective way, even if it commonly results in the formation of agglomerated NCs. The agglomeration of NCs gives rise to micrometer-sized particles, and they cannot disperse well in colloidal medium, posing challenges for future biological applications of these nanomaterials. Hence, efforts to improve the synthesis process under solvothermal conditions have been carried out in parallel to obtain monodispersed Nd^{3+}-Yb^{3+} co-doped YAG NCs. In addition, advancements in silica coating of these NCs to perform protected annealing and increase their PL emission intensity are exposed. Finally, it is presented the nanothermometry experiments based on the Luminescence Intensity Ratio (LIR) technique to obtain the calibration curve and assess the efficiency of utilizing YAG: Nd^{3+}-Yb^{3+} NCs as nanothermometers according to its relative thermal sensitivity (Sr), thermal resolution (δT), and repeatability of results.

Chapter III brings up a similar analysis of Y_2O_3 co-doped with Nd^{3+} and Yb^{3+} for nanothermometry. First, co-doping engineering was performed via the modified

Pechini syntheses to determine the composition of the dopants that yield intense PL emission for yttria. Then, to surpass the typical issue of NC agglomeration from the modified Pechini synthesis, the two-step urea-based route (solvothermal synthesis followed by calcination) was employed, and its parameters were deeply explored. Lastly, the thermal sensing performance of Nd^{3+}-Yb^{3+} co-doped yttria is highlighted, in terms of its sensitivity to temperature changes and ability to detect small values of temperature.

Chapter IV provides an overview of YAM as a nanothermometer when it is both single-doped with Nd^{3+} and co-doped with Nd^{3+} and Yb^{3+}. The analysis consisted of the synthesis via the modified Pechini method, structural and optical characterizations, and nanothermometry tests. In this chapter, it is also introduced a novel synthesis method for YAM using the two-step urea-based approach.

Overall, this thesis sheds light on the challenges to be addressed and the importance of working on them thoroughly during the early phase of the development of the thermal probes before moving forward to biological tests.

Chapter I: Introduction

1.1 General concepts of Nanothermometry

The design of thermal probes is constantly evolving, driven by the critical role that temperature plays in several physical, chemical, and biological processes. This brings massive importance to temperature measurement in industrial processes (e.g. manufacturing, maintenance of machinery), research, meteorology and environment, food safety, and health sciences [3–7]. Concerning the latter field, monitoring temperature can be not only beneficial for a full understanding of processes happening within the cells but also for the localization of inflammatory areas, monitoring of brain activity, performing early diagnosis of cancer, and assisting in hyperthermia treatments [8–13].

However, most of the thermal sensors available on the market still require direct contact with the object, which can cause interferences in the measurements, compromising the accuracy of the readout, besides being impractical in harsh environments. Others can work remotely but fail to achieve spatial resolution finer than the micrometer scale [14].

Therefore, nanosensors based on the principles of luminescence nanothermometry arise as an insightful alternative for gauging the temperature remotely, providing both high spatial resolution for temperature mapping (< 10 μm), and good thermal resolution (~ 0.10 K). In addition, the luminescent nanothermometers can work in different conditions [15,16].

Luminescent materials can emit spontaneous light after absorbing electromagnetic radiation (photons) — a process known as photoluminescence (PL). When there is a change in temperature, some modification in PL emission spectrum may occur, either in the spectral band shape, intensity, bandwidth, peak position, lifetime, or polarization (**Figure 1**). In this way, the temperature can be found by correlating the alteration in the optical signal with the temperature [17].

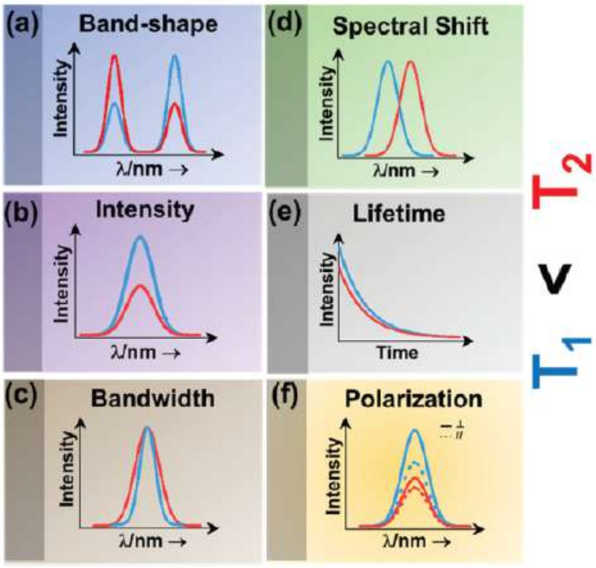

Figure 1. Types of variations in PL emission spectrum after a temperature change in **(a)** band-shape, **(b)** intensity, **(c)** bandwidth, **(d)** spectral shift, **(e)** lifetime, and **(f)** polarization [15].

1.1.1. Thermal sensing by LIR approach

Research on luminescence thermometry dates back to the decade of 1930s, but it experienced a significant boom in the 2010s [18]. These studies encompass the investigation of distinguished parameters for the development of nanothermometers, such as types of materials, luminescent centers, nanothermometry techniques, etc[15,17–20]. Regarding this latter factor, the one based on modifications in the band-shape has emerged as promising for the development of nanothermometers.

This approach consists of monitoring the variation in the ratio between two emission lines as a function of temperature. This ratio is referred to as Luminescence Intensity Ratio (LIR). One emission peak involved in LIR serves as an internal reference to the other, allowing a self-calibration of the system and mitigating the fluctuations by external factors during the measurement [14]. Additionally, the other advantages offered by this method rely on enhanced sensitivity to temperature changes, less influence of the emitter concentration, broad applicability (e.g. microelectronics, plasmonics, biomedicine, microfluids), and ease of use [20–22]. Some mechanisms can contribute to the influence of the temperature in the PL emission intensity, which includes thermal activation of non-radiative decay processes, re-distribution of population between excited levels according to Boltzmann’s statistics, energy transfer processes to quenching centers or between luminescent centers [17].

The thermometric parameter LIR can be formed either by two emission lines coming from the same luminescence emitter (single-center emission) or from two different luminescence emitters (dual-center emission). For materials presenting just one type of luminescence emitter, consider the scheme presented in **Figure 2**. When electromagnetic radiation is focused on the material, the state $|1\rangle$ is populated from the fundamental level $|0\rangle$. However, if the state $|1\rangle$ is close enough to the next upper level (hereafter referred to as state $|2\rangle$), with an energy gap (ΔE) smaller than 2000 cm^{-1}, the thermal energy might be sufficient to generate a population redistribution between the two excited states as long as it occurs more rapidly than any other competing radiative or nonradiative depopulation rate. As a consequence, these levels are regarded as thermally coupled levels (TCLs), and Boltzmann's Law can be applied to model the relation of LIR between the two TCLs with the temperature [14].

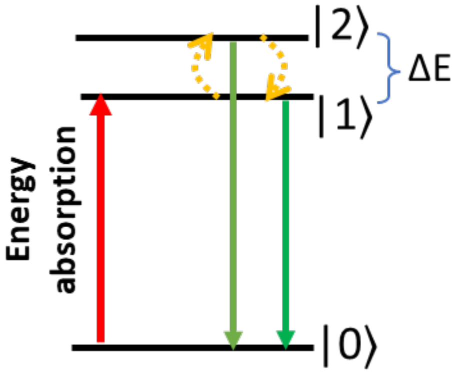

Figure 2. Simple energy-level scheme showing the dynamic between two thermally coupled states after light irradiation (Created by the author).

Considering N_1 and N_2 as the populations of states $|1\rangle$ and $|2\rangle$, respectively, they are related as follows

$$N_2 = N_1 \left(\frac{g_2}{g_1}\right) \exp\left(\frac{-\Delta E}{k_B T}\right) \tag{1}$$

where g_1 and g_2 are the degeneracies of states $|1\rangle$ and $|2\rangle$ respectively, k_B is the Boltzmann constant, and T is the temperature given in Kelvin (K). Generally, the luminescence intensity (I) from an excited state to the fundamental level can be described by expression 2,

$$I_i \propto \hbar\omega_i A_i N_i \tag{2}$$

where the index i indicates the excited state (i = 1, 2), ħ is the reduced Planck constant, ω is the angular frequency of the transition, and A is the total spontaneous emission rate. Combining the two expressions above, the equation correlating LIR with temperature for the single-center emission case is

$$\text{LIR (T)} = \frac{I_2}{I_1} = \text{B}\exp\left(\frac{-\Delta E}{k_B T}\right) \tag{3}$$

with $B = \frac{\omega_2 A_2 g_2}{\omega_1 A_1 g_1}$.

Therefore, by collecting the LIR of a single-center emitter at different temperatures and plotting the points on a graph LIR versus temperature (in K), the calibration curve of the nanothermometer is obtained when equation 3 is used to fit the points.

Regarding the thermal quality of the probe, some figures of merit can be referenced. The most used is the relative thermal sensitivity (S_r), which is used to compare different types of luminescent nanothermometers and indicates how the thermometric parameter (LIR, for example) varies per degree of temperature change. Thus, the higher Sr, the more sensitive the nanothermometer will be to temperature variations. The Sr is calculated by equation 4,

$$S_r = \frac{1}{\text{LIR}}\left|\frac{\partial \text{LIR}}{\partial T}\right| \tag{4}$$

where $\frac{\partial \text{LIR}}{\partial T}$ is denominated the absolute sensitivity (S_{abs}). Merging equations 3 and 4, Sr for a single-center emission becomes in %.K^{-1} (equation 5):

$$S_r(T) = \frac{\Delta E}{k_B T^2} \tag{5}$$

It is equally important to assess what is the minimum temperature change the nanothermometer can detect. This feature is represented by the thermal resolution (δT) in K, given by equation 6,

$$\delta T = \frac{1}{S_r}\left(\frac{\delta \text{LIR}}{\text{LIR}}\right) \tag{6}$$

with δLIR as the uncertainty of LIR. This is calculated by equation 7, in which δ_{I_1} and δ_{I_2} are the uncertainties of the PL intensities, and I_1 and I_2 are the average of a set of values.

$$\delta\mathrm{LIR} = \sqrt{\left(\frac{\delta_{I_1}}{I_1}\right)^2 + \left(\frac{\delta_{I_2}}{I_2}\right)^2} \tag{7}$$

From the expressions above, it is inferred δT is linked to both Sr and δLIR. As shown in equation 7, this latter parameter encompasses the intensity uncertainties (δ_{I_1} and δ_{I_2}), which are calculated from the standard deviation of multiple recorded PL spectra. If the signal-to-noise ratio of PL emissions is low, and fluctuations in the spectra are observed, δLIR tends to rise and, consequently, δT will be high. Hence, to achieve high thermal resolution, that is, the lowest resolvable temperature values, it is essential to produce a highly sensitive nanothermometer with strong PL emission intensity, and to enhance the experimental setup to ensure the stability of PL measurements.

In addition to Sr and δT, it is of great interest that the output is repeatable. Thus, the precision in a measurement system can be taken by performing heating and cooling cycles on the nanoprobes under similar conditions. For every cycle, the LIR at a given temperature is calculated, and the repeatability (R) is estimated by the following equation:

$$\mathrm{R} = 1 - \frac{\max(|\mathrm{LIR_c} - \mathrm{LIR_i}|)}{\mathrm{LIR_c}} \tag{8}$$

where $\mathrm{LIR_c}$ is the LIR extracted from the calibration curve, and $\mathrm{LIR_i}$ is the LIR collected at every temperature during the cycles. The closer R is from 100%, the better is the repeatability of the thermal sensor.

Although the temperature readout from a single-center emitter nanoprobe is very simple and easy to get, the demanding of two TCLs limits the nanothermometer improvement, because Sr depends directly on ΔE, as demonstrated in equation 5. If this energy difference is less than 200 $\mathrm{cm^{-1}}$, there is a high probability the peaks will overlap, leading to distorted results of temperature measurement. On the other hand, an energy gap larger than 2000 $\mathrm{cm^{-1}}$ might not provide the coupling of the excited states. To address this situation, one alternative is to develop materials with dual-center emission, presenting two different PL emitters that interact with each other through non-radiative energy transfer. As illustrated in **Figure 3**, one emitter harvests the excited energy and transfers part of it to the second one, and both of them emit PL.

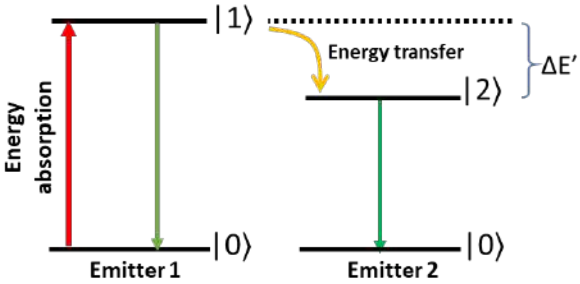

Figure 3. Simple energy-level scheme to illustrate the energy transfer of one emitter to the other in dual-center emission materials (Created by the author).

This energy transfer can be resonant if the excited states of the two ions are closely matched in energy. On the contrary, the process is non-resonant, being assisted by phonons or requiring a simultaneous transfer to a third ion [23]. When phonons are involved, the inter-ionic energy transfer (W_{PAET} (T)) can be described according to Miyakawa-Dexter formalism by the following expression:

$$W_{PAET}(T) = W_{PAET}(0).\left[\frac{1}{\exp\left(\frac{h\nu}{k_B T}\right) - 1} \pm 1\right]^n \tag{9}$$

where W_{PAET} (0) is a constant, hν is the phonon energy of the host, and n is the number of phonons in the process. If it requires phonons absorption, the operation inside the brackets is a sum. Otherwise, the operation is a subtraction [24,25]. Based on equation 9, it is reasonable to assume the emission of the ion that receives the energy mediated by phonons is going to be strongly dependent on the temperature, as the energy transfer is too [25–27]. However, it is also possible that the energy transfer involves contributions from both resonant and non-resonant processes, rather than being purely one or the other [28].

Overall, for a dual-center emitter, the LIR will be between two emission lines coming from different luminescent centers. The calibration curve is found by doing an appropriate fitting on the points of LIR versus temperature, and the thermometer performance is assessed with equations 4, 6 and 8. Hence, it is expected that working with a nanothermometer with dual center emission paves the way for achieving even better thermal performance in comparison to those based on Boltzmann's law.

1.1.2. Luminescent nanocrystals for LIR nanothermometry

1.1.2.1. Basic requirements of luminescent materials for biological applications

The development of a nanothermometer for thermal sensing in living beings is a challenging task as certain fundamental prerequisites must be met. Generally, the luminescent nanothermometer must exhibit low or negligible toxicity, stability and dispersibility in physiological medium, high brightness, biocompatibility, and photostability [15,16].

The size of the nanothermometer is a critical factor, because it influences the colloidal stability, physical properties (e.g. optical absorption), body and tissue distribution (flow in the bloodstream and clearance), cellular response and uptake, etc. In general, the nanoparticles (NPs) must be large enough (> 10 nm) to avoid their clearance by the kidney, since the glomerular filter pore of this organ is 2 – 8 nm; but small enough to not be captured by the mononuclear phagocyte system (< 200 nm). However, the size needs to be set according to the specific application and the targeted biosystem. For example, if the aim is reaching a tumor, NPs larger than 200 nm will be removed by the spleen, but the ones smaller than 30 nm can go back to the blood vessels. Therefore, it is recommended that inorganic NPs are smaller than 100 nm and have a narrow size distribution to ensure high dispersion stability. Consequently, this will facilitate their ability to travel from the injection site to the target site via blood circulation, minimizing the risk of uneven biodistribution [29–31]. Additionally, it is stated that spherical morphology provides lower toxicity compared to other types of morphology, such as tubes, fibers, plates, and needles[32]. On the other hand, rod-shaped NPs are easier to reach the target and exhibit a prolonged lifespan in the bloodstream [29,33].

Attention must also be given to the optical properties of the NPs, especially the spectral working range. The visible range (400 – 700 nm) is usually not recommended when targeting bio applications due to the large absorption of light by the physiological components (e.g. fat, hemoglobin), causing a shallow penetration of the light. In contrast, operating in the transparent optical BWs enables deep tissue signal detection with minimal interference [34]. The BWs fall in the Near Infrared (NIR) spectrum where absorption and scattering of both excitation and emission light by tissues, skin, and lipids are reduced. They are divided into BW-I, BW-II and BW-III, corresponding to the ranges of 750 – 950 nm, 1000 – 1350 nm (BW-IIa in **Figure 4**), and 1500 – 1800 nm (BW-IIb in **Figure 4**) respectively, in which the extinction coefficient of human skin and components and the light scattering are minimized [35,36].

Even working in the BWs, the tissue extinction is not completely negligible and may misshape the emission spectrum, compromising the reliability of *in vivo* thermal reading [37]. Thus, care must be taken regarding the autofluorescence of the tissues (green stars in **Figure 4**), because most of them present a broad autofluorescence band, which can overlap with the emission spectrum of the nanothermometer, resulting in erroneous readout. For this reason, it is preferable to work with NPs that exhibit narrow emission lines [38].

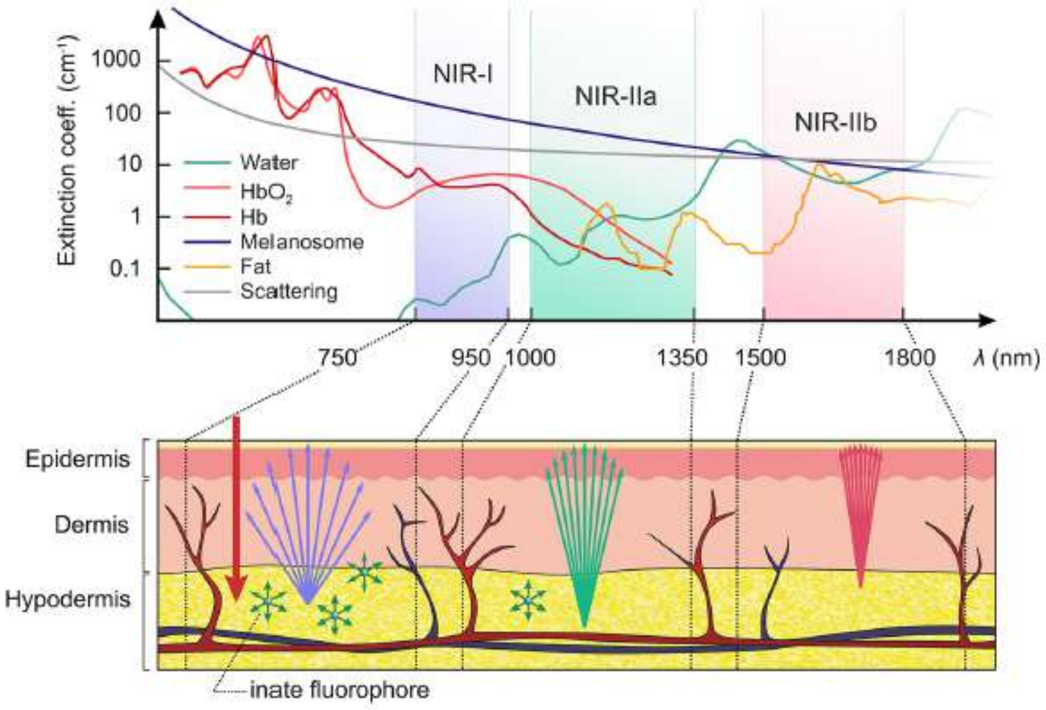

Figure 4. Absorption spectrum of human skin, displaying the BWs. The green stars represent endogenous autofluorescence, and the arrows are related to the degree of light scattering. In BW-IIb, the reduced light scattering provides a higher spatial resolution compared to the other BWs [36].

Concerning the type of materials, many have been exploited and reported in the literature, like semiconductor quantum dots (QDs), organic-inorganic hybrids, organic dyes, metal organic frameworks (MOFs) and rare-earth doped NPs. QDs (e.g. Ag_2S, PbS) are semiconductors that draws attention for presenting high quantum yield and easily tunable luminescence features, but they can present toxicity problems, induce changes in genes, and display unreliable thermal reading, due to the dependency of luminescence properties on the environment. This latter problem is also encountered with organic dyes, as their performance can be affected by factors such as pH, solvent, and temperature, requiring a unique calibration curve for each specific environment. A key advantage of organic dyes is their sensitivity to temperature changes. Likewise, organic-inorganic hybrids and MOFs are very sensitive, but they can only emit in the visible range (VIS) and are toxic, respectively [15].

Conversely, rare-earth-doped NPs are particularly attractive. Rare-earth ions belong to an ensemble formed by the lanthanides (Ln^{3+}) and yttrium, that are characterized for having an incomplete 4f sublevel, shielded by $5s^2$ and $5p^6$ orbitals. Owing to this shield, their emission lines are stable, narrow, and not significantly altered when the rare-earth ions are embedded in different hosts. Furthermore, they present long lifetime (from µs to ms), high emission quantum yields in general, good stability in physiological medium, and the possibility of being excited with economically viable commercial sources, without demanding high power to excite them [15,17]. Accordingly, NPs doped with rare-earth ions come as promising candidates for nanothermometry applied to the biological domain.

1.1.2.2. Selection of the rare-earth ions

The great variety of rare-earth ions offers numerous opportunities to build nanothermometers. Indeed, many works on nanothermometry about NPs doped with Er^{3+}, Nd^{3+}, double doped with Er^{3+} and Yb^{3+} or Ho^{3+} and Tm^{3+} have been reported over the past years [15,20,22]. Nonetheless, as mentioned earlier, it is essential that these luminescent NPs attend the requirement of working within the BWs.

Under this framework, Nd^{3+} is a well-known Ln^{3+} used in the fabrication of efficient solid-state lasers, but it has gained good perspectives to be applied in fluorescent biocompatible NCs [39,40]. Nd^{3+} ions can be excited inside the BW-I at a wavelength around 800 nm, which allows deep penetration of light in tissues with minimal heating, thereby causing low damages to the cells — as long as an appropriate power excitation source is used. Moreover, low-cost diode laser operating at this wavelength can be easily found on the market [16,36,39].

Upon excitation, a transition is promoted from the ground level $^4F_{9/2}$ to the excited levels $^4F_{5/2}$ and $^2H_{9/2}$. After a fast non-radiative decay to the excited level $^4F_{3/2}$, Nd^{3+} exhibits radiative transitions of $^4F_{3/2} \rightarrow {}^4I_{9/2}$ (~850 nm), $^4F_{3/2} \rightarrow {}^4I_{11/2}$ (~1060 nm), and

$^4F_{3/2} \rightarrow {}^4I_{13/2}$ (~1340 nm) (**Figure 5.(a)**). The narrow Stark lines arising from the transitions $^4F_{3/2} \rightarrow {}^4I_{9/2}$ and $^4F_{3/2} \rightarrow {}^4I_{11/2}$ have been widely employed for LIR nanothermometry governed by Boltzmann's law. The latter transition, in particular, is notable for enabling temperature sensing at tissue depth of a few millimeters due to the higher intensity of its emission Stark lines [41].

Yb^{3+} is another favorable rare-earth ion for luminescent nanothermometers. It has a simple electronic configuration with $^2F_{7/2}$ as the fundamental state and $^2F_{5/2}$ as the excited state (**Figure 5.(b)**), with an energy gap between them of approximately 10000 cm^{-1}. Such large inter-manifold gap does not favor multiphonon non-radiative relaxation, leading to an efficient PL emission with a long excited-state lifetime in the millisecond range. Furthermore, Yb^{3+} has a strong ion-lattice coupling as its electronic configuration makes the 4f electrons less shielded than that of other Ln^{3+} ions, resulting in an effective light absorption. Because of its large absorption cross-section at ~980 nm, Yb^{3+} can absorb radiation efficiently and, consequently, transfer energy to other ions [42–44]. Even though it features these major advantages, and highly sensitive thermometers have already been produced using Yb^{3+} as a sensitizer (with Sr at least above $1.00\%.K^{-1}$) [45–49], it becomes less suitable towards *in vivo* applications. A radiation at ~980 nm causes an undesired light absorption of the water, owing to the presence of water absorption in this range. This can lead to unwanted heating and, as a result, cell damages or even cellular death [36,39,50,51].

However, a system combining Nd^{3+} and Yb^{3+} holds promise for nanothermometry in the biological context. Nd^{3+} can be irradiated at around 800 nm — ensuring a gain signal at larger depths in tissues and avoiding the overheating caused by water absorption[36] — and sensitize Yb^{3+} through a non-radiative process of energy transfer. This process can be either resonant or mediated by phonons, depending on the energy gap between the excited levels $^4F_{3/2}$ and $^2F_{5/2}$ of Nd^{3+} andYb^{3+} in the respective order, as well as on the overlap of donor emission (Nd^{3+}) and acceptor absorption (Yb^{3+}) spectra. In the literature, the interaction between the two Ln^{3+} ions in crystals and glasses through an energy transfer is well established [26,27,52–55].

The temperature sensing of Nd^{3+} - Yb^{3+} co-doped NPs is performed by observing the emission changes of one Ln^{3+} relative to the emission of the other. That is, the LIR is taken between the emission intensities of Nd^{3+} and of Yb^{3+}. Even if the emission of Yb^{3+} ($^2F_{5/2} \rightarrow {}^2F_{7/2}$) is commonly located at around 980 nm, this peak can split into different lines due to the Stark effect. It involves the break of the energy states degeneracy in sublevels separated by only 100 cm^{-1} due to the action of the crystal field in a crystalline environment. One can have up to 2J+1 and J+1/2 energy levels for even and odd electron numbers, respectively [56]. Thus, as demonstrated by previous works [27,52,53,57,58], some stark lines may fall inside the BW-II (1000 – 1350 nm), making it possible to still work with Yb^{3+} emission without the concern of water absorption at 980 nm. However, it is important to highlight this system is still not so simple, as other types of energy transfer in the system may occur depending on the concentration of the Ln^{3+} inside the matrix, such as the back energy transfer from Yb^{3+} to Nd^{3+} and the Yb^{3+}-Yb^{3+} diffusion energy [27,59]. These processes are shown in **Figure 5.(c)**.

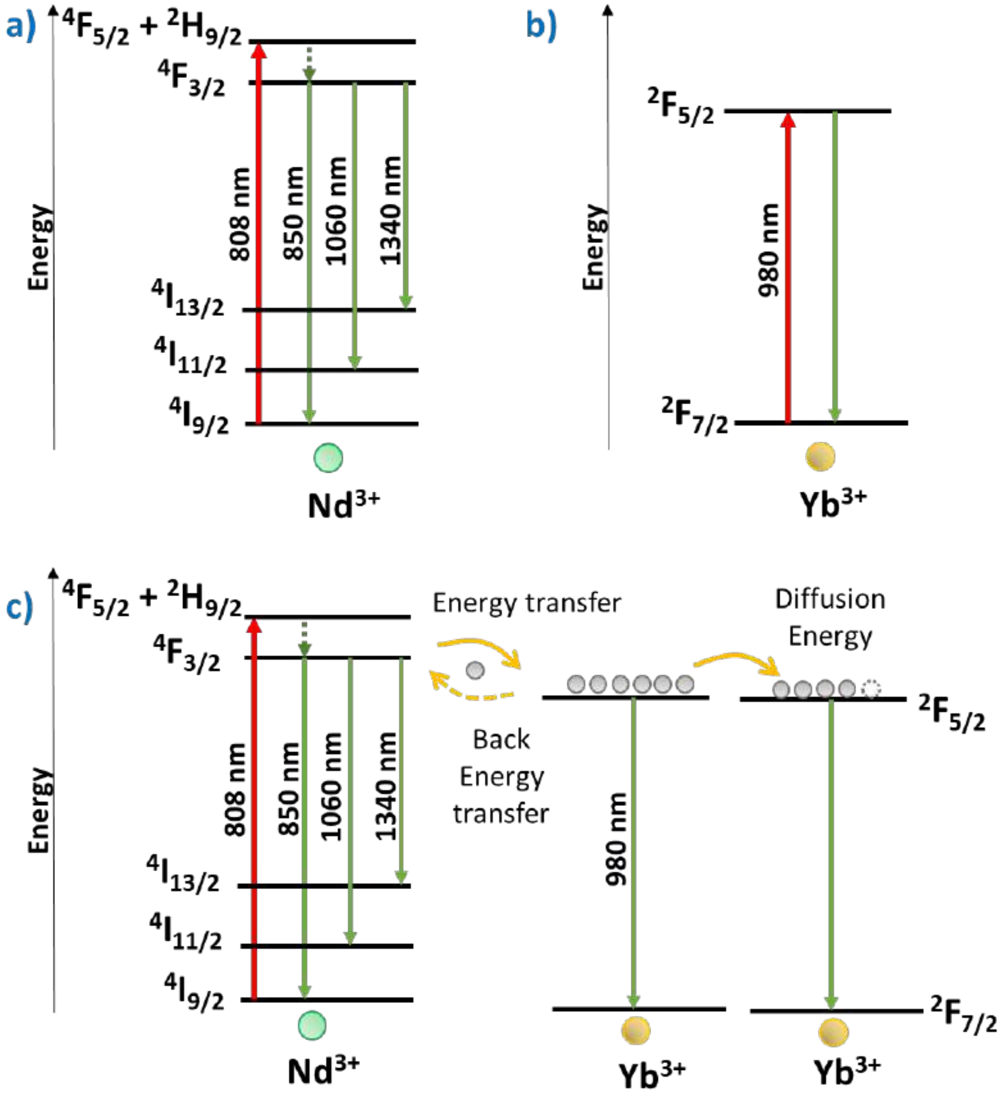

Figure 5. **(a)** Energy level diagram of Nd^{3+}; **(b)** Energy level diagram of Yb^{3+}, **(c)** Scheme showing the dynamics of Nd^{3+} - Yb^{3+}, with indication of energy transfer of Nd^{3+} → Yb^{3+}, back energy transfer of Yb^{3+} → Nd^{3+} and diffusion (migration) energy of Yb^{3+} - Yb^{3+} (Created by the author).

Works of luminescence nanothermometry on NPs doped with Nd^{3+} and co-doped with Nd^{3+} and Yb^{3+} are summarized in **Table 1**. This tabulation was limited only to those that went for λ_{exc} in the BW-I (750 – 950 nm) and presented Sr in the physiological temperature interval. In general, the single-doped materials with Nd^{3+} exhibit Sr extending from around 0.10 to 0.60%.K^{-1}, since the LIR is taken between the Stark sublevels of the transition $^4F_{3/2} \rightarrow$ $^4I_{9/2}$ or $^4F_{3/2} \rightarrow$ $^4I_{11/2}$, and the energy difference between the involved sublevels tends to be very small. Other studies on Nd^{3+}-based nanothermometers have already reported even higher Sr, such as YVO_4: Nd^{3+} (1.50%.K^{-1} at 300K)[60], Y_2O_3: Nd^{3+} (1.59%.K^{-1} at ~303 K)[61], Gd_2O_3: Nd^{3+} (1.75%.K^{-1} at 288 K)[62], and $YAlO_3$: Nd^{3+} (1.83%.K^{-1} at 293 K)[63]. In spite of operating with Stark sublevels, the LIR was regarded between the transitions $^4F_{5/2} \rightarrow$ $^4I_{9/2}$ and $^4F_{3/2} \rightarrow$ $^4I_{9/2}$ in these cases, which was only possible thanks to the excitation in the visible range (532 nm [60,61,63] and 580 nm[62]), that is, outside the BWs. Concerning the Nd^{3+} - Yb^{3+} co-activated materials, Sr is very similar on average to those Nd^{3+}-single-doped ones, but the great majority still worked with the Stark emission line at ~ 980 nm of Yb^{3+}, which overlaps with the water absorption band. Unfortunately, most of the works did not report the thermal resolution as well. In summary, this short overview unveils how challenging it is to work with Nd^{3+} and Yb^{3+} within the BWs and achieve optimal thermal performance simultaneously.

Table 1. Summary of Nd^{3+}-doped and Nd^{3+}-Yb^{3+} co-doped NPs with corresponding thermal performance published in the literature. The selection of these works was restricted to the excitation wavelength (**λ_{exc}**) in the BW-I.

Host	λ_{exc} (nm)	Temperature range (K)	Emission lines for LIR (nm)	Sr (%.K^{-1})	δT (K)	Ref.
Y_3BO_6: Nd^{3+}	804	298 - 328	1072/1083	0.07 (at 308 K)	–	64
YBO_3: Nd^{3+}	804	298 - 328	1056/1060.5	0.10 (at 308 K)	–	64
$NaYF_4$: Nd^{3+}	830	273 - 432	863/870	0.13 (at 308 K)	–	65
$Y_3Al_5O_{12}$: Nd^{3+}	808	283 - 343	936/946	0.15 (at 343 K)	0.30	66
$Y_3Al_5O_{12}$: Nd^{3+}	804	298 - 328	1052/1074	0.16 (at 308 K)	-	64
CaF_2: Nd^{3+}, Y^{3+}	808	~295 - ~335	1053/1062	0.18 (at 300 K)	-	67
$Gd_3Sc_2Al_3O_{12}$: Nd^{3+}	806	293 - 323	936/946	0.20 (at 298 K)	-	40
LaF_3: Nd^{3+}	808	283 - 333	865/885	0.26 (at 283 K)	-	68

Table 1. Continued.

Host	λ_{exc} (nm)	Temperature range (K)	Emission lines for LIR (nm)	Sr (%.K^{-1})	δT (K)	Ref.
Y_2O_3: Nd^{3+}	800	303 - 333	878/947	0.29 (at 293 K)	-	69
$Y_2Ge_2O_7$: Nd^{3+}	804	298 - 328	1056/1074.5	0.29 (at 308 K)	-	64
Y_2O_3: Nd^{3+}	804	298 - 328	1056/1074	0.34 (at 308 K)	-	64
Y_2O_3: Nd^{3+}	808	298 - 333	1053/1075	0.43 (at ~298 K)	< 1.0	61
$LiLuF_4$: Nd^{3+}@ $LiLuF_4$	793	293 - 318	1047/1056 887/913	0.48 (at 293 K) 0.58 (at 293 K)	0.30	41
LaF_3: Nd^{3+}-Yb^{3+}	790	283 - 323	1300/1000	0.10 (at 283 K)	-	70
YF_3: Nd^{3+}-Yb^{3+}	790	80 - 320	866/986	0.10 – 0.40	-	71
YVO_4: Nd^{3+}-Yb^{3+}	808	123 - 423	~870/~980	0.14 (at 273 K)	-	72
Y_3BO_6: Nd^{3+}-Yb^{3+}	804	298 - 328	1072/977	0.18 (at 308 K)	-	57
$LuVO_4$: Nd^{3+}-Yb^{3+}	808	123 - 573	~1060/~975	0.20 (at ~299 K)	2.0	73
YBO_3: Nd^{3+}-Yb^{3+}	804	298 - 328	1056/971	0.21 (at 308 K)	-	57
$Y_2Ge_2O_7$: Nd^{3+}-Yb^{3+}	804	298 - 328	1056/978	0.22 (at 308 K)	-	57
β-BaB_2O_4: Nd^{3+}-Yb^{3+}	804	298 - 328	979/1058.5	0.28 (at 298 K)	-	74
$Y_2Ba_3B_4O_{12}$: Nd^{3+}-Yb^{3+}	804	298 - 328	897/978	0.31 (at 298 K)	0.54	75
$Y_3Al_5O_{12}$: Nd^{3+}-Yb^{3+}	804	298 - 328	1051/965.5	0.33 (at 308 K)	-	57
$LiLaP_4O_{12}$: Nd^{3+}-Yb^{3+}	808	93 - 663	870/1000	0.40 (at 330 K)	-	27
Y_2O_3: Nd^{3+}-Yb^{3+}	804	298 - 328	1055/976	0.48 (at 308 K)	0.36	57
LaF_3:Yb^{3+} @ LaF_3:Nd^{3+}	808	288 - 323	1350/1000	0.74 (at 293 K)	-	76

1.1.2.3. Selection of the nanocrystalline inorganic host matrices

Alongside the doping elements, the selection of the host lattice material must also be thorough. Indeed, the host matrix can dictate the PL efficiency, since it depends on the phonon energy, structure, crystal field, and local symmetry. Among these features, host matrices presenting low phonon energy have been preferable for presenting reduced probability of non-radiative processes, as more phonons are necessary to bridge the gap amongst excited and fundamental states in this case [77]. Regarding this fact, the scientific community has been extensively working with fluoride-based inorganic materials for nanothermometry, because their phonon energies can range between 300 and 600 cm^{-1} (e.g. 350 cm^{-1} for $NaYF_4$) [36,77,78]. In addition, the synthesis of monodispersed and nanometric-sized particles of fluoride-based host materials is well established in the literature [79,80]. Although low phonon energy can result in enhanced brightness, this is not a guarantee that a high thermal sensitivity will be provided too. Other parameters can influence in the thermal performance of the nanothermometer, such as bond covalency and the effect of the local site symmetry [22,78,81].

As an alternative to fluoride-based NCs, oxides can provide competitive advantages of convenient synthesis methods, non-toxicity, mechanical and chemical stability, especially after their functionalization[40,82]. In this respect, aluminate oxides, belonging to the Al_2O_3-Y_2O_3 binary system, and Y_2O_3 may be promising hosts for embedding Nd^{3+} and Yb^{3+} because these rare-earth ions present the same oxidation state and have ionic radii closely matching those of Y^{3+} species. It enables the replacement of Y^{3+} by them, with less formation of crystal defects and lattice stresses [77].

The Al_2O_3-Y_2O_3 binary system comprises four crystalline phases: $YAlO_3$ in orthorhombic (YAP) and hexagonal (YAH) structures, $Y_3Al_5O_{12}$ (YAG) and $Y_4Al_2O_9$ (YAM). Particularly, YAG has been deeply studied and is well-known for its efficient performance as solid-state lasers, LED-based lighting, and nanoprobes in the biological field [83]. It presents a garnet structure, with a cubic unit cell of 160 atoms (space group *Ia3d*), and a single Y^{3+} site of D_2 symmetry (**Figure 6**). The general formula is given by $A_3B_2C_3O_{12}$, where A, B and C represent the cations occupying 24(c) sites of YO_8 (dodecahedral coordination), 16(a) sites of AlO_6 (octahedral coordination) and 24 (d) sites of AlO_4 (tetrahedral coordination), respectively. Concerning the phonon energy, YAG has a cutoff of ~856 cm^{-1} [25].

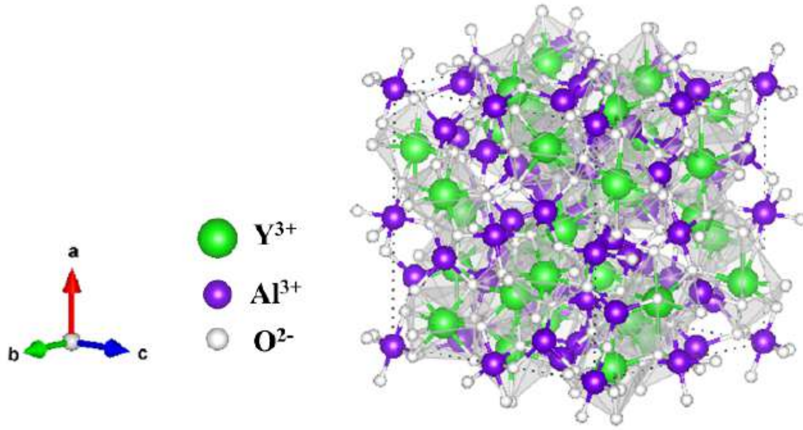

Figure 6. YAG crystal structure. This scheme was reproduced in the software Vesta based on the ICSD CIF 17663.

Derived from the same system, YAM is a stable compound, which presents a structure with lower symmetry than YAG. Although it is still less studied than YAG, some works have shown that YAM can be a promising optically active host [44,84,85]. Its crystal structure is monoclinic and belongs to the $P2_1/c$ space group. In accordance with **Figure 7**, YAM has multisite structure, possessing four yttrium sites with C_1 symmetry, and a total of nine non-equivalent oxygens. Two yttrium sites are coordinated to seven oxygens (YO_7) whereas the other two have six oxygen atoms in the neighborhood (YO_6), exhibiting a slight deviation from inversion symmetry. Two AlO_4 groups are united by one apical oxygen forming double-tetrahedral Al_2O_7 in the unit cell. These structural features make YAM interesting for multiple doping, offering several possibilities for the occupation of yttrium sites by rare-earth ions [44,86,87].

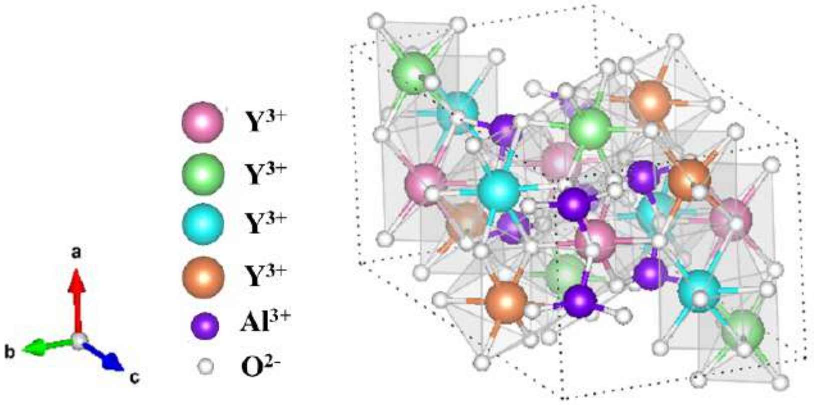

Figure 7. YAM crystal structure. This scheme was reproduced in the software Vesta based on the ICSD CIF 230984.

Finally, Y_2O_3 is a host favored in many studies due to its chemical and thermal stability, presenting a melting point above 2000°C. This sesquioxide crystallizes in cubic phase, in the *Ia-3* space group. The unit cell contains yttrium in two structural sites, surrounded by six oxygen atoms (YO_6) with C_2 and C_{3i} symmetries (**Figure 8**) [88]. A good shortcoming from Y_2O_3 is its comparable low phonon energy to fluorides, which is approximately 600 cm^{-1} [25,89].

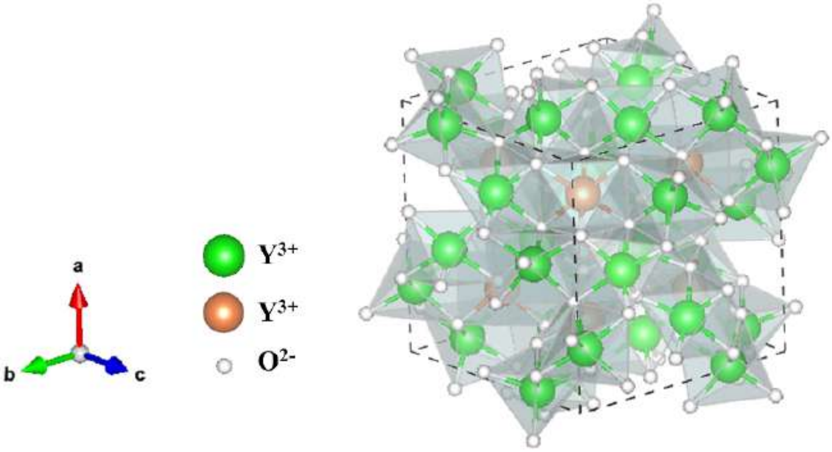

Figure 8. Y_2O_3 crystal structure. This scheme was reproduced in the software Vesta based on the ICSD CIF 26190.

1.1.2.4. Implementation of luminescent nanothermometers in biomedicine

Even working with appropriate conditions from the material science perspective, the direct implementation of luminescent NPs in living organisms is still not simple and entails some considerations. Prior to the application of NPs in the biological system, their physicochemical properties (colloidal stability, surface composition, and surface charge) must be tailored to ensure biocompatibility, and to avoid toxicity issues [90]. In light of this, silica coating is an effective method to passivate the surface, because silica is highly regarded in the scientific community for its thermal stability, chemical inertness, and optical transparency. It enhances the stability of NPs in colloidal medium, facilitates further functionalization with other molecules, and can act as a protective layer to the NPs for post-annealing treatments, to avoid both uncontrolled growth and irreversible agglomeration, besides improving the crystallinity[91–93].

Concerning the toxicity of silica, there is enough evidence to classify crystalline silica (quartz and cristobalite) as carcinogenic to humans (group 1 by the IARC – International Agency for Research on Cancer), but amorphous silica has been considered safe without indication for carcinogenicity (group 3 by the IARC). Still, there is a controversial position about amorphous silica safety in the literature, due to cases of hemolysis and death of cells in culture when silica is involved. However, the hemolytic potential of silica is strictly related to the presence of silanol groups, which can bond to phosphate ester groups of membrane phospholipids and secondary amide groups of proteins, disturbing the cellular membrane. This issue is overcome with heat treatments to reduce the silanol concentration or by going for mesoporous structure of silica, because the porosity reduces its area contact with the membrane and, thus, the effective silanol concentration [94].

Within the nanothermometry context, the core-shell structure, with luminescent inorganic NC as the core and amorphous silica as the shell, provided enhanced PL properties, making the NPs more effective as temperature sensors. In the study of YPO_4: Er^{3+}-Yb^{3+}, surrounding the NCs with a silica shell attenuated the surface defects, and an increase of PL emission in 12 times was observed. It resulted in the reduction of the non-radiative rates, leading to an increase of ΔE between TCLs, causing, consequently, an improvement in the Sr from 1.00 to 1.25%.K^{-1} at 303 K [95]. An enhancement in the sensitivity to temperature changes was also observed for $GdVO_4$: Er^{3+}- Yb^{3+} [96] and YVO_4: Nd^{3+} NPs [97]. In addition, the silica shell provided stability in colloidal environment and facilitated the entry of $GdVO_4$:Tm^{3+}- Yb^{3+} in HeLa (Human cervical cancer cell line) cells during *in vitro* assays for tests of thermal sensing [98]. Going beyond the biological realm, the silica shell endowed $NaFY_4$:Er^{3+}- Yb^{3+} with improved thermal stability, allowing the shelled NPs to operate at temperatures exceeding 900 K, above which they normally do without the shell (~600K) [99].

The *in vivo* administration of nanothermometers hinges on the specific application model. For example, to keep track of hyperthermia, the NPs are either administered intravenously or injected straight into the organ of interest. On the other hand, subcutaneous or intradermal injections are performed when it is necessary to have a precise control over the NPs and minimum interference of the tissue [100]. The escape of the NPs from the physiological system is also a critical aspect and involves two main pathways: renal and hepatic. The former is often the preferred route for being rapid, but it is more effective for small and positively charged NPs due to the size of the glomerular pore of the kidney (< 10 nm), and their interaction with the negatively charged components of the glomerular filtration barrier. The hepatic pathway regards the capture of the NPs by the mononuclear phagocyte system (e.g. liver), leading to the excretion via bile into the intestines. Hence, this provides a longer exposure of the NPs to the body, which can result in their accumulation in organs, posing risks of toxicity [101,102].

These facts demonstrate it is crucial to determine a balance between effective clearance and NPs distribution efficacy. In this way, further functionalization of the NPs is necessary for the improvement of their interaction with biological interfaces. It can be accomplished by combining NC@SiO_2 (NC coated with silica) with molecules such as small proteins, natural or synthetic polymers, oligosaccharides, for example. In bio applications, the synthetic biopolymer polyethylene glycol (PEG) is one of the most used molecules [90]. This polymer has chemical structure of $HO\text{-}[CH_2\text{-}CH_2\text{-}O]_n\text{-}H$, where n is the quantity of ethylene oxide units, and is popularly used in drug formulations, and food products. Through the "PEGylation" process, the PEG chains create a hydrophilic barrier around the NPs, diminishing their interactions with plasma proteins, thereby prolonging their circulation time in the bloodstream with reduced risks. Moreover, PEG can reduce immunogenicity— an immune response in the body caused by foreign species —, avoid the aggregation, and improve the delivery efficiency of the NPs in the targeted biosystems [90,103–105].

The concentration of NPs is also of key importance to reach the targeted systems at an appropriate dose to function effectively as designed. According to the guidelines proposed by Bednarkiewicz et al.[16], this concentration should be no more than 0.5 mg per mL to guarantee the *in vivo* safety. According to the spectroscopy conditions, the authors stated in the same work that the excitation power density should be no higher than 0.3 $W.cm^{-2}$ for an excitation wavelength at 808 nm, because this value is the Maximum Permitted Exposure (MPE) defined by the International Commission on Non-Ionizing Radiation Protection in the ANSI Z136.1-2000. Indeed, the lack of attention to excitation power density generates extra heating on the sample, resulting in mistaken readouts and possible damage to the cells. Lastly, the calibration curve must be acquired in both aqueous media and the targeted organs for the study using *ex vivo* models. Particularly, chicken breast has been utilized for this assay, because it exhibits homogeneous tissue, reduced absorption properties, and enough thickness to evaluate the laser penetration depth. In contrast, phantom tissues (e.g. breast, cartilage, skin, etc.) are also applied, but they do not resemble the chemical environment of real tissues [100].

Notwithstanding the boom of studies in nanothermometry, works encompassing *in vivo* experiments with inorganic NPs co-doped with Nd^{3+} and Yb^{3+} and satisfying all the requirements presented here are very scarce. However, an example is the work from

2016 conducted by Ximendes et al.[70], who reported the subcutaneous thermal sensing in a mouse by using core-shell LaF$_3$:Nd^{3+} @ LaF$_3$: Yb^{3+} NPs. Before the *in vivo* experiment, the authors acquired the calibration curve of the NPs in aqueous medium, pumped at 790 nm, and got a Sr equal to 0.41 ± 0.01 %.C^{-1} with δT ~1.6°C. Next, 1% in mass of the NPs were dispersed in 200 µL phosphate-buffered saline (PBS) and injected into a mouse. To assure the presence of the NPs in the mouse, they were illuminated at 808 nm with power density of 0.35 W.cm^{-2}, and a fluorescence image was registered (**Figure 9.(a)**), which enabled the NPs to be clearly located. Then, the power was doubled deliberately in order to promote the temperature rise from 34.2 up to 40.5°C (**Figure 9.(c)**). In the end of the heating, the natural thermal relaxation was monitored by exciting the same NPs at 790 nm instead, and the temperature estimated with the calibration curve was 39 ± 1 °C, rather similar to 38°C acquired with an infrared thermal camera (**Figure 9.(f)**). In addition to these promising results, the authors demonstrated that the PL spectrum is not affected by the environment, when comparing the emission spectrum in aqueous solution and in a chicken breast (*ex vivo* model).

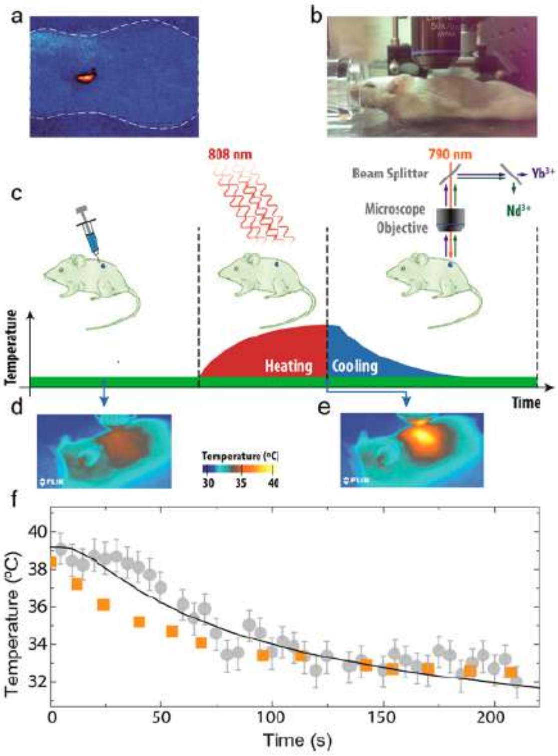

Figure 9. (a) Fluorescence image showing the presence of LaF$_3$:Nd^{3+}@ LaF$_3$: Yb^{3+} NPs in the mouse body; **(b)** Picture of the mouse during the experiments; **(c)** Scheme illustrating the procedure for thermal sensing; **(d)** Thermal infrared images before and **(e)** in the end of the heating; **(f)** Evolution of measured temperature with calibration curve (gray points) and infrared thermal camera (orange squares) in time [70].

1.2. Preparation of nanocrystals: general concepts and mechanisms

The general preparation of NCs can be done either through a solid-state synthesis or from a wet chemical approach. While the first one requires specialized and expensive set up to conduct the synthesis at specific conditions of pressure, temperature, and environment, the last one is relatively simpler and permits a better control on size, composition, and morphology of the NCs. Several wet chemical methods have been employed to obtain oxide NCs, such as aqueous and non-aqueous sol-gel, coprecipitation, microwave-assisted, solvothermal, and others [106]. However, this work will be restricted to the modified Pechini and solvothermal methods in view of synthesizing YAG, Y_2O_3 and YAM NCs co-doped with Nd^{3+} and Yb^{3+} for nanothermometry.

1.2.1. Modified Pechini method

The Pechini method is a simple, direct, and generic way to obtain oxide materials, which was first introduced in a patent in 1967 by Pechini [107]. The author proposed to form polybasic acid chelates with different cations by using a combination of metal oxides, hydroxides, alkoxides, or carbonates as precursors, along with alpha-hydroxycarboxylic acids (e.g., citric acid and glycolic acid). By heating these chelates with a polyhydroxy alcohol, polyesterification reactions are promoted, resulting in a resin. This resin is then calcined to remove organics, leaving behind the oxide material.

Nevertheless, some modifications have been made over the years with focus on reducing the amount of organic products, and the “modified Pechini method” came up. In this case, aqueous solutions containing cations in stochiometric proportions are used along with a chelate agent for the metal complexation with citrate anions. Successive polyesterification reactions occur by including polyalcohol at controlled temperature, giving rise to a rigid cross-linked polymeric resin comprising metal atoms bonded with oxygen and organic radicals. Next, the resin is finally calcined (under air or controlled atmosphere) for the crystallization of nanometer-sized metal oxides and removal of organics [108]. It should be noted that ethylene glycol is typically the polyalcohol used in this method, but it can be successfully replaced by D-sorbitol for improved photophysical properties [109]. The reactions involved in the modified Pechini method, with D-sorbitol as the polyalcohol, are illustrated in **Figure 10**.

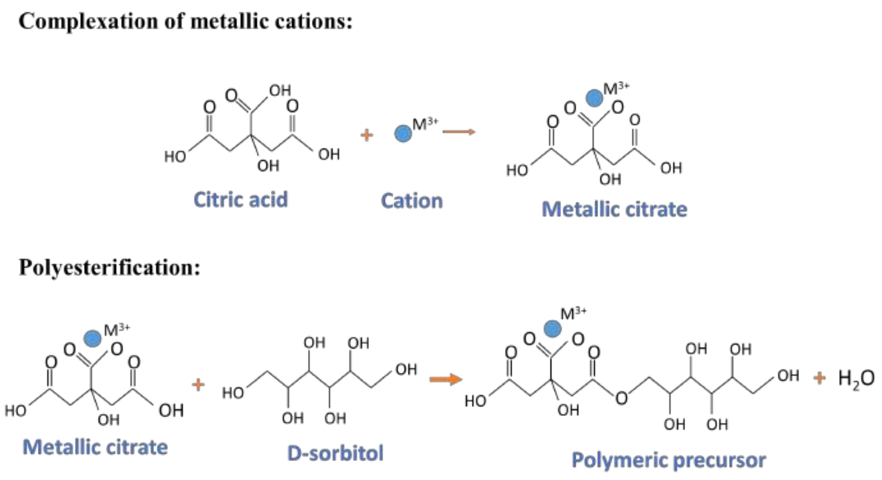

Figure 10. Chemical reaction involved in the modified Pechini method (Created by the author).

This procedure is reproducible, fast, and cost-effective. It is also versatile, offering excellent dispersion of metal cations due to the complexation and the formation of a polymer resin. After calcination, this process results in the creation of highly homogeneous oxide compounds[108]. Therefore, it is largely used for producing nanomaterials, even YAG [110,111], Y_2O_3 [57,64] and YAM [84,86]. However, as the phase crystallization requires the final annealing at high temperature, this ends up leading to aggregation and agglomeration of NCs.

1.2.2. Synthesis from solution

To overcome the undesired NCs agglomeration from the modified Pechini synthesis, an alternative route is to produce NCs from solution. Based on LaMer's model[112] presented in **Figure 11**, the precursors in the solution initially decompose into monomers by heating. As the monomer concentration increases, the solution achieves a supersaturated state and exceeds the nucleation threshold, becoming out of the thermodynamic equilibrium. The level of saturation S (equation 10) is defined as the ratio between C, the monomer concentration in the solution, and C_{eq}, the solid-liquid equilibrium concentration. Thus, for a supersaturated solution, $S > 1$.

$$S = \frac{C}{C_{eq}} \tag{10}$$

In the supersaturated solution, a burst of nucleation takes place, that is, the monomers begin to aggregate into nuclei by self-aggregation. The thermodynamics of this process depends on the Gibbs free energy ($\Delta G(r)$), that can be expressed for a spherical nucleus formation in homogeneous nucleation by equation 11:

$$\Delta G(r) = 4\pi r^2\gamma + \frac{4}{3}\pi r^3 \Delta G_v \tag{11}$$

where r is the radius of the nuclei, γ is the surface free energy per unit volume of the crystal, and ΔG_v is the change of Gibbs free energy per unit volume of the solid-liquid phase. By deriving the equation 11 relative to r and equalizing it to zero, the critical (minimum) radius r_c of the nuclei is found as follows [113]:

$$r_c = -\frac{2\gamma}{\Delta G_v} \tag{12}$$

Therefore, for $r > r_c$, the particles will grow whereas the ones with $r < r_c$ will redissolve. The nucleation rate of nuclei (J), which represents the nuclei generation per unit volume, is described by expression 13,

$$J = A \exp\left(-\frac{16\pi\gamma^3 V_m^2}{3k_B^3 T^3 \ln(S)^2}\right) \tag{13}$$

with V_m as the molar volume of bulk crystal and T as the reaction temperature [113]. This equation shows that supersaturation, temperature, and surface energy are parameters that directly influence in the nucleation. Hence, rapid nucleation makes the monomers keep being consumed to generate the nuclei until the monomer concentration is not sufficient anymore to support this process. Then, S decreases, and the nucleation step is suppressed. The just-formed nuclei start to grow into NCs by diffusion and incorporation of monomers [113].

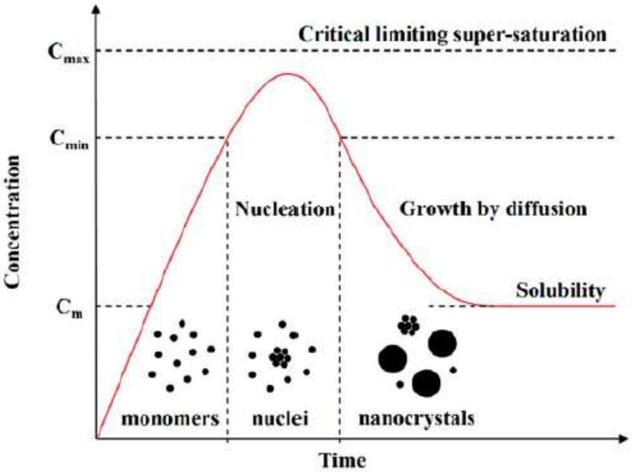

Figure 11. LaMer's diagram, displaying the nucleation and growth steps of the synthesis from solution[114].

To guarantee NCs with uniform size, it is important that the nucleation step occurs only once in a short period of time ("burst of nucleation"), and the subsequent growth is well controlled. This growth can be constrained by promoting a capping layer around the generated particles through the attachment of organic ligands on their surface [113].

The supersaturation condition can easily be applied through a precipitation reaction, which is stated as follows:

$$XA^{y+}_{(solution)} + YB^{x-}_{(solution)} \rightarrow AxBy_{(solid)} \tag{14}$$

where A^{y+} e B^{x-} are the anions and cations, respectively, and X and Y are stoichiometric constants. The product, A_xB_y, is a new phase solid, with low solubility in the solution. Based on this reaction, a typical precipitation synthesis can be done at ambient conditions of temperature and pressure. It offers good repeatability, scalability, ease of operation, and economic viability. Nonetheless, the control over the particle size and morphology is limited, since it depends on several factors, such as pH, order and velocity of the addition of precursors, nature of salts, etc. [115]

Alternatively, there is the solvothermal approach. In a standard process, the precursors and the solvent are loaded into an autoclave, enabling the synthesis to be performed at temperatures reaching up to 400°C and high pressure, above the critical point of the solvent. Such conditions can improve the ability of the solvent to dissolve the reactants, especially of those that do not dissolve at environmental conditions. When utilizing this method, it is not only possible to produce NCs with high chemical homogeneity and good crystallinity, but also manage the size and shape of them. Indeed, adjustments in the temperature and pressure can make the nucleation step speed up, resulting in the synthesis of NCs with good polydispersity [115].

To verify the size dispersity of the NCs, the Polydispersity Index (PDI) is calculated according to the equation 15:

$$\mathrm{PDI} = \left(\frac{\sigma}{\mathrm{d}}\right)^2 \tag{15}$$

where σ and d are the standard deviation and the mean size (diameter) of NCs, respectively. According to International standards organizations (ISOs), PDI < 0.05 means that NCs are monodisperse, while values above 0.70 indicate that they are polydisperse [116].

1.2.3. Coating with amorphous silica

The techniques employed for silica coating of NCs line up with those used to produce colloidal silica particles, with Stöber and water-in-oil (W/O) microemulsions standing out as the most common approaches. The W/O microemulsion consists of mixing oil phase with a surfactant and water containing silica precursors. Within the water droplets of the microemulsion, the silica coating occurs through hydrolysis and condensation of the silica reactant, providing a uniform and controlled deposition of the silica layer around the NCs. Owing to the confined space of the droplets, silica-coated NPs with better polydispersity are obtained. In contrast, the Stöber process relies on the hydrolysis and condensation of tetraethyl orthosilicate (TEOS) in an alcoholic solution (e.g. ethanol) in the presence of a base catalyst. Despite its popularity, it is not possible to employ this technique to coat NCs that cannot be suspended in water-alcohol media, i.e., NCs that exhibit hydrophobic surfaces [117,118].

An alternative to these both methods is to apply the biphasic approach to obtain NCs coated with mesoporous silica shell. With the aid of a catalyst, the silica precursor is gradually transferred from a top organic phase to the bottom aqueous phase, which contains the NCs stabilized with a surfactant. This whole process comprises the hydrolysis and condensation of silica precursor at a controlled rate, enabling a precise control over the thickness and porosity of the silica shell, and the coating of NCs that present water-repellent surfaces. Therefore, such features make this method versatile and promising [118,119].

1.3. Objectives

The design of a luminescent nanothermometer for future biological applications is a challenging task, because it needs to be highly sensitive to temperature changes, perform an accurate temperature measurement, and present appropriate key factors related to the structure to not cause damages in living organisms. For this reason, efforts to produce and optimize the nanomaterials before moving to biological assays must be prioritized, especially during the synthesis step. In this context, the goals of this thesis are:

i. Synthesize NCs of YAG co-doped with Nd^{3+} and Yb^{3+} and conduct a study concerning their structural and optical properties. Firstly, the modified Pechini synthesis is employed to find the co-doping composition that yields an optimal PL emission. Then, monodispersed NCs (< 50 nm) are synthesized by the solvothermal method, which will be silica-coated for a protected annealing. This is to avoid the suppression of PL emission by surface defects and the presence of typical quenchers. This part was conducted in partnership with Majed Ibrahim (Nanochemistry master's student at Université Grenoble Alpes 2022 – 2024), who was supervised by Dr. Xavier Cattoën (Researcher at Institut Néel of CNRS).

ii. Likewise, synthesize Y_2O_3 co-doped with Nd^{3+} and Yb^{3+} through the modified Pechini method to select the Ln^{3+} composition for optimal PL emission. To obtain individual NCs, the two-step urea-based route is applied, which concerns a synthesis under solvothermal conditions followed by calcination. The synthesis parameters were tested to achieve NCs with size < 50 nm.

iii. Study a third matrix, YAM, once it has a multisite structure, with lower symmetry compared to YAG and Y_2O_3, and it could be beneficial to investigate how these attributes impact on the thermal sensing performance of Ln^{3+}-doped YAM as a nanothermometer. In order to perform a deeper investigation, the goal is to study both Nd^{3+} single-doped and Nd^{3+}-Yb^{3+} co-doped YAM. For this study, the modified Pechini method will be used, but synthesis route to obtain YAM from solution will be tested as well.

iv. Conduct nanothermometry analysis on NCs of YAG and Y_2O_3 co-doped with Nd^{3+} and Yb^{3+}, as well as YAM single-doped with Nd^{3+} and co-doped with Nd^{3+} and Yb^{3+}. Based on the LIR technique, the objective is to gather the calibration curves and assess the thermal sensing performances of these nanomaterials, focusing on achieving Sr at around $0.50\%.K^{-1} – 1.00\%.K^{-1}$, $\delta T = 0.1 – 0.2$ K, and repeatability above 95%.

Chapter II: Enhancement of photoluminescence emission and thermal sensing properties of YAG: Nd^{3+} - Yb^{3+} nanocrystals for nanothermometry

2.1. Introduction

Yttrium aluminum garnet, commonly known as YAG with chemical formula of $Y_3Al_5O_{12}$, is an oxide that has been widely used as laser material, but ultimately has shown potential to be applied in bioimaging [120] and as thermal sensor [66,121,122]. Combined with its high chemical stability, the cubic crystal structure endows YAG with a versatile doping capability with diverse Ln^{3+} ions, allowing for tuning of emission wavelengths and making this inorganic material suitable for specific applications. Particularly, when embedding YAG with Nd^{3+} and Yb^{3+} ions, it becomes suitable for acting as a luminescent nanothermometer in living organisms, since these doping ions operate well within the BWs.

The application of Nd^{3+}-Yb^{3+} co-doped YAG NCs as nanothermometers in the biomedical context also requires a strong control of the size. Different synthesis techniques have been employed to produce nanometric-sized NCs, such as combustion, the modified Pechini method, microwave, sol-gel, co-precipitation and solvothermal [123,124]. In accordance with previous studies [40,83,120,125], the latter method holds promise to synthesize individual YAG NCs by heating a solution containing yttrium acetate and aluminum isopropoxide in 1,4-butanediol at temperatures up to 400°C. The synthesized NCs can attain dimensions well below 100 nm, with sizes potentially reaching as small as 4 nm, contingent upon the precise modulation of synthesis parameters, including temperature, pressure, reaction duration, and precursor concentration. The main benefit of this procedure is pure YAG phase with good crystal quality can be produced without any post-treatment at high temperature, avoiding the NCs coalescence.

Yet, the Ln^{3+} ions may be localized near the surface of the synthesized NCs and interact with residual organic compounds and hydroxyl groups arising from the synthesis[120]. This contributes to increasing the probability of non-radiative processes, hampering the PL emission of the luminescent centers. This becomes a major concern to use luminescent NPs to assess the temperature since high PL intensity is necessary to enhance the signal-to-noise ratio, thereby providing reliable and stable measurements [18].

To address this issue, one approach regards the appropriate selection of the Nd^{3+} and Yb^{3+} concentrations, striving for achieving an optimal PL emission from these luminescent ions. The second potential solution is to produce a core-shell structure by growing an amorphous silica shell around the YAG: Nd^{3+} - Yb^{3+} NCs. This method allows for protected annealing, a heat treatment process that tunes the PL emission without affecting the size and dispersion of the NCs [126].

Hence, the work presented in this chapter focused on producing YAG NCs co-doped with Nd^{3+} and Yb^{3+} aiming at significantly enhancing their PL emission for future nanothermometry applications in the biological field. Initially, co-doping engineering was performed using the modified Pechini method, chosen for its rapid execution, versatility, and flexibility. Then, dispersed NCs in solution, with narrow size distribution, were obtained by a refined solvothermal method protocol. Lastly, the NCs were coated with amorphous silica in order to carry out a protected annealing. The thermal sensing evaluation was done based on the LIR approach between PL intensities of Nd^{3+} and Yb^{3+}, to determine the calibration curve, Sr, δT, and repeatability.

2.2. Experimental protocol

2.2.1. Materials syntheses

2.2.1.1. Modified Pechini method

Based on previous studies [57,64], the synthesis of YAG co-doped with Nd^{3+} and Yb^{3+} involved first the dissolution of $Y(NO_3)_3.6H_2O$ (Acros organics, ≥99.9%), $Al(NO_3)_3.9H_2O$ (Riedel-de-Haën, 98.5%), $Nd(NO_3)_3.6H_2O$ (Sigma-Aldrich, ≥99.9%), $Yb(NO_3)_3.5H_2O$ (Sigma-Aldrich, ≥99.9%), citric acid ($C_6H_8O_7$, Thermo scientific, ≥99.5%), and D-sorbitol ($C_6H_{14}O_6$, Fisher chemical, ≥97.0%) in distilled water in individual flasks at ambient temperature. The precursor quantities were calculated considering stoichiometric proportions for the metal nitrates, a molar ratio between citric acid and the metals of 3:1, and a mass ratio between D-sorbitol and citric acid of 3:2. Dopants were inserted in YAG at several concentrations in relation to the total metals of 0.25, 0.50, and 0.75% mol of Nd^{3+} and 0.25, 0.38, 0.50, 0.75, and 1.00% mol of Yb^{3+}. The aqueous solutions containing yttrium, aluminum, neodymium, and ytterbium were added in this order to the one of citric acid under stirring, for metal complexation. Then, the solution of D-sorbitol was poured into it to provide polyesterification reactions. This final solution was kept under vigorous stirring at 100°C and reflux overnight for the resin formation. Next, the resin was dried in an oven at two stages: at 80°C/2h, with a heating rate of 160°C.h^{-1}, and at 250°C/30 minutes, with a slower heating rate of 30°C.h^{-1}. After cooling down, the resulting soft and porous black solid (hereafter referred to as *puff*) was ground manually in an agate mortar. The powder was transferred to a crucible for annealing at 1000°C/10 minutes in a tubular furnace under flux of O_2 (10 mL.min^{-1}), at a heating rate of 10°C.min^{-1}. This process is described by the flowchart in **Figure 12**.

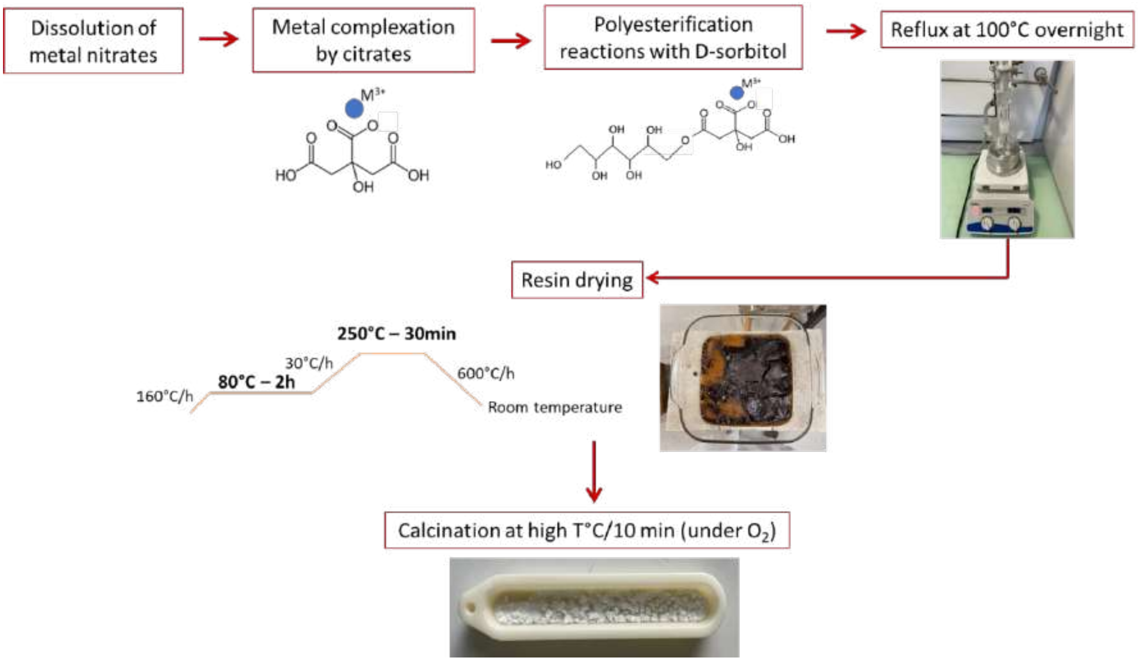

Figure 12. Flowchart of the modified Pechini synthesis (Created by the author).

2.2.1.2. Solvothermal method

The reactants used in the solvothermal synthesis were metal acetates and aluminum isopropoxide to be dissolved in a mixture of 1,4-butanediol and diethylene glycol (DEG). First, yttrium acetate tetrahydrate ($Y(CH_3CO_2)_3.4H_2O$, Sigma-Aldrich, ≥99.9%) underwent a dehydration process in a glass oven connected to a vacuum line, in the presence of P_2O_5, at 150°C for 4h (**Figure 13**). This step was crucial to prevent the uncontrolled hydrolysis of aluminum isopropoxide during the solvothermal synthesis and, consequently, the formation of aluminum oxyhydroxide (boehmite) as a spurious phase[125–127].

Figure 13. Dehydration of yttrium acetate tetrahydrate in a glass oven connected to a vacuum line, in the presence of P_2O_5 (Created by the author).

Next, 18 mmol of aluminum isopropoxide anhydrous ($C_9H_{21}AlO_3$, Acros organics, 98%) [2,83], 10.70 mmol of yttrium acetate dehydrated ($Y(CH_3CO_2)_3$), 0.22 mmol of neodymium acetate dihydrate ($Nd(CH_3CO_2)_3.2H_2O$, Sigma-Aldrich, ≥99.9%), and 0.14 mmol of ytterbium acetate pentahydrate ($Yb(CH_3CO_2)_3.5H_2O$, Sigma-Aldrich, ≥99.9%) were dissolved in 100 ml of solvents (1,4-butanediol from Thermo scientific, 99%, and DEG from Sigma-Aldrich, 99%) with the aid of stirring and ultrasonication. With a tip sonicator, acoustic cavitation cycles are generated in the solution, through the formation, growth, and collapse of microbubbles. It enhances the efficiency of precursor dissolution, enabling to conduct this step in less than one hour, which is faster compared to just applying a 48-hour magnetic stirring [83]. However, ultrasonication generates hot spots, that increases the temperature of the solution. So, the dissolution with ultrasonication was performed for 25 minutes overall (power ~60W), with stops every 3 minutes to cool down the solution with an ice bath.

After dissolving the precursors, the solution was placed inside a 500-ml autoclave, which was purged with argon to achieve an initial pressure of 75 bar and heated to 300°C at a rate equal to $600°C.h^{-1}$. This condition was maintained for 2 hours and 30 minutes, reaching a maximum pressure of about 200 bar. After cooling down to room temperature, the precipitate was rinsed with three centrifugations (7800 rpm, 15 minutes) intercalated with 30-minute redispersions in ethanol in an ultrasound bath. The powder was dried at 60°C/2h. **Figure 14** displays the flowchart of YAG solvothermal synthesis.

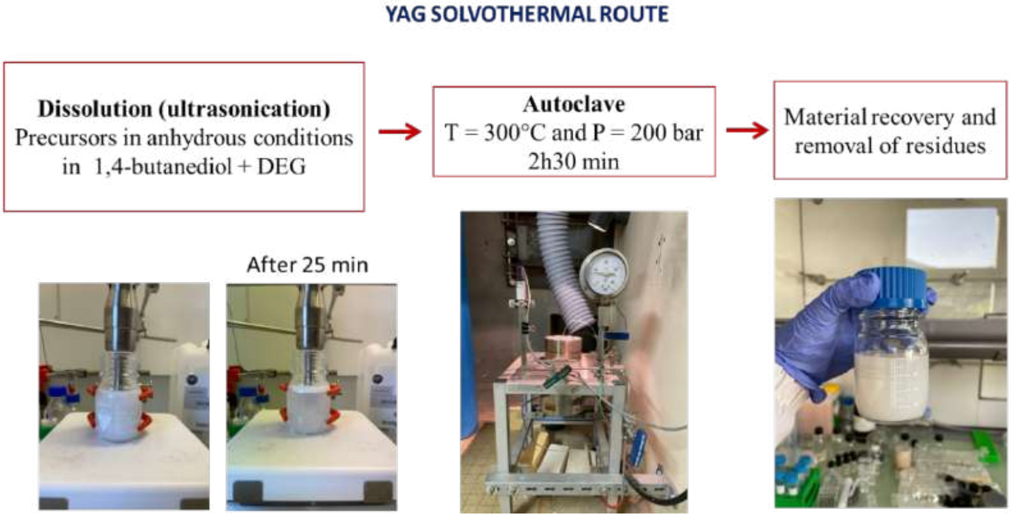

Figure 14. Flowchart describing the solvothermal route for YAG synthesis (Created by the author).

2.2.1.3. Silica-coating of YAG nanocrystals via the biphasic method

The following procedure was established in the master's work of Majed Ibrahim (Nanochesmitry - Université Grenoble Alpes – 2022/2024), who was supervised by Dr. Xavier Cattoën (Researcher at Institut Néel of CNRS). Silica coating experiments started with the dispersion of 29.6 mg of YAG: Nd^{3+}-Yb^{3+} NCs in 25 ml water for 30 minutes in an ultrasound bath. This aqueous solution was placed in a 100-ml round bottom flask with 91.1 mg of cetyltrimethylammonium bromide (CTAB, Sigma-Aldrich, ≥98,0%) and 39.4 mg of L-arginine (Sigma-Aldrich, ≥98.0%), as a surfactant and a base catalyst, respectively. The solution was stirred vigorously (> 800 rpm) and heated to 70°C on a hot plate. In parallel, an organic solution containing 2 ml of ethyl acetate (Fisher Scientific, ≥ 99.8%), and 0.40 ml of TEOS (Acros Organics, 98.0%) was prepared. After slowing down the stirring speed (~120 rpm), the organic solution was introduced carefully into the round bottom flask by streaming it from a syringe into the inner walls of the flask. The final solution was kept under these conditions of temperature and stirring for 16 hours. Then, the material was recovered and washed with ethanol + 2% in vol. of HCl and water. Subsequently, the sample was dried at 60°C/2h. For the protected annealing, the samples were thermally treated under O_2 flux (10 $mL.min^{-1}$) at a given temperature for 1h, with heating and cooling ramps of $5°C.min^{-1}$ and $10°C.min^{-1}$, respectively. A brief flowchart describing the silica coating procedure is illustrated in **Figure 15**.

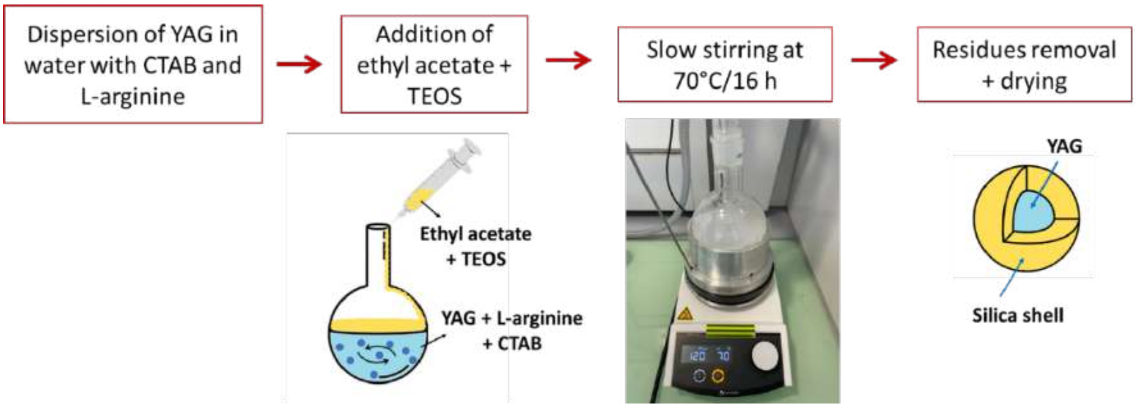

Figure 15. Flowchart illustrating the process of silica coating YAG nanocrystals through the biphasic method (Created by the author).

2.2.2. Characterization techniques

The phase was determined by X-ray diffraction (XRD) analysis on a small quantity of powder deposited onto a silicon wafer, using a D8 Endeavor Bruker diffractometer (λ_{Cu} = 1.54056 Å) in the 2θ range of 10° - 110°, with an acquisition time of 4s per 0.01° of step. The cell parameters and the coherence length (Lc) were estimated with the Le Bail method applied on high-resolution X-ray diffraction (HR-XRD) by using the FullProf software. The high-resolution patterns were collected using a Siemens D8 Advance diffractometer (λ_{Cu} = 1.54056 Å) from 10° to 110°, with a longer integration time of 7s per 0.01° of step. Both instruments are located at Institut Néel – CNRS in Grenoble (France).

The size, morphology, and crystal quality of the NPs were characterized using electron microscopy images. The sample preparation involved dispersing the NPs in isopropyl alcohol with an ultrasonic bath for 15 to 30 minutes. When the NPs were significantly aggregated due to electrostatic forces, Eppendorf tubes filled with isopropyl alcohol and a small quantity of powder were placed in a beaker with 200 ml of water. A tip sonicator in contact with the water was then used to disperse the NPs by applying 210 mW of power in pulsed mode for 5 minutes.

For Field Emission – Scanning Electron Microscopy (FE-SEM), droplets of the NPs suspension were deposited on a silicon wafer and let it dry naturally in the air. The measurements were performed with a beam acceleration voltage of 3 kV and working distance of approximately 4 mm, in a Zeiss Ultra+ microscope, located at Institut Néel – CNRS in Grenoble (France). For Transmission Electron Microscopy (TEM), droplets of the solution were evaporated on the surface of a carbon coated copper grid (400 mesh). Images were recorded in a JEM-2100 JEOL equipment operating at 200 kV, at LabMic – Universidade Federal de Goiás in Goiânia (Brazil). The same prepared samples were also visualized in a FE-SEM JEOL JSM7100F microscope with acceleration voltage of 30 kV, using a module to detect transmitted electrons in the dark field to provide the Scanning-Transmission Electron Microscopy (STEM) images. This equipment is localized at CRTI – Universidade Federal de Goiás in Goiânia (Brazil). The size distribution of NCs was determined by measuring the dimensions of 150 to 200 particles across various electron microscopy images using the ImageJ software.

To assess the hydrodynamic size of NPs in colloidal suspensions and record the corresponding temporal autocorrelation function, Dynamic Light Scaterring (DLS) analysis was performed using a Vasco Kin instrument by Cordouan technologies at Institut Néel – CNRS in Grenoble (France). The NPs were dispersed in distilled water with a concentration below 1 mg/ml and the DLS was measured at room temperature.

Thermogravimetry and differential thermal calorimetry (TG/DSC) analysis was conducted on powdered sample placed inside a platinum crucible from 35°C to 1450°C, at a heating rate of 10°C.min^{-1}, under a flowing mixture composed by 50 mL.min^{-1} of O_2 and 50 mL.min^{-1} of N_2. Mass spectrometry was acquired in the temperature range of 35°C to 800°C, at a heating rate of 5°C.min^{-1}, under the same atmosphere. The instrument used for both analyses is Netzsch STA 449 F3 Nevio, located at CRTI – Universidade Federal de Goiás in Goiânia (Brazil).

The Fourier Transform Infrared spectroscopy (FTIR) analysis was carried out on prepared pellets of 1 mg of the sample with 135 mg of KBr to detect the vibrational modes of chemical bonds. The spectra were recorded in the range of 400 cm^{-1} to 4000 cm^{-1} using a Bruker VERTEX 70 v spectrometer, at Institut Néel – CNRS in Grenoble (France).

The light absorption bands of Nd^{3+} and Yb^{3+} were observed owing to the acquisition of Diffuse Reflectance (DR) spectra on powdered samples from 200 to 1000 nm, with step size of 0.5 nm, with the PerkinElmer WB1050 UV/Vis/NIR spectrophotometer and a Praying Mantis accessory, installed at Instituto de Física – Universidade Federal de Goiás in Goiânia (Brazil). Barium sulphate powder ($BaSO_4$, Sigma-Aldrich) was used as a standard reference material.

The PL emission was obtained on powders, using a spectrofluorometer Fluorog-QM 75-22-C Horiba at Institut Néel – CNRS in Grenoble (France). The samples were irradiated continuously at 808 nm (370 mW.cm^{-2}) with a laser diode Lumics LU808M250 as an external source, connected to a Thorlabs ITC 4005 controller. The emission signal was collected by an InGaAs Fliga 17 detector in the range of 850 nm to 1150 nm, with step size of 0.5 nm, integration time of 0.2 s, and 2-nm slits. Whenever a study consisted of analysis of comparative nature (e.g. PL emission of samples with different co-doping concentrations), the PL spectra were acquired under the same instrumental conditions and on the same day.

For thermal sensing evaluation of YAG: Nd^{3+} - Yb^{3+} NCs, the photoluminescence as a function of temperature (PL(T)) was carried out on both powder and colloidal suspension. The analysis of powder involved its deposition inside an aluminum sample holder, which was then placed in a LINKAM THMS 600 with thermal resolution of 0.1 K. This device was destined to adjust the sample temperature, allowing the nanopowders to remain thermally isolated from the external environment thanks to a sealing lid. This lid features a 0.5 mm of thick glass window that is transparent in the VIS/NIR range, preventing any interferences in the PL emission of the nanomaterials (**Figure 16.(a)** and **(b)**). To record the temperature sample, a K-type thermocouple (Fluke 5411B) was put in direct contact with the powder as shown in **Figure 16.(b)**.

For PL (T) measurements in solution, the powder was dispersed in distilled water (3 mg/ml) with an ultrasonic bath for 30 minutes and poured into a cuvette made of quartz glass (Hellma Analytics, light path 10 x 10 mm). The top of the cuvette was covered with Parafilm M® to avoid evaporation of the water during the measurements (inset of **Figure 16.(c)**). A customized system was built for the temperature control of the NPs in solution, composed by an aluminum mounting, for the cuvette, positioned on a hot plate. This system was housed within an insulated foam box to minimize heat exchanges with the surrounding environment (**Figure 16.(c)** and **(d)**). The K-type thermocouple (Fluke 5411B) was used in direct contact with the solution to acquire its real temperature, while it was kept under stirring during the whole analysis. The measurements were performed using the same spectrofluorometer, laser diode and detector, applying equal conditions of step size, acquisition time, and slit size as previously mentioned. The power density used to pump the NPs suspended in solution was 3W.cm^{-2} though.

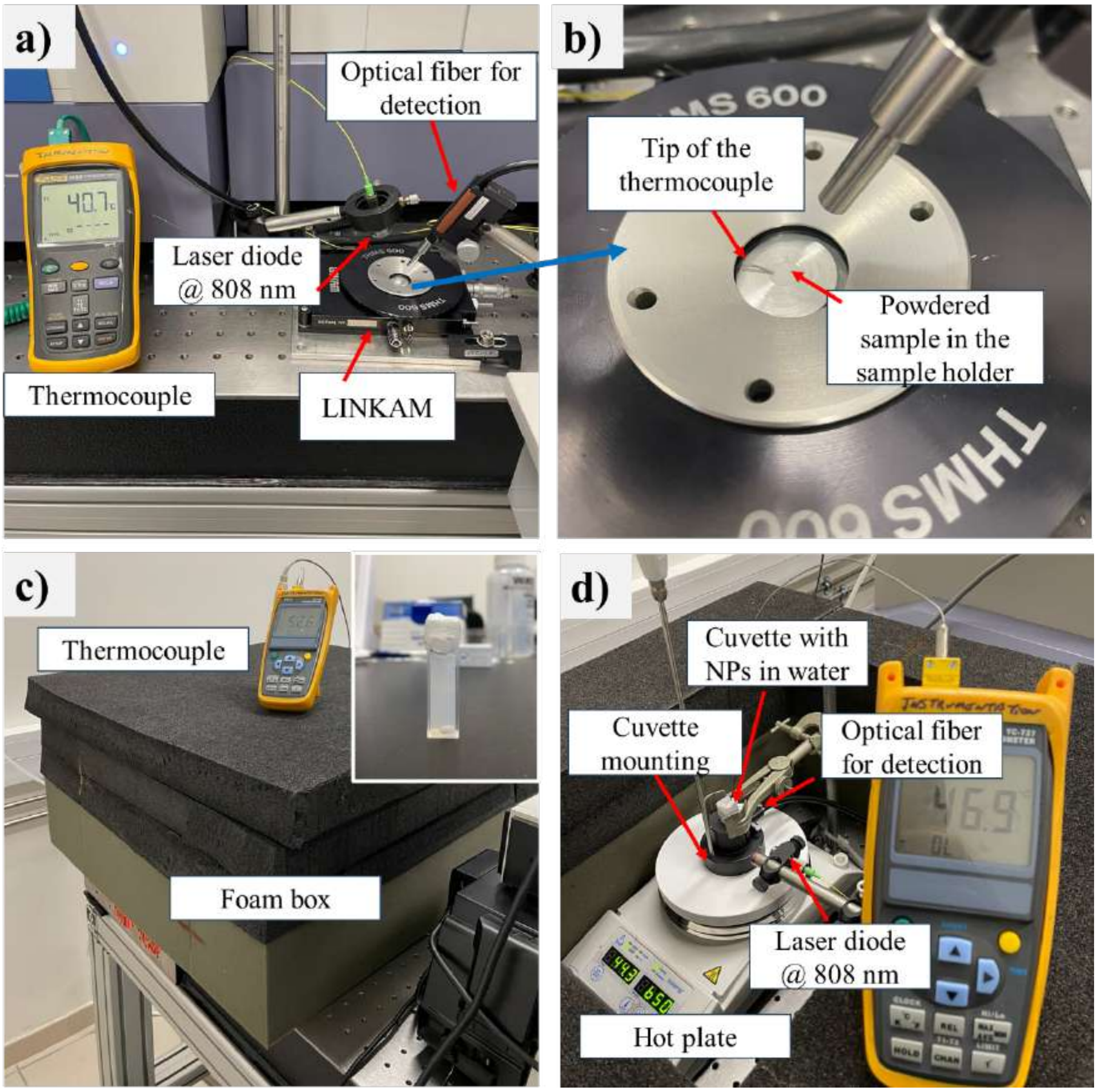

Figure 16. **(a)** Experimental set up for thermometry measurements of powder. **(b)** A close view showing the sample inside a sample-holder, placed in the LINKAM device. **(c)** The foam box built to insulate the thermometry measurements in solution. **(d)** The view from inside the foam box, showing the set up made with a hot plate, the cuvette placed inside the black mounting, the laser diode, and the optical fiber to collect the emission signal to the detector (Created by the author).

2.3. Results and discussion

2.3.1. Co-doping engineering for an optimal photoluminescence emission of YAG: Nd^{3+} - Yb^{3+} nanocrystals

Samples of YAG NCs co-doped with Nd^{3+} and Yb^{3+} were synthesized via the modified Pechini method. Three concentrations of Nd^{3+} (0.25, 0.50, and 0.75% mol) were tested with five concentrations of Yb^{3+} (0.25, 0.38, 0.50, 0.75, and 1.00 % mol), resulting in 15 different possibilities of co-doping of YAG. For simplicity, co-doping concentrations will be expressed as % mol relative to all metals throughout this text, but the corresponding chemical formulas are described in **Table 2**.

Table 2. Nd^{3+} and Yb^{3+} concentrations of YAG samples in % mol relative to all metals (yttrium and aluminum) with corresponding chemical formula.

YAG: Nd^{3+}-Yb^{3+}

		Nd^{3+}		
		0.25% mol	**0.50% mol**	**0.75% mol**
Yb^{3+}	**0.25% mol**	$Y_{2.96}Nd_{0.02}Yb_{0.02}Al_5O_{12}$	$Y_{2.94}Nd_{0.04}Yb_{0.02}Al_5O_{12}$	$Y_{2.92}Nd_{0.06}Yb_{0.02}Al_5O_{12}$
	0.38% mol	$Y_{2.95}Nd_{0.02}Yb_{0.03}Al_5O_{12}$	$Y_{2.93}Nd_{0.04}Yb_{0.03}Al_5O_{12}$	$Y_{2.91}Nd_{0.06}Yb_{0.03}Al_5O_{12}$
	0.50% mol	$Y_{2.94}Nd_{0.02}Yb_{0.04}Al_5O_{12}$	$Y_{2.92}Nd_{0.04}Yb_{0.04}Al_5O_{12}$	$Y_{2.90}Nd_{0.06}Yb_{0.04}Al_5O_{12}$
	0.75% mol	$Y_{2.92}Nd_{0.02}Yb_{0.06}Al_5O_{12}$	$Y_{2.90}Nd_{0.04}Yb_{0.06}Al_5O_{12}$	$Y_{2.88}Nd_{0.06}Yb_{0.06}Al_5O_{12}$
	1.00% mol	$Y_{2.90}Nd_{0.02}Yb_{0.08}Al_5O_{12}$	$Y_{2.88}Nd_{0.04}Yb_{0.08}Al_5O_{12}$	$Y_{2.86}Nd_{0.06}Yb_{0.08}Al_5O_{12}$

Pure crystalline YAG phases were obtained for all synthesized Nd^{3+}-Yb^{3+} co-doped samples, without any evidence of secondary phases, as it was confirmed by XRD results when compared to the reference PDF 01-079-1891 (**Figure 17.(a) – (c)**). The composition 0.75% mol Nd^{3+} and 0.50% mol Yb^{3+} was considered as an example for the further exploration of structural features of YAG: Nd^{3+}-Yb^{3+}. Therefore, its cell parameters were estimated through the profile adjustment of HR-XRD based on the Le Bail fit method (**Figure 17.(d)**). The outcomes in **Table 3** show the unit cell is expanded compared to what is stated in the corresponding reference. The dopants are incorporated in yttrium sites, whose ionic radius is 1.019 Å for eight-fold coordination whereas Nd^{3+}

and Yb^{3+} ionic radii are 1.109 Å and 0.985 Å, respectively [128]. Since more Nd^{3+} than Yb^{3+} ions replace Y^{3+} for the given composition, it is indeed expected this expansion of the unit cell.

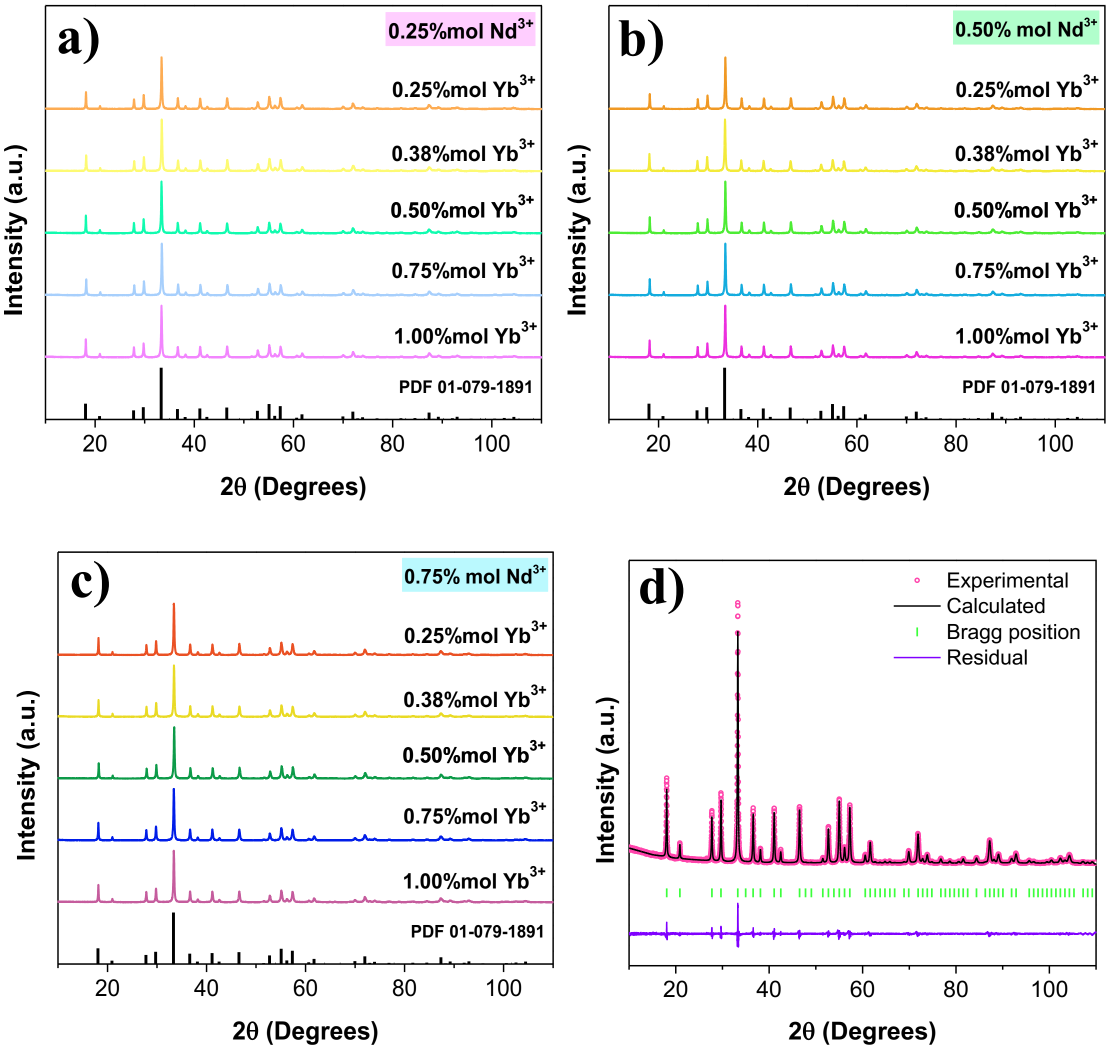

Figure 17. XRD patterns of YAG co-doped with different % mol Yb^{3+} when Nd^{3+} concentration is fixed at **(a)** 0.25, **(b)** 0.50, and **(c)** 0.75% mol. **(d)** HR-XRD (black curve) with calculated Le Bail fit (pink circles) of YAG: 0.75% mol Nd^{3+}, 0.50% mol Yb^{3+} NCs.

Table 3. Cell parameters and Lc of YAG: 0.75% mol Nd^{3+}, 0.50% mol Yb^{3+} NCs synthesized by the modified Pechin method.

Material	***a* (Å)**	***b* (Å)**	***c* (Å)**	**Volume ($Å^3$)**	**Lc (nm)**	**χ^2**	**Rp (%)**	**Rwp (%)**
YAG: 0.75% mol Nd^{3+}, 0.50% mol Yb^{3+}	12.027	12.027	12.027	1739.86	43 ± 1	2.56	12.5	13.9
Ref.[129]	12.016	12.016	12.016	1732.32	-	-	-	-

Regarding the size, the sample exhibited Lc of 43 nm (**Table 3**), which is in line with the mean size of the grains extracted from the FE-SEM image (**Figure 18**). This demonstrates the material is formed by single NCs with high crystal quality, but they ended up agglomerating due to the calcination at high temperature (1000°C) for the oxide crystallization.

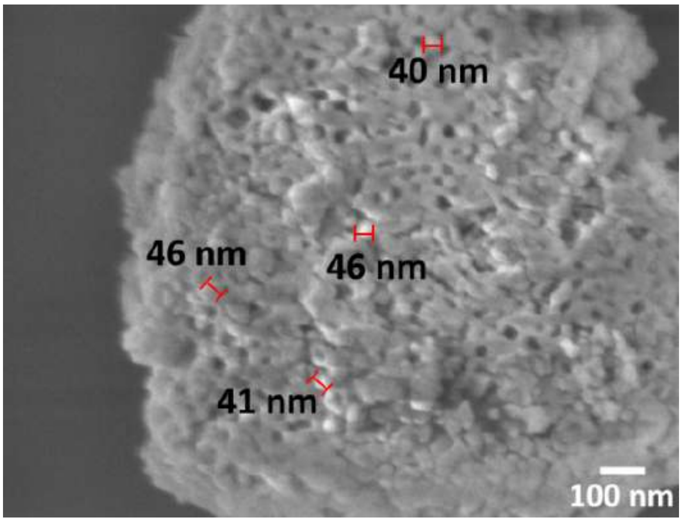

Figure 18. FE- SEM image of YAG: 0.75% mol Nd^{3+}, 0.50% mol Yb^{3+} obtained by the modified Pechini method.

The optical characterization began with the absorption analysis of YAG: Nd^{3+}-Yb^{3+} NCs using the DR measurements. This analysis focused on the sample with the highest concentrations of both Nd^{3+} and Yb^{3+} (0.75% mol Nd^{3+} and 1.00% mol Yb^{3+}). As shown in the curve of DR versus wavelength in **Figure 19.(a)**, the sample presented absorption bands attributed to the transitions from the fundamental level $^4I_{9/2}$ to meta-state levels of Nd^{3+} and the transition $^2F_{7/2} \rightarrow {}^2F_{5/2}$ of Yb^{3+}, which were identified in agreement with the literature [130–132]. It is noteworthy that there are intense absorption bands around 808 nm ($^4I_{9/2} \rightarrow {}^4F_{5/2}$, $^2H_{9/2}$) of Nd^{3+} ions, that are suitable for the excitation of YAG: Nd^{3+}-Yb^{3+} NCs in biological applications, since it is located within the BW-I (750 – 950 nm). Moreover, the sample exhibited a reflectance exceeding 90% across the spectrum, with the absorption edge falling in the ultraviolet region.

The estimation of the optical bandgap energy (E_g) can be found based on its relation with the linear absorption coefficient (α) through the Tauc expression, as follows:

$$(\alpha h\nu)^n = C_1(h\nu - E_g) \quad (16)$$

with hν as the energy of incident photon and C_1 as a proportionality constant. The factor n depends on the nature of the electronic transition: n = ½ is for indirect while n = 2 for direct allowed transitions band gap, respectively. In parallel, the Kubelka-Munk function ($F(R_\infty)$) can be applied to transform the reflectance to the corresponding absorption spectrum according to the equation 17:

$$F(R_\infty) = \frac{K}{S} = \frac{(1 - R_\infty)^2}{2R_\infty} \qquad (17)$$

where K and S are the absorption and the scattering coefficients, respectively, and R_∞ is the ratio between the DR from the YAG: Nd^{3+}-Yb^{3+} sample and a non-absorbing reference ($BaSO_4$ in this study). K will be equal to 2α whether the material scatters the light in a diffuse way efficiently. Considering S constant relative to wavelength, the expressions 16 and 17 are combined, giving rise to the equation 18:

$$[F(R_\infty)h\nu]^n = C_1(h\nu - E_g) \qquad (18)$$

From the plot of $[F(R_\infty)h\nu]^n$ versus energy in eV, for n = 2, E_g was extracted by extrapolating the points linearly fitted for $[F(R_\infty)h\nu]^2 = 0$ (**Figure 19.(b)**) [133–135]. In the case of YAG: 0.75% mol Nd^{3+}, 1.00% mol Yb^{3+}, the value of 5.25 eV was determined, which is smaller than the E_g of 6.5 eV reported in the literature for YAG [136,137]. In this case, such band gap narrowing may be related to the elevated co-doping concentration that provides a lattice deformation and, consequently, changes the electronic band structure.

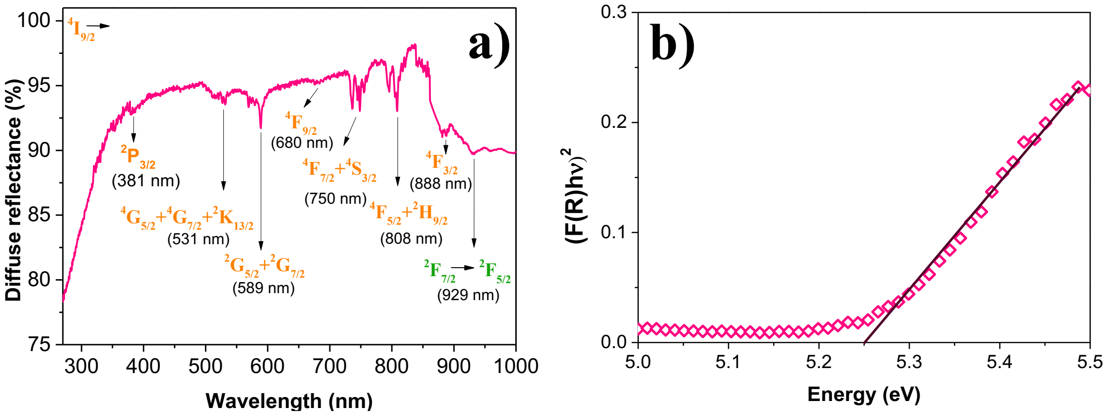

Figure 19. (a) DR spectrum and **(b)** determination of the optical bandgap energy of YAG: 0.75% mol Nd^{3+}, 1.00% mol Yb^{3+}.

Next, the PL emission spectra of all samples were recorded at room temperature, by irradiating the powdered samples at 808 nm. The PL emission spectra as a function of % mol Yb^{3+} are illustrated for each series of Nd^{3+} concentration fixed at 0.25, 0.50, and 0.75% mol in **Figure 20.(a), (b),** and **(c)**, respectively**.** Under continuous excitation at 808 nm, the Nd^{3+} ions are promoted from the fundamental level ${}^4I_{9/2}$ to the excited levels ${}^4F_{5/2}$ and ${}^2H_{9/2}$. After a fast non-radiative decay to the metastable state ${}^4F_{3/2}$, two emissions coming from Nd^{3+} ions are observed in the spectra: ${}^4F_{3/2} \rightarrow {}^4I_{9/2}$ (860 – 950 nm) and ${}^4F_{3/2} \rightarrow {}^4I_{11/2}$ (1040 – 1130 nm). A third emission is present, corresponding to the transition ${}^2F_{5/2} \rightarrow {}^2F_{7/2}$ (960 – 1040 nm) from Yb^{3+} ions, which was enabled through an energy transfer from Nd^{3+} to Yb^{3+}.

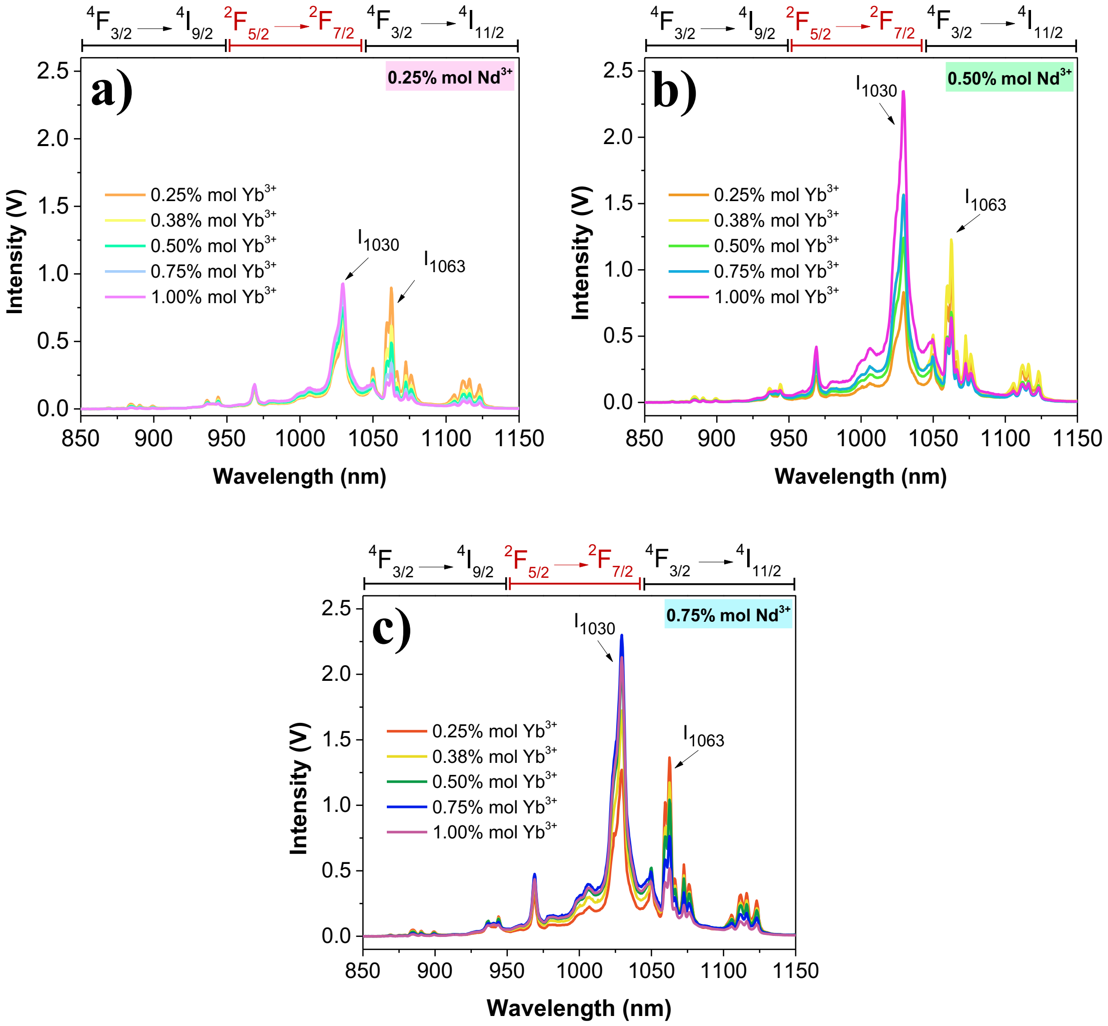

Figure 20. PL emission spectra of YAG for different % mol Yb^{3+} considering Nd^{3+} concentration fixed at **(a)** 0.25, **(b)** 0.50, and **(c)** 0.75% mol.

As per the work led by Lupei et al.[138], the energy transfer $Nd^{3+} \rightarrow Yb^{3+}$ is resonant in YAG, as the authors clearly demonstrated an overlap of the absorption spectrum of YAG: Yb^{3+} and the emission spectrum of YAG: Nd^{3+}. Using the energy level diagram of YAG co-doped with Nd^{3+} and Yb^{3+} (**Figure 21**) — built upon the outcomes achieved here and the published literature [139,140]— the authors showed that the process involved the electronic transitions $^4F_{3/2}$ (R_1, R_2) → $^4I_{9/2}$ (Z_5) of Nd^{3+} and $^2F_{7/2}$ (1) → $^2F_{5/2}$(6) of Yb^{3+}. This finding is further supported by the fact that the lower excited Stark level of $^4F_{3/2}$ (R_1) and the upper excited Stark level of $^2F_{5/2}$ (7) of Nd^{3+} and Yb^{3+}, respectively, are mismatched by only 480 cm^{-1}. Comparable cases have been documented in former research, in which phonon-assistance energy transfer became less necessary owing to the non-vanishing overlap between donor and acceptor spectra, and the small energy gap between the excited states of Nd^{3+} and Yb^{3+} [141–143].

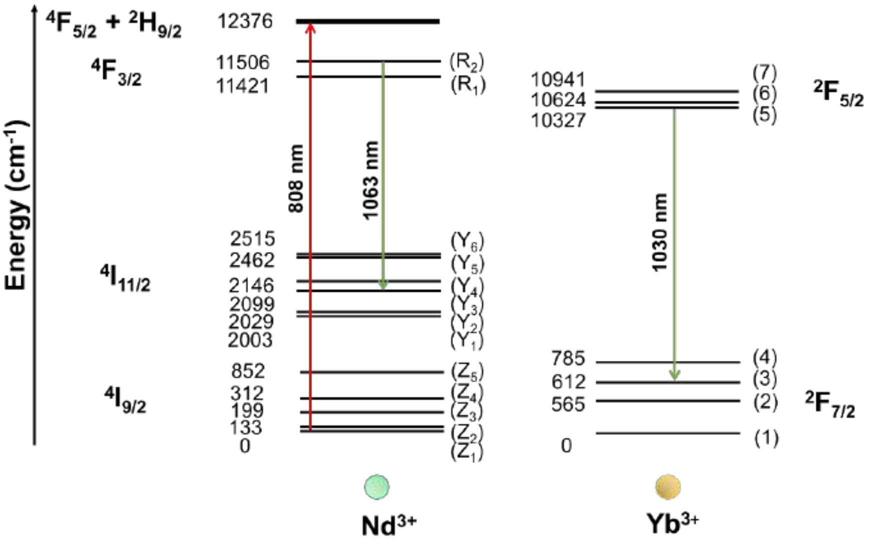

Figure 21. Energy level diagram of YAG co-doped with Nd^{3+} and Yb^{3+}. The numbers indicate the energy values in cm^{-1}, and the acronyms in the parenthesis designate each Stark level (Created by the author).

Hence, the PL emission characterization laid the groundwork for co-doping engineering of YAG due to the changes in PL intensity according to the concentration of dopants inserted into the matrix. The criteria adopted in this work focused on the PL emission peaks at 1030 nm and 1063 nm, referring to the transitions 5 → 3 and $R_2 \rightarrow Y_3$ in **Figure 21** of Yb^{3+} and Nd^{3+}, respectively. They are not only the most intense ones in the case of YAG but also known to be a good match for BW-II luminescence nanothermometers with Nd^{3+} and Yb^{3+} [57]. Therefore, the PL intensities at 1030 nm (I_{1030}) and 1063 nm (I_{1063}) were integrated after converting the PL spectra from the wavelength domain to the wavenumber domain and are represented as a function of % mol Yb^{3+} for each fixed Nd^{3+} concentration in **Figure 22**.

In accordance with the integration results, as more Nd^{3+} ions are incorporated into the YAG matrix without changing Yb^{3+} content, the PL intensity of Yb^{3+} increases. For example, by tripling the concentration of Nd^{3+} (from 0.25 to 0.75% mol), Yb^{3+} PL intensity can increase by more than 2-fold. This behavior has its source in the shortening of Nd^{3+} - Yb^{3+} distance d as Nd^{3+} concentration is incremented in the host. The parameter d is given by $d = \left(\frac{3}{4}\pi N\right)^{\frac{1}{3}}$, with N being the total density of trivalent Nd^{3+} and Yb^{3+} cations [54,59]. In this way, the efficiency of energy transfer $Nd^{3+} \rightarrow Yb^{3+}$ is enhanced. Namely, Jaque et al. [59] observed a boost from 40% to 65% of efficiency by inserting 50 times more of Nd^{3+} ions in $YAl_3(BO3)_4$ without changing Yb^{3+} concentration.

The presence of Yb^{3+} ions itself can enhance this energy transfer efficiency, by promoting a better distribution of Nd^{3+} ions in the host, thereby reducing its probability of self-quenching (energy migration ($^4F_{3/2}$, $^4I_{9/2} \rightarrow {}^4F_{3/2}$, $^4I_{9/2}$) and cross-relaxation ($^4F_{3/2}$, $^4I_{9/2} \rightarrow {}^4I_{15/2}$, $^4I_{15/2}$)) [52,54]. To illustrate it, no changes were observed in the PL intensity of Nd^{3+} between YAG samples with 0.25% mol Nd^{3+} and 0.25% mol Yb^{3+} versus that with 0.50% mol Nd^{3+} and 0.25% mol Yb^{3+}. This lack of variation in PL intensity was also evident between samples with 0.50% mol Nd^{3+} and 0.38% mol Yb^{3+} compared to that with 0.75% mol Nd^{3+} and 0.38% mol Yb^{3+}.

In contrast, if the amount of Nd^{3+} is kept constant, its PL emission tends to be less intense the more Yb^{3+} ions are introduced into YAG. For heavily doped YAG (e.g. 1.00% mol Nd^{3+}, 1.00% mol Yb^{3+}), the quenching concentration of PL emission takes place due to the competition of Nd^{3+} - Nd^{3+} and Yb^{3+} - Yb^{3+}. Finally, the back energy transfer $Yb^{3+} \rightarrow Nd^{3+}$ has been considered negligible for YAG co-doped with different Nd^{3+} and Yb^{3+} concentrations as published by previous works [144,145].

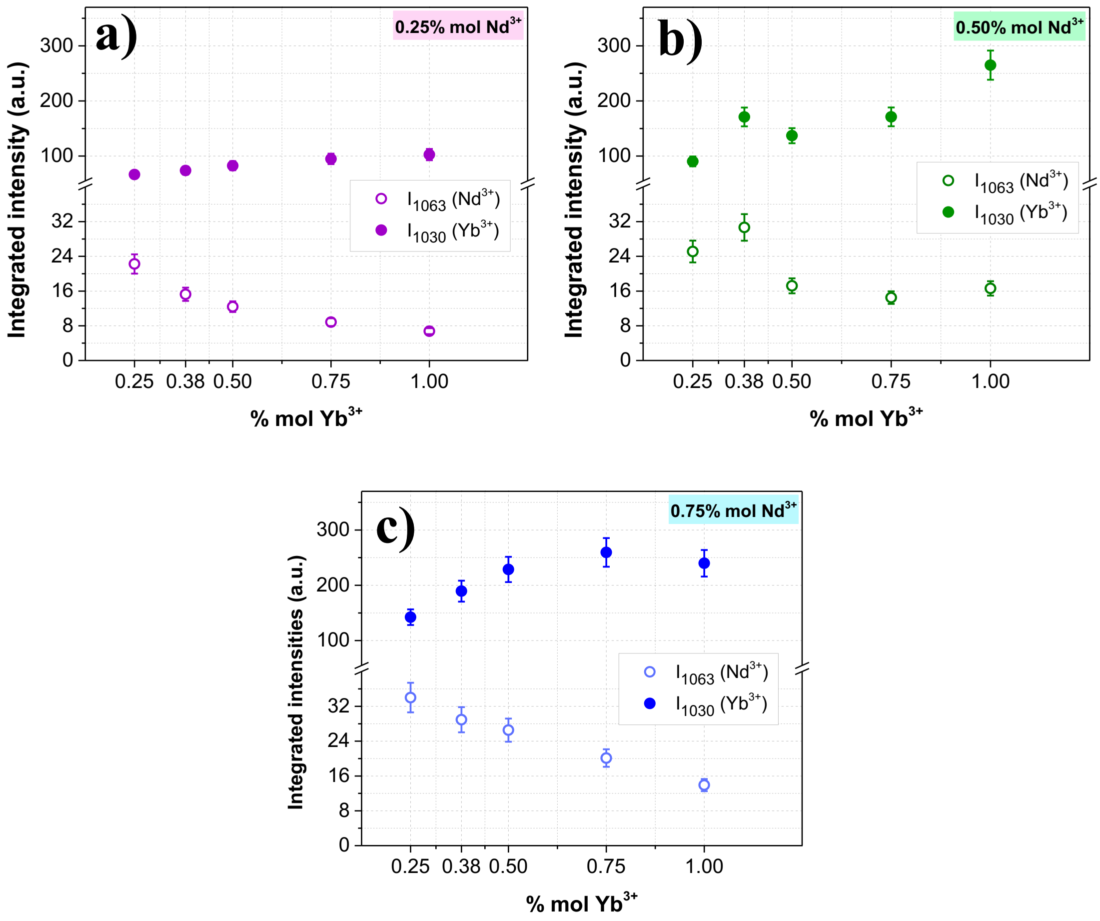

Figure 22. Integrated intensities at 1030 nm (I_{1030}) and 1063 nm (I_{1063}) as a function of % mol Yb^{3+} when Nd^{3+} concentration is fixed at **(a)** 0.25, **(b)**0.50, and **(c)** 0.75% mol. All the graphs are on the same scale for a better comparison.

Given this dynamic relationship between Nd^{3+} and Yb^{3+} ions and considering that the LIR method will be applied to the PL intensities coming from both Ln^{3+}, their emissions must be sufficiently intense. This ensures a high signal-to-noise ratio of the PL bands, positively impacting the accuracy of thermal measurements. Thus, the strategy adopted in this work involved first analyzing the Yb^{3+} emission to select the samples with better emissivity at 1030 nm. Following this screening, a final evaluation was conducted based on the PL intensity of Nd^{3+} at 1063 nm. The composition with the highest Nd^{3+} intensity was then considered as the optimal co-doping concentration.

As illustrated in **Figure 23.(a)**, four compositions (marked with red arrows) stand out in terms of Yb^{3+} PL intensity: 0.75% mol Nd^{3+} and 1.00% mol Yb^{3+}, as well as 0.75% mol Nd^{3+} combined with 0.50, 0.75, and 1.00% mol Yb^{3+}. Then, when considering only the Nd^{3+} PL intensity, the analysis revealed that the co-doping concentration of 0.75% mol Nd^{3+} and 0.50% mol Yb^{3+} yielded the highest PL emission of Nd^{3+} among the four selected samples, providing the best balance between Nd^{3+} and Yb^{3+} emissions (red arrow in **Figure 23**.**(b)**). Therefore, this concentration will be adopted for co-doping YAG NCs for nanothermometry.

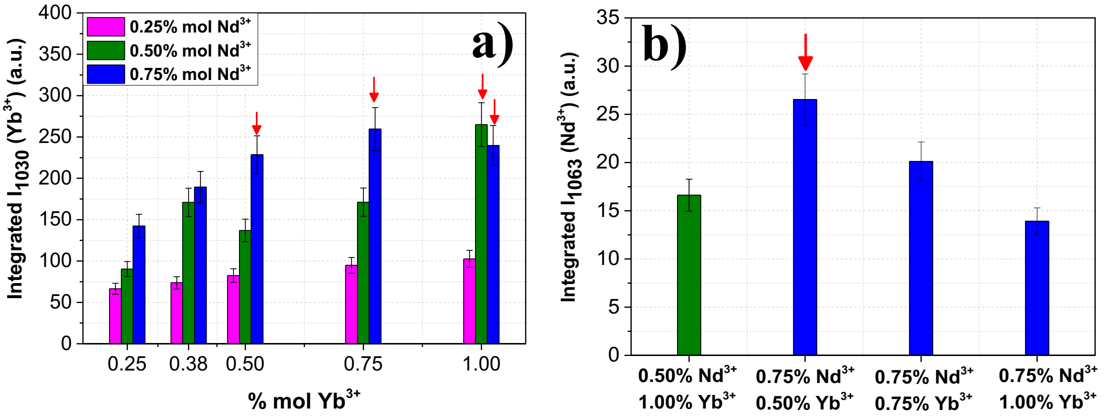

Figure 23. (a) Comparison of integrated intensity at 1030 nm (Yb^{3+}) for all samples. The red arrows indicate the four samples with higher Yb^{3+} PL emission. **(b)** The emissivity of Nd^{3+} of the samples that presented highest Yb^{3+} PL intensities. The red arrow points out to the composition that gave highest Nd^{3+} emission among the four samples previously selected.

2.3.2. Preparation of individual core-shell YAG: Nd^{3+}-Yb^{3+} @ SiO_2 nanoparticles

2.3.2.1. Optimization of the solvothermal synthesis of YAG nanocrystals

To surpass the NCs agglomeration issue of the modified Pechini method, the solvothermal synthesis was adopted to yield individual NCs of YAG: Nd^{3+}-Yb^{3+}. The first report on this route was made by Inoue et al.[127], and it involves promoting the attachment of 1,4-butanediol (solvent) to aluminum isopropoxide, followed by a cyclisation reaction of the solvent, triggered at high temperature (above 250°C). From it, an aluminate ion is originated, which binds with Y^{3+} coming from the yttrium acetate, to form Al-O-Y linkages (**Figure 24**). After a single burst of nucleation, YAG NCs grow through either diffusion or coalescence of primary particles to provide well-crystalized NCs. Such conditions allow to reach rapidly a supersaturation and a supercritical state of the solvent, favoring a confinement in time of nucleation.

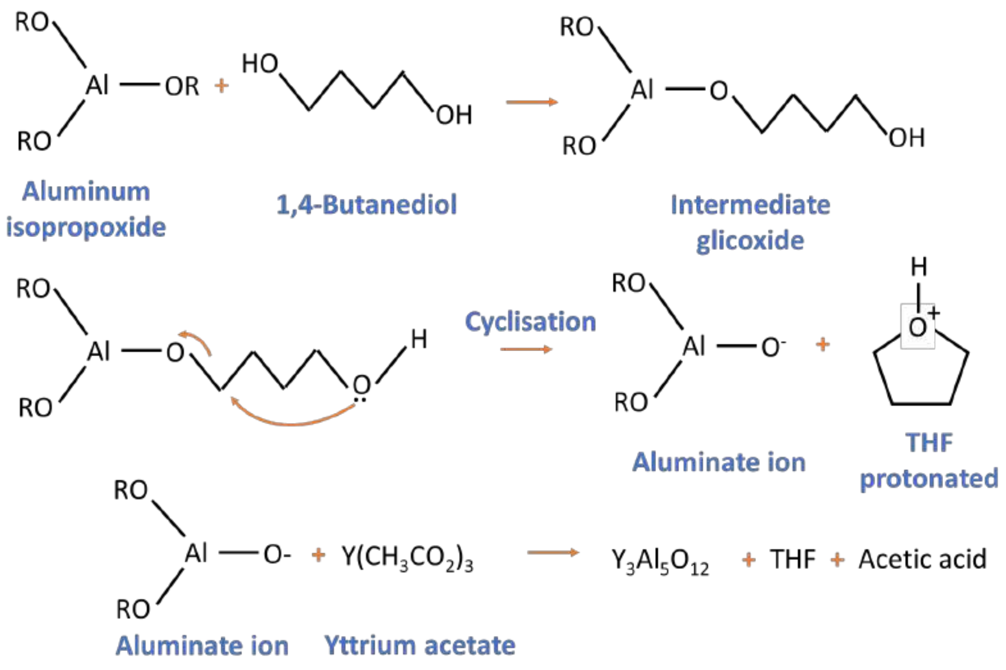

Figure 24. Mechanism to obtain YAG by the solvothermal method. R means C_3H_7 (Created by the author).

Dantelle et al.[83] explored in depth how the parameters of the solvothermal synthesis can directly influence the size and the degree of dispersion of YAG NCs. This study indicated that while high external pressure (200 bar) can trigger a single burst of nucleation, excessively high pressure (400 bar) leads to a dense formation of small NCs, causing their agglomeration with increased polydispersity. NCs also become agglomerated if low concentrations of the aluminum precursor are used. With regard to the size, it evolves with aluminum concentration, temperature, and reaction time, but at high levels of any, the size distribution widens. The conclusion reached is that a balance needs to be found among the factors to produce single NCs of YAG free of agglomeration. Nonetheless, the study showed that it was still challenging to produce NCs with dimensions between 20 and 30 nm cost-effectively.

On the other hand, Odziomek et al. [125] obtained ultra-small YAG NCs, with dimensions below 5 nm, via similar solvothermal route, but controlling the growth step with the addition of 15% in volume of DEG as a co-solvent involving a significant ligand effect. However, such a small size can be harmful for obtaining intense PL emission as the surface-to-volume ratio is increased, and more Ln^{3+} ions will be located near the surface, prone to interact with PL quenchers (e.g. OH groups).

Considering both works, five experiments of solvothermal synthesis were carried out, by testing different amounts of DEG in order to produce YAG NCs with sizes around 20 – 30 nm. To avoid very small size and keep a narrow size distribution, the quantity of DEG varied by 0.00, 0.50, 1.00, 2.00, and 3.00% in volume.

Figure 25 displays the HR-XRD patterns of the five samples, showing that pure crystalline YAG phases were successfully obtained in accordance with the reference 01-079-1891, with no evidence of other phases, such as $YAlO_3$ or $Y_4Al_2O_9$. The cell parameters were determined using the Le Bail fit method (**Figure S1** in **Appendix**) and were found to remain consistent regardless of the DEG volume used (**Table 4**). However, these parameters are larger than both the reference values and those of the sample prepared using the modified Pechini method with the same co-doping concentration, as presented in **Table 3**. This increase in lattice parameters is related to internal stresses coming from the local defects and closed voids — with OH attached to the surfaces — that originate when primary particles diffuse or coalesce to form YAG NCs. Similar lattice expansion has been previously observed in studies on undoped YAG [146], YAG: Ce^{3+} [83], and YAG: Nd^{3+} [40] synthesized via the solvothermal route.

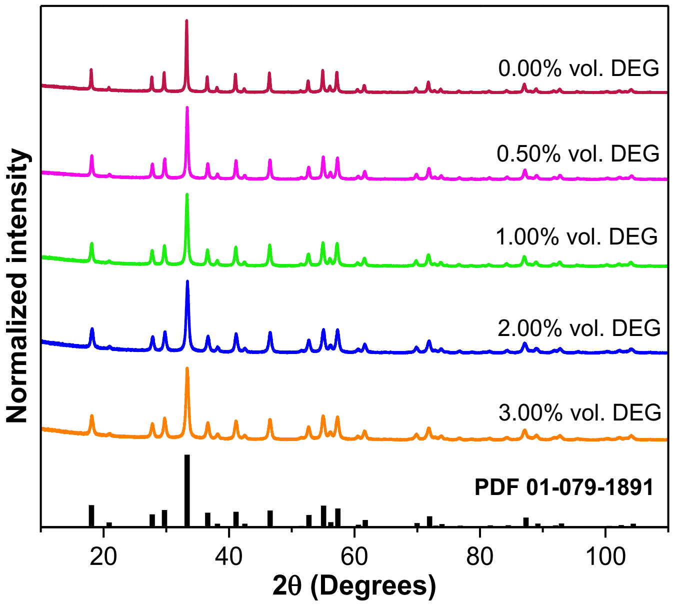

Figure 25. HR-XRD of YAG NCs synthesized with different % in volume of DEG. All diffractograms were indexed as YAG and no spurious phase was detected. The samples were co-doped with 0.75% mol Nd^{3+} and 0.50% mol Yb^{3+}.

Table 4. Cell parameters and refinement parameters according to the Le Bail fit of YAG: Nd^{3+}-Yb^{3+} synthesized by the solvothermal method. The co-doping concentration used was 0.75% mol Nd^{3+} and 0.50% mol Yb^{3+}.

DEG (% vol.)	*a* (Å)	*b* (Å)	*c* (Å)	Volume (Å^3)	χ^2	Rp (%)	Rwp (%)
0.00	12.046	12.046	12.046	1748.07	1.88	13.9	15.2
0.50	12.048	12.048	12.048	1748.88	1.50	10.9	12.1
1.00	12.054	12.054	12.054	1751.65	1.44	11.2	12.1
2.00	12.053	12.053	12.053	1751.25	1.75	13.5	14.3
3.00	12.054	12.054	12.054	1751.34	1.63	11.9	13.1
Ref.[129]	12.016	12.016	12.016	1732.32	-	-	-

The influence of DEG on the NC size was examined through TEM analysis, with the corresponding images presented in **Figure 26**, and the dimension and PDI values outlined in **Table 5**. Without the addition of DEG, the sample already exhibited isolated NCs measuring 51± 20 nm (**Figure 26.(a)**), though a few agglomerates of small NCs were found (marked with dashed orange circle), resulting in a cauliflower-like morphology. Additionally, this sample displayed a polydisperse nature, as indicated by the PDI of 0.10. By adding a quantity of DEG as low as 0.50% in volume (0.50 ml in a 100-ml solution), the size decreased abruptly to 23 ± 10 nm, and the size distribution narrowed, with PDI equal to 0.05 (**Figure 26.(b)**). The dimension of the YAG NCs continued to decrease consistently with increasing DEG volume (**Figure 26.(c) – (e)**), reaching the smallest size in the studied series, 14 ± 10 nm, for 3.00% in volume of DEG. These findings reinforce the efficient ligand effect of DEG, which reduced the growth rate of NCs, suppressing their agglomeration and narrowing their size distribution (**Figure S2** in **Appendix**). Furthermore, the NC dimensions are in good agreement with the Lc values, estimated with the Le Bail fit method, when DEG is employed in the synthesis (**Table 5**). This consistency suggests the single-crystal nature of YAG, an observation further supported by HR-TEM (**Figure 26.(f)**), which unveiled homogeneous atomic planes throughout the NC.

Regarding the state of NC aggregation in solution, **Table 5** also summarizes the DLS results of NCs suspended in water. It shows that the hydrodynamic sizes are around 2 - 3 times larger than the ones measured in TEM images. This discrepancy between DLS and TEM images may arise from a slight aggregation of as-prepared NCs in aqueous solution, without previous functionalization. For example, Asakura et al. [147] observed in their work the hydrodynamic size of YAG NCs was 46.8 nm while the average size determined by TEM was only 9.5 nm. Nonetheless, it is also common to have this enlargement of the hydrodynamic size because it comprises the NP diameter along with the diffusion layer surrounding its surface. Such observation was highlighted in the works of Odziomek et al.[125] and Dantelle et al. [40], who obtained YAG NCs of average sizes of 8.5 and 45 nm, respectively, but the hydrodynamic size was around 50% larger in both cases. Despite this minor aggregation issue, the samples remained colloidally stable during 24 h, without any evidence of sedimentation, even if they were not previously functionalized. This marks the good colloidal stability of YAG synthesized by the solvothermal method.

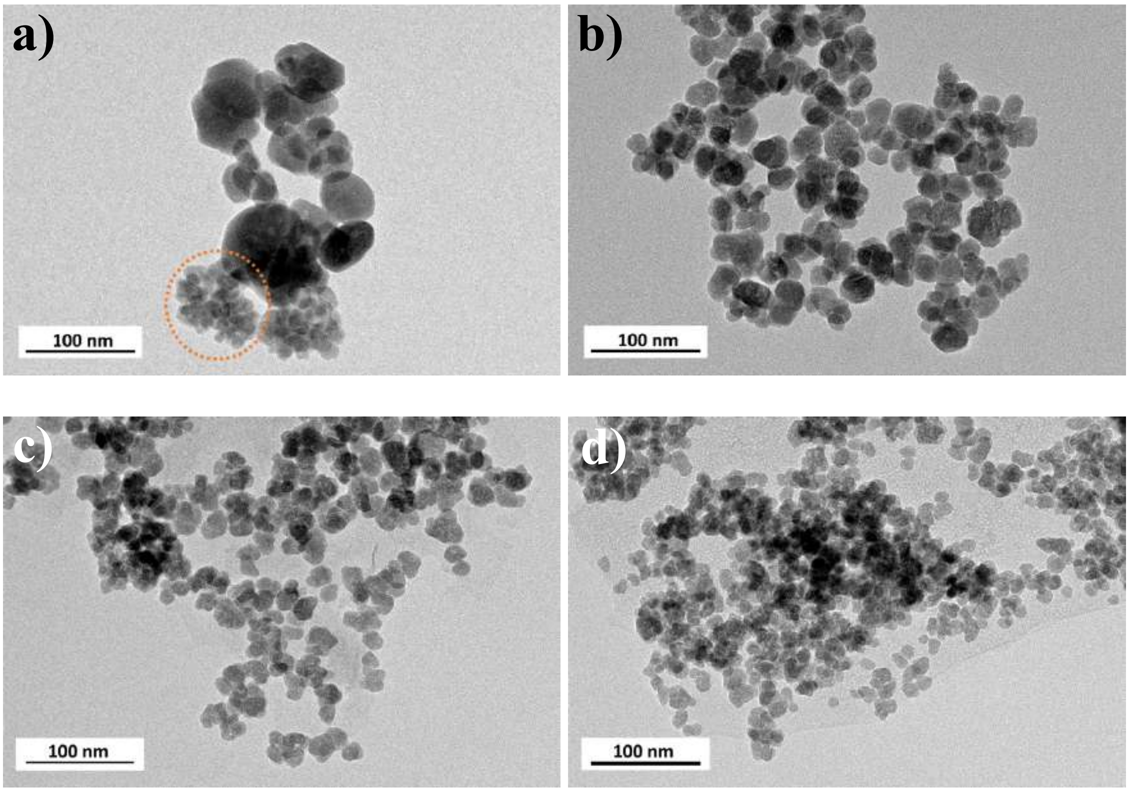

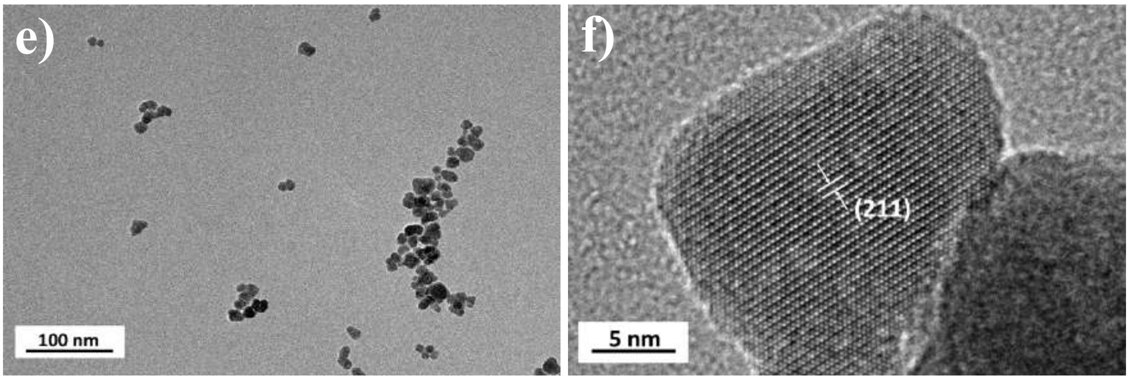

Figure 26. TEM images of YAG NCs prepared with **(a)** 0.00, **(b)** 0.50, **(c)** 1.00, **(d)** 2.00, and **(e)** 3.00% in volume of DEG. **(f)** HR-TEM of YAG NC (0.00% volume DEG). All samples were co-doped with 0.75% mol Nd^{3+} and 0.50% mol Yb^{3+}.

Table 5. Summary of Lc, NC size, degree of polydispersity, and hydrodynamic size of YAG: 0.75% mol Nd^{3+}, 0.50% mol Yb^{3+} NCs

DEG (% vol.)	Lc determined by HR-XRD (nm)	Size determined by TEM (nm)	PDI (TEM)	Hydrodynamic size determined by DLS (nm)	PDI (DLS)
0.00	28 ± 1	51 ± 20	0.10	78 ± 30	0.19
0.50	22 ± 1	23 ± 10	0.05	59 ± 30	0.21
1.00	18 ± 1	19 ± 10	0.05	37 ± 20	0.19
2.00	15 ± 1	16 ± 10	0.05	40 ± 20	0.16
3.00	14 ± 1	14 ± 10	0.04	48 ± 20	0.15

This NC aggregation in water possibly arises from the residues of solvent molecules lying on the surface of the NCs, enabling the bonding of two or three NCs through weak interactions [148]. Several peaks of organic residual groups are indeed detectable in the FTIR spectrum, depicted in **Figure 27**. The contribution of stretching C-O bonding appears at 1066 cm^{-1}. The peaks at 1330 cm^{-1} and 1456 cm^{-1} are related to wagging and symmetric bending of CH_2, respectively. The peak at 1565 cm^{-1} is due to the asymmetric stretching of COO-, which derives from the use of acetates as precursors. A small peak at 2950 cm^{-1} is assigned to the stretching of C-H bonding. The broad band in the 3000 - 3700 cm^{-1} surroundings is attributed to the presence of hydroxyl groups. The fingerprint range (inset of **Figure 27**) contains peaks of Y-O stretching, at 517, 565, and 729 cm^{-1}, whereas the peaks at 696 and 795 cm^{-1} concern the stretching of Al-O linkages[147–150].

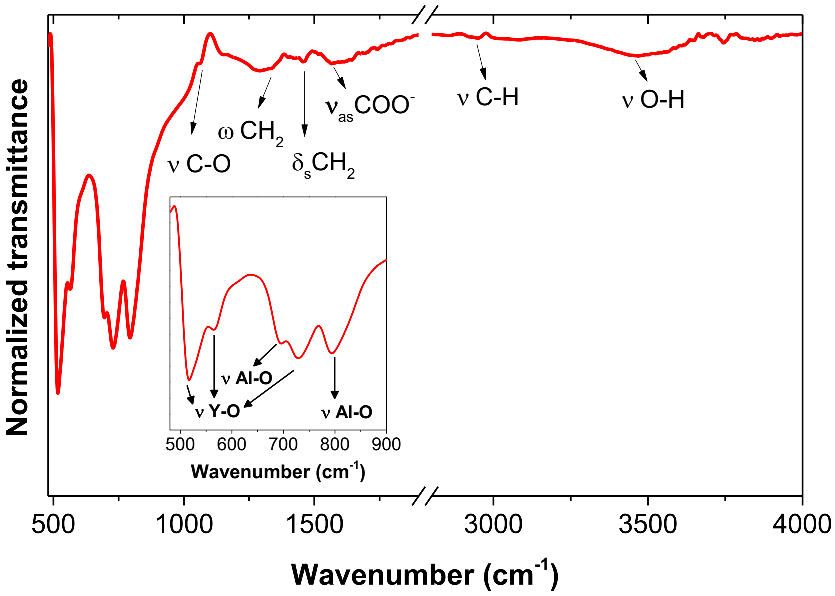

Figure 27. FTIR spectrum of YAG: 0.75% mol Nd^{3+}, 0.50% mol Yb^{3+} synthesized by the solvothermal method. ν: stretching, δ: bending, ω: wagging.

Aside from the aggregation difficulty, the presence of residual organic species is undesired since it can deactivate radiative processes of luminescent ions lying near the surface of the NCs, affecting the PL emission of Nd^{3+} - Yb^{3+} co-doped YAG. Vorsthove and Kynast [148] tried several ways of removing this organic layer of YAG NCs with chemicals, such as polyalcohol, organic and inorganic acids, and chelating agents, but they were not successful. Thermal decomposition of these organic species using high-temperature treatments may be a good solution provided that coalescence of NCs and outbreak of surface defects are avoided.

In this way, the next step of this work consisted of growing an amorphous silica shell to perform a protected annealing, so that these organics could be removed, preventing the coalescence and diffusion of NCs, and, consequently, improving their PL emission. Henceforth, experiments will be done on YAG NCs synthesized with 0.50% in volume of DEG, which makes it possible to obtain NCs measuring in between 20 and 30 nm. This condition was selected to prevent excessively small NCs, which have a high surface-to-volume ratio and as a result, more luminescent ions can be exposed on the surface, making them prone to the interaction with PL quenchers. Conversely, for future biological applications, it is important to use NCs with uniform shape and narrow size distribution. Therefore, using 0.50% in volume of DEG meets these criteria.

2.3.2.2. Silica-coating of YAG: Nd^{3+}-Yb^{3+} nanocrystals and protected annealing

Cichos and Karbowiak[118] introduced a procedure for growing an amorphous silica layer around inorganic NCs using a two-phase system. It consists of entailing the gradual hydrolysis of TEOS (silica precursor) to deliver silicate species, in the presence of a hydrolysis catalyst, from the top organic layer (first phase) to the bottom aqueous layer containing the NCs stabilized by a surfactant (second phase). Compared to classical silica coating methods like Stöber and microemulsion processes, the TEOS hydrolysis and condensation run at slower rate, making the process controllable and repeatable.

In the biphasic method, the surfactant plays a major role in stabilizing hydrophobic NCs in aqueous solution. CTAB was found to be the one that provides a better stabilization of the NCs in water prior to the silica-coating [118,119]. Another factor that is important during the coating procedure is the pH of the medium, which strongly affects the rate of TEOS hydrolysis and condensation. At low pH, the hydrolysis of TEOS occurs fast while condensation is slow, leading to the formation of fewer Si-O-Si bonds and, consequently, to a high porosity in the shell. On the contrary, under basic conditions, the hydrolysis of TEOS occurs at a sluggish rate whereas condensation proceeds rapidly, resulting in the formation of highly branched polymeric structures [151]. Therefore, in view of obtaining a denser shell with fewer pores, the use of a basic catalyst, such as L-arginine (pH = 10.8), is more recommended. The reactions concerning the formation of silica shell in a basic medium are described below.

Hydrolysis

$$\equiv \mathrm{Si}-\mathrm{O}-\mathrm{C_2H_5} + \mathrm{OH^-} \rightarrow \equiv \mathrm{Si}-\mathrm{O^-} + \mathrm{C_2H_6O} \qquad (19)$$

Condensation

$$\equiv \mathrm{Si}-\mathrm{O^-} + \equiv \mathrm{Si}-\mathrm{O}-\mathrm{C_2H_5} + \mathrm{H_2O} \rightarrow \equiv \mathrm{Si}-\mathrm{O}-\mathrm{Si}\equiv + \mathrm{C_2H_6O} + \mathrm{OH^-} \qquad (20)$$

$$\equiv \mathrm{Si}-\mathrm{O^-} + \equiv \mathrm{Si}-\mathrm{OH} \rightarrow \equiv \mathrm{Si}-\mathrm{O}-\mathrm{Si}\equiv + \mathrm{OH^-} \qquad (21)$$

The pores of the silica shell are also significantly affected by the solvent used for the dilution of TEOS. In general, the higher the solvent polarity, the lower the shell porosity. Namely, Wiercigroch-Walkosz et al.[119] observed that cyclohexane (polarity index of 0.006) provided a silica shell with pores of around 4 nm whereas the use of ethyl acetate (polarity index of 0.228) resulted in a denser silica shell. However, the authors also affirmed that above a certain value of polarity, multiple NCs are coated by the shell, as it occurred when using octan-1-ol (polarity index of 0.537).

The size of the core-shell NPs is directly influenced by both the amount of TEOS, and the quantity of nanoparticles used in the experiment. If an insufficient amount of TEOS is used, there is a risk of leaving some NCs uncoated, while increasing the amount of TEOS results in a thicker silica shell. In contrast, if many NCs are employed in the coating experiment, the thickness of the silica shell becomes thinner [118,119,152,153].

Bearing these facts in mind, YAG: 0.75% mol Nd^{3+}, 0.50% mol Yb^{3+} NCs were coated using CTAB, L-arginine and ethyl acetate as surfactant, base catalyst and solvent for TEOS, respectively (see the concentration values in **section 2.2.1.3**). The resulting core-shell NPs can be visualized in the FE-SEM images, depicted in **Figure 28.(a)**. According to them, the average final size of YAG: 0.75% mol Nd^{3+}, 0.50% mol Yb^{3+} @SiO_2 NPs was estimated as 106 ± 20 nm. When images are acquired with a STEM module, the differing electron densities between the core and shell create a distinct contrast, clearly revealing a mesoporous silica layer surrounding the nude YAG: 0.75% mol Nd^{3+}, 0.50% mol Yb^{3+} NCs (**Figure 28.(b)**). Besides, no uncoated NCs have been found. This is attributed to the use of a cationic surfactant, CTAB, as a capping layer, that facilitates interactions with anionic silicate species. When other types of surfactants are applied (anionic or non-ionic) in a basic medium, just a few NCs or none are coated with silica [119]. Based on STEM images, the silica shell thickness was measured as 21 ± 10 nm.

However, it was found some NPs involving multiple cores by the same shell, as unveiled by the STEM analysis as an example (**Figure 28.(b)**). In line with the previous discussion of DLS and FTIR of nude YAG NCs, the presence of molecules residing in the vicinity of the YAG surface provided difficulties in fully dispersing them prior to the silica coating experiments. Hence, the presence of some large core-shell NPs ended up contributing to the enlargement of its hydrodynamic size to values around 200 nm measured by DLS (**Figure 28.(c)**). Even so, the material maintained colloidal stability when suspended in water as demonstrated by the autocorrelation function in **Figure 28.(d)**.

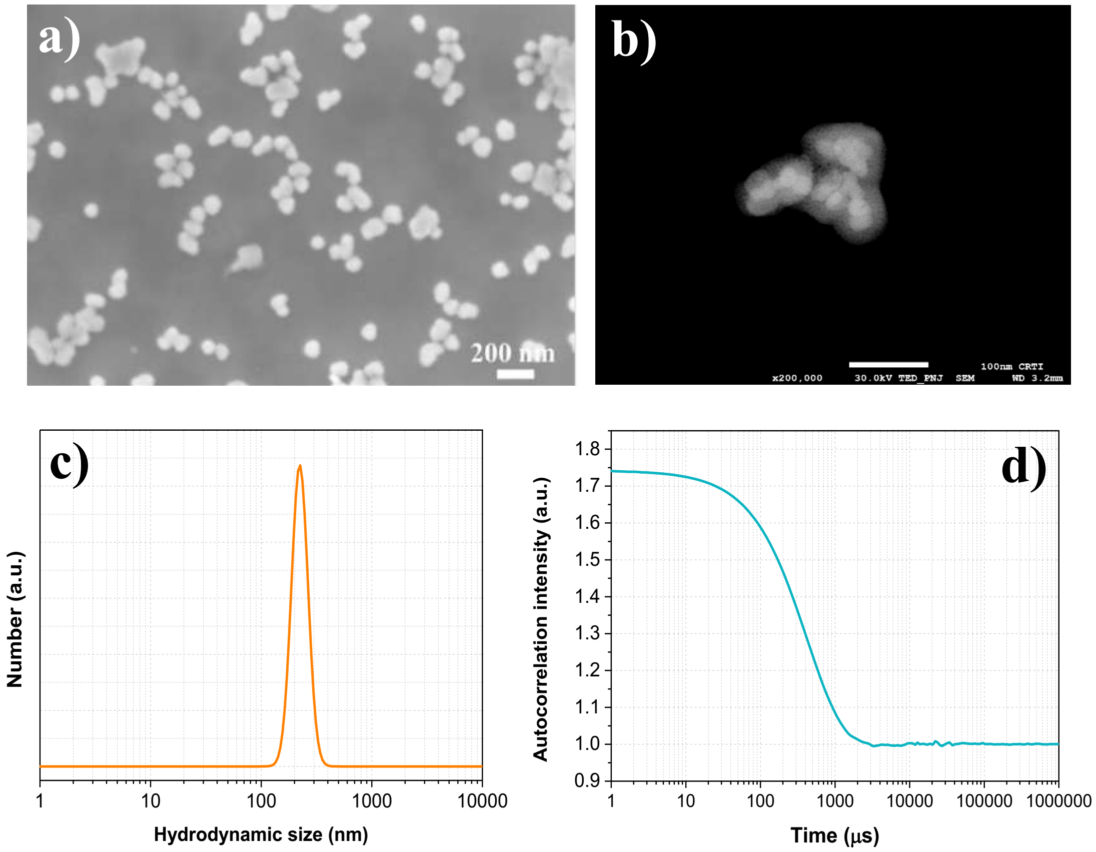

Figure 28. (a) FE-SEM, and **(b)** STEM images of YAG: 0.75% mol Nd^{3+}, 0.50% mol Yb^{3+}@SiO_2 NPs. **(c)** Hydrodynamic size, and **(d)** autocorrelation function when these core-shell NPs are suspended in water.

TG/DSC analysis combined with mass spectrometry were conducted on YAG: 0.75% mol Nd^{3+}, 0.50% mol Yb^{3+} @SiO_2 NPs, to provide insights into the thermal behavior of the material. As shown in the TG/DSC curves in **Figure 29.(a)**, between 100°C and 200°C, a slight dehydration occurs, corresponding to the water desorption from the NPs. Up to 600°C, solvent molecules adsorbed on the surface of the NPs are removed, as confirmed by the elimination of H_2O and CO_2 in the mass spectrometry (**Figure 29.(b)**), resulting in a total mass loss of 7.50% [126]. A small endothermic peak at 455°C in DSC curve, accompanied by a mass loss, indicates the conversion of boehmite to γ-alumina. This is followed by a transition to α-alumina, as signalized by the exothermic peak at 998°C in DSC [154–157]. The formation of boehmite may come from the solvothermal synthesis of YAG due to the hydrolysis of aluminum isopropoxide, despite efforts to prevent it. Nevertheless, the boehmite content is likely minimal, as no spurious peaks appeared in the HR-XRD of YAG: 0.75% mol Nd^{3+}, 0.50% mol Yb^{3+} displayed before in **Figure 25**. Notably, no exothermic events associated with the crystallization of YAG, typically taking place around 800°C to 900°C [158–162], were observed in the DSC curve. This corroborates that the solvothermal method produces YAG NCs with high crystal quality, consistent with the HR-XRD and HR-TEM results. Lastly, the exothermic peak at 1189°C in DSC is ascribed to the crystallization of amorphous silica into cristobalite [163]. In this way, the protected annealing should be performed at temperatures above 600°C to eliminate organic molecules and hydroxyl groups, but below 1100°C to avoid the crystallization of the silica shell.

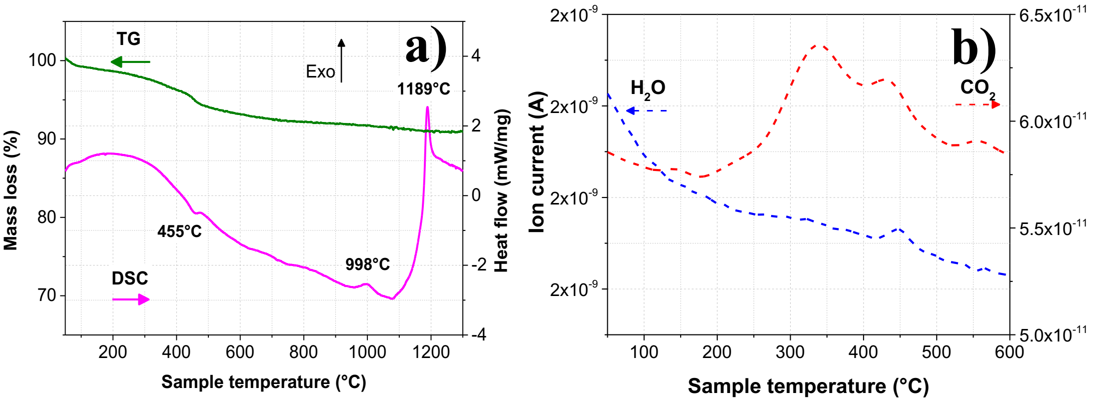

Figure 29. (a) TG/DSC and **(b)** mass spectrometry of YAG: 0.75% mol Nd^{3+}, 0.50% mol Yb^{3+}@SiO$_2$ NPs.

Then, different tests of thermal treatment were performed on YAG: 0.75% mol Nd^{3+}, 0.50% mol Yb^{3+}@SiO$_2$ NPs to check the effect of annealing temperature on structural and optical properties. Four different temperatures were evaluated: 700°C, 850°C, 1000°C, and 1100°C. The duration and the heating rate remained constant at 1 hour and 5°C.min^{-1}, in the respective order, for all experiments. According to FE-SEM images, there is no sign of NP agglomeration when treated below 1000°C (**Figure 30.(a) – (c)**). On the other hand, the presence of large and agglomerated NPs when heat-treated at 1100°C is evident as expected, caused by the start of silica crystallization (**Figure 30.(d)**)

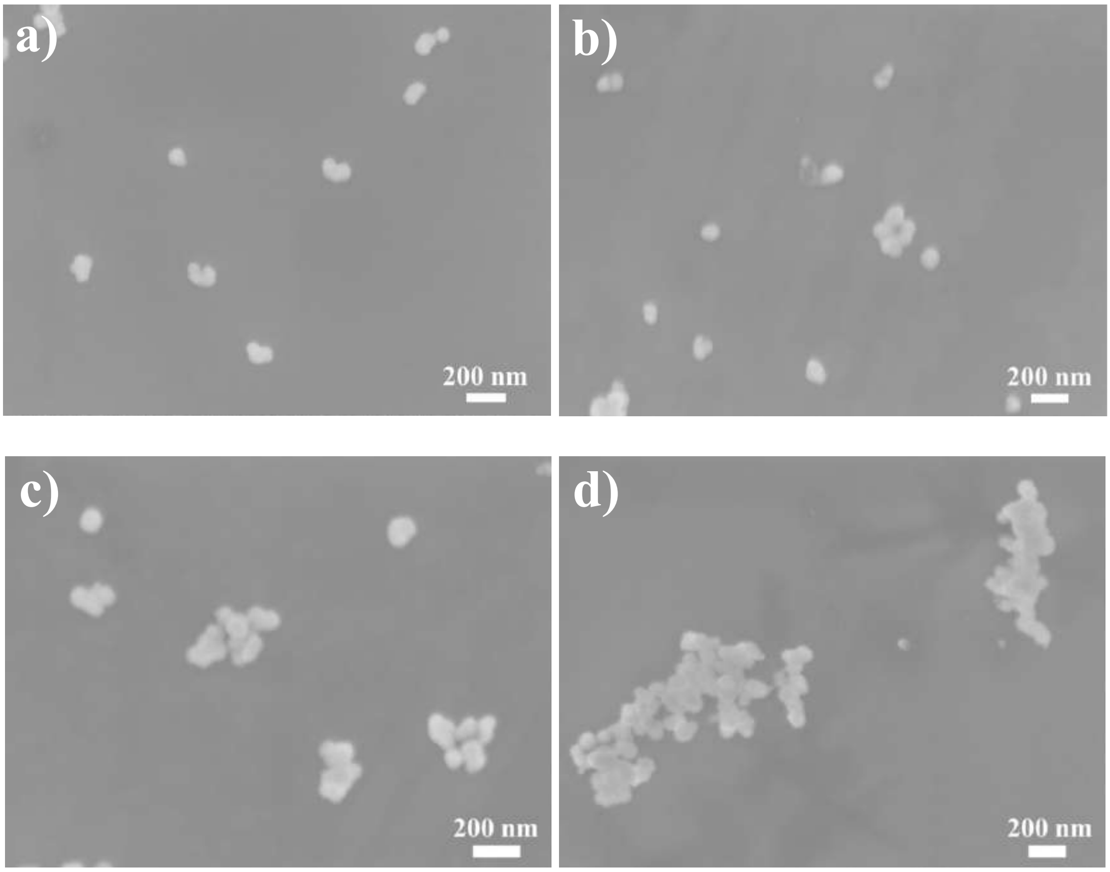

Figure 30. FE-SEM images of YAG: 0.75% mol Nd^{3+}, 0.50% molYb^{3+}@SiO_2 NPs annealed at **(a)** 700°C, **(b)** 850°C, **(c)** 1000°C, and **(d)** 1100°C for 1h.

FTIR experiments were carried out on the core-shell NPs before and after their heat treatments at 700°C, 850°C, 1000°C and 1100°C, and the curves along with the band assignments are presented below in **Figure 31**. Compared to the FTIR spectrum of nude YAG NCs in **Figure 27**, most bands associated with organic species disappear after silica coating, but this is complete after the annealing. Furthermore, the usual peaks corresponding to YAG in the fingerprint area were observed. Stretching modes at 530, 561, and 729 cm^{-1} originate from Y-O linkages, while those at 696 and 795 cm^{-1} arise from Al-O linkages.

Peaks regarding the silica shell appeared at 956 cm^{-1} and 1097 cm^{-1} in YAG: 0.75% mol Nd^{3+}, 0.50% mol Yb^{3+}@SiO_2 before annealing. The one at 956 cm^{-1} is assigned to the stretching mode of Si-O in silanol groups (Si-OH) attached to the surface of the NPs. This type of species can still be found due to incomplete reactions of condensation, but it is removed after the thermal treatment, as signalized by the disappearance of the corresponding peak in FTIR spectra [164,165]. The peak at 1097 cm^{-1} concerns the asymmetric stretching of Si-O-X (X = Si, Al, Y, Nd, Yb), which effectively confirms the formation of silica shell around YAG NCs. It not only shifts towards higher wavenumbers but also the shoulder at 1220 cm^{-1} becomes more prominent by increasing the annealing temperature, indicating the tightening of bonds [147,166,167]. A third peak related to the symmetric stretching of Si-O-Si can be present at around 775 cm^{-1}, but it is overlapped with the stretching mode of Al-O [165,168].

Weak bands associated with the bending and stretching vibrations of OH groups at 1620 and 3400 cm^{-1}, respectively [169], appeared in FTIR spectra of all samples. Silanol groups and absorbed H_2O were eliminated with calcinations, but the silica shell is mesoporous, with a golf ball-like surface, and OH groups can still accommodate inside them, even though the mesopores are presumably very small (below 4 nm) [118].

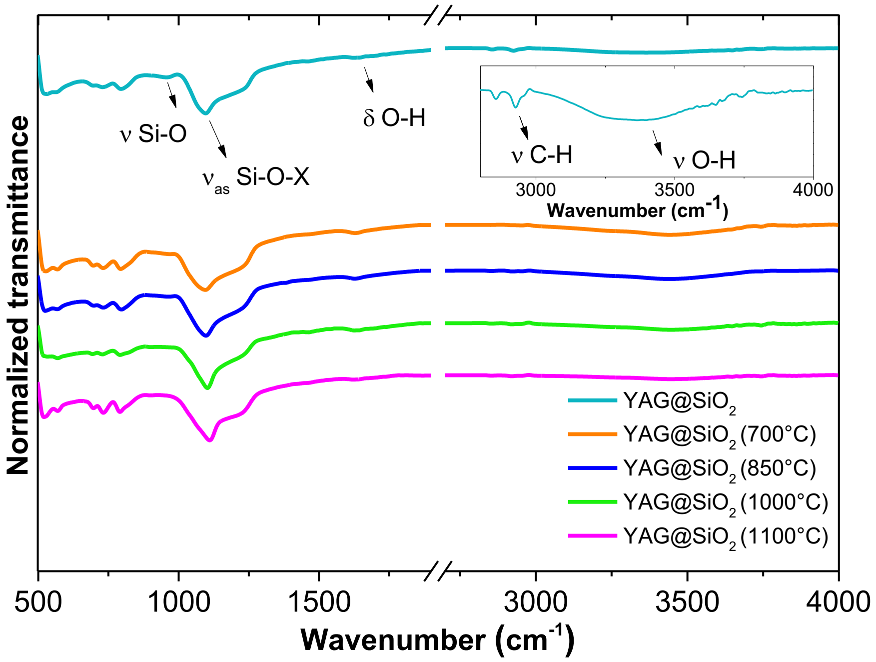

Figure 31. FTIR of YAG: 0.75% mol Nd^{3+}, 0.50% mol Yb^{3+}@SiO_2 NPs before and after heat treatments. The temperature written inside the parenthesis refers to the annealing temperature. ν: stretching, δ: bending.

Next, nude YAG: 0.75% mol Nd^{3+}, 0.50% mol Yb^{3+} NCs alongside the silica-coated YAG: 0.75% mol Nd^{3+}, 0.50% mol Yb^{3+} NPs annealed at 700°C, 850°C, 1000°C and 1100°C were dispersed in aqueous solutions, with a concentration of 3.00 mg/ml, for recording the PL emission spectra under 808-nm continuous pump. During the analysis, the solutions were kept under magnetic stirring. It is worth mentioning that this type of preparation was chosen over a powder one to avoid eventual distorted results caused by varying degrees of grain compaction and H_2O absorption from the environment (moisture).

The outcomes presented in **Figure 32.(a)** reveal the typical transitions of Nd^{3+} ($^4F_{3/2} \rightarrow {}^4I_{9/2}$ and $^4F_{3/2} \rightarrow {}^4I_{11/2}$) and Yb^{3+} ($^2F_{5/2} \rightarrow {}^2F_{7/2}$), and neither the presence of silica envelope nor the calcination affected the emission shape of the luminescent ions. In contrast, the PL intensity is significantly enhanced when annealing is performed. The NPs showed an emission improvement that peaked when they were heat-treated at 850°C and remained relatively similar when annealed at 1000°C, indicated by the overlap of their PL curves (dark blue – 850°C and green – 1000°C in **Figure 32.(a)**). On the other hand, when treated at 1100°C, the PL emission in general is less improved. A quantitative comparison was carried out based on the integrated PL lines that will be used for LIR nanothermometry (1063 nm – Nd^{3+} and 1030 nm – Yb^{3+}) and is displayed in **Figure 32.(b)**. The Stark line at 1063 nm (I_{1063}) had a maximum 4.0-fold improvement whereas the one at 1030 nm (I_{1030}) had an impressive 15-fold gain upon annealing at either 850°C or 1000°C.

The observed enhancement in PL intensity can be attributed to the effective eradication of PL quenchers through the heat treatment. According to Cantarano et al.[120], Ln^{3+}-doped YAG NCs synthesized via the solvothermal method may feature luminescent ions near their surfaces that are highly susceptible to de-excitation by organic species and OH groups. With the removal of such typical PL quenchers, the non-radiative depopulation of Nd^{3+} caused by them is decreased. Consequently, it enhances not only the radiative transition of Nd^{3+} ions but also the efficiency of the energy transfer $Nd^{3+} \rightarrow Yb^{3+}$, thereby providing this incredible improvement of Yb^{3+} emission [170]. It is worthy of note that the complete crystallization of YAG NCs due to the annealing [126,171] can be overlooked in this case, because the NCs have already a good crystal quality, as previously checked by HR-XRD (**Figure 25**), HR-TEM (**Figure 26.(d)**), and TG/DSC (**Figure 29**) analysis. Furthermore, no differences of peak widths in the HR-XRD and neither in the coherence lengths of YAG were verified before and after thermal treatment at 850°C (**Figure S3** and **Table S1** in **Appendix**). Concerning the declination of PL intensity for NPs heat-treated at 1100°C, it may be due to the interaction of core and shell, resulted from the onset of amorphous silica transformation into cristobalite [126]. In light of these remarks, the temperature of 850°C was definitively adopted for protected annealing since the PL was improved more efficiently — lower temperature and less time-consuming than at 1000°C.

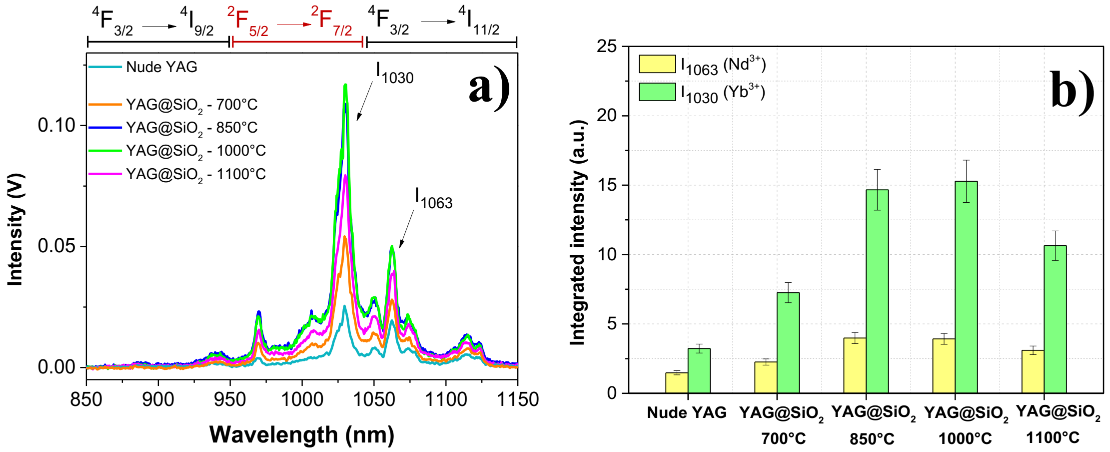

Figure 32. (a) PL spectra of nude YAG NCs compared to YAG@SiO2 NPs annealed at 700°C, 850°C, 1000°C, and 1100°C for 1h. **(b)** Integrated PL emissions at 1063 nm and 1030 nm of Nd^{3+} and Yb^{3+}, respectively, for the different annealing temperatures compared to nude YAG. All the samples were co-doped with 0.75% mol Nd^{3+}and 0.50% mol Yb^{3+}.

The PL intensity can be further improved if a thinner silica shell is anchored around the YAG: 0.75% mol Nd^{3+}, 0.50% mol Yb^{3+} NCs. This conclusion was drawn from a last experiment in which TEOS was reduced by 60% whereas all other parameters remained unchanged for silica-coating. It generated NPs of YAG: 0.75% mol Nd^{3+}, 0.50% mol Yb^{3+} fully coated with amorphous silica, measuring 87 ± 20 nm in size (**Figure 33.(a)**). Based on different microscopy images acquired with STEM module (**Figure 33.(b)**), the shell thickness was estimated as 17 ± 10 nm, which is 19% thinner relative to the thickness of the core-shell NPs previously obtained (21 ± 10 nm). After annealing this sample at 850°C, the PL emission spectrum was attained by continuously irradiating the sample dispersed in water at 808 nm (**Figure 33.(c)**). Then, it was observed the PL improvement was 5.2-fold and 21.0-fold for Nd^{3+} and Yb^{3+} emissions, respectively, compared to nude YAG: 0.75% mol Nd^{3+}, 0.50% mol Yb^{3+} NCs (**Figure 33.(d)**).

The impact of shell thickness on PL emission enhancement is linked to the presence of pores in the silica shell. While it is expected that pore size remains consistent regardless of shell thicknesses — given that factors typically influencing pore size, such as reaction temperature and the TEOS solvent, were kept constant [118,119] — there appear to be more pores per surface area in the thicker shell (STEM image in **Figure 28.(b)**) compared to the thinner shell (**Figure 33.(b)**). Consequently, reducing the shell thickness can lead to less PL quenching, as fewer OH groups would be lodged in the pores, thus reducing their ability to interact with Nd^{3+} and Yb^{3+} ions.

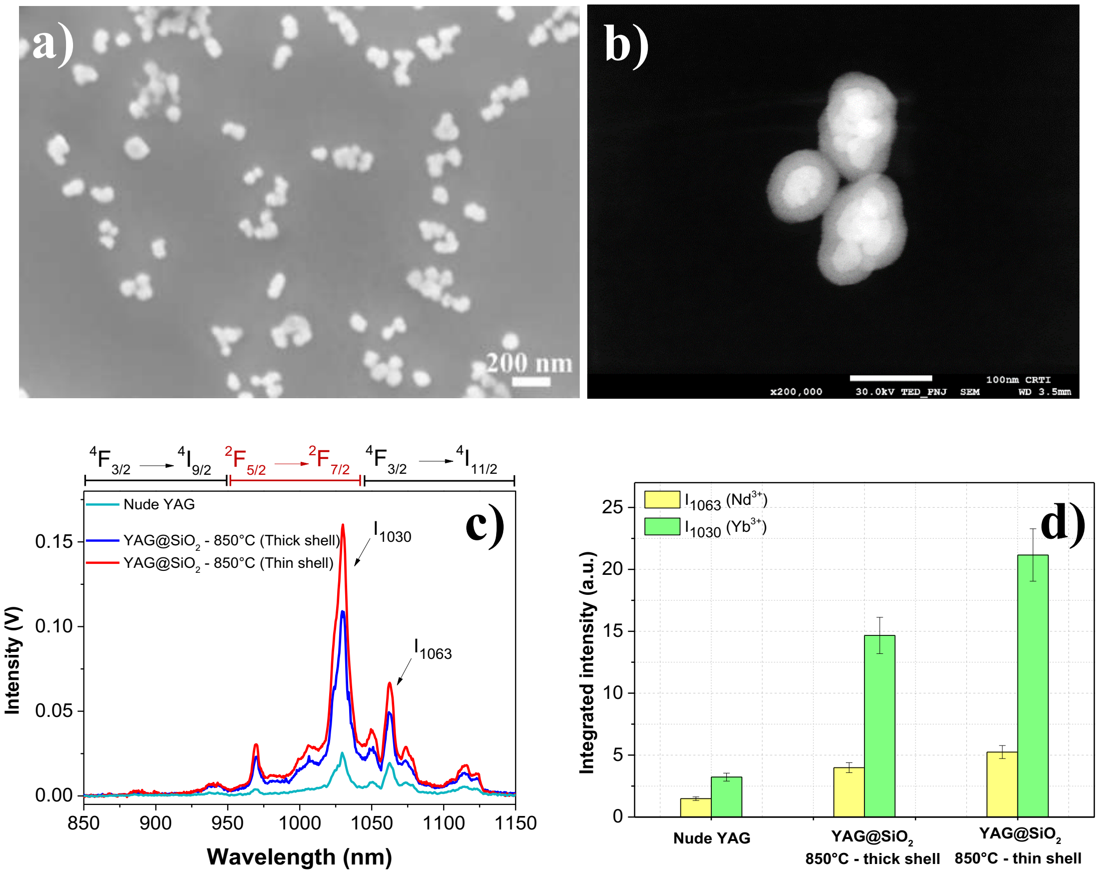

Figure 33. (a) FE-SEM, and **(b)** STEM images of YAG: 0.75% mol Nd^{3+}, 0.50% mol Yb^{3+}@SiO_2 NPs with thin shell (17 ± 2 nm). **(c)** PL spectra of nude YAG NCs compared to YAG@SiO_2 NPs annealed at 850°C with thick shell (21 ± 4 nm) and thin shell (17 ± 2 nm). **(d)** Integrated PL emissions at 1063 nm and 1030 nm of Nd^{3+} and Yb^{3+}, respectively, for different shell thickness compared to nude YAG. All the samples were co-doped with 0.75% mol $Nd^{3+}$and 0.50% mol Yb^{3+}.

The influence of hydroxyl molecules on PL emission was further verified by conducting the PL analysis both before and after the introduction of H_2O droplets onto powdered YAG: 0.75% mol Nd^{3+}, 0.50% mol Yb^{3+}@SiO_2 NPs with thin shell (17 ± 10 nm). During the analysis, it was ensured that no other variables were altered (sample position, sample mass, excitation power). As shown in the PL emission spectra in **Figure 34.(a)**, a pronounced quenching effect of PL emission occurred due to the interaction of OH groups with the Ln^{3+} ions following the H_2O application. In comparison, a parallel analysis using deuterium water (D_2O) showed no such quenching effect (**Figure 34.(b)**). This difference can be attributed to the higher vibrational energy of OH groups compared to OD groups (3400 cm^{-1} for OH versus 2500 cm^{-1} for OD), hence necessitating fewer phonons to bridge the gap between the excited and fundamental states of Nd^{3+} and Yb^{3+} ions [172,173].

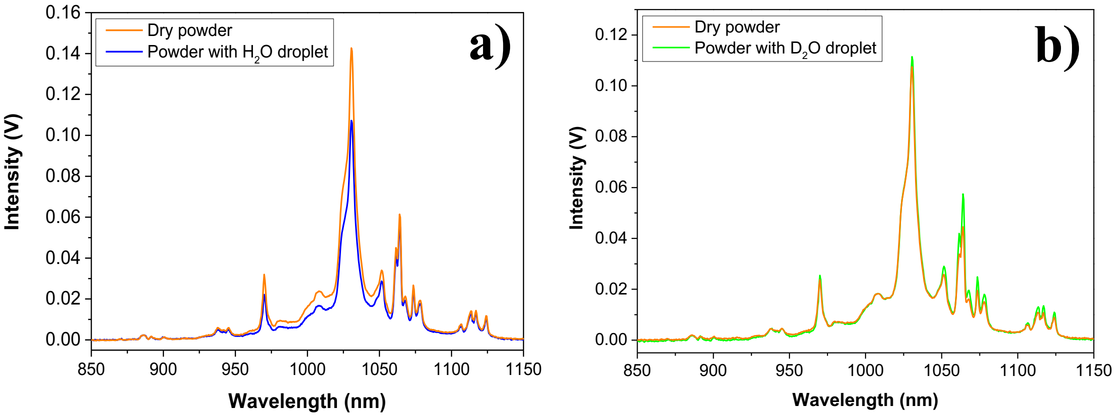

Figure 34. **(a)** PL emission spectra of powdered YAG: 0.75% mol Nd^{3+}, 0.50% mol Yb^{3+}@SiO$_2$ before and after dripping H_2O. **(b)** PL emission spectra of powdered YAG: 0.75% mol Nd^{3+}, 0.50% mol Yb^{3+}@SiO$_2$ before and after dripping D_2O.

Considering these findings, combine the strategies of selecting 0.75% mol and 0.50% mol as optimal concentrations of Nd^{3+} and Yb^{3+} respectively, and surrounding the Nd^{3+}-Yb^{3+} co-doped YAG NCs with a thin silica layer for protected annealing at 850°C provided promising results of enhancement of PL intensity. These most favorable conditions were employed to carry out the nanothermometry analysis, which are presented in the following section.

2.3.3. Nanothermometry of YAG: Nd^{3+}-Yb^{3+} nanocrystals

The thermal sensing performance of the samples was evaluated through the measurements of PL(T), under continuous 808 nm irradiation within the thermal range of 297 K – 333 K (24°C – 60°C), for the implementation of the LIR technique. Initially, this analysis was conducted on both agglomerated NCs obtained via the modified Pechini method and core-shell NPs annealed at 850°C (thin shell, 17 ± 10 nm) to verify the impact of the synthesis techniques on thermal sensing. Subsequently, a comparative analysis focusing exclusively on YAG: 0.75% mol Nd^{3+}, 0.50% mol Yb^{3+}@SiO$_2$ NPs was carried out to evaluate the influence of the sample preparation — whether as slightly compacted powder or dispersed in an aqueous solution — on the thermal sensing properties.

The PL(T) spectra of YAG: 0.75% mol Nd^{3+}, 0.50% mol Yb^{3+} synthesized via the modified Pechini method and YAG: 0.75% mol Nd^{3+}, 0.50% mol Yb^{3+}@SiO$_2$ NPs (thin shell and annealed at 850°C) presented in **Figure 35.(a)** and **(c)**, respectively, reveal consistent spectral profiles across both synthesis methods, except for the PL intensity. Likewise, the only significant difference observed of the PL (T) of YAG: 0.75% mol Nd^{3+}, 0.50% mol Yb^{3+}@SiO_2 NPs in powder form (**Figure 35.(c)**) compared to those dispersed in water (**Figure 35.(e)**) is the reduction in PL intensity, associated with the quenching by OH groups lodged inside the mesopores. In all three spectra, Nd^{3+} emissions are constant across the temperature range, but the Yb^{3+} transition $^2F_{5/2} \rightarrow {}^2F_{7/2}$ exhibited a strong dependency on the temperature.

To obtain the calibration curve and calculate Sr and δT, the PL spectra were collected in the range of 1000 - 1090 nm for each temperature, as the peaks of interest are 1063 nm (Nd^{3+}) and 1030 nm (Yb^{3+}) for LIR. After converting the emission spectrum from wavelength-dependent to wavenumber-dependent format, the LIR between emission lines at 1063 nm (I_{1063}) and 1030 nm (I_{1030}) was calculated as follows for each temperature:

$$\mathrm{LIR}(\tilde{\nu}, \mathrm{T}) = \frac{\int_{9380}^{9420} \mathrm{I}_{1063}(\tilde{\nu}, \mathrm{T})\, \mathrm{d}\tilde{\nu}}{\int_{9690}^{9828} \mathrm{I}_{1030}(\tilde{\nu}, \mathrm{T})\, \mathrm{d}\tilde{\nu}} \tag{22}$$

where $\tilde{\nu}$ is wavenumber, given in cm^{-1}.

Targeting in achieving values of δT below 0.2 K involves both improvement of Sr and minimization of uncertainties associated with LIR, in accordance with equation 6 in **Chapter I**. As the last parameter has a close relation to the quality of statistics, several spectra were registered at constant temperature of 309.3 K to settle the number of spectra necessary in providing minimal δLIR, for reliable measurements. Based on the plot number of PL spectra versus δLIR depicted in **Figure 36**, δLIR achieves the lowest values when above 40 PL emission spectra are registered. Therefore, for each temperature, 40 to 50 PL emission spectra were collected.

Hence, seven points of LIR were plotted on a graph LIR versus temperature in Kelvin scale. A linear fit in the form of LIR = aT + b, with a and b as constants, was applied to each sample to establish the corresponding calibration curves (**Figure 35.(b)**, **(d)**, and **(f)**). The linear approximation was deemed appropriate as the temperature range studied is narrow, reflecting the focus on potential biological applications. Indeed, statistical R^2 values greater than 0.995 were reached for all analysis, indicating an excellent fit quality.

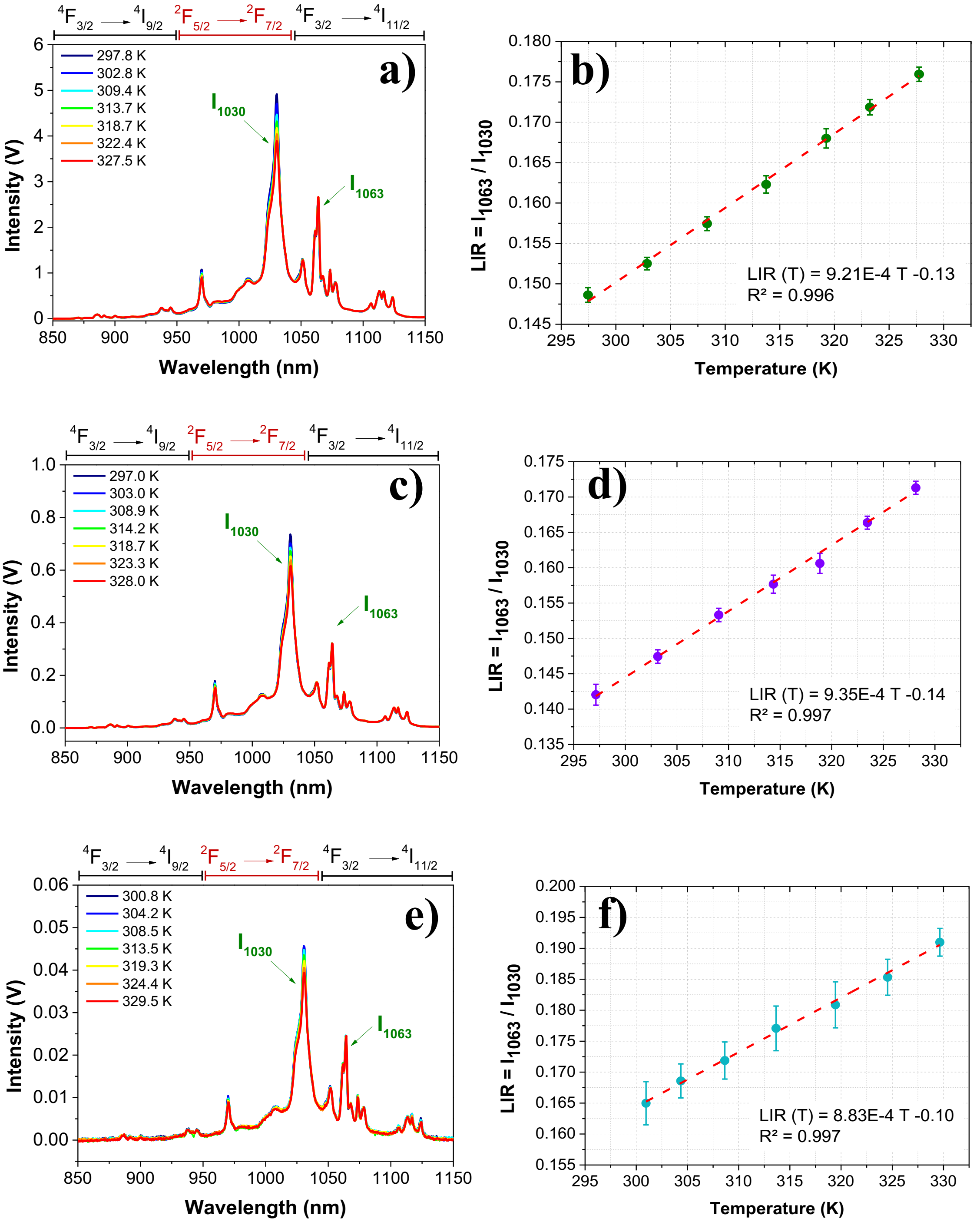

Figure 35. **(a)** PL(T) and **(b)** calibration curve of YAG synthesized by modified Pechini method. **(c)** PL(T) and **(d)** calibration curve of YAG@SiO$_2$ (solvothermal route + protected annealing) in powder. **(e)** PL(T) and **(f)** calibration curve of YAG@SiO$_2$ dispersed in water. The samples were co-doped with 0.75% mol Nd^{3+} and 0.50% mol Yb^{3+}.

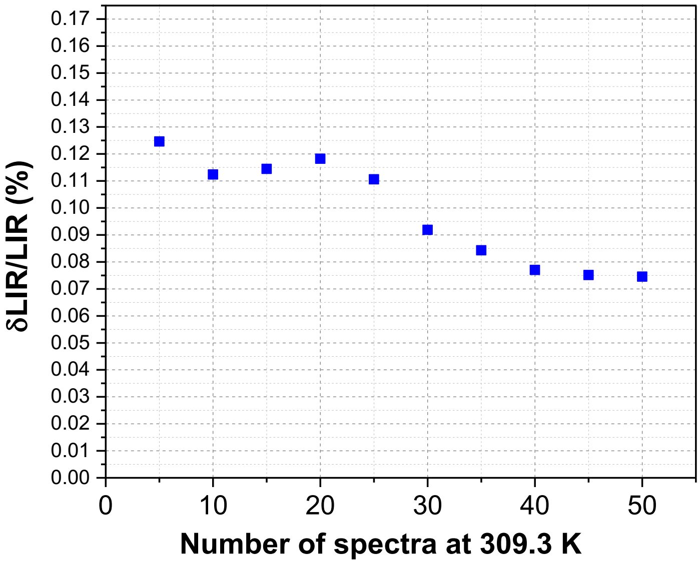

Figure 36. Number of PL spectra at 309.3 ± 0.1 K versus δLIR/LIR

The Sr and δT were calculated for each temperature using the equations 4 and 6, respectively. According to the Sr results displayed in **Figure 37.(a)**, the synthesis methods adopted in this work did not impact how the dynamic between Nd^{3+} and Yb^{3+} responds to temperature variation, as Sr values remained very close. Considering the powdered samples first, YAG: 0.75% mol Nd^{3+}, 0.50% mol Yb^{3+} NCs synthesized via the modified Pechini method exhibited Sr worth $0.58\%.K^{-1}$ at body temperature, peaking at $0.62\%.K^{-1}$ at room temperature. Similarly, YAG: 0.75% mol Nd^{3+}, 0.50% mol Yb^{3+}@SiO_2 NPs possessed Sr = $0.60\%.\ K^{-1}$ at physiological temperature, reaching to $0.65\%.K^{-1}$ at ambient temperature. These S_r values are superior to most of those published for such a Nd^{3+} - Yb^{3+} system, limited to the LIR method, as already summarized in **Table 1** in **Chapter I**.

As observed in the PL(T) spectra from **Figure 35**, the temperature-invariant emission of Nd^{3+} in YAG makes it an ideal reference for monitoring the temperature-dependent emission of Yb^{3+}. This creates a significant variation of $\frac{\partial LIR}{\partial T}$, which enhances the S_r as per the formula $S_r = \frac{1}{LIR}\left|\frac{\partial LIR}{\partial T}\right|$. A possible explanation for this distinguished thermal behavior of Nd^{3+} and Yb^{3+} emissions lies in the structural characteristics of YAG. This host features a simple crystalline structure with just a single Y^{3+} site, enabling the homogeneous arrangement of Nd^{3+} and Yb^{3+} ions throughout the host and thus, favoring the energy transfer $Nd^{3+} \rightarrow Yb^{3+}$. As the temperature increases, this energy transfer may become even more pronounced due to enhanced vibrational modes that potentially strengthen the coupling Nd^{3+} and Yb^{3+}. This, in turn, compensates for the non-radiative energy losses by Nd^{3+} ions. Conversely, the rising temperature also accelerates non-radiative relaxation pathways, leading to the reduction of Yb^{3+} emission intensity. Additionally, the back energy transfer $Yb^{3+} \rightarrow Nd^{3+}$ may be triggered with the temperature variation, but further investigation is required to verify this.

Co-doping engineering also played a key role in this process by optimizing the distribution of Nd^{3+} and Yb^{3+} ions within the YAG matrix. Ximendes et al.[70] demonstrated a similar strategy of controlling the distance of Nd^{3+} - Yb^{3+} by producing a core of LaF_3: Yb^{3+} surrounded by a shell of LaF_3: Nd^{3+}. Although their work reported a Sr = $0.74\%.K^{-1}$ at 293 K, it is worth highlighting that the Sr of 0.60 ~$0.65\%.K^{-1}$ (at ~297 K) could be obtained here by using a host matrix with a relatively higher cutoff phonon energy (856 cm^{-1} against 350 cm^{-1} of LaF_3) and without such complex core-shell engineering.

Regarding the thermal resolution of the powdered samples, the values remained between 0.1 and 0.3 K throughout the temperature range for both synthesis approaches. It reached 0.2 K for both YAG: 0.75% mol Nd^{3+}, 0.50% mol Yb^{3+} NCs synthesized via the modified Pechini method and YAG: 0.75% mol Nd^{3+}, 0.50% mol Yb^{3+}@SiO_2 NPs, at physiological temperature (**Figure 37.(b)**). This value is much lower than those published for the same Nd^{3+} - Yb^{3+} system that lied between 0.4 K and 0.6 K, meaning a better thermal resolution was obtained in this work [57,75].

Such good results of δT are directly linked to the optimized experimental conditions for PL (T) measurements. Indeed, working with an efficient sample heater like LINKAM, which isolated the sample very well from the environment, and recording 40-50 PL spectra for every temperature certainly resulted in a more stable measurement. Additionally, high emission intensities provided the increase of the signal-to-noise ratio, lowering δLIR, and thus, reaching δT equal to 0.2 K at body temperature. Such a result is very promising for potential applications in the biological domain.

When YAG: 0.75% mol Nd^{3+}, 0.50% mol Yb^{3+}@SiO_2 NPs is dispersed in an aqueous medium, Sr is slightly lower, being $0.51\%.K^{-1}$ at 309 K and reaching $0.53\%.K^{-1}$ as a maximum at room temperature. It suggests that the medium does not affect this thermometric parameter, regardless of the change in PL intensities. On the other hand, δT is up to 4-fold higher than that of the powdered sample. In this case, the interaction of Ln^{3+} with OH groups quenched the PL emission when the core-shell NPs are suspended in water, providing a low signal-to-noise ratio. This feature favored the increase of δLIR and, hence, a higher δT was obtained. This demonstrated that more optimizations are still needed to prevent the PL quenching caused by OH groups to reach a δT as good as it was achieved for the nanopowder sample.

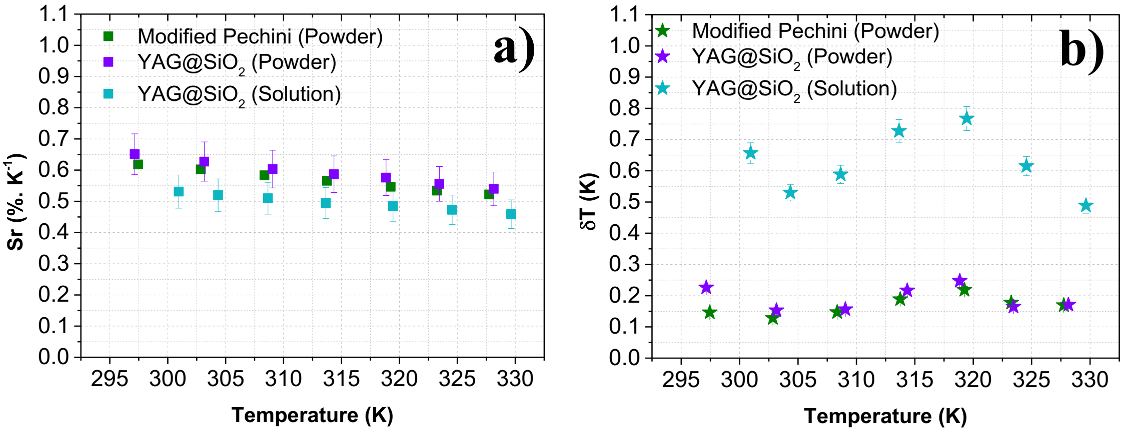

Figure 37. (a) Sr and **(b)** δT of YAG: 0.75% mol Nd^{3+}, 0.50% mol Yb^{3+} NCs synthesized by the modified Pechini method in powder and YAG: 0.75% mol Nd^{3+}, 0.50% mol Yb^{3+} @ SiO$_2$ NPs in powder and solution.

Finally, the repeatability of Nd^{3+} - Yb^{3+} co-doped YAG samples was tested by applying 11 heating-cooling cycles, from 296 K to 328 K (23°C to 55°C). Repeatability of 98.7% was achieved for YAG: 0.75% mol Nd^{3+}, 0.50% mol Yb^{3+} synthesized by the modified Pechini method whereas 98.0% for YAG: 0.75% mol Nd^{3+}, 0.50% mol Yb^{3+}@SiO$_2$ NPs, both in dry powder (**Figure 38**). This means that across 11 consecutive temperature cycles, less than 5.0% of experimental deviation is observed, which is reasonable for this thermal probe [14].

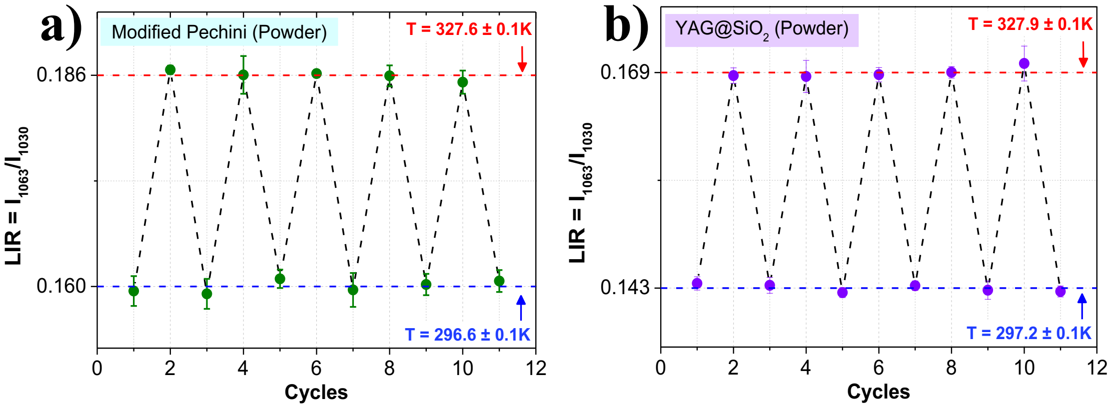

Figure 38. Recording of LIR over 11 heating-cooling cycles of **(a)** YAG: 0.75% mol Nd^{3+}, 0.50% mol Yb^{3+} NCs obtained by the modified Pechini method and **(b)** YAG: 0.75% mol Nd^{3+}, 0.50% mol Yb^{3+} @ SiO$_2$ NPs in powder. The repeatability is ≥ 98.0% or both cases.

2.4. General Remarks and perspectives

This chapter focused mostly on presenting means to enhance the PL emission of YAG: Nd^{3+} - Yb^{3+} NCs. The strategy involved first performing co-doping engineering by trying out different compositions of Nd^{3+} and Yb^{3+} through the modified Pechini synthesis. After assessing the steady-state PL emission of the samples, the composition that provided the optimal PL emission intensity for the two bands involved in the LIR method (1063 nm for Nd^{3+} and 1030 nm for Yb^{3+}) was 0.75% mol Nd^{3+} and 0.50% mol Yb^{3+}. Although this synthesis method is easy and fast to carry out, it yields agglomerated NCs, which is not ideal for biological applications, because it hinders the well dispersion of them.

Hence, a solvothermal route was employed, by adding 0.50% in volume of DEG as a co-solvent. Owing to the significant ligand effect of DEG, the uncontrolled growth of the NCs was prevented, resulting in NCs possessing dimensions of 23 ± 10 nm with a narrow size distribution (PDI = 0.05). However, the PL emission of YAG: 0.75% mol Nd^{3+}, 0.50% mol Yb^{3+} NCs obtained by this method is still very low even though the optimal Nd^{3+}-Yb^{3+} composition is used. FTIR and TG/DSC analyses indicated the presence of remaining organics and OH groups, which are typical PL quenchers.

Silica coating of YAG NCs was conducted via the biphasic method to produce core-shell NPs, which were then annealed at 850°C. The protected annealing provided a notable enhancement of 5.2-fold and 21.0-fold of Nd^{3+} and Yb^{3+} emissions, respectively, and there were no signs of agglomeration of YAG: 0.75% mol Nd^{3+}, 0.50% mol Yb^{3+} NCs coated with a silica shell as thick as 17 ± 10 nm. Lastly, the nanothermometry analysis revealed that the core-shell NPs presented $S_r = 0.60\%.K^{-1}$ and $\delta T = 0.2$ K at physiological temperature, with a repeatability of at least 98.0%.

Notwithstanding the good results obtained in powder, δT increased to 0.6 K when the core-shell NPs were dispersed in aqueous medium. This owes to the presence of mesopores in the silica shell that can still accommodate OH groups inside them and interact with Ln^{3+} ions in the vicinity of the YAG surface, causing a partial quenching effect of PL. This affects negatively the signal-to-noise ratio of PL emission, making δLIR to increase and, consequently, the thermal resolution worsens. A first possibility to underscore this interaction of Ln^{3+} with OH groups would be growing undoped YAG around YAG: 0.75% mol Nd^{3+}, 0.50% mol Yb^{3+} NCs as a protective shell. For this purpose, after the growth of YAG:Nd^{3+}-Yb^{3+} NCs in autoclave, a second solvothermal growth step could be carried out under lower supersaturation using reduced concentration of YAG precursors (yttrium acetate, aluminum isopropoxide, and 1,4-butanediol), so that any spurious nucleation of pure YAG is avoided. This protective shell would reduce the surface defects and vibrational coupling with hydroxyl groups and ligands of YAG:Nd^{3+}-Yb^{3+} NCs.

The next step involves the coating of these YAG@YAG:0.75% mol Nd^{3+}, 0.50% mol Yb^{3+} NPs with a denser and porosity-free silica shell for the protected annealing at 850°C. In this procedure, further optimization is needed in order to have a single core enveloped by the silica shell — in the case of the biphasic method, managing the TEOS concentration and the quantity of NPs is recommended. Finally, a last functionalization (with PEG, for example) will have to be performed to improve the biocompatibility in physiological environments.

Chapter III: Synthesis and characterization of yttria nanocrystals co-doped with Nd^{3+} and Yb^{3+} for nanothermometry

3.1 Introduction

Over the years, Y_2O_3 has captured the interest of the scientific community due to its favorable properties, such as good chemical stability, high thermal expansion, low phonon energy, high thermal conductivity and especially, high thermal stability. This latter feature is particularly valuable for applications in the biological field, including photodynamic therapy, biological imaging, and luminescence nanothermometry [174].

Regarding general applications in luminescence nanothermometry, several works focused on Y_2O_3 NCs doped with different rare-earth ions [61,175–179]. However, to be suitable for bio applications, it is crucial that these NCs not only work within the BWs but also possess spherical morphology, diameter below 100 nm, and good dispersion for higher feasibility in flowing in the bloodstream and entering in the cells [32]. Thus, the synthesis method plays a vital role in fulfilling such requirements.

The literature has already reported different synthesis methods to obtain Y_2O_3 NCs, namely sol-gel [180–182], co-precipitation [49,177,183,184], thermal decomposition [185], but individual NCs of this oxide cannot be formed straightforward from solution under solvothermal conditions [186]. Thermal post-treatments are usually required, which results in the coalescence of the NCs. However, some studies have demonstrated the possibility of obtaining individual yttria NCs through a two-step urea-based procedure [89,186–191]. The first step involves the decomposition of urea at between 70°C and 90°C, to originate CO_3^{2-} and OH^- that bind with Y^{3+} and form the amorphous phase $Y(OH)CO_3.H_2O$. The second step consists of submitting this phase to a heat treatment to crystallize it to Y_2O_3.

In this chapter, the potential of Y_2O_3 co-doped with Nd^{3+} and Yb^{3+} as a nanothermometer is evaluated. Initially, a selection of Nd^{3+}-Yb^{3+} composition was conducted by applying the modified Pechini method to tune the PL intensity emitted by the dopants. Afterwards, yttria NCs were synthesized through the two-step urea-based route in order to obtain individual NCs of size less than 50 nm. Regarding this procedure, the size of $Y(OH)CO_3.H_2O$ was first controlled by carrying out experiments with organic co-solvents. Then, some calcination tests were performed to yield pure Y_2O_3. In the end, the thermal sensing properties of Y_2O_3: Nd^{3+}-Yb^{3+} NCs synthesized via both methods were evaluated in accordance with the LIR approach, such as the sensitivity to temperature variations, thermal resolution, and repeatability of results.

3.2 Experimental protocol

3.2.1. Materials syntheses

3.2.1.1. Modified Pechini method

The synthesis of Y_2O_3 co-doped with Nd^{3+} and Yb^{3+} was conducted in a similar way as previously described in **Chapter II** for YAG: Nd^{3+} - Yb^{3+}, excluding the use of aluminum and modifying the final stage concerning the heat treatment. In this study, two conditions of calcination were tested: 1) 900°C/10 minutes, as reported by Barbosa et al.[64], and 2) 450°C/12h and 1000°C/1h.

3.2.1.2. Two-step urea-based route

For the first step of the synthesis process, $Y(NO_3)_3.6H_2O$ (Acros organics, ≥99.9%), $Nd(NO_3)_3.6H_2O$ (Sigma-Aldrich, ≥99.9%), $Yb(NO_3)_3.5H_2O$ (Sigma-Aldrich, ≥99.9%), and urea (Sigma-Aldrich, > 99%) were dissolved in distilled water in separated flasks at room temperature. The amount of yttrium was fixed at 7.50 $mmol.L^{-1}$, the urea concentration varied between 0.10 $mol.L^{-1}$ and 3.0 $mol.L^{-1}$, and the co-doping content was chosen based on the PL results of the modified Pechini syntheses. All aqueous solutions were mixed under stirring and then, an organic co-solvent was added to achieve a total volume of 100 ml. The solvent adjustment involved selecting from 1-propanol (Fisher Scientific, ≥ 99.0%), 2-propanol (Fisher Scientific, ≥ 99.0%), 1,4-butanediol (Thermoscientific, 99.0%), and a mixture of ethanol and 1-butanol with a volume ratio of 1:2 (Honeywell II Riedel-de-Haën, ≥99.8% and Sigma-Aldrich, 99.9%, respectively). The organic co-solvent varied between 50 and 83% in volume. The reactant solution was placed inside a 120-ml autoclave, and heated in an oven at 85°C/24h. The as-obtained powder went through three centrifugations (7800 rpm, 15 minutes) with ethanol to remove the byproducts and was dried at 60°C/2h.

In the second step, the as-obtained powders were annealed in a tubular furnace under flowing O_2 (10 $mL.min^{-1}$) to produce yttria NCs. The heat treatment conditions were tested in this study, by adjusting the temperature from 550°C to 900°C, the heating rate from 1°$C.min^{-1}$ to 10°$C.min^{-1}$, and the duration from 5 minutes to 120 minutes.

Furthermore, NaCl was also explored as a separating media to prevent the coalescence and agglomeration of yttria NCs during thermal treatments. When the salt-matrix was employed, the as-obtained powder was ground manually together with dried NaCl powder in an agata mortar for 90 minutes, and this mixture was then calcined. After several centrifugations with distilled water to eliminate NaCl, the powder was dried at 60°C/2h.

3.2.2. Characterization techniques

All characterization measurements concerning XRD, HR-XRD, FE-SEM, TEM, DLS, FTIR, DR, PL emission at room temperature, and PL(T) of Nd^{3+}-Yb^{3+} co-doped yttria samples were carried out as detailed in **section 2.2.2** in **Chapter II**. Thermogravimetry Differential Thermal Analysis (TG/DTA) along with mass spectrometry were performed on powders placed in a platinum crucible from 50°C to 1200°C, under O_2 atmosphere and heating rate of $10°C.min^{-1}$, using a Setaram TAG 16 equipment, located at Institut Néel – CNRS in Grenoble (France).

3.3 Results and discussion

3.3.1. Calcination tests of the samples obtained by the modified Pechini method

This study begins with the synthesis by the modified Pechini method to select a suitable composition of Nd^{3+} and Yb^{3+} for yttrium oxide in order to enhance their PL emission intensity. This procedure is versatile and can provide the production of various oxide matrices [52,57,64,74,75,84], but some modifications in the route may be necessary when switching from one phase to another to achieve the phase purity or at least a better crystal quality.

Hence, in the first part of this work on yttria NCs synthesis, a refinement of the modified Pechini protocol is put forward after exploring two different conditions of heat treatment while keeping the other steps of the route unchanged — similar to the YAG synthesis, as laid out in **section 2.2.1.1** in **Chapter II**. In the first test, the ground *puff* (resin dried at 250°C) was subjected to a rapid heat treatment for 10 minutes at 900°C under pure oxygen as was reported in the literature [64]. In the second test, an intermediate treatment at 450°C for 12 hours was performed, followed by a calcination at 1000°C under pure oxygen for 1 hour. The heating rate remained at $10°C.min^{-1}$ for both conditions. Furthermore, the sample was initially co-doped with 1.00% mol Nd^{3+} and

0.50% mol Yb^{3+} for these two experiments in order to check the annealing effect on both structural and optical properties. Based on the characterization analyses, a heat treatment condition was selected to conduct the study with this synthesis method for co-doping engineering, presented in the next section (**topic 3.3.2**).

Starting with XRD characterization on powder, the peaks were indexed as yttria, with cubic structure (*Ia-3* space group), by the PDF 00-041-1105, and no spurious phase was detected for any heat treatment condition. The profile adjustment employing the Le Bail fit method on HR-XRD was done (**Figure 39.(a)** and **(c)**), and the results concerning the cell parameters, and the Lc are displayed in **Table 6**.

The cell parameter *a* is the same for both calcination tests, but is slightly different from the reference due to the replacement of Y^{3+} by the Ln^{3+} ions. In Y_2O_3 unit cell, yttrium is placed in two different sites (C_2 or C_{3i}), and they are coordinated with six oxygens. For such an environment, Y^{3+} has an ionic radius of 0.900 Å while the one of Nd^{3+} is 0.983 Å. In turn, Yb^{3+} possesses a smaller ionic radius, which is worth 0.868 Å [128]. Because of the similarity of the ionic radii of these rare-earth ions, only a slight lattice expansion occurred.

On the other hand, the Lc extracted from HR-XRD was affected by the changes in the heat treatment. Such average size of single crystal domains augmented considerably from 24 ± 1 nm to 48 ± 1 nm when a longer heat treatment in two steps is performed rather than at lower temperature for a shorter period of time (**Table 6**). In this case, not only was particle growth promoted, but crystallinity was also enhanced. The Lc values correspond to the sizes measured in the TEM images for heat treatment at 900°C/10 minutes and 450°C/12h and 1000°C/1h, as depicted in **Figure 39.(b)** and **(d)**, in the respective order. In the insets of the correlated TEM images, one finds the HR-TEM showing clearly the ordered atomic planes of yttria, and the grain boundaries of two fused NCs. In summary, these outcomes indicate the samples are constituted by NCs with high crystallinity, but ended up clumping together and forming large micrometer-sized agglomerates, which is typical of this type of synthesis.

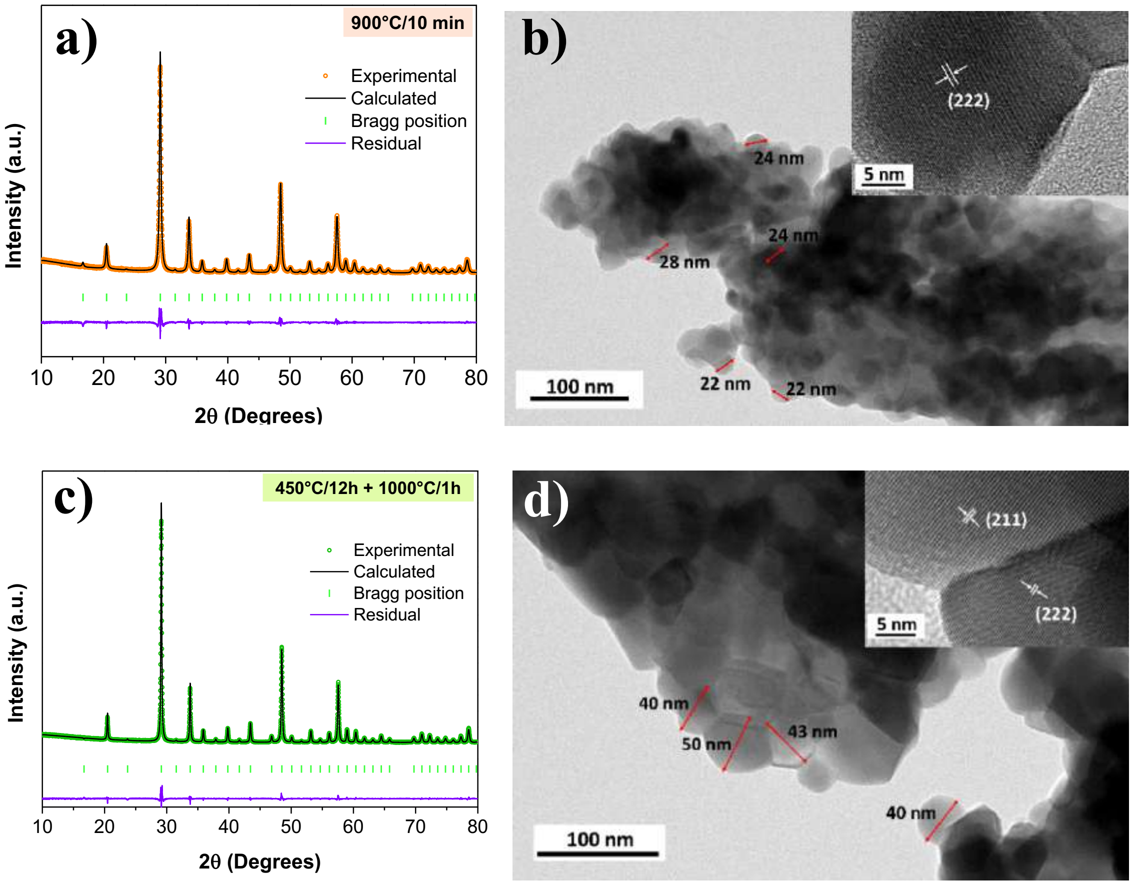

Figure 39. (a) HR-XRD pattern (orange circles) with calculated Le Bail fit (solid black line), and **(b)** TEM with an inset of HR-TEM of Y_2O_3 heat-treated at 900°C/10 min**. (c)** HR-XRD (green circles) with calculated Le Bail fit (solid black line), and **(d)** TEM with an inset of HR-TEM of Y_2O_3 heat-treated at 450°C/12 h and 1000°C/1h. The sizes were measured with the ImageJ software.

Table 6. Cell parameters, Lc, and refinement parameter according to the Le Bail fit of Y_2O_3: 1.00% mol Nd^{3+}, 0.50% mol Yb^{3+}.

Annealing condition	***a*** **(Å)**	***b*** **(Å)**	***c*** **(Å)**	**Volume ($Å^3$)**	**Lc (nm)**	**χ^2**	**Rp (%)**	**Rwp (%)**
900°C/10 minutes	10.610	10.610	10.610	1194.46	24 ± 1	2.05	10.2	11.8
450°C/12h + 1000°C/1h	10.610	10.610	10.610	1194.33	48 ± 1	2.06	10.1	11.5
Ref.[192]	10.604	10.604	10.604	1192.40	-	-	-	-

In **Figure 40.(a)**, FTIR spectra of both samples are illustrated. In the fingerprint area, two peaks at 516 – 518 cm^{-1} and 565 cm^{-1} related to the stretching mode of Y – O bonding are present in both FTIR spectra, confirming the formation of Y_2O_3. It is noticeable there are remaining organics from the precursor synthesis in both samples, because bands of deformation (673 cm^{-1} and 769 cm^{-1}), asymmetric stretching (around 962 cm^{-1}), and symmetric stretching (1392 cm^{-1} and 1513 cm^{-1}) of C – O linkages, as well as the stretching mode of OH groups, appeared in the spectra [89,187,188]. However, their intensities lower when calcination at 1000°C/1h preceded by an intermediate treatment at 450°C/12 h is carried out.

In the sequence, the PL emission spectra of both materials are displayed in **Figure 40.(b)**. The detailed analysis of PL emission spectrum of Y_2O_3: Nd^{3+}- Yb^{3+} will be handed out in the next section (**topic 3.3.2**). Briefly, after a continuous pump at 808 nm, the Nd^{3+} ions absorbed the energy and presented emissions in the ranges of 870 - 960 nm and 1050 - 1150 nm, referring to the transitions $^4F_{3/2} \rightarrow {}^4I_{9/2}$ and $^4F_{3/2} \rightarrow {}^4I_{11/2}$, respectively. Part of this absorbed energy by Nd^{3+} was transferred to Yb^{3+} ions as well, and thus, its corresponding emission lines showed up in the range 960 - 1050 nm ($^2F_{5/2} \rightarrow {}^2F_{7/2}$). Concerning the effect of heat treatment on the PL emission, the spectrum of the sample calcined at 900°C/10 minutes featured a noisy aspect and intensity fluctuations when comparing several spectra recorded consecutively. In contrast, the spectrum gets smoother with a better signal-to-noise ratio when calcination conditions are changed to 450°C/12h and 1000°C/1h. This occurred due to the more efficient removal of organic species and hydroxyl groups (typical PL quenchers) from the material.

Achieving a stable and intense PL signal is of huge interest in this work because it interferes directly in the calculation of LIR error (δLIR, equation 7 in **Chapter I**) and, consequently, in the thermal resolution (equation 6 in **Chapter I**) of Nd^{3+} - Yb^{3+} co-doped yttria NCs as a nanothermometer. Thus, on account of these results, it was decided to perform the modified Pechini synthesis of Y_2O_3 NCs by involving an intermediate treatment at 450°C/12h followed by a heat treatment at 1000°C/1h.

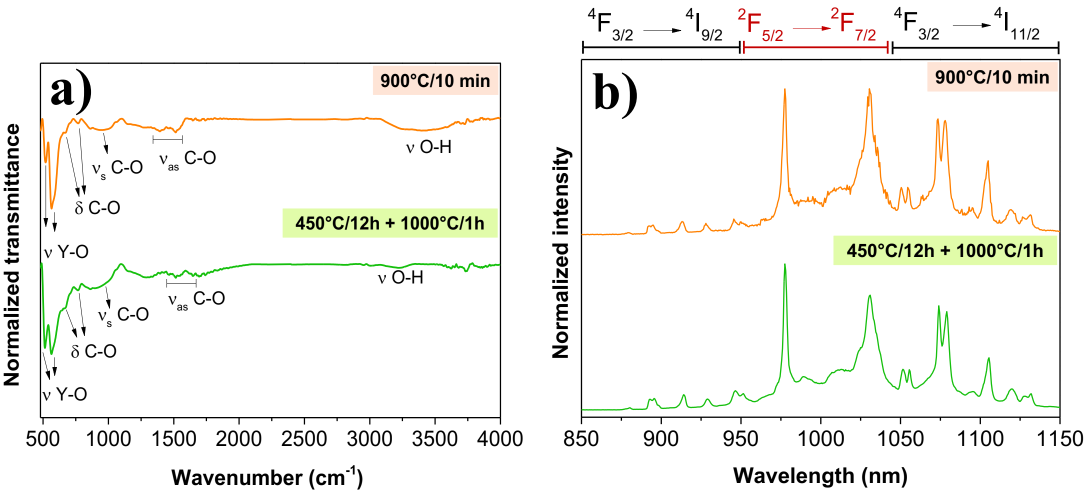

Figure 40. (a) FTIR, and **(b)** PL emission spectra of Y_2O_3 after calcining the *puff* at 900°C/10 minutes, and at 1000°C/1h preceded by an intermediate treatment at 450°C/12h. Both samples were co-doped with 1.00% mol Nd^{3+} and 0.50% mol Yb^{3+}.

3.3.2. Co-doping engineering to achieve an optimal photoluminescence emission intensity of Y_2O_3: Nd^{3+}-Yb^{3+} NCs

In **Chapter II**, appropriate doping amounts of Nd^{3+} and Yb^{3+} were selected in order to obtain an optimal PL emission intensity of both Ln^{3+} inserted into the YAG host matrix. The quantity of dopants to be embedded in yttria will not be the same as that of YAG, because host-related factors can affect their emission, such as the host phonon energy, and the distance between the Ln^{3+} ions. In this way, co-doping engineering was conducted to ascertain the concentrations of Nd^{3+} and Yb^{3+} for effective co-doping of Y_2O_3.

12 samples of Y_2O_3: Nd^{3+}- Yb^{3+} NCs were synthesized by trying out three concentrations of Nd^{3+} (0.25, 0.50, and 0.75% mol) combined with four of Yb^{3+} (0.10, 0.25, 0.50, and 1.00% mol). The synthesis was carried out via the modified Pechini procedure, considering the two-stage calcination (450°C/12h and 1000°C/1h) as established in the previous section. The chemical formulas for each % mol combination of Nd^{3+} and Yb^{3+} are summarized in **Table 7**.

Table 7. Nd^{3+} and Yb^{3+} concentrations of Y_2O_3 in % mol in relation to yttrium with corresponding chemical formulas.

$Y_2O_3 : Nd^{3+}$ -Yb^{3+}

		Nd^{3+}		
		0.25% mol	**0.50% mol**	**1.00% mol**
Yb^{3+}	**0.10% mol**	$Y_{1.993}Nd_{0.005}Yb_{0.002}O_3$	$Y_{1.988}Nd_{0.01}Yb_{0.002}O_3$	$Y_{1.978}Nd_{0.02}Yb_{0.002}O_3$
	0.25% mol	$Y_{1.990}Nd_{0.005}Yb_{0.005}O_3$	$Y_{1.985}Nd_{0.01}Yb_{0.005}O_3$	$Y_{1.975}Nd_{0.02}Yb_{0.005}O_3$
	0.50% mol	$Y_{1.985}Nd_{0.005}Yb_{0.01}O_3$	$Y_{1.980}Nd_{0.01}Yb_{0.01}O_3$	$Y_{1.970}Nd_{0.02}Yb_{0.01}O_3$
	1.00% mol	$Y_{1.975}Nd_{0.005}Yb_{0.02}O_3$	$Y_{1.970}Nd_{0.01}Yb_{0.02}O_3$	$Y_{1.960}Nd_{0.02}Yb_{0.02}O_3$

The X-ray diffractograms of Y_2O_3: Nd^{3+} - Yb^{3+} for different % mol Yb^{3+} with Nd^{3+} fixed at 0.25, 0.50, and 1.00% mol are shown in **Figure 41.(a)**, **(b)**, and **(c)**, respectively. For all tested co-doping concentrations, the phases crystallized as pure Y_2O_3, since the peaks matched the reference pattern (black bars in the figures) contained in PDF 00-041-1106. The replacement of some Y^{3+} by Nd^{3+} and Yb^{3+} ions did not alter the type of crystalline structure, even when the host matrix was heavily doped with 1.00% mol Nd^{3+} and 1.00% mol Yb^{3+}. As seen previously for Y_2O_3: 1.00% mol Nd^{3+} and 0.50% mol Yb^{3+}, the unit cell got slightly expanded owing to the small differences of ionic radii of the dopants in respect of yttrium.

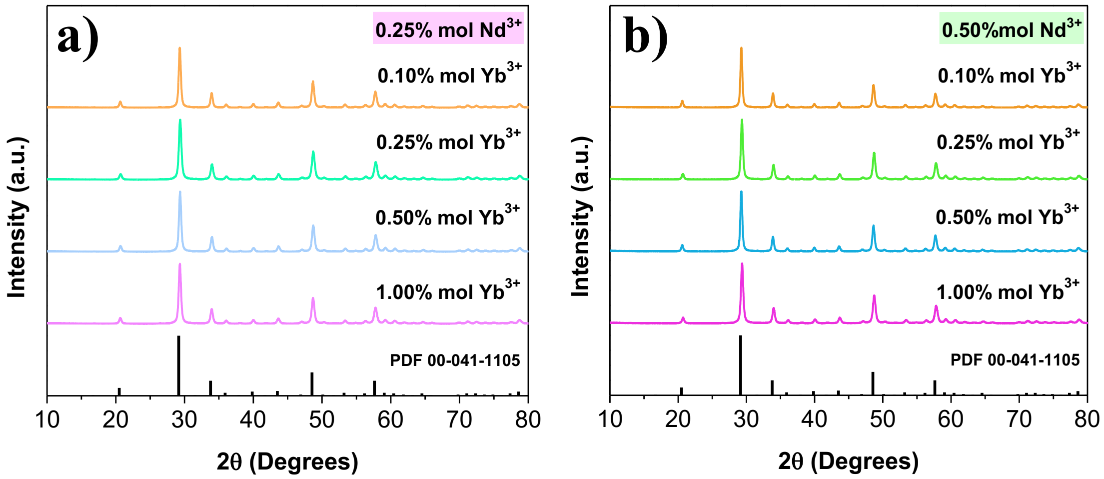

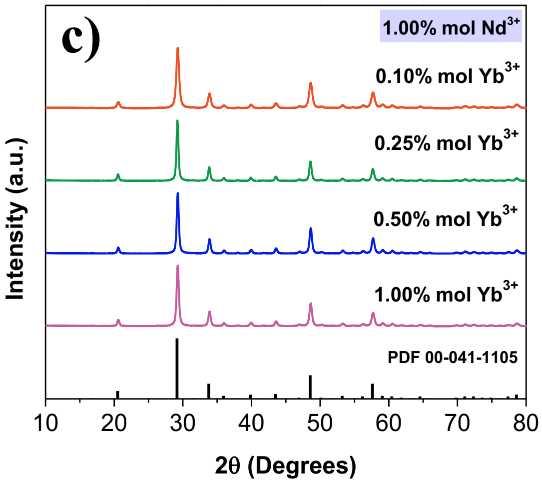

Figure 41. X-ray diffractograms of Nd^{3+}- Yb^{3+} co-doped Y_2O_3 for different % mol Yb^{3+} when Nd^{3+} concentration fixed at **(a)** 0.25, **(b)** 0.50, and **(c)** 1.00% mol.

The light absorption by Y_2O_3: Nd^{3+}-Yb^{3+} NCs was evaluated by DR measurement. This analysis was run in the sample with the highest concentration of dopants (1.00% mol Nd^{3+} and 1.00% mol Yb^{3+}), and the resulting curve is shown in **Figure 42.(a)**. The material exhibited a reflectance above 90%, and absorption bands from the fundamental level $^4I_{9/2}$ to meta-state levels between the valence and conduction bands of Nd^{3+}, as well as a band from Yb^{3+} related to the transition $^2F_{7/2} \rightarrow {}^2F_{5/2}$. All bands are labelled in the same figure, whose assignments were made in agreement with published literature [130–132]. Note that absorption bands at around 807 nm ($^4I_{9/2} \rightarrow {}^4F_{5/2}, {}^2H_{9/2}$) of Nd^{3+} ions are present, which fall within the BW-I (750 – 950 nm) and are available to use for the excitation of Y_2O_3: Nd^{3+}-Yb^{3+} NCs in biological applications.

For the estimation of the E_g, the Kubelka-Munk (equation 18 from **Chapter II**) was applied to the DR data in order to plot $(F(R_\infty)h\nu)^n$ versus energy. For n equal to 2, that is, a plot of $(F(R_\infty)h\nu)^2$ versus energy (in eV) resulted in a region of points linearly disposed, suggesting that the electron transitions take place directly in Y_2O_3: Nd^{3+}-Yb^{3+}. From the linear fitting of experimental points, with R^2 worth 0.9844, the curve was extrapolated for $(F(R_\infty)h\nu)^2 = 0$, and the optical bandgap energy of 5.71 eV was determined. This large bandgap demonstrates the insulating feature of Y_2O_3 NCs and agrees with what is usually stated in the literature for this host matrix [135,193–195].

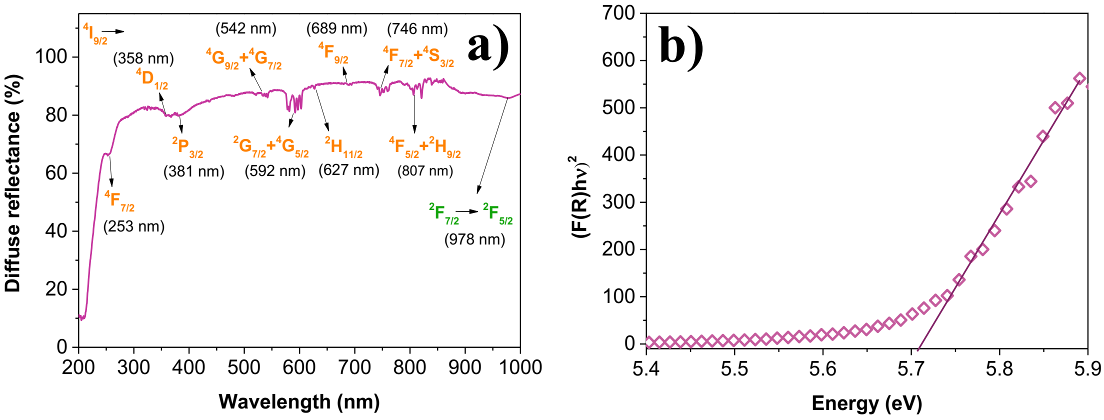

Figure 42.(a) DR spectrum and **(b)** determination of the optical bandgap energy of Y_2O_3: 1.00% mol Nd^{3+}, 1.00% mol Yb^{3+}.

Considering the Nd^{3+} absorption in the BW-I (750 – 950 nm), Nd^{3+}-Yb^{3+} co-doped yttria samples were continuously excited under an 808-nm excitation of NIR light to record their PL emissions. The associated PL emission spectra are displayed as a function of % mol Yb^{3+} for each series of fixed Nd^{3+} concentrations at 0.25, 0.50, and 1.00% mol in **Figure 43.(a)**, **(b)**, and **(c)**, in the respective order. Upon an excitation at 808 nm, Nd^{3+} ions are promoted from the fundamental state $^4I_{9/2}$ to the excited levels $^4F_{5/2}$, $^2H_{9/2}$, but de-excite through non-radiative processes, and populate the lower level $^4F_{3/2}$ in the sequence. This state is then depopulated through radiative transitions of Nd^{3+} in the regions of 870 nm to 960 nm ($^4F_{3/2} \rightarrow {}^4I_{9/2}$) and 1050 nm to 1150 nm ($^4F_{3/2} \rightarrow {}^4I_{9/2}$), besides an energy transfer to Yb^{3+} ions.

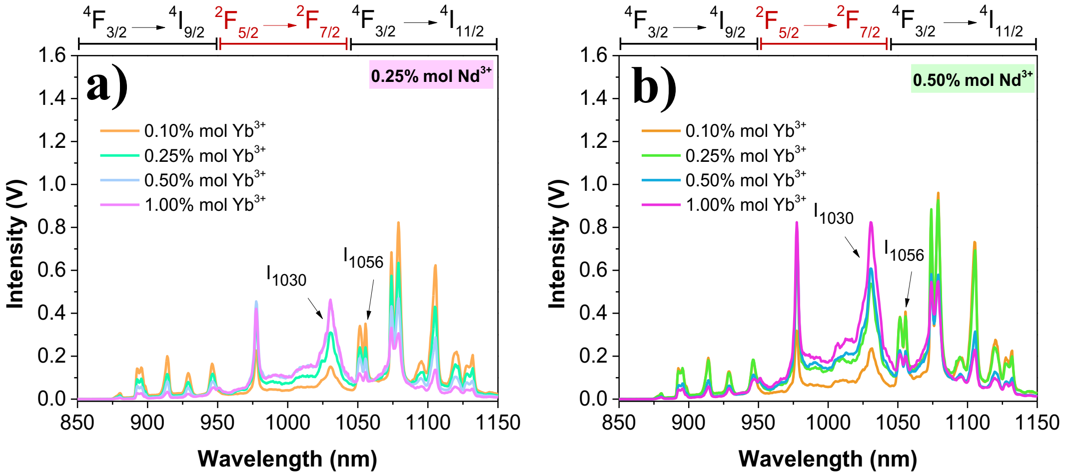

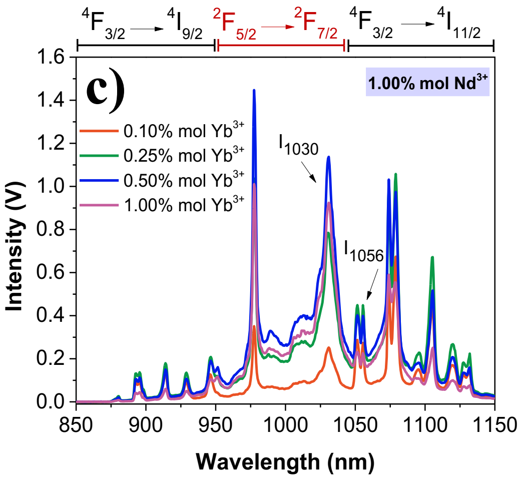

Figure 43. PL emission spectra of yttrium oxide for different % mol Yb^{3+} considering Nd^{3+} concentration fixed at **(a)** 0.25, **(b)** 0.50, and **(c)** 1.00% mol.

To shed a light on the energy transfer from Nd^{3+} to Yb^{3+}, Lupei and co-workers published a work [88] affirming that it is a resonant type of energy transfer in Nd^{3+}-Yb^{3+} co-doped yttria, since there is a significant overlap of the absorption spectrum of Y_2O_3: Yb^{3+} with the emission spectrum of Y_2O_3: Nd^{3+} at low temperature. Indeed, in the energy levels diagram built upon the data of this work along with those reported elsewhere [88,139,196], one finds a small energy difference of 171 cm^{-1} between the lowest crystal field component of the excited state $^4F_{3/2}$ (R_1) of Nd^{3+} and the highest Stark level of the excited state $^2F_{5/2}$ (7) of Yb^{3+} (**Figure 44**). Such a low energy gap combined with the superposition between donor emission (Nd^{3+}) and acceptor absorption (Yb^{3+}) spectrum strongly indicates the phonon assistance is actually not necessary in the energy transfer $Nd^{3+} \rightarrow Yb^{3+}$ herein. A similar situation was previously reported in the works of Balda et al.[141,142] and Caldiño et al.[143].

In addition, the energy transfer $Nd^{3+} \rightarrow Yb^{3+}$ usually dominates over non-radiative cross relaxation ($^4F_{3/2}$; $^4I_{9/2} \rightarrow {}^4I_{15/2}$; $^4I_{15/2}$) of Nd^{3+} ions, but the energy diffusion of Yb^{3+} - Yb^{3+} can be significant for high amounts of this Ln^{3+} [55]. Finally, the back energy transfer $Yb^{3+} \rightarrow Nd^{3+}$ is negligible in Nd^{3+} - Yb^{3+} co-doped Y_2O_3, in view of the weak superposition of the absorption spectrum of Y_2O_3: Nd^{3+} and the emission spectrum of Y_2O_3: Yb^{3+}. Thus, the changes seen in PL emission intensities for different dopant concentrations rely on mainly the energy transfer from Nd^{3+} to Yb^{3+} and from Yb^{3+} to Yb^{3+} [88,138].

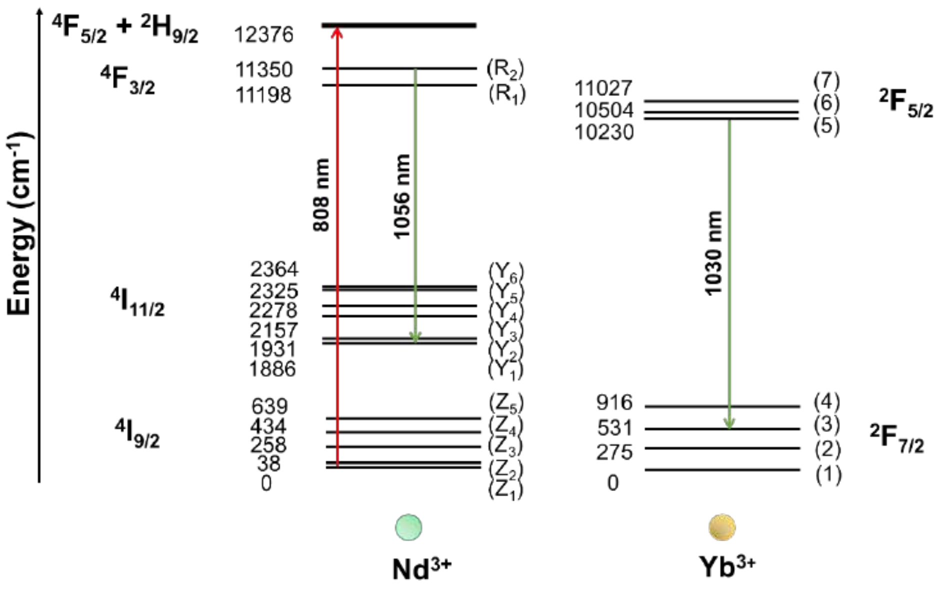

Figure 44. Energy level diagram of yttrium oxide co-doped with Nd^{3+} and Yb^{3+}. The numbers indicate the energy values in cm^{-1}, and the acronyms in the parenthesis designate each Stark level (Created by the author).

To develop a sensitive nanothermometer based on the LIR approach, the co-doping composition must be properly chosen since it affects markedly the PL intensities. The guideline adopted for co-doping engineering is to analyze the intensity of the two PL peaks from the different emitting centers that will be applied in the LIR method. Literature points out that the PL emissions at 1030 nm (transition 5 → 3 of Yb^{3+}) and 1056 nm (transition of $R_2 \rightarrow Y_1$ of Nd^{3+}), indicated in the PL spectra of **Figure 43** and in the energy level diagram in **Figure 44**, compose an effective pair for LIR nanothermometry of Y_2O_3: Nd^{3+} - Yb^{3+}. Besides being relatively intense and within the BW-II (1000 – 1350 nm), the stark line at 1030 nm is highly temperature-dependent. On the other side, the PL peak at 1056 nm is not the strongest among all Nd^{3+} emissions, but it serves as a reliable reference to monitor the Yb^{3+} emission due to its lower dependency on the temperature [57].

When closely examining the integrated PL intensities at 1030 and 1056 nm (**Figure 45**), the same trend observed for YAG: Nd^{3+}-Yb^{3+} is found here: as more Nd^{3+} ions are put into Y_2O_3, Yb^{3+} PL intensity increases at the expense of Nd^{3+} intensity, attesting the energy transfer Nd^{3+} → Yb^{3+}. Indeed, there is a consistent rise of Yb^{3+} PL intensity when its concentration is fixed, and only Nd^{3+} content is incremented. For both concentrations of 0.50 and 1.00% mol Nd^{3+}, the PL intensity of Yb^{3+} quenches at its concentration of 1.00% mol owing to the increase in diffusion energy Yb^{3+} - Yb^{3+}.

Conversely, there is a loss in the PL intensity of Nd^{3+} as more Yb^{3+} ions are present in Y_2O_3, stemming from the energy transfer $Nd^{3+} \rightarrow Yb^{3+}$. An exception was though observed in the series of Nd^{3+} concentration fixed at 1.00% mol (see **Figure 45.(c)**). The Nd^{3+} PL intensity initially increases as the Yb^{3+} concentration changes from 0.10 to 0.25% mol, remains nearly constant at 0.50% mol Yb^{3+}, and ends up decreasing at 1.00% mol Yb^{3+}. Presumably, for such high content of Nd^{3+}, a priori the presence of Yb^{3+} allowed a homogeneous distribution of Nd^{3+} ions inside the matrix, diminishing the probability of non-radiative processes and hence, the Nd^{3+} PL intensity raised. However, the effect of the energy transfer $Nd^{3+} \rightarrow Yb^{3+}$ became accentuated by including more Yb^{3+} ions, which cut down the Nd^{3+} PL intensity.

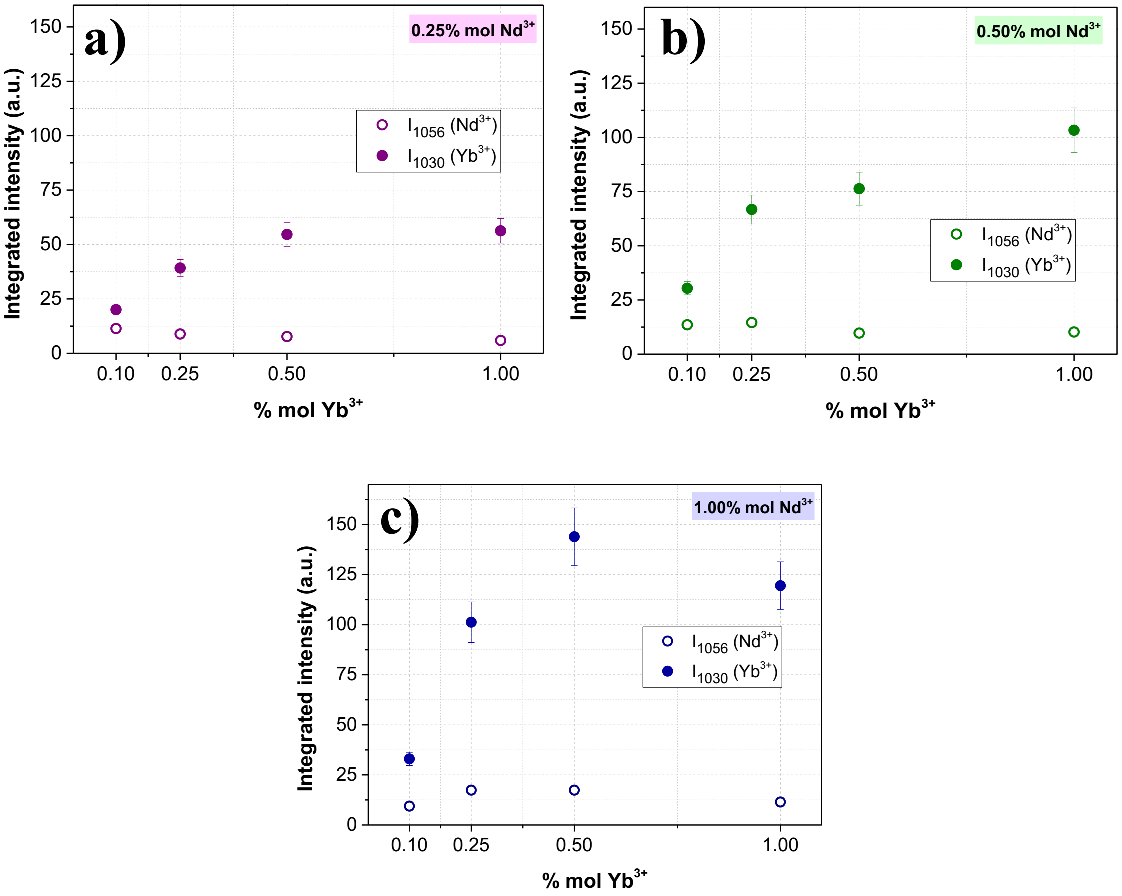

Figure 45. Integrated intensities at 1030 nm (I_{1030}) and 1056 nm (I_{1063}) as a function of % mol Yb^{3+} when Nd^{3+} concentration is fixed at **(a)** 0.25, **(b)** 0.50, and **(c)** 1.00% mol in Y_2O_3. All the graphs are on the same scale for a better comparison.

In this way, analogous to the YAG study, the co-doping engineering approach consisted of looking into the Yb^{3+} emission to pick out the samples with better emissivity at 1030 nm. Subsequent to this initial selection, a final assessment was made based on the

Nd^{3+} intensity at 1056 nm. The Nd^{3+} - Yb^{3+} composition with the highest Nd^{3+} PL intensity from this second round was then deemed as the optimal co-doping concentration for yttria.

In **Figure 46.(a)**, the red arrows point out to the four compositions that possessed better emissivity at 1030 nm: 0.50% mol Nd^{3+} and 1.00% mol Yb^{3+}, as well as 1.00% mol Nd^{3+} co-doped with 0.25, 0.50 and 1.00% mol Yb^{3+}. From this set of four samples, the ones co-doped with 1.00% mol Nd^{3+} and 0.25 or 0.50% mol Yb^{3+} culminated in having the highest Nd^{3+} PL emission. Between the two of them, the co-doping concentration of 1.00% Nd^{3+} and 0.50% Yb^{3+} was singled out for presenting both the highest PL intensities at 1030 nm and 1056 nm (marked by a red arrow in **Figure 46.(b)**). Hence, this composition was adopted for co-doping yttria samples.

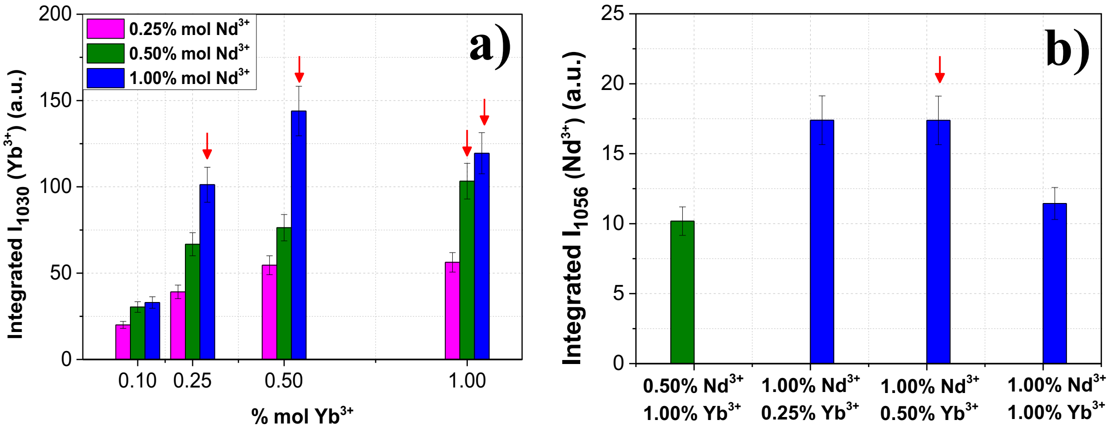

Figure 46.(a) Comparison of integrated intensity at 1030 nm (Yb^{3+}) for Y_2O_3: Nd^{3+}-Yb^{3+} samples. The red arrows indicate the four samples with higher Yb^{3+} emission. **(b)** The emissivity of $Nd^{3+}$of the samples that presented highest Yb^{3+} PL intensities. The red arrow points out to the composition that gave highest Nd^{3+} emission among the four samples previously selected.

3.3.3. Synthesis of Y_2O_3 nanocrystals by the two-step urea-based process: optimization of the experimental protocol

To produce individual yttria NCs, the two-step urea-based process was selected, which consists of the formation of amorphous $Y(OH)CO_3.H_2O$ NPs followed by a calcination to obtain Y_2O_3 NCs. Hence, this study initiated with the size control of $Y(OH)CO_3.H_2O$, and then, the conditions of calcination were refined.

3.3.3.1. Size control of $Y(OH)CO_3.H_2O$

The first step of the synthesis consists of reacting CO_3^{2-} and OH^-, from the decomposition of urea, with Y^{3+}, to produce $Y(OH)CO_3.H_2O$. The chemical reactions involved in its formation are presented below [197]:

Urea decomposition

$$(NH_2)_2CO \rightarrow NH_4^+ + OCN^- \tag{23}$$

$$OCN^- + 2H^+ + H_2O \rightarrow CO_2 + NH_4^+ \tag{24}$$

Hydrolysis of Y^{3+}

$$Y^{3+} + H_2O \rightarrow [Y(OH)]^{2+} + H^+ \tag{25}$$

Reaction to form the basic yttrium carbonate

$$Y^{3+} + (NH_2)_2CO + 4H_2O \rightarrow Y(OH)CO_3.H_2O + 2NH_4^+ + 2H^+ \tag{26}$$

According to Sohn et al. [197], depending on the precursor concentration (yttrium nitrate and urea), monodispersed spherical NPs of $Y(OH)CO_3.H_2O$ are obtained. After the thermal treatment, this morphology is retained, but the yttria size is usually smaller compared to that of $Y(OH)CO_3.H_2O$ due to the elimination of organics and dehydration[188,189].

Nevertheless, reaching small diameters of Y_2O_3 below 100 nm without any agglomeration remains a complex issue. One strategy commonly used was to control the $Y(OH)CO_3.H_2O$ size by playing on the precursor concentration. In particular, the lower Y^{3+} concentration, the smaller the size of $Y(OH)CO_3.H_2O$ NP [187,197]. For example, considering 0.5 $mol.L^{-1}$ urea, Sung et al.[189] obtained $Y(OH)CO_3.H_2O$ NPs measuring 110 nm for 9.0 $mmol.L^{-1}$ of yttrium nitrate while Li et al.[186] produced particles above 400 nm by using 15.0 $mmol.L^{-1}$ of Y^{3+} reactant. However, the synthesis yield becomes very low when using small amounts of yttrium nitrate as underlined in another work [198].

Alternatively, when urea amount is increased, it is possible to achieve a high supersaturation and consequently, to promote a burst of nucleation, causing the reduction of particle size. In this case, the higher urea concentration, the smaller the $Y(OH)CO_3.H_2O$ NPs. To illustrate it, Lima et al.[190] used a urea concentration as high as

3.0 mol.L^{-1} with 7.5 mmol.L^{-1} of yttrium nitrate and synthesized $Y(OH)CO_3.H_2O$ NPs of 150 nm. The urea concentration can be further increased until 7.0 mol.L^{-1}, which was defined as the upper limit before the NPs get agglomerated and end up constituting a network structure[197]. Although it is an interesting way to control the NP size, the excess of reactant concentration can make the synthesis impractical, especially to upscale it.

Another possibility to control the size is to change the nature of the medium. When synthesizing Gd_2O_3 NCs through the two-step urea-based route, with 10.0 mmol.L^{-1} and 0.50 mol.L^{-1} of gadolinium nitrate and urea, respectively, Li et al.[198] accomplished the task of size reducing from 429 nm to 58 nm by adding 60% in volume of 1-butanol as co-solvent. Based on this work, the addition of organic co-solvent can be a very promising way of controlling the growth of $Y(OH)CO_3.H_2O$ NPs without using reactants in excess.

Hence, to modulate the diameter of $Y(OH)CO_3.H_2O$ NPs, the strategy consisted in adjusting the nature of the medium with the addition of different organic co-solvents, such as 1-propanol, 2-propanol, 1,4-butanediol, and a mixture of 1-butanol with ethanol Besides, concentrations of urea varying from 0.1 to 3.0 mol.L^{-1} were tested as well whereas the other parameters were kept constant as previously described in **section 3.2.1.2**. For each experiment, the diameter was checked and measured with FE-SEM analysis, with approximately 200 NPs counted for accuracy. No Ln^{3+} dopants were used in this part of the study.

In **Table 8**, the results of these experiments are presented. It is clear how the organic co-solvent indeed affects the size of the basic yttrium carbonate. For example, considering 3.0 mol.L^{-1} of urea and 60% in volume of 1-propanol, 2-propanol, and 1-butanol + ethanol, the diameters varied significantly between 72 ± 10 to 134 ± 20 nm. However, among the organic co-solvents tested, 1,4-butanediol was the one that provided a significant size reduction of $Y(OH)CO_3.H_2O$ NPs to below 60 nm. Two factors contributed to this outcome: the solubility of $Y(OH)CO_3.H_2O$, and the viscosity of 1,4-butanediol.

Consider the equation 27 to express the solubility of $Y(OH)CO_3.H_2O$:

$$C_s \approx \exp\left[-\frac{z^+ z^- e^2}{4\pi\epsilon_0\epsilon_r k_B T(r^{z+} + r^{z-})}\right] \tag{27}$$

where z^+ and z^- are the ions, whose radii are r^{z+} and r^{z-}, respectively; ε_0 is the permittivity in vacuum; ε_r represents the relative dielectric permittivity of the solvent; k_B is the Boltzmann constant, and T is temperature in Kelvin scale [198,199]. The presence of 1,4-butanediol brought down the dielectric constant of the solution since it has a low dielectric permittivity compared to that of the water (~30.0 of 1,4-butanediol against ~80.0 of water at 298 K [198,200,201]). According to equation 27, a low dielectric permittivity reduces the solubility of $Y(OH)CO_3.H_2O$ NPs, which, in turn, ramps up the supersaturation of the solution and leads to a higher nucleation frequency (equation 13 in **Chapter I**). In consequence, this brings about a reduction of the average diameter of the as-grown $Y(OH)CO_3.H_2O$ NPs.

Although the other organic co-solvents present even lower dielectric constant (around 20 at 298 K [198]), 1,4-butanediol kept standing out due to its ligand role and high viscosity. This latter property is approximately 72 mPa.s and much superior to the viscosities of the other co-solvents at 298 K (1-propanol ≈ 1.94 mPa.s, 2-propanol ≈ 2.05 mPa.s and ethanol + 1-butanol ≈ 2.02 mPa.s) [202–205]. In this way, the stabilizing capping layer around $Y(OH)CO_3.H_2O$ NPs formed by 1,4-butanediol, along with its high viscosity, reduced the diffusion of crystallizing entities (Y^{3+}, OH^-, CO_3^{2-}), thereby significantly decreasing the growth rate of the primary particles.

The addition of 1,4-butanediol also minimized the need for high concentrations of urea. In comparison to previous studies that worked with the same concentration of yttrium nitrate and solvothermal conditions [190,191], it was possible to scale back the urea amount by up to 30 times (from 3.0 to 0.1 $mol.L^{-1}$) and still end up with $Y(OH)CO_3.H_2O$ diameters between 30 and 60 nm.

Table 8. Summary of the conditions for the synthesis of $Y(OH)CO_3.H_2O$: nature of the organic co-solvent, its percentage in volume relative to water, urea amount, size of NPs measured with FE-SEM images, and PDI.

Co-solvent	% vol.	Urea (mol L^{-1})	$Y(OH)CO_3.H_2O$ size (nm)	PDI
2-Propanol	60	3.0	134 ± 20	0.02
Ethanol + 1-Butanol (1:2 proportion in vol.)	60	3.0	96 ± 10	0.01
1-Propanol	60	3.0	72 ± 10	0.02
	66	1.5	181 ± 20	0.01
1,4-Butanediol	75	1.5	36 ± 10	0.03
	80	0.5	39 ± 10	0.02
	83	0.2	44 ± 10	0.02
	50	0.2	58 ± 10	0.04
	80	0.1	50 ± 10	0.04

For further experiments, the conditions of 83% in volume of 1,4-butanediol and 0.2 $mol.L^{-1}$ of urea were established definitively, as they presented the best compromise in between reactant concentration and physical features of $Y(OH)CO_3.H_2O$ (size and polydispersity). **Figure 47** displays both the typical XRD pattern, revealing the amorphous nature of these $Y(OH)CO_3.H_2O$ NPs **(a)**, and their spherical morphology visualized by FE-SEM **(b)**.

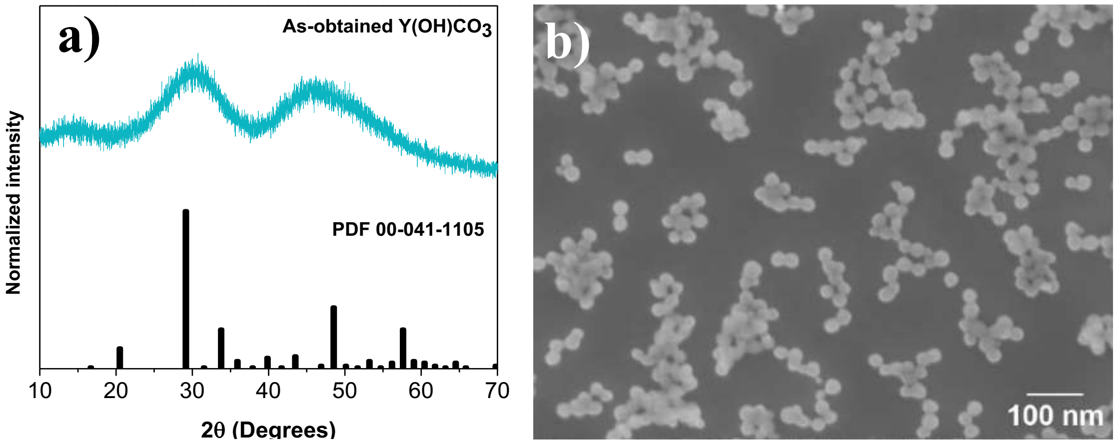

Figure 47.(a) XRD pattern and **(b)** FE-SEM image of $Y(OH)CO_3.H_2O$ NPs synthesized by using 83% in volume of 1,4-butanediol and 0.2 $mol.L^{-1}$ of urea.

Hence, the incorporation of 1,4-butanediol as a co-solvent in the synthesis provided a series of advantages, from decreasing the particle size to opening up the possibility of upscaling synthesis with reasonable amounts of urea. Finally, it is worth highlighting that going for 1,4-butanediol in this context is quite original, as no previous works on yttria have reported experiments with this co-solvent. Next, experiments are presented to define the conditions for the thermal treatment to produce yttrium oxide NCs.

3.3.3.2. Calcination tests of $Y(OH)CO_3.H_2O$ nanoparticles to yield Y_2O_3 nanocrystals

The transformation of $Y(OH)CO_3.H_2O$ to Y_2O_3 with calcination is represented by the reactions below [188]:

$$Y(OH)CO_3.H_2O \rightarrow Y(OH)CO_3 + H_2O \qquad (28)$$

$$2Y(OH)CO_3 \rightarrow Y_2O(CO_3)_2 + H_2O \qquad (29)$$

$$Y_2O(CO_3)_2 \rightarrow Y_2O_3 + 2CO_2 \qquad (30)$$

Figure 48 illustrates the TG/DTA alongside mass spectrometry of $Y(OH)CO_3.H_2O$ NPs, covering the temperature range from 50°C to 800°C under O_2 atmosphere. The first mass loss (~10%) corresponds to a broad endothermic peak in DTA, peaking at 145°C, related to the removal of both adsorbed water on the surface of the NPs and the release of crystal water from the structure of $Y(OH)CO_3.H_2O$, turning into $Y(OH)CO_3$ (expression 28). Subsequently, one finds the second mass loss (~19%) occurring at 400°C due to the transformation of $Y(OH)CO_3$ to $Y_2O(CO_3)_2$ through the release of crystal water from the structure (expression 29). In the range of 500°C to700°C, CO_2 is liberated (~19% of mass loss), with the crystallization of $Y_2O(CO_3)_2$ to Y_2O_3 beginning at 545°C and achieving a maximum at 586°C (expression 30) [188]. After 800°C and up to 1200°C, no events were observed.

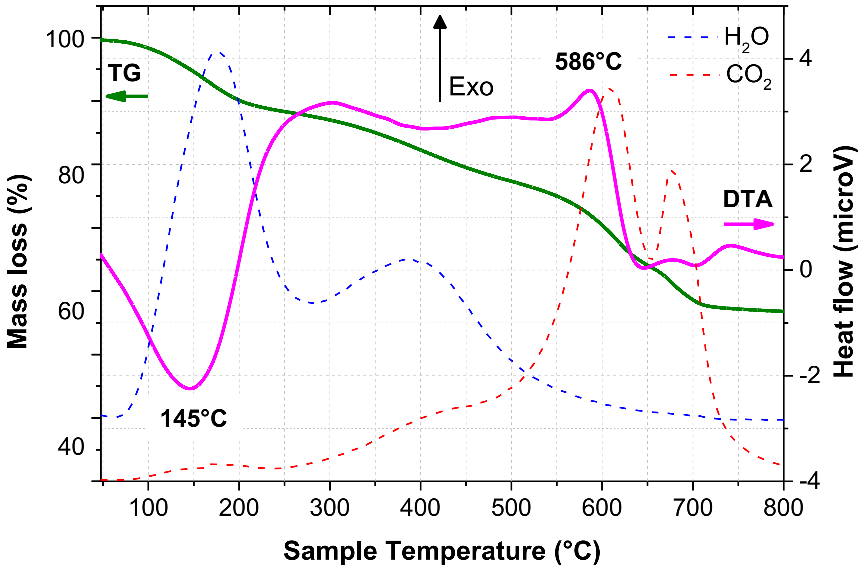

Figure 48. Thermal analysis along with mass spectrometry of $Y(OH)CO_3.H_2O$ NPs under oxygen atmosphere. The mass spectrometry of H_2O and CO_2 is given in arbitrary units.

Based on this TG/DTA analysis, heat treatment tests on $Y(OH)CO_3.H_2O$ NPs (synthesized with 83% in volume of 1,4-butanediol and 0.2 mol.L^{-1} urea) were conducted in a tubular furnace under O_2 atmosphere by trying out different conditions of temperature, heating rate, and duration. All the conditions tested are summarized in **Table 9**. **Figure 49** present the corresponding X-ray diffractograms of samples after calcination. In every case, yttrium oxide was produced, with the XRD peaks indexed in accordance with the reference PDF 00-041-1105. Besides that, as the calcination temperature increased, the XRD peaks became narrower, showing the crystallinity improved in this way.

Table 9. Conditions tested to obtain Y_2O_3 from heat treatment of $Y(OH)CO_3.H_2O$ under O_2 atmosphere in a tubular furnace.

Temperature (°C)	**Heating rate (°C.min^{-1})**	**Duration (minutes)**
700	1	5
700	1	120
800	1	5
800	1	120
900	10	60

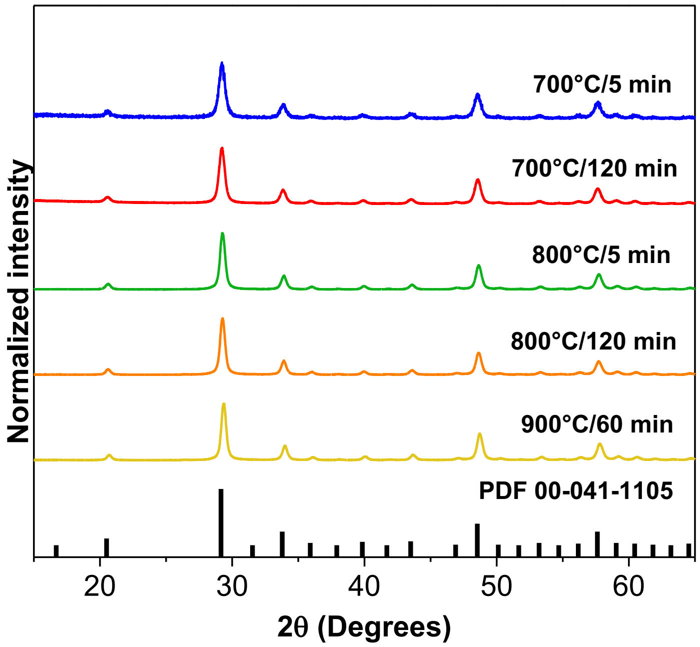

Figure 49. Diffractograms of Y_2O_3 after calcining $Y(OH)CO_3.H_2O$ NPs under different conditions. The XRD peaks were compared with the reference PDF 00-041-1105.

Figure 50 unveils TEM images when $Y(OH)CO_3.H_2O$ NPs are calcined at **(a)** 700°C/5 minutes, **(b)** 700°C/120 minutes, **(c)** 800°C/5 minutes, **(d)** 800°C/120 minutes, all with a slow heating rate of 1°C.min^{-1}; and at **(e)** 900°C/60 minutes with a faster heating rate of 10°C.min^{-1}. In all tests, some dispersed NCs are visible, but others fused together, signalized by the appearance of necks, and gave rise to agglomerates extending from 60 to 200 nm. When the thermal treatment is carried out at 700°C, fewer agglomerates showed up compared to higher temperatures, regardless of the duration. On the other hand, when the temperature is increased, it appears the heating rate influences more significantly in the NCs coalescence and agglomeration than the temperature itself. Thus, more clusters are present when annealing is conducted at 800°C with a heating rate of 1°C.min^{-1} rather than at 900°C with heating rate of 10°C.min^{-1}.

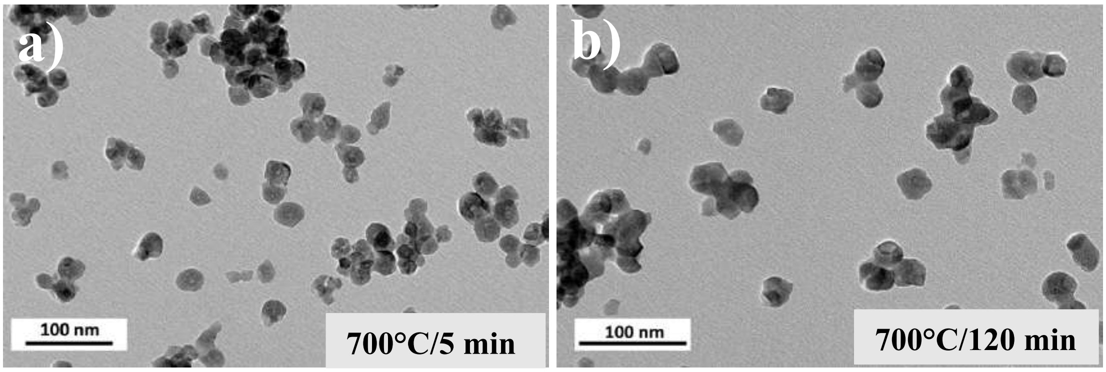

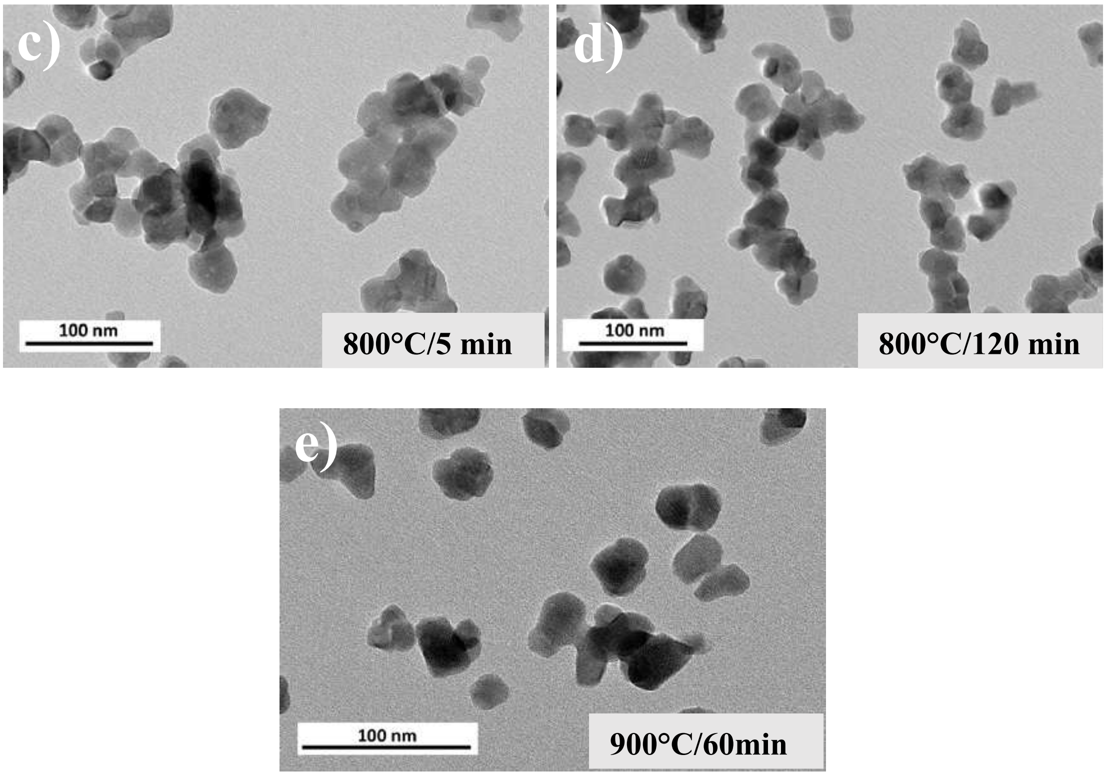

Figure 50. TEM images of Y_2O_3 NCs after calcination at **(a)** 700°C/5 minutes, **(b)** 700°C/120 minutes, **(c)** 800°C/5 minutes, **(d)** 800°C/120 minutes, considering a slow heating rate of 1°C.min^{-1}; **(e)** 900°C/1h with a 10 times faster heating rate, that is, equal to 10°C.min^{-1}.

Since the $Y(OH)CO_3.H_2O$ NPs already present a small size, and, consequently, a high surface-to-volume ratio, they are prone to agglomerate during the heat treatment more easily. Therefore, a final test involved the inclusion of NaCl as a separating media to prevent the coalescence of the NPs. This condition was based on the work of Rong et al. [206], who proceeded to obtain monodisperse NPs of $L1_0$ – FePt with a size of less than 8 nm after annealing 0.25% in mass of fcc FePt (face-centered cubic FePt) with NaCl at 700°C/4h.

First, dry powder of NaCl and 1.0% in mass of $Y(OH)CO_3.H_2O$ NPs were ground together and then calcined for 1 hour at 700°C, with a heating rate of 10°C.min^{-1}. The diffractogram shown in **Figure 51** (brown curve) confirms the formation of Y_2O_3 phase, but traces of impurity were detected. This heat treatment was performed close enough to the melting point of NaCl (799 ~ 801°C [207]), likely causing an interaction between $Y(OH)CO_3.H_2O$ and NaCl. This interaction culminated in the appearance of low-intensity XRD peaks at 18.25°, 27.95°, 36.76° and 41.26° (indicated by * in corresponding XRD in **Figure 51**), which were identified as sodium chloride yttrium oxide (PDF 04-010-9094).

By reducing both temperature and duration of thermal treatment to 550°C and 20 minutes, respectively, pure yttria phase was obtained (pink curve in **Figure 51**). Such outcome confirms well that even a low temperature as 550°C was enough to transform $Y(OH)CO_3.H_2O$ into Y_2O_3, as previously shown in TG/DTA analysis (**Figure 48**), and it is preferable to work at lower temperatures and for shorter durations when using NaCl-matrix for calcination.

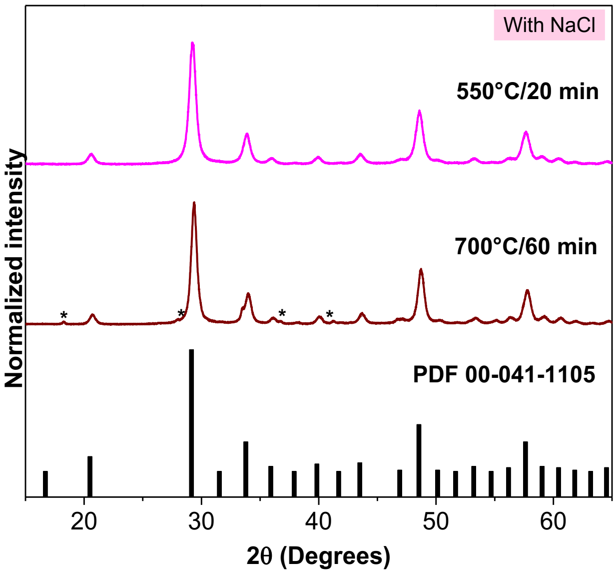

Figure 51. X-ray diffractograms of Y_2O_3 after calcination of $Y(OH)CO_3.H_2O$ NPs with NaCl under different conditions. The symbol * indicates the presence of sodium yttrium chloride oxide, identified based on the reference PDF 04-010-9094.

In the continuity of this study, the following conditions were established for the two-step urea-based route: 1) co-doping composition of 1.00% mol Nd^{3+} and 0.50% mol Yb^{3+}, 2) 83% in volume of 1,4-butanediol and 0.2 $mol.L^{-1}$ of urea to synthesize $Y(OH)CO_3.H_2O$ NPs, 3) heat treatment at 550°C/20 min in NaCl-matrix for the crystallization of yttrium oxide. In the sequence, the characterization of Y_2O_3: Nd^{3+}-Yb^{3+} obtained under these conditions is presented.

3.3.3.3. Structural characterization and photoluminescence measurement of Y_2O_3: Nd^{3+}-Yb^{3+} nanocrystals

The structural features of a sample synthesized by employing the optimized conditions were evaluated based on HR-XRD and TEM analysis. According to the Le Bail fit on the HR-XRD data (**Figure 52.(a)**), the NCs have a cubic structure with a cell parameter a = 10.626 Å, which is larger compared to the sample synthesized by the modified Pechini method with the same co-doping composition (*a* = 10.610 Å in **Table 6**). Sung et al.[189] also noted this feature in their work of Y_2O_3 using the two-step urea-based route and possibly, mechanical strains in the NCs promoted the expansion of the lattice parameters.

The single crystal domain Lc extracted from the HR-XRD by the Le Bail method measures 11 ± 3 nm and is smaller than the NP diameter of 22 ± 10 nm (PDI = 0.05) observed in TEM images (**Figure 52.(b)**). This is a sign the NCs own a polycrystalline nature, and previous studies have already reported it when calcination is performed below 1200 °C [190,191]. Moreover, the TEM image unveils dispersed NCs, but the agglomeration of some NCs still persisted.

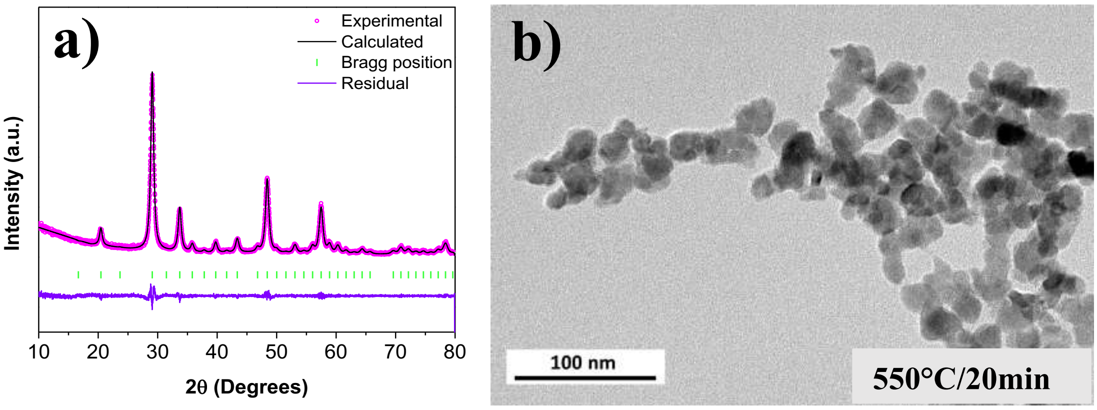

Figure 52. (a) HR-XRD pattern (pink circles) with calculated Le Bail fit (black solid line), and **(b)** TEM images of Y_2O_3: 1.00% mol Nd^{3+}, 0.50% mol Yb^{3+} synthesized via the two-step urea-based route.

To check the stability of Y_2O_3: 1.00% mol Nd^{3+}, 0.50% mol Yb^{3+} NCs in solution, the DLS data of this sample was acquired. The hydrodynamic size averaged around 150 nm (pink curve in **Figure 53.(a)**), which is much larger than the diameter of 22 nm observed in TEM, indicating the presence of both aggregates and agglomerates. However, this hydrodynamic size is practically half of the one of the yttria obtained from heat treatment at 700°C/5min without NaCl-matrix (318 nm — blue curve in **Figure 53.(a)**). Furthermore, the autocorrelation function has become more stable, demonstrating the colloidal stability of Y_2O_3: 1.00% mol Nd^{3+}, 0.50% mol Yb^{3+} NCs synthesized from heat treatment with NaCl (**Figure 53.(b)**).

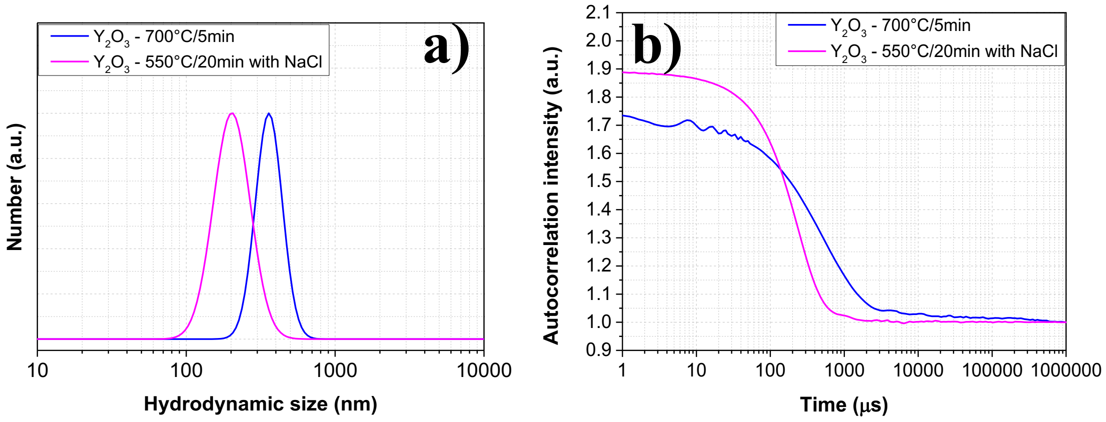

Figure 53. (a) Hydrodynamic sizes and **(b)** autocorrelation function of Y_2O_3: 1.00% mol Nd^{3+}, 0.50% mol Yb^{3+} NCs after annealing at 700°C/5 minutes (blue curves) and 550°C/20 min with NaCl (pink curves).

Next, FTIR analysis was performed on pellets of $Y(OH)CO_3.H_2O$ NPs and Y_2O_3 NCs with KBr and the spectra are depicted in **Figure 54**. This measurement also confirms the formation of Y_2O_3, since a characteristic peak of Y-O stretching at 565 cm^{-1} is evident in the FTIR spectrum of Y_2O_3. Compared to the FTIR spectrum of $Y(OH)CO_3.H_2O$ NPs, the bands related to the symmetric stretching (985 – 1200 cm^{-1}) of C-O and the stretching of C-H linkages did not show up, but the deformation vibrations (670 – 850 cm^{-1}), and the asymmetric stretching (1350 – 1530 cm^{-1}) of C-O and the stretching mode of OH (3400 cm^{-1}) still appeared at a lower intensity [89,187,188]. From the TG/DTA results shown earlier in **Figure 48**, these bands would disappear for calcination above 800°C, when CO_2 is eliminated, and $Y(OH)CO_3.H_2O$ is completely decomposed.

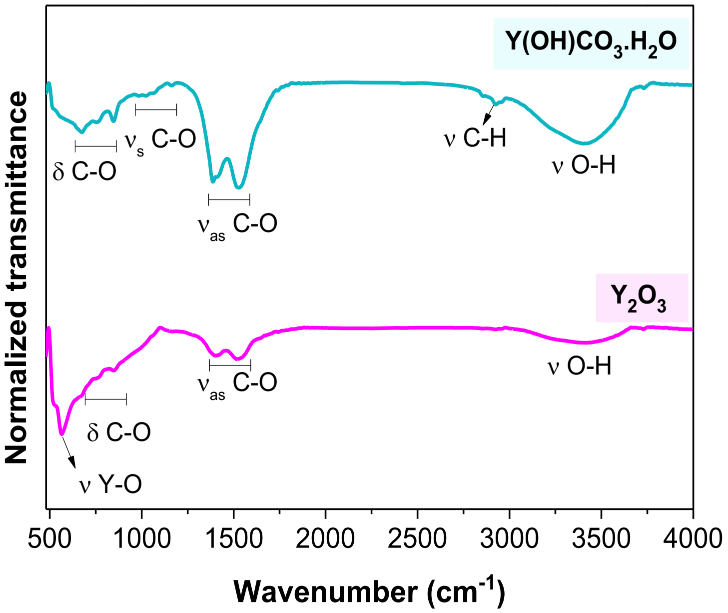

Figure 54. FTIR spectra of $Y(OH)CO_3.H_2O$ NPs and Y_2O_3 NCs synthesized via the two-step urea-based route.

Lastly, the PL emission measurement was carried out by pumping continuously the powdered yttria NCs co-doped with 1.00% mol Nd^{3+} and 0.50% mol Yb^{3+} at 808 nm. Upon this excitation, the PL emission spectrum in **Figure 55** shows the emissions of Nd^{3+} from the excited state $^4F_{3/2}$ to the levels $^4I_{9/2}$ and $^4I_{11/2}$, in the ranges of 875 – 960 nm and 1047 – 1150 nm, respectively. Thanks to the energy transfer $Nd^{3+} \rightarrow Yb^{3+}$, the emission $^2F_{5/2} \rightarrow {}^2F_{7/2}$ of Yb^{3+} ions is present in the range from 960 nm to 1047 nm, with a very strong stark emission at 1030 nm, falling within the BW-II (1000 – 1350 nm).

In comparison with the PL emission spectrum of Y_2O_3: 1.00% mol Nd^{3+}, 0.50% mol Yb^{3+} synthesized via the modified Pechini method, the spectrum profile is similar, but the overall PL intensity is much lower. In particular, the integrated emission from Nd^{3+} at 1056 nm is 10-fold lower whereas the one from Yb^{3+} at 1030 nm is 14-fold lower. The calcination at low temperature did not promote either the complete crystallization of Y_2O_3: 1.00% mol Nd^{3+}, 0.50% mol Yb^{3+} NCs or the total removal of organic moieties and hydroxyl groups, thus favoring non-radiative de-excitation of the luminescent ions. It is also important to highlight that yttria NCs prepared from the two-step urea-based route presents small size (22 ± 10 nm), so more Ln^{3+} ions are usually localized near the NC surface and are susceptible to interact with PL quenchers. Finally, defects can be present in the crystallite boundaries (grain boundaries), since the NCs are polycrystalline, and consequently, this can provide the relaxation of the excited states as well.

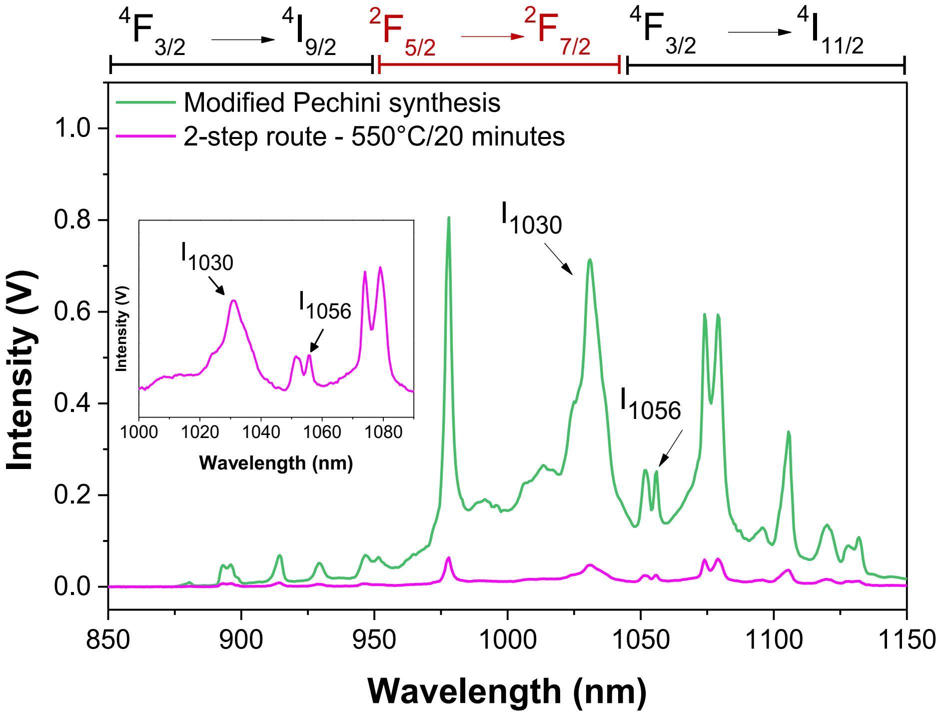

Figure 55. PL emission spectra of Y_2O_3 NCs synthesized by the two-step urea-based route (550°C/20 min with NaCl) and the modified Pechini method. The same co-doping concentration of 1.00% mol Nd^{3+} and 0.50% mol Yb^{3+} was applied to both samples.

Further optimization of the synthesis procedure is surely required to surpass the agglomeration problem totally and achieve a complete crystallization of yttria NCs. Nonetheless, the outcomes of this work still pave the way for obtaining individual Y_2O_3 NCs with dimensions of less than 50 nm. Next, the primary results regarding the assessment of thermal sensing of Y_2O_3: Nd^{3+} - Yb^{3+} NCs is presented.

3.3.4. Nanothermometry of Y_2O_3: Nd^{3+}-Yb^{3+} nanocrystals

The evaluation of the thermal sensing properties of Y_2O_3: 1.00% mol Nd^{3+}, 0.50% mol Yb^{3+} NCs was made based on the PL(T) measurements on powder, upon continuous radiation at 808 nm. The powdered sample was heated in a LINKAM device, and 80 spectra were recorded for each temperature in the range of 297 – 328 K (24 – 55°C). The complete experimental conditions are the same as laid out in **section 2.2.2** in **Chapter II**. Here, a comparison will be made between the samples synthesized via the modified Pechini method (450°C/12h + 1000°C/1h) and the two-step urea-based process (550°C/20 minutes dispersed in NaCl).

In **Figure 56.(a)** and **(c)**, the PL (T) spectra of Y_2O_3: 1.00% mol Nd^{3+}, 0.50% mol Yb^{3+} NCs synthesized by the modified Pechini method, and the two-step urea-based route are depicted, respectively. The profiles of both spectra looked very similar, featuring emission peaks that vary as temperature changes. Notice that not only does the Yb^{3+} PL peak evolves with temperature, but the Nd^{3+} PL peak does as well across the entire thermal range. This dependence on the temperature may be attributed to the fact that the Nd^{3+} - Yb^{3+} dipole-dipole coupling is very dependent on the Y^{3+} sites that the two ions occupy, besides being different for distinguished pairs [43]. Indeed, given the unit cell of Y_2O_3, the Ln^{3+} ions have two possibilities to replace Y^{3+}: C_2 (non-centrosymmetric) and C_{3i} (centrosymmetric) sites. Nd^{3+} ions possibly reside only in C_2 sites because their transitions are electric-dipole induced, and they are not allowed in the sites with higher symmetry. Nonetheless, the sensitization of Yb^{3+} through the energy transfer $Nd^{3+} \rightarrow Yb^{3+}$ can occur either at C_2 or C_{3i} Yb^{3+} centers [88,208].

By looking into the several possibilities for calculating LIR between Nd^{3+} and Yb^{3+} peaks, the best pair is formed by the PL intensities at 1030 nm and 1056 nm, as already reported by Barbosa et al. previously [57]. First, the Yb^{3+} PL intensity at 1030 nm must be considered rather than the one at 978 nm, because it does not overlap with the absorption band of water and thus, extra heating can be avoided when exciting the samples [50,51]. Second, the peak of Nd^{3+} at 1056 nm has the lowest temperature dependency of all the Nd^{3+} emission intensities, constituting a rather good reference to monitor Yb^{3+} emission as a function of temperature.

For each sample, the emission spectrum was converted from wavelength-dependent to wavenumber-dependent format, and the LIR between emission lines at 1056 nm (I_{1056}) and 1030 nm (I_{1030}) was calculated as follows for each temperature:

$$\mathrm{LIR}(\tilde{\nu},\mathrm{T}) = \frac{\int_{9438}^{9492} \mathrm{I}_{1056}(\tilde{\nu},\mathrm{T})\,d\tilde{\nu}}{\int_{9629}^{9718} \mathrm{I}_{1030}(\tilde{\nu},\mathrm{T})\,d\tilde{\nu}} \tag{31}$$

where $\tilde{\nu}$ is wavenumber, in cm^{-1}. 80 spectra were acquired for each temperature with the aim of obtaining reliable calibration results. Hence, seven LIR points were plotted in a graph LIR (T) versus temperature, given in Kelvin scale. To determine the calibration curve that correlates LIR and T, a linear fit was applied to the data points, following the form $LIR(T) = aT + b$, where a and b are constants. R^2 statistical values of 0.994 - 0.995 were reached, demonstrating the good accuracy of the regression analysis. The resulting curves are found in **Figure 56.(b)** and **(d)** for Nd^{3+} - Yb^{3+} co-doped yttrium oxide NCs obtained by the modified Pechini and the two-step urea-based methods, respectively.

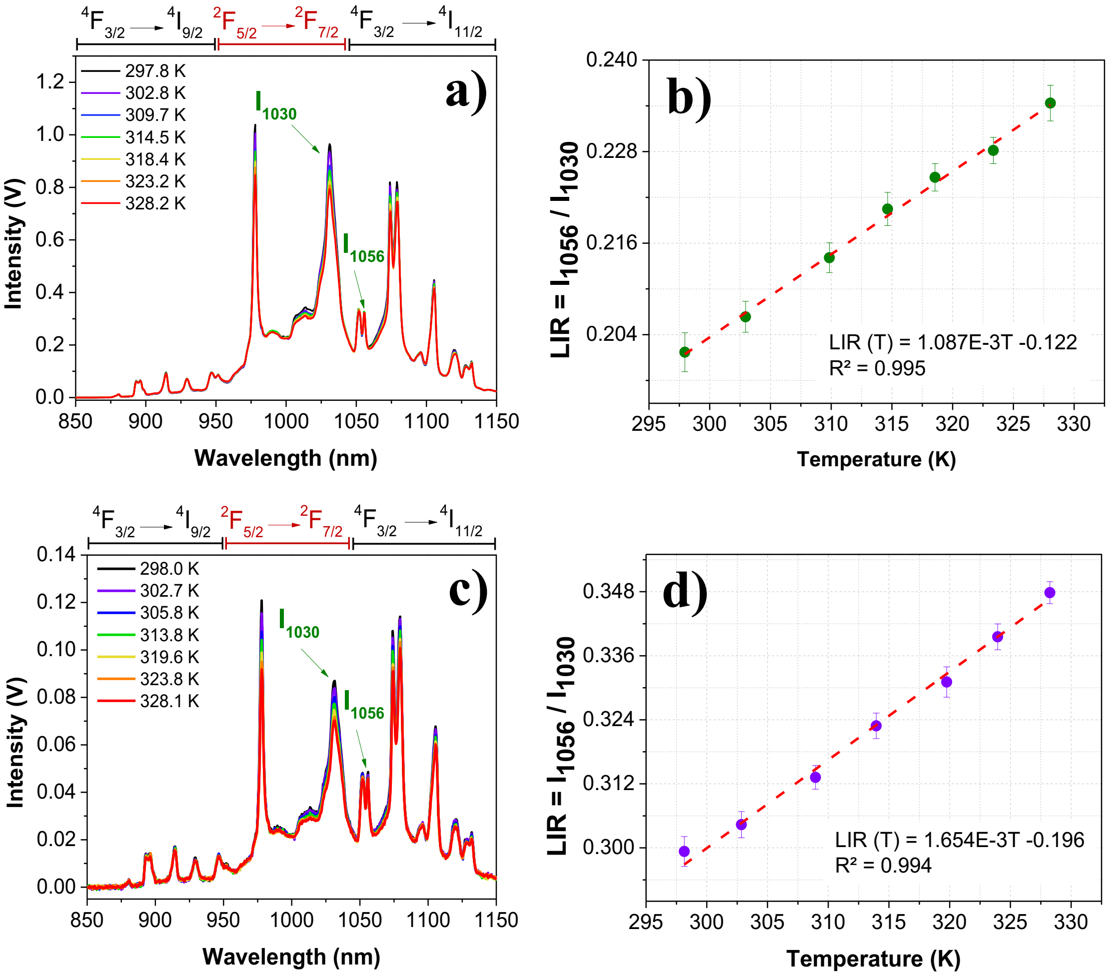

Figure 56. (a) PL(T) and **(b)** calibration curve of Y_2O_3 synthesized by modified Pechini method. **(c)** PL(T) and **(d)** calibration curve of Y_2O_3 synthesized by the two-step urea-based route. Both samples were co-doped with 1.00% mol Nd^{3+} and 0.50% mol Yb^{3+}.

Both materials exhibited similar relative thermal sensitivity and thermal resolution, calculated by equations 4 and 6 from **Chapter I**, respectively. Y_2O_3: Nd^{3+} - Yb^{3+} showed a decreasing Sr of 0.55%.K^{-1} to 0.47%.K^{-1} across the temperature interval. At body temperature, it reached Sr = 0.51%.K^{-1} with δT = 0.4 K for the modified Pechini method, and Sr = 0.52%.K^{-1} with δT = 0.4 K for the two-step urea-based route (**Figure 57.(a)**). As was the case with YAG: Nd^{3+}-Yb^{3+}, the synthesis process does not interfere in the temperature sensor performances.

Note that these Sr values of Y_2O_3: 1.00% mol Nd^{3+}, 0.50% mol Yb^{3+} NCs resemble those achieved for YAG: 0.75% mol Nd^{3+}, 0.50% mol Yb^{3+} NCs (**Figure

37.(a)), but the thermal resolution values are significantly higher. Even though analogous experimental conditions for PL (T) were applied, $\frac{\delta \mathrm{LIR}}{\mathrm{LIR}}$ of PL emission of Y_2O_3: 1.00% mol Nd^{3+}, 0.50% mol Yb^{3+} was relatively high (~0.20% against to ~0.08% of YAG: 0.75% mol Nd^{3+}, 0.50% mol Yb^{3+}). This arose from the decrease in the signal-to-noise ratio as a consequence of the PL fluctuations caused by the still incomplete removal of organic molecules and OH groups (as seen in FTIR displayed in **Figure 54**). This ended up degrading the precision of PL measurement and hence, impairing the nanothermometer's ability to detect small variations in temperature [18].

Even so, the Sr values of this work are quite competitive in respect of most published studies on Nd^{3+} - Yb^{3+} co-doped inorganic hosts under NIR excitation in BW-I (750 – 950 nm). This especially includes those that worked with Yb^{3+} emission outside the BWs, such as Y_3BO_6 (0.18 %.K^{-1} at 308 K) [57], YBO_3 (0.21%.K^{-1} at 308 K) [57], $Y_2Ba_3B_4O_{12}$ (0.31% %.K^{-1} at 298 K) [75], and Y_2O_3 itself (0.48%.K^{-1} at 308 K) [57]. Still, the sensitivity to temperature changes achieved here with Y_2O_3: 1.00% mol Nd^{3+}, 0.50% mol Yb^{3+} NCs remained higher than $LiLaP_4O_{12}$ (0.40%. K^{-1} at 330 K) from the work of Marciniak et al. [27], that worked completely within the BWs.

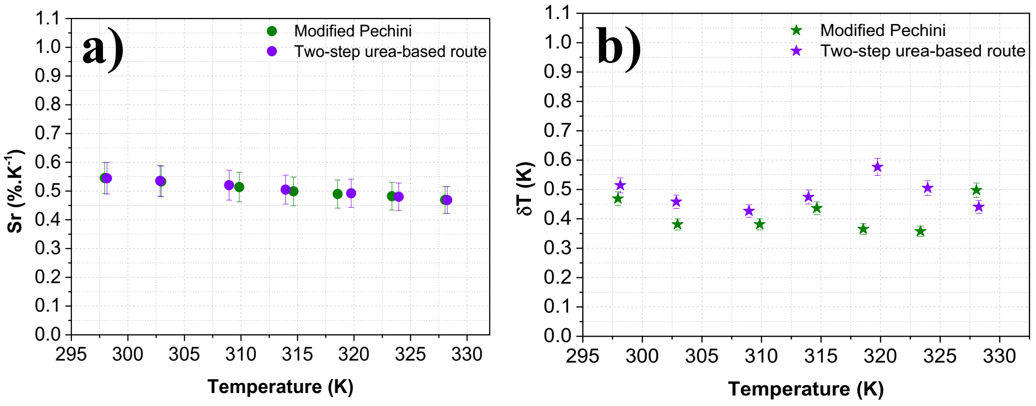

Figure 57.(a) Sr and **(b)** δT values of Y_2O_3: 1.00% mol Nd^{3+}, 0.50% mol Yb^{3+} NCs as a function of the temperature for both synthesis procedures employed in this work.

Finally, the LIR values of Y_2O_3: 1.00% mol Nd^{3+}, 0.50% mol Yb^{3+} NCs synthesized by the two methods were measured within 11 heating-cooling cycles from around 298 K to 328 K (25°C to 55 °C), which are shown in **Figure 58**. The computed repeatability was at least 99.4% for each sample. Therefore, 0.6% of experimental deviation of LIR over successive temperature cycles indicates that variations in the temperature extracted from the calibration curves are less than 2 x δT [14]. This outcome demonstrates a high reversibility of LIR in Y_2O_3: Nd^{3+} - Yb^{3+} with temperature changes, and the suitability of Nd^{3+} - Yb^{3+} co-doped yttria as a luminescent nanothermometer.

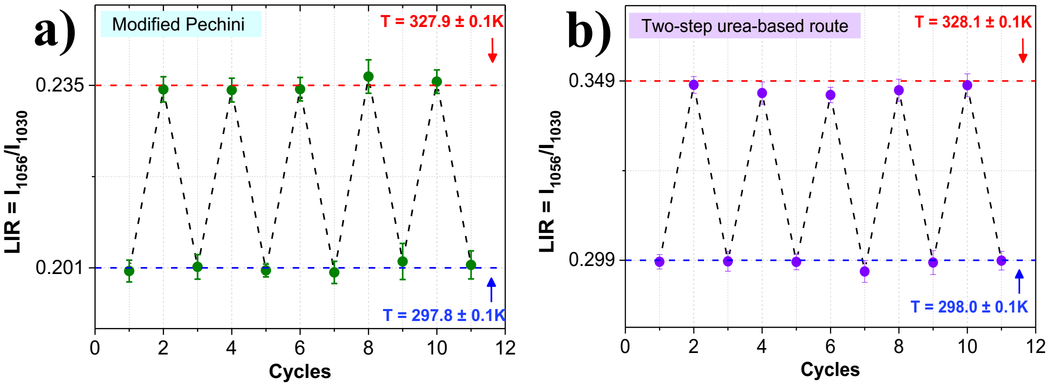

Figure 58. Measurements of LIR over 11 heating- cooling cycles of Y_2O_3: 1.00% mol Nd^{3+} , 0.50% mol Yb^{3+} obtained by **(a)** the modified Pechini method and **(b)** the two-step urea-based route. The repeatability is 99.4% for both cases.

3.4 General remarks and perspectives

In summary, a study on NCs of Y_2O_3 co-doped with Nd^{3+} and Yb^{3+} was conducted aiming at future applications in luminescence nanothermometry in the biological field. Initially, the proper selection of the co-doping composition was conducted by employing the modified Pechini method. The conclusion drawn from this first part is that 1.00% mol Nd^{3+} and 0.50% mol Yb^{3+} provided a boosted signal of PL emission.

Targeting at producing individual and dispersed yttria NCs, the two-step urea-based route was applied. In order to yield small NCs, a refinement of the experimental protocol was proposed. It involved the addition of 1,4-butanediol to the reactant solution to form $Y(OH)CO_3.H_2O$ NPs measuring less than 60 nm and then, a calcination of the as-obtained yttrium hydroxycarbonate at 550°C/20 minutes dispersed in a NaCl-matrix. This resulted in yttria NCs with 22 ± 10 nm, but with a partial degree of agglomeration.

Concerning the thermal sensing performance, Y_2O_3: 1.00% mol Nd^{3+}, 0.50% mol Yb^{3+} NCs presented Sr around $0.50\%.K^{-1}$ and $\delta T \sim 0.40$ K at physiological temperature, as well repeatability of 99.4% over 11 heating-cooling cycles. The synthesis method — whether the modified Pechini method or the two-step urea-based route — did not have an impact on these results.

Hence, it is important to point out that further improvements in the NC synthesis are necessary since the results showed the nanomaterial is still not appropriate for the next steps in biological tests yet. First, NC agglomeration is still a problem to be overcome. Applying a salt-matrix to heat-treat $Y(OH)CO_3.H_2O$ was a promising strategy as it improved the dispersion state, but using more excess of NaCl to disperse better $Y(OH)CO_3.H_2O$ NPs should be tested. Nonetheless, the major disadvantage of NaCl as a separating media is its lower melting point in relation to the temperature for a complete crystallization of Y_2O_3. In this way, for future works, some strategies that can be put into practice are: 1) to try at maximum to have individual Y_2O_3 NCs after calcination with more excess of NaCl and conduct a coating with amorphous silica for a second heat treatment at higher temperature (up to 1000°C); 2) to use K_2SO_4 as matrix via a microemulsion method to coat the $Y(OH)CO_3.H_2O$ NPs and perform the thermal treatment at high temperature. This latter proposal derives from the work of Song et al.[209], who applied a urea precipitation method to prepare YAG: Ce^{3+} NCs. The as-prepared precipitates were dispersed in K_2SO_4, which presents melting point of 1067°C, and calcined at 1000°C for 2h for crystallization, resulting in individual YAG: Ce^{3+} NCs of small size (~5 nm).

Second, adjustments in the synthesis to surpass the agglomeration problem can contribute to the improvement of the signal-to-noise ratio of PL emission and, thus, minimize the parameter related to the uncertainty of LIR ($\frac{\delta LIR}{LIR}$). This could lead to a significant reduction in thermal resolution in order to reach a target value at least below 0.2 K.

On the other hand, the lifetime approach to nanothermometry analysis should be considered for NCs of Y_2O_3 co-doped with Nd^{3+} and Yb^{3+}. It consists of using the lifetime of excited states as a thermometric parameter, instead of LIR, and it requires the monitoring of only one PL transition. Since Y_2O_3 co-doped with Nd^{3+} and Yb^{3+} NCs offer different possibilities of PL emission peaks that evolve with temperature, it is worth testing this thermometry technique in order to find high Sr and better δT values.

These optimizations are crucial to move forward to biological trials, but it should be noted that the primary outcomes attained in this thesis chapter lay the groundwork for producing small NCs of Nd^{3+} - Yb^{3+} co-doped Y_2O_3 as luminescent nanothermometers.

Chapter IV: A study of YAM: Nd^{3+} and YAM: Nd^{3+}-Yb^{3+} as luminescent nanothermometers

4.1 Introduction

Belonging to the same Y_2O_3-Al_2O_3 binary system as YAG, yttrium aluminum oxide in its monoclinic structure ($Y_4Al_2O_9$), commonly known as YAM, has garnered significant interest in the fields of materials science and nanotechnology. Although it is still less studied than its YAG counterpart, YAM is renowned for its remarkable thermal stability, with a high melting point of approximately 2000°C, low thermal conductivity of 3.50 W/m.K at 300K, wide bandgap of around 4.5 eV, and its ability to host various dopants [84,86,210,211]. This latter feature is remarkably engaging since this oxide possesses four distinct crystallographic sites of yttrium, with C_1 symmetry. This makes YAM a favorable candidate for vast doping assays with rare-earth ions, since they tend to replace yttrium ions [87].

Owing to these key characteristics of YAM, some research has been being developed to investigate its spectroscopic properties when doped with different Ln^{3+} ions[212–215]. Moreover, the scientific community has also invested in studying Ln^{3+}-doped YAM for cutting-edge technologies to keep pace with the demands of industry and academic research. This includes applications for light [87,216–218], displays [219,220], thermal barriers to provide thermal protection of metallic mechanical components [221–223], and fingerprint detection [224].

Nevertheless, the use of lanthanide-doped YAM in nanothermometry is still very scarce. So far, it has been reported only one work by Boruc et al.[85] of YAM crystals doped with Dy^{3+} for temperature sensing. By exciting the YAM: Dy^{3+} particles at 355 nm, the authors informed that accomplished an absolute thermal sensitivity (S_{abs}) more than $0.30\%.°C^{-1}$ in the range of 873 – 1073 K involving the LIR method between the emission lines at 455 nm and 481 nm. However, no further information on relative thermal sensitivity and thermal resolution was given. Besides that, another work conducted by Boruc et al.[225] about the temperature dependence of YAM doped with Tb^{3+} crystals pointed out briefly the possible usefulness of employing the LIR method between the emission lines at 437 nm and 542 nm for temperature measurement above 700 K. No evaluation of the thermal performance was carried out though. In both works, the authors stated that the crystals presented the shape of rods, whose dimensions (diameter and length) were in the order of millimeters.

Usually, the synthesis of nanometric-sized YAM particles is dominated by the sol-gel process (conventional[211,213,226] and combined with a combustion process[219,227,228]), but other synthesis procedures have also been reported, such as high-temperature solid-state reaction (direct sintering of oxides) [220,229,230], co-precipitation associated with molten salt[231], the modified Pechini method [84,86], and solvothermal synthesis followed by calcination [210,232]. Still, controlling the size and the dispersion state of the NCs continues to be a relevant obstacle in the synthesis of YAM.

In this chapter, a study of YAM doped with rare-earth ions for nanothermometry is built up, with the target to offer an overview of YAM: Nd^{3+} and YAM: Nd^{3+} - Yb^{3+} as nanothermometers, extending beyond the requirements for biological applications. By employing the modified Pechini synthesis, this work was split into two parts. First, the potential of YAM single-doped with Nd^{3+} was examined closely in terms of its structural and optical properties, and the optimal concentration of Nd^{3+} was defined. Building on this, the parameters relative to the thermal sensing performance were assessed, such as the relative thermal sensitivity, thermal resolution, and the reversibility of the thermometric parameter when the temperature returns to ambient levels. Then, the optimal Nd^{3+} concentration was fixed for a co-doping with Yb^{3+} in the second part, to verify its effect on the efficacy of temperature measurement. Lastly, a new synthesis method of YAM NCs via the two-step urea-based route was put forward.

4.2 Experimental protocol

4.2.1. Materials syntheses

4.2.1.1. Modified Pechini method

The syntheses of the Nd^{3+} doped and the Nd^{3+}-Yb^{3+} co-doped YAM NCs were conducted by sticking to a protocol similar to that of YAG NCs presented in **section 2.2.1.1** of **Chapter II** for YAG: Nd^{3+}-Yb^{3+}, with one modification: the amount of D-sorbitol used. Instead of the typical 3:2 mass ratio of D-sorbitol to citric acid, a proportion of 3 mols of D-sorbitol to 2 mols of citric acid was established, as done by Gomes et al.[84] and Gasparotto et al.[86] previously. The Nd^{3+} content for single-doped YAM varied across concentrations of 0.33, 0.50, 0.67, 0.83, 1.00, and 1.50% mol relative to the total metals.

Subsequently, the concentration of Nd^{3+} that yielded the highest PL emission of YAM: Nd^{3+} was fixed, and Yb^{3+} was introduced at concentrations of 0.17, 0.50, 0.67, 1.00, 1.50% mol.

4.2.1.2. Two-step urea-based route

To synthesize individual and dispersed YAM NCs, experiments were performed under solvothermal conditions in the course of this work, utilizing a method comparable to that applied for YAG, as described in **Chapter II**. The stoichiometric concentrations of the precursors were adjusted for YAM, and different pressures and temperatures were tested. Despite these efforts, no YAM was successfully produced, confirming previous observations [158].

Herein, a novel synthesis route, analogous to the two-step urea-based route of Y_2O_3, is proposed for YAM. The synthesis of Nd^{3+} single-doped YAM by this procedure involved the dissolution of $Y(NO_3)_3.6H_2O$ (Acros organics, ≥ 99.9%), $Al(NO_3)_3.9H_2O$ (Riedel-de-Haën, 98.5%), $Nd(NO_3)_3.6H_2O$ (Sigma-Aldrich, ≥99.9%), and urea (Sigma-Aldrich, > 99%) in distilled water in separated flasks at room temperature. The aqueous solutions were mixed under stirring, followed by the addition of 1,4-butanediol (Thermo Scientific, 99.0%) to achieve a final volume of 100 ml. This mixture was transferred to a 120-ml autoclave and heated in an oven for 24h. The resulting powder was centrifuged three times (7800 rpm, 15 minutes) with ethanol to remove the byproducts and then dried at 60°C/2h. Finally, the dried powder was heat-treated in a tubular furnace under flowing O_2 (10 $ml.min^{-1}$) at 1000°C for 1 hour, with a heating rate of 10°$C.min^{-1}$.

In this study, various experimental conditions were tested: the amount of yttrium ranged from 2.50 to 7.50 $mmol.L^{-1}$, urea from 0.10 to 0.50 $mol.L^{-1}$, reaction temperature from 70 to 85°C, 1,4-butanediol from 0 to 80% in volume, and the pH of the precursor solution was altered with NH_3 addition. The aluminum concentration was kept stoichiometric relative to yttrium (molar ratio Y: Al equal to 4:2), and the Nd^{3+} amount was singled out based on the results of the modified Pechini method.

4.2.2. Characterization techniques

All characterization measurements concerning XRD, HR-XRD, TEM, FE-SEM, FTIR, PL emission, and PL (T) of YAM: Nd^{3+} and YAM: Nd^{3+} - Yb^{3+} samples were conducted as detailed in **topic 2.2.2** of **Chapter II**.

Raman spectrum was acquired using a Horiba LabRAM HR Evolution Raman spectrometer located at LabMic – Universidade Federal de Goiás in Goiânia (Brazil). The spectrum was collected in the 150 – 1500 cm^{-1} range, using a 633–nm line of a HeNe laser. This analysis was made on ground and undoped YAM powders.

4.3 Results and discussion

4.3.1. YAM synthesized by the modified Pechini method: synthesis and nanothermometry analysis

4.3.1.1. Nd^{3+} single-doped YAM nanocrystals

Seven YAM samples doped with Nd^{3+} concentrations ranging from 0.33 to 1.50% mol relative to the total metals were first synthesized by the modified Pechini method. The Nd^{3+} amounts in molar percentage along with the associated chemical formula are tabulated in **Table 10**.

Table 10. Concentration of Nd^{3+} in % mol in relation to all metals, and the corresponding chemical formulas.

$Y_4Al_2O_9$: Nd^{3+}

Nd^{3+}					
0.33% mol	**0.50% mol**	**0.67% mol**	**0.83% mol**	**1.00% mol**	**1.50% mol**
$Y_{3.98}Nd_{0.02}Al_2O_9$	$Y_{3.97}Nd_{0.03}Al_2O_9$	$Y_{3.96}Nd_{0.04}Al_2O_9$	$Y_{3.95}Nd_{0.05}Al_2O_9$	$Y_{3.94}Nd_{0.06}Al_2O_9$	$Y_{3.91}Nd_{0.09}Al_2O_9$

The high-resolution diffractograms of all single-doped samples matched the standard reference for YAM contained in PDF 04-013-3313 (**Figure 59.(a)**). No impurities were detected with the increasing of Nd^{3+} doping, indicating the successful replacement of Y^{3+} by the dopant. By applying the Le Bail fit method on HR-XRD patterns (**Figure S4** in **Appendix**), the evolution of the cell parameters *a*, *b*, and *c* as a function of Nd^{3+} concentration is displayed in **Figure 59.(b)** (see the exact values in **Table S2** in **Appendix**). As more Nd^{3+} ions are inserted into the YAM structure, all the three lattice parameters present an increase, expanding the unit cell. Since the ionic radius of Nd^{3+} (0.983Å in six-fold coordination) is larger than the one of Y^{3+} (0.900Å and 0.960 Å in six-fold and seven-fold coordination, in the respective order), it causes a slight expansion of the crystallographic lattice [128]. Kumar et al.[219] and Liu et al.[217] reported a similar trend in their works with YAM doped with Er^{3+} and Eu^{3+}, respectively. However, the former authors observed a logical contraction in the lattice as Er^{3+} possesses ionic radius of 0.890 Å for six-fold and 0.945 Å for seven-fold coordination [128].

In addition, one can notice in **Figure 59.(b)** there is a linear evolution of each parameter as Nd^{3+} concentration increases, following Vegard's law. Basically, it corresponds to a linear dependence between the lattice parameter and the concentrations of the constituents of the crystalline structure, in the case of a solid solution. Consequently, it means a homogeneous incorporation of Nd^{3+} ions into the crystallographic sites of Y^{3+} in YAM crystalline matrix, regardless of the doping concentration up to 1.50% mol.

On the other hand, the Nd^{3+} concentration does not affect the coherence length calculated by the Le Bail fit. Indeed, the Lc remains nearly constant at around 45 nm (**Figure 59.(c)**), whatever the doping concentration, and it pairs well the NC size visualized by TEM. This means that YAM is formed by NCs with high crystal quality, but they agglomerate due to the coalescence effect caused by the heat treatment at 1000°C (**Figure 59.(d)**). Additionally, the NC size obtained here is smaller than those published by Gasparotto et al.[86] for YAM: Eu^{3+} (86 nm – calcination at 1000°C) and Gomes et al.[84] for YAM: Yb^{3+} - Ho^{3+} - Tm^{3+} (80 nm – calcination at 1100°C), using the same modified Pechini method.

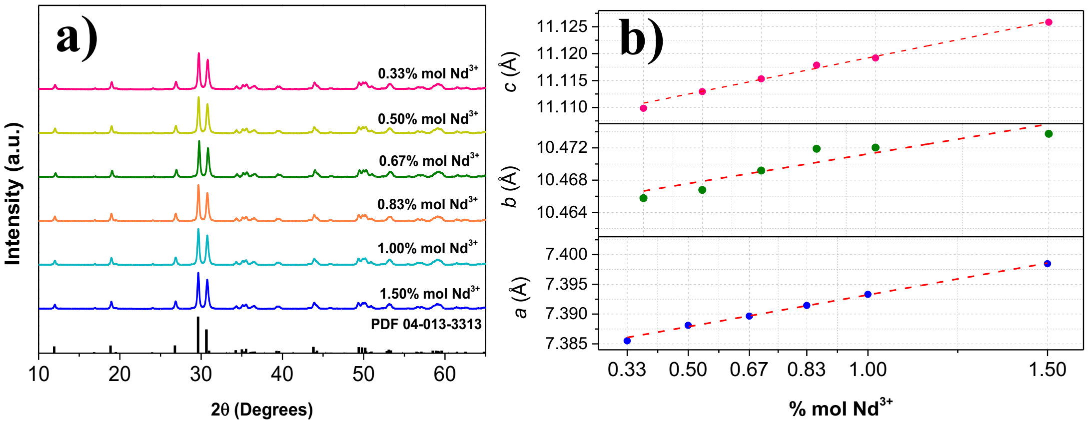

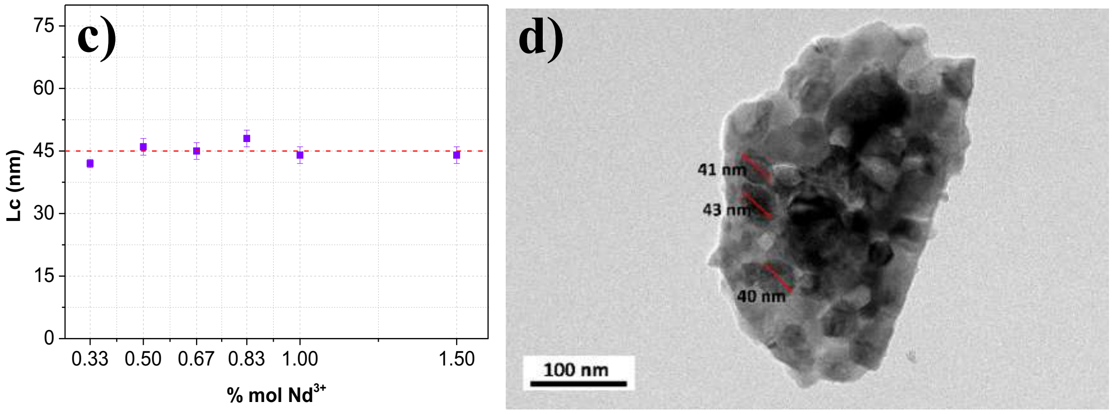

Figure 59. (a) HR-XRD of YAM doped with different concentrations of % mol Nd^{3+}. **(b)** Evolution of the cell parameters *a*, *b*, and *c*, and **(c)** coherence length (Lc) with the Nd^{3+}concentration. **(d)** TEM image of YAM: 0.83% mol Nd^{3+}.

The chemical bonds of YAM were analyzed using FTIR and Raman spectroscopy (**Figure 60**). In the low-energy region below 275 cm^{-1} of the Raman spectrum, the translatory motions of Y^{3+}, Nd^{3+} and Al^{3+} ions take part in vibrations. In the 275 to 406 cm^{-1} range, the Raman spectrum is dominated by bands correlated to the translation and rotation of AlO_4 units, as well as the translation, librational and bending vibrations of Y-O polyhedra. From 450 to 900 cm^{-1} in both FTIR and Raman spectra, stretching modes of Y-O and Al-O are observed. Specifically, in the FTIR spectrum, the bands at 515, 557 and 711 cm^{-1} (also Raman-active) are ascribed for Y-O linkages whereas the ones at 792, 875, and 900 cm^{-1} for Al-O bonds. The other bands above 900 cm^{-1} are related to chemical bonding from the remaining organics of the synthesis, such as C-O at 1288 cm^{-1}, COO^{-} at 1515 cm^{-1}, NH_2 at 1646 cm^{-1}, hydroxyl groups in the surroundings of 3000 cm^{-1} [87,147,228,233–235]. These organic residues are due to the brevity of the calcination (10 minutes) to limit the growth of YAM NCs.

Concerning the phonon energy of YAM crystalline host matrix, the cutoff is defined as the mode at the highest energy frequency in the Raman spectrum. Therefore, it corresponds to 812 cm^{-1}, which lines up well with the works of Boruc et al. (813 cm^{-1})[85], and Lemański et al. (814 cm^{-1})[234]. The broad band at 1081 cm^{-1} is due to CO_3^{2-} species [217]. Notice that compared to the other two oxides studied in this thesis, the phonon energy is higher than that of Y_2O_3 (600 cm^{-1}), but slightly lower than that of YAG (856 cm^{-1}) [25,89].

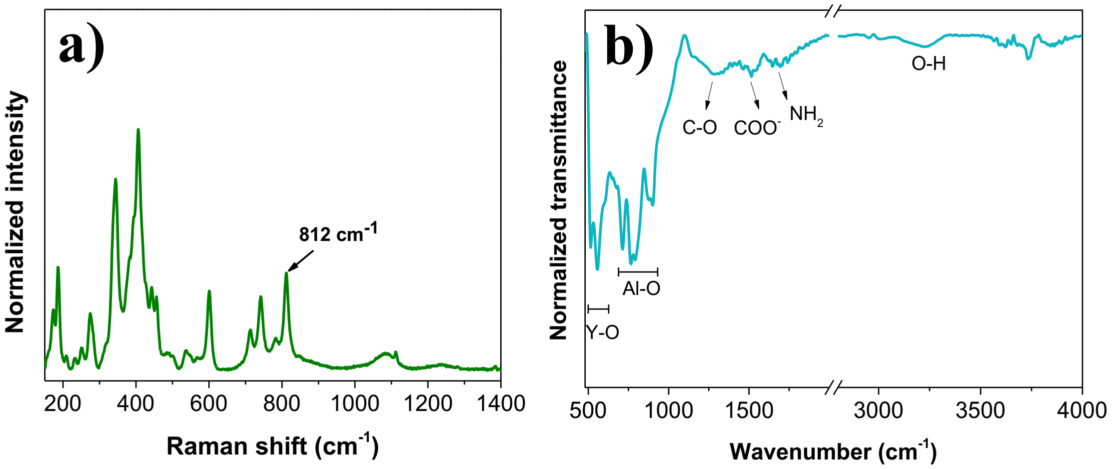

Figure 60. (a) Raman and **(b)** FTIR spectra of YAM doped with 0.83% mol Nd^{3+}.

The PL emission of each YAM: Nd^{3+} sample was investigated under irradiation with NIR light at 808 nm at room temperature. Upon excitation, the electrons are elevated to the excited levels $^4F_{5/2}$, $^2H_{9/2}$, followed by a fast non-radiative transition to the excited state $^4F_{3/2}$. Several PL peaks emerged in the ranges of 860 - 950 nm and 1020 - 1140 nm, relative to the transitions from the excited state $^4F_{3/2}$ to the levels $^4I_{9/2}$ and $^4I_{11/2}$ (**Figure 61.(a))**. A simple energy level scheme of Nd^{3+} in YAM is displayed in **Figure 61.(b)**. Based on the total integrated area of each PL spectrum, the effect of Nd^{3+} concentration on the PL intensity was evaluated. The overall intensity increased with Nd^{3+} doping, reaching a maximum for 0.83% mol Nd^{3+} (**Figure 61.(c)**). Beyond this optimal concentration, the PL quenching was noted, mainly due to energy migration ($^4F_{3/2}$, $^4I_{9/2}$ → $^4F_{3/2}$, $^4I_{9/2}$), and cross-relaxation processes ($^4F_{3/2}$, $^4I_{9/2}$ → $^4I_{15/2}$, $^4I_{15/2}$)[54].

This result demonstrated that YAM permits higher Nd^{3+} doping levels before the PL concentration quenching occurs, compared to YAG (0.50% mol Nd^{3+}) and Y_2O_3 (0.25% mol Nd^{3+}) synthesized via the modified Pechini method as reported by Barbosa et al. [64]. This might be due to the YAM structure, as there are four different crystallographic sites of yttrium, linked to oxygens at different distances, where Nd^{3+} could replace Y^{3+}. Nonetheless, which yttrium site Nd^{3+} ions exactly occupy is still an open question. Ryba et al.[226] concluded with PL emission measurements at 10K that the surroundings of Nd^{3+} are nearly the same, suggesting that Nd^{3+} ions possibly enter in one type of site among the four existing ones. Since the position and splitting of the 4f levels are directly related to the coordination number and the average distance of the central ion and the surrounding oxygen atoms, this uncertainty about the location of Nd^{3+} in YAM hinders the construction of its energy level diagram with the exact assignments of the energy positions for each Stark component.

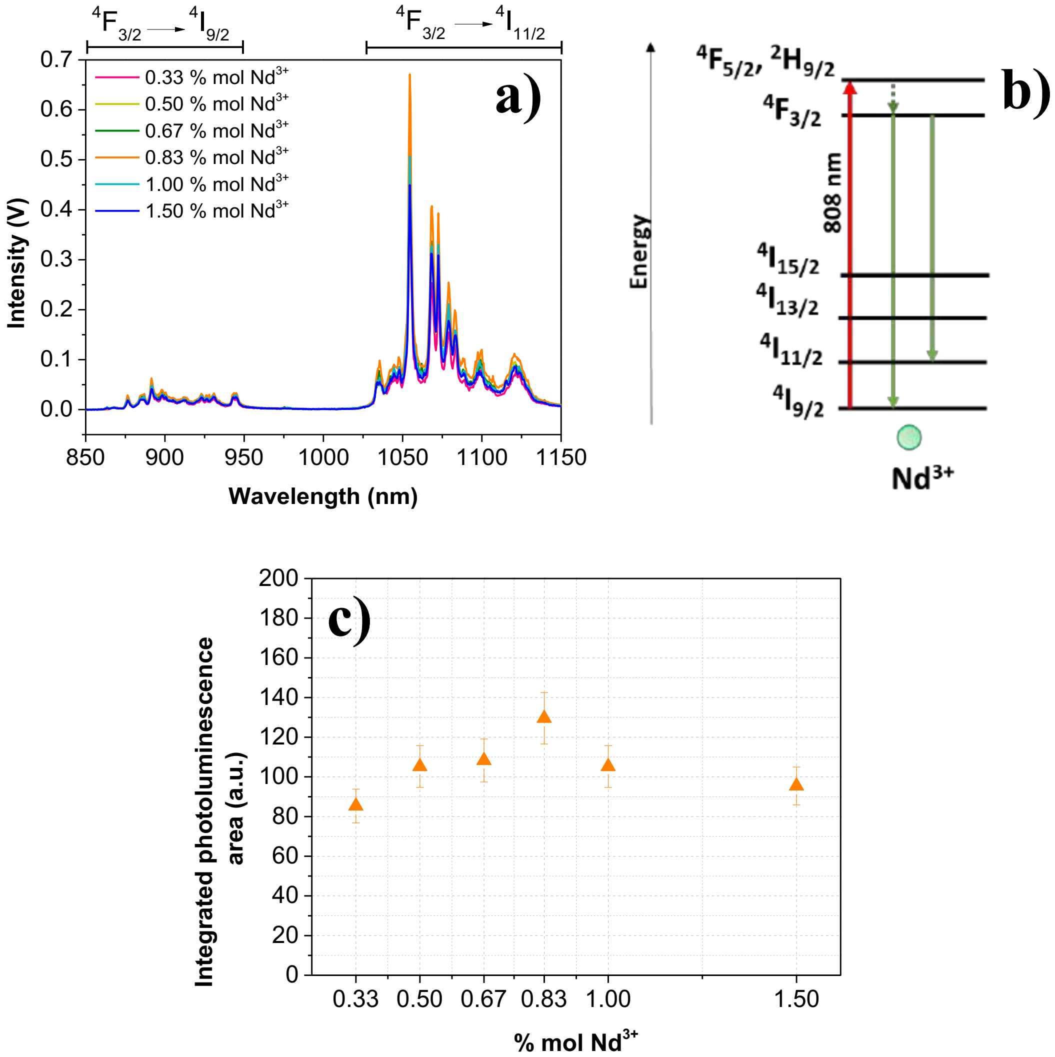

Figure 61. (a) PL emission spectra of YAM doped with different concentrations of % mol Nd^{3+}, **(b)** Simple energy-level diagram of Nd^{3+} in YAM, and **(c)** Integrated area of PL spectrum of YAM: Nd^{3+} as a function of % mol Nd^{3+}.

For nanothermometry analysis, the PL(T) measurement was performed on the powdered sample of YAM: 0.83% mol Nd^{3+} — the optimized Nd^{3+} composition —, using the same experimental procedure as described in **section 2.2.2** in **Chapter II** for YAG: Nd^{3+}-Yb^{3+}. The temperature dependence of PL emission spectrum is shown in **Figure 62.(a)**. In the case of single emitting center materials, the luminescence temperature sensing can be done through the exploitation of LIR between two emission peaks due to radiative transitions from two TCLs. This temperature dependence is modeled by Boltzmann's law, given by $\mathrm{LIR}\ (\mathrm{T}) = \mathrm{B}\exp\left(\frac{-\Delta \mathrm{E}}{\mathrm{k_B T}}\right)$ (equation 3 in **Chapter I)**. Here, ΔE,

k_B, T, and B stand for the energy gap between the two TCLs, the Boltzmann constant, the temperature in Kelvin, and a constant, respectively. It is important to mention that this modelling is valid provided that $200 \leq \Delta E \leq 2000$ cm^{-1}. When working outside this range, any nanothermometer can lead to distorted thermal readout [236].

An upside of the PL spectrum of YAM: Nd^{3+} is its composition of diverse PL peaks stemming from the Stark effect. Since the number of Stark components is dependent on the local ion symmetry, the YAM structure gives several possibilities for LIR exploitation. By looking into them in the PL(T) spectrum, especially the emission lines in respect of the transition $^4F_{3/2} \rightarrow {}^4I_{11/2}$, the pairs formed by the peak at 1049 nm with one of the Stark sublevels centered at 1080 nm, 1084 nm, and 1100 nm provided thermal behaviors that are well-described by Boltzmann's law. Notably, the Stark line at 1049 nm rises as the temperature augments, whereas the other ones drop, hinting the nonradiative thermalization occurs faster than any depopulation channel of the involved excited levels. Moreover, the range referred to the transition $^4F_{3/2} \rightarrow {}^4I_{9/2}$ was ruled out of this analysis, because unreliable results of thermal sensing could be obtained due to the low intensity of the peaks. Lastly, even though the peak at 1055 nm is the most intense, it was checked that no LIR with this peak follows Boltzmann's law.

Thus, **Figure 62.(b)** unveils the evolution of LIR as a function of temperature in a graph of ln (LIR) versus 1/Temperature (in K^{-1}) for ratios of I_{1049}/I_{1080}, I_{1049}/I_{1084}, and I_{1049}/I_{1100}. Each ratio was calculated between integrated intensities after converting the PL spectrum from wavelength-dependent to wavenumber-dependent. The experimental data were accurately fitted by the Boltzmann formula, resulting in calibration curves of LIR(T), with R^2 above 0.996. From these calibration curves, the energy gap could be estimated for each ratio of TCLs (hereafter referred to as ΔE_{calc}) and compared with the energy difference measured between the barycenter of the peaks in the PL emission spectrum (ΔE_{exp}). All these outcomes are summarized in **Table 11**. There is a good alignment between ΔE_{calc} and ΔE_{exp} for LIR = I_{1049}/I_{1084}, suggesting that the emissions originate from the two distinguished Stark multiplets of $^4F_{3/2}$ to the same sublevel of $^4I_{11/2}$. On the other hand, ΔE_{calc} and ΔE_{exp} become divergent for the other two pairs of peaks, which implies that the emission lines at 1049 nm, 1080 nm, and 1100 nm possibly derive from the different Stark sublevels of $^4F_{3/2}$ and decay to different Stark sublevels of $^4I_{11/2}$.

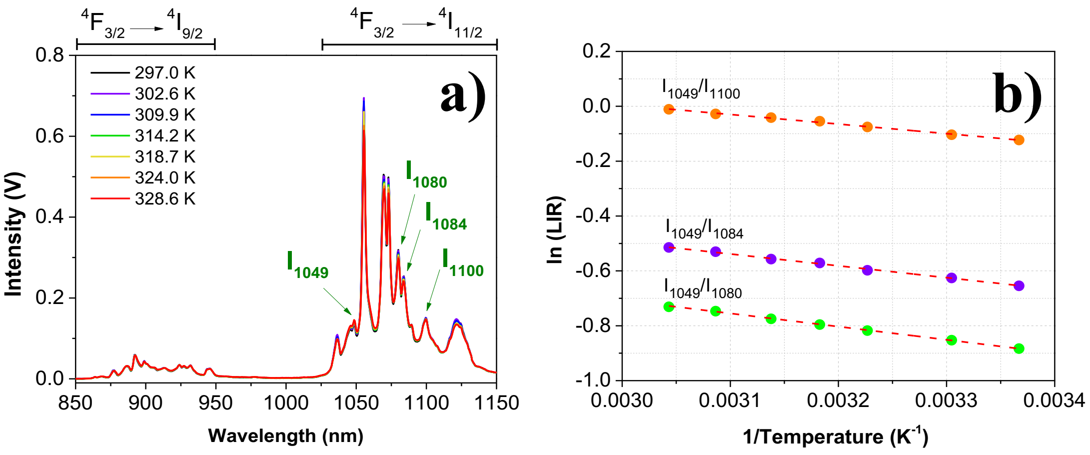

Figure 62. (a) PL emission spectrum as a function of temperature of YAM: 0.83% $Nd^{3+}$and **(b)** Calibration curves obtained of LIR formed by the peaks at 1049 nm and 1080 nm, 1084 nm, and 1100 nm over the thermal range. The errors associated with ln (LIR) are in the order of 10^{-3} and thus, the error bars became too small to be displayed in the figure.

Table 11. Calibration curves, energy difference between TCLs extracted from the calibration curves (ΔE_{calc}) and from the PL emission spectrum (ΔE_{exp}) for each LIR. R^2 is the statistical value attesting a good fitting of the points.

Ratio	**Calibration curve**	**ΔE_{calc}**	**ΔE_{exp}**	**R^2**
I_{1049}/I_{1080}	LIR(T) =2.085 exp(-480.606/T)	334.03	273.63	0.999
I_{1049}/I_{1084}	LIR(T) =2.226 exp(-431.789/T)	300.11	307.80	0.998
I_{1049}/I_{1100}	LIR(T) =2.863 exp(-349.151/T)	242.67	441.98	0.997

The Sr values were calculated according to the equation 5 of **Chapter I**, $S_r(T) = \frac{\Delta E}{k_B T^2}$, for each ratio across the temperature range, as presented in **Figure 63.(a)**. The LIR between the PL lines at 1049 nm and 1080 nm yielded a higher sensitivity to the temperature changes, with a maximum Sr of 0.54%.K^{-1} at room temperature (~298 K), and 0.50%.K^{-1} at body temperature (~309 K). In contrast to the studies of inorganic host matrices single-doped with Nd^{3+}, particularly those also working with Stark sublevels of $^4F_{3/2} \rightarrow {}^4I_{11/2}$, the relative thermal sensitivity of YAM: Nd^{3+} is superior. This includes other oxides such as YAG: Nd^{3+} (0.16 %.K^{-1} at 308 K)[64], $Y_2Ge_2O_7$: Nd^{3+} (0.29%.K^{-1} at 308 K)[64], and Y_2O_3: Nd^{3+} (0.43 %.K^{-1} at ~298 K)[61], as well as fluorides like $NaYF_4$: Nd^{3+} (0.13%.K^{-1} at 308 K)[65], and $LiLuF_4$: Nd^{3+} shelled with undoped $LiLuF_4$ (0.48%.K^{-1} at 298 K)[41]. The other luminescence ratios also unveiled competitive thermal responses, such as

0.49%.K^{-1} and 0.40%.K^{-1} at room temperature (~298 K), and 0.45%.K^{-1} and 0.36%.K^{-1} at physiological temperature (~309 K), for LIR of I_{1049}/I_{1084} and I_{1049}/I_{1100}, respectively.

Such a good result for a simple Nd^{3+}-based nanothermometer, that is, without considering co-doping with other rare-earth ions or even a more complex core-shell engineering, can be explained based on the YAM structure. It is composed of several Y-O bonds, whose average length lies around 2.28 ~ 2.38 Å, depending on the yttrium site[237,238]. For being relatively short, namely than the Y-O bonds in YAG (2.40 ~2.42 Å)[239,240], this brings a more covalent nature to the Y-O linkages of YAM, which directly influences the thermal sensitivity. According to a study led by Maciejewska et al.[241], the authors made a conclusion that the shorter the metal-oxygen bonds, the higher the covalency degree, and the larger the energy gap between the thermally coupled excited states. Since the Sr is directly proportional to ΔE, it leads to an improvement in the thermal response. Moreover, the nature of the bonds also has an impact on the non-radiative coupling rates of the two excited levels. These rates will be more intense whether the degree of covalency of metal-oxygen is also high, sustaining the Boltzmann equilibrium[242].

This result about YAM illustrates well why Nd^{3+} single-doped YAM performed better even though this host has a higher phonon energy of 812 cm^{-1} in respect of fluorides (~350 cm^{-1}) and comparable to YAG (835 cm^{-1}) [25]. In another work conducted by Suo et al. [78], they compared the relative thermal sensitivity of three different Er^{3+}-Yb^{3+} co-doped host matrices: YF_3 (yttrium fluoride), YOF (yttrium oxyfluoride), and Y_2O_3. In spite of the latter possessing higher phonon energy (566 cm^{-1}) relative to the other ones (353 cm^{-1} for YF_3, and 482 cm^{-1} for YOF), Y_2O_3: Er^{3+} - Yb^{3+} presented a Sr of 0.85%. K^{-1} against to 0.60%. K^{-1} of YOF: Er^{3+} - Yb^{3+} and 0.27%. K^{-1} of YF_3: Er^{3+} - Yb^{3+}. The explanation lies in the higher bond covalency of Y_2O_3 in comparison with that of YOF and YF_3, in this order.

Thus, when designing a nanothermometer, the selection of the host goes beyond its phonon energy. Bond lengths, covalency, and local symmetry must be taken into account, since they affect the energy, splitting, and overlapping of the electronic states involved in the absorption and luminescence spectra, and the probability of interionic energy transfer. In the end, this can be decisive in the thermal performance of the material[241,243].

Figure 63.(b) displays the thermal resolution as the second figure of merit evaluated in this work, calculated using the formula $\delta T = \frac{1}{S_r}\left(\frac{\delta LIR}{LIR}\right)$ (equation 6 in **Chapter I**). Notice that better δT values are accomplished by using LIR = I_{1049}/I_{1080}, with δT = 0.3 K at physiological temperature (~309 K). This can be credited to the higher Sr obtained with this ratio relative to the others, as shown in **Figure 63.(a)**. The other parameter that impacts δT, $\frac{\delta LIR}{LIR}$, remained around 0.11% ~ 0.30%. So, small differences of temperature will be able to be detected as long as $\frac{\delta LIR}{LIR}$ is decreased by enhancing the signal-to-noise ratio of PL of YAM: 0.83% mol Nd^{3+} [244]. However, the δT determined here aligns with the published literature on inorganic hosts doped with Nd^{3+} [41,61,66,176].

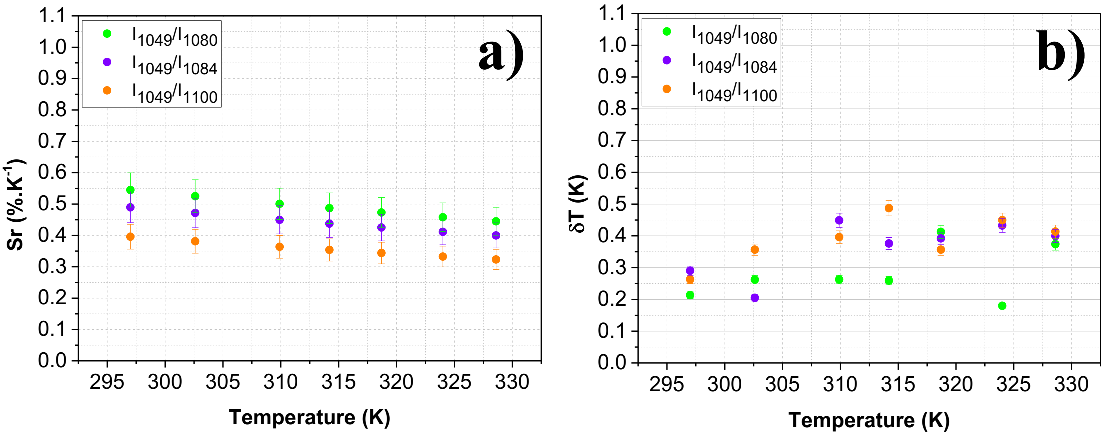

Figure 63.(a) Sr and **(b)** δT of YAM: 0.83% mol Nd^{3+} as a function of temperature. Both thermal parameters were calculated for the LIR of I_{1049}/I_{1080}, I_{1049}/I_{1084}, and I_{1049}/I_{1100}.

Lastly, the repeatability was checked over 11 heating-cooling cycles for each LIR, extending from 297 K to 328.6 K. By using the intensity ratio between 1049 nm and 1080 nm peaks, one has not only the highest relative thermal sensitivity and the best thermal resolution, but also the best repeatability, computed as 97.1% (**Figure 64.(a)**). This indicates that there is a deviation of 2.9% of the temperature measured experimentally (e.g. with a thermocouple) in relation to the one extracted from the calibration curve. This deviation slightly increases to 4.9% when using the LIR of 1049 nm over 1084 nm, meaning that the repeatability is 95.1% (**Figure 64.(b)**). On the other hand, there is a lack of reliability for LIR = I_{1049}/I_{1100} because this ratio provided the poorest repeatability: 91.8% (**Figure 64.(c)**). The decrease in repeatability when using peaks of 1049 nm with 1084 nm or 1100 nm may be related to their lower PL intensities.

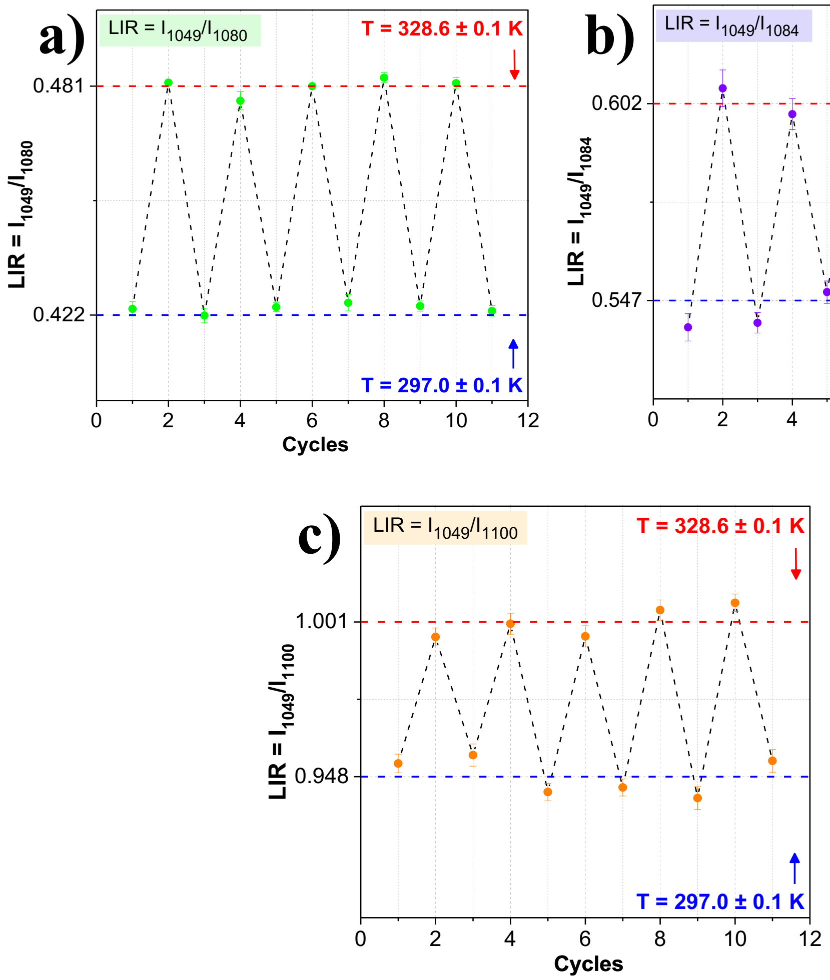

Figure 64. Measurement of LIR over 11 heating- cooling cycles of YAM: 0.83% mol Nd^{3+} for LIR equal to **(a)** I_{1049}/I_{1080}, **(b)** I_{1049}/I_{1084}, and **(c)** I_{1049}/I_{1100}.

In summary, YAM has shown to be an interesting host for embedding Nd^{3+} ions for nanothermometry thanks to its specific structure. Even if the Stark sublevels were held for applying the LIR approach, good thermal response can be obtained depending on the pair of luminescence intensities considered. In the sequence, the introduction of Yb^{3+} together with Nd^{3+} is presented in order to check how this co-doping affects the thermal sensing.

4.3.1.2. Effect of Yb^{3+} co-doping

A series of YAM: Nd^{3+} - Yb^{3+} samples was produced using the modified Pechini method. The previously optimized Nd^{3+} concentration was kept constant at 0.83% mol whereas the Yb^{3+} amount varied across five different concentrations: 0.17, 0.50, 0.67, 1.00, and 1.50% mol. In **Table 12**, the molar percentage of Yb^{3+} corresponding to the chemical formulas are summarized.

Table 12. Concentration of Yb^{3+} in % mol in relation to all metals and the corresponding chemical formulas. The content of Nd^{3+} was set constant at 0.83% mol for all compounds.

$Y_4Al_2O_9$: Nd^{3+}-Yb^{3+}

Yb^{3+}				
0.17% mol	**0.50% mol**	**0.67% mol**	**1.00% mol**	**1.50% mol**
$Y_{3.94}Nd_{0.05}Yb_{0.01}Al_2O_9$	$Y_{3.92}Nd_{0.05}Yb_{0.03}Al_2O_9$	$Y_{3.91}Nd_{0.05}Yb_{0.04}Al_2O_9$	$Y_{3.89}Nd_{0.05}Yb_{0.06}Al_2O_9$	$Y_{3.86}Nd_{0.05}Yb_{0.09}Al_2O_9$

By examining the HR-XRD in **Figure 65.(a)**, the pure phase of YAM was obtained for all samples according to the reference PDF 04-013-3313, without any evidence of formation of other phases or contamination. According to the Le Bail fit method on the HR-XRD patterns (**Figure S5** in **Appendix**), a contraction of the unit cell is observed, indicated by the linear decrease of the cell parameters, as more Yb^{3+} ions replace yttrium (in perfect agreement with Vergad's law **Figure 65.(b)**) (see the exact values in **Table S3** in **Appendix**). The presence of Yb^{3+} tends to cause this type of contraction since its ionic radius is smaller than the ones of yttrium. When coordinated with six oxygens, the ionic radii of Yb^{3+} and Y^{3+} are 0.868 and 0.900 Å, respectively. In seven-fold coordination, these ionic radii are 0.925 Å for Yb^{3+} and 0.960 Å for Y^{3+}[128].

On the other hand, the dopants do not affect the average size of single crystal domains (Lc), as it remained constant at around 48 nm for all Nd^{3+} - Yb^{3+} concentrations (**Figure 65.(c)**). Additionally, the coherence length matches very well the size observed in FE-SEM images, indicating the formation of high quality single-crystals, similar to the Nd^{3+}-doped NCs presented earlier. As was the case for YAG: Nd^{3+}-Yb^{3+} and Y_2O_3: Nd^{3+}-Yb^{3+} synthesized by the modified Pechini method, the YAM NCs coalescence during the thermal treatment at high temperature, forming large agglomerates (**Figure 65.(d)**)

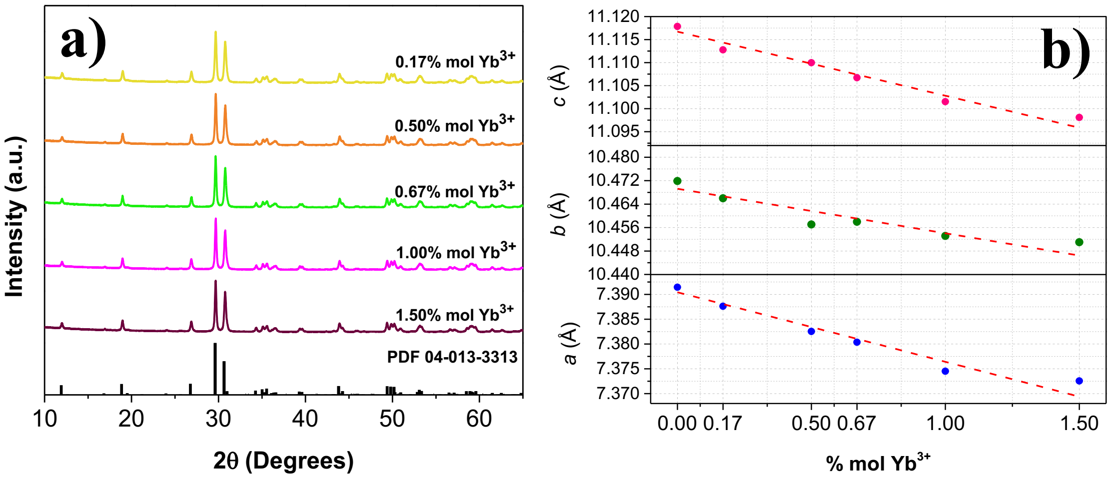

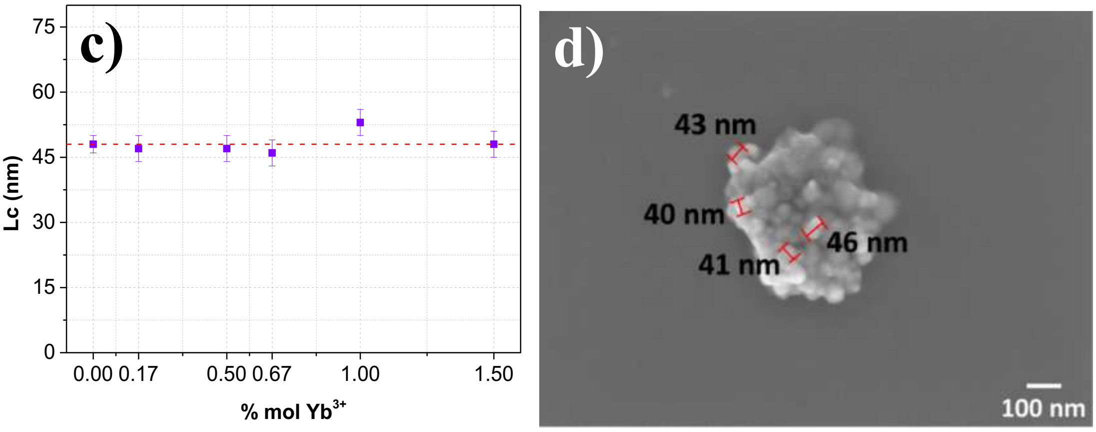

Figure 65. **(a)** HR-XRD of YAM doped with 0.83% mol Nd^{3+} and different concentrations of % mol Yb^{3+},**(b)** Evolution of cell parameters *a*, *b*, and *c* and **(c)** coherence length (Lc) with the Yb^{3+} concentration, **(d)** FE-SEM image of YAM: 0.83% mol Nd^{3+}, 0.17% mol Yb^{3+}.

Upon excitation at 808nm, the levels $^4F_{5/2}$, $^2H_{9/2}$ of Nd^{3+} are populated. This process is followed by a rapid non-radiative relaxation, which then populates the state $^4F_{3/2}$. From this excited level, radiative transitions of Nd^{3+} are observed in all samples in the ranges 860 – 950 nm ($^4F_{3/2} \rightarrow {}^4I_{9/2}$) and 1032 – 1140 nm ($^4F_{3/2} \rightarrow {}^4I_{11/2}$), besides the emission peaks in the range of 955 – 1032 nm ($^2F_{5/2} \rightarrow {}^2F_{7/2}$) from Yb^{3+} (**Figure 66.(a)**). Even for a low content of Yb^{3+}, the presence of its PL emission lines is clear evidence that Nd^{3+} transferred part of the harvested energy to Yb^{3+} non-radiatively, enabling its emission. The essential features of the kinetics of the Nd^{3+} - Yb^{3+} energy transfer can be illustrated by considering the simplified energy-level system depicted in **Figure 66.(b)**.

Overall, as more Yb^{3+} ions are inserted into the matrix, the lower is the contribution of Nd^{3+} in emission spectrum. Furthermore, the emission peaks are broad and become poorly resolved for higher Yb^{3+} content. This is because this Ln^{3+} can occupy any of the four crystallographic sites of yttrium in YAM and thus, presents transitions mediated by both electric-dipole induced and magnetic-dipole, as pointed out by Kaczkan et al.[44]. Moreover, the same study revealed that the energy positions of each Stark sublevel of the states $^2F_{5/2}$ and $^2F_{7/2}$ differ for each yttrium site. Bearing this in mind, Yb^{3+} located in different sites end up emitting at slightly different wavelengths, causing an overlap of several emissions and resulting in the broadening of the peaks.

The energy gap between the excited states $^4F_{3/2}$ and $^2F_{5/2}$ of Nd^{3+} and Yb^{3+}, respectively, varies according to where Yb^{3+} is located. As per the published literature[44,226], the lowest crystal field level of $^4F_{3/2}$ of Nd^{3+} is 11431 cm^{-1}, and the highest

Stark component of ${}^2F_{5/2}$ of Yb^{3+} varies from 10986 to 11255 cm^{-1}, so the energy mismatch extends from 176 to 445 cm^{-1}. Such values of energy mismatch indicate that the energy transfer $Nd^{3+} \rightarrow Yb^{3+}$ might be resonant, like in YAG: Nd^{3+} - Yb^{3+} and Y_2O_3: Nd^{3+} - Yb^{3+}. However, further investigation is necessary to confirm this, such as checking of the overlap between the emission and absorption spectra of YAM: Nd^{3+} and YAM: Yb^{3+}, respectively.

For the analysis of PL (T) and the evaluation of YAM: Nd^{3+}-Yb^{3+} NCs as a nanothermometer, the criteria adopted was to pick the sample that presented the highest PL integrated area. Therefore, based on the integrated PL intensities shown in **Figure 66.(c)**, the sample co-doped with 0.83% mol Nd^{3+} and the lower amount of Yb^{3+}, that is, 0.17% mol Yb^{3+}, was chosen. Note that this sample also exhibited better resolved PL peaks of both rare-earth ions

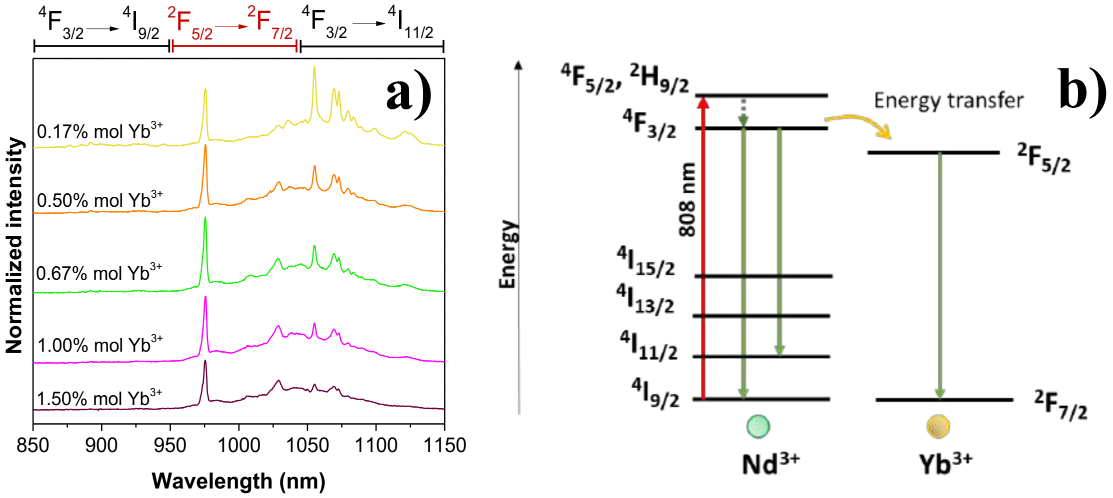

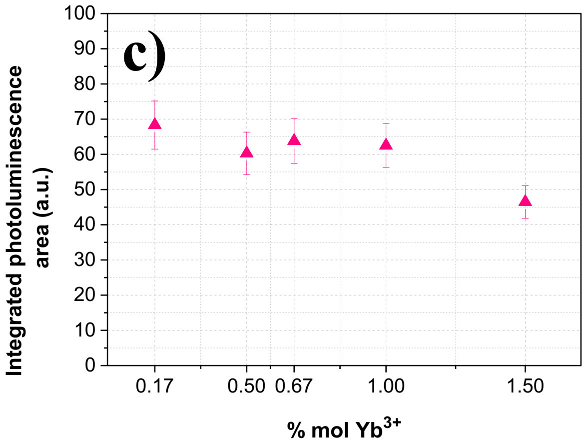

Figure 66.(a) PL emission spectra of YAM co-doped with 0.83% mol Nd^{3+} and different concentrations of % mol Yb^{3+}, **(b)** Simplified energy level scheme of Nd^{3+} and Yb^{3+}, **(c)** Integrated PL area as a function of % mol Yb^{3+}.

As displayed in **Figure 67.(a)**, there is gradual decrease in PL intensity of Nd^{3+} and Yb^{3+} emissions as temperature rises from 297.5K (ambient temperature) to 329.1 K. This can be induced by the intensification of the lattice vibration due to the temperature, which in turn enhances the lattice relation mode of the luminescent centers, thereby favoring the probability of non-radiative transitions. Conversely, the temperature may trigger an essential change of the state of the luminescent centers or their local surroundings, causing this general PL quenching [216]. To figure out which emission lines can be used to apply the LIR approach in nanothermometry, all the possibilities of ratio formed by a peak from Nd^{3+} over another one from Yb^{3+} were analyzed through the linear fitting of LIR (T) versus temperature, following the form LIR(T) = aT + b, with a and b as constants.

Two options of LIR composed of PL intensities from Nd^{3+} and Yb^{3+} come up with a good correlation of LIR with temperature: I_{1049}/I_{976} and I_{1049}/I_{1029}, where the emission peak at 1049 nm refers to Nd^{3+}, and the ones at 1029 nm and 976 nm derive from Yb^{3+}. Both fittings of LIR versus temperature provided R^2 above 0.985, as presented in **Figure 67.(b)** along with the corresponding calibration curves. These two luminescence ratios exhibit this thermal behavior because, although the Nd^{3+} and Yb^{3+} emissions decline with rising temperature, the thermal dependence of the PL intensity at 1049 nm is lower than the ones from Yb^{3+} at 976 nm and 1029 nm. Hence, this allows for Nd^{3+} intensity to serve as an internal reference to monitor Yb^{3+} emission according to the temperature.

Additionally, note that the thermal behavior of PL intensity at 1049 nm is opposite to what occurs in Nd^{3+} single-doped YAM; it reduces instead of rising when temperature is augmented. This is because the presence of Yb^{3+} suppresses the Boltzmann's equilibrium between the Stark sublevels of $^4F_{3/2}$ from Nd^{3+}. Indeed, by narrowing the analysis only to Nd^{3+} intensities, no pairs of Nd^{3+} radiative peaks resulted in LIR that correlates well with temperature, even when considering the same ratios for YAM: 0.83% mol Nd^{3+}.

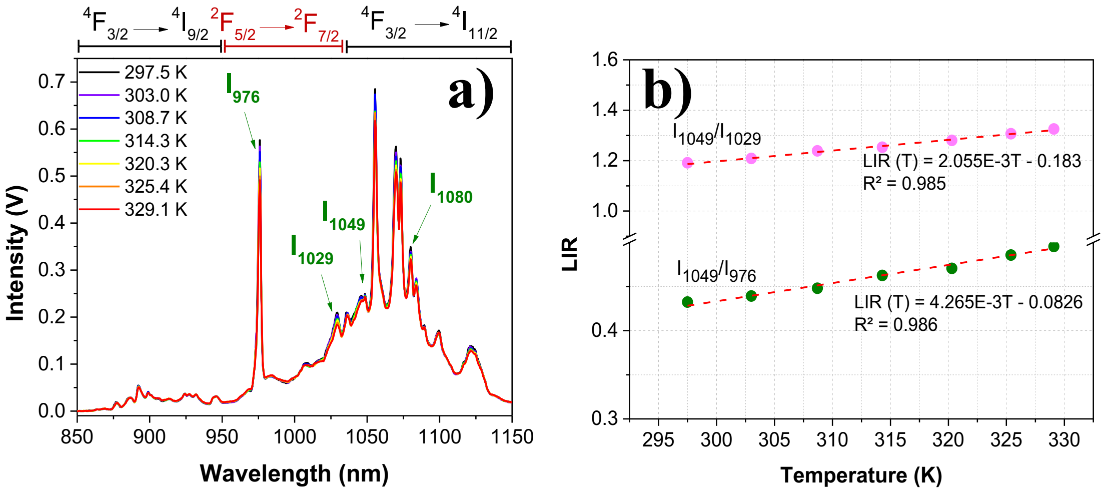

Figure 67. (a) PL(T) spectra of YAM: 0.83% mol Nd^{3+} and 0.17% mol Yb^{3+}, **(b)** LIR vs temperature for ratios I_{1049}/ I_{1029} and I_{1049}/I_{976}. The error bars of LIR are in the order of 10^{-3}, which are too small to show up in the figure.

Figure 68 shows the relative sensitivity to the temperature **(a),** and the thermal resolution **(b)** of YAM: Nd^{3+}-Yb^{3+} calculated by employing the two luminescence intensity ratios in $S_r = \frac{1}{LIR}\left|\frac{\partial LIR}{\partial T}\right|$ and $\delta T = \frac{1}{S_r}\left(\frac{\delta LIR}{LIR}\right)$, respectively. Better results are achieved if LIR is I_{1049}/I_{976}, with maximum Sr = 0.48%.K^{-1} at room temperature, and δT between 0.3 and 0.4 K across the established temperature range. Nonetheless, the maximum thermal sensitivity drops to 0.36%.K^{-1} whereas the thermal resolution fluctuates between 0.3 and 0.7 K for LIR I_{1049}/I_{1029}. Presumably, owing to the fact that Yb^{3+} can emit from different sites, causing the broadening of peaks, there might be an influence of one PL intensity on another one that reflects on the thermal efficiency. Additionally, the peak at 1029 nm is less intense than the one at 976 nm, exhibiting, thus, a lower signal-to-noise ratio, which contributes to high values of thermal resolution.

It is worth noting that the Sr did not improve with the presence of Yb^{3+} in the case of YAM, contrary to what occurs in other oxides, such as Y_2O_3, YAG, YBO_3 and

Y_3BO_4[57]. This observation is based on a study that employed the same strategy to select the content of Nd^{3+} and Yb^{3+}, similar emission peaks for LIR, and the same synthesis method [57]. As seen in the previous section, the maximum Sr of YAM: Nd^{3+} was found as 0.54%.K^{-1}, which is very close to Sr = 0.48%.K^{-1} when Yb^{3+} is embedded into YAM along with Nd^{3+}. However, the detailed treatment of the kinetics between Nd^{3+} and Yb^{3+} in YAM with the corresponding temperature dependence is complex. The strength of their coupling is very dependent upon the lattice sites of the two ions, and YAM possesses multiple different crystallographic sites, unveiling distinguished couplings for different Nd^{3+} - Yb^{3+} pairings. Therefore, for a better understanding of the dynamics between Nd^{3+} and Yb^{3+} in YAM and its influence in the efficiency in thermal sensing, further investigation is required.

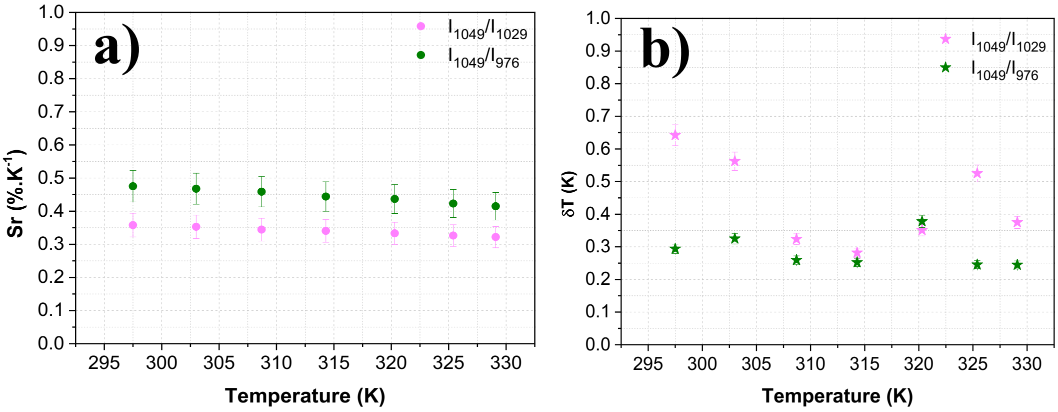

Figure 68. (a) Sr and **(b)** δT of YAM: 0.83% mol Nd^{3+}, 0.17% mol Yb^{3+} for LIR of I_{1049}/I_{1029} (pink symbols) and I_{1049}/I_{976} (dark green symbols).

4.3.2. The two-step urea-based route: an alternative way of synthesizing YAM nanocrystals

As reported in previously published research, nanosized YAM particles can be produced by different routes, among which the sol-gel procedure is mainly implemented[211,213,219,226–228]. In this section, a novel method to obtain YAM NCs is proposed, based on the analogous two-step process presented for Y_2O_3 in **Chapter III**, **section 3.2.1.2**. To recall it, the process is divided into two parts: the synthesis of an amorphous phase under solvothermal conditions and a final heat treatment. For YAM, the first step concerns the reaction of anions CO_3^{2-} and OH^-, produced by the decomposition of urea under controlled temperature (70°C ~ 90°C), with Y^{3+} and Al^{3+} cations, resulting from the hydrolysis of yttrium nitrate and aluminum nitrate, respectively. The as-obtained product is then heat-treated above crystallization temperature of YAM, which is around 800°C [245].

For the first step, some experiments were run by changing the precursor quantities (urea, yttrium, and aluminum), reaction temperature, and the inclusion of 1,4-butanediol as an organic co-solvent to verify which effect these parameters would have on the characteristics of the as-obtained product. No dopants were considered primarily, and the tested conditions are summarized in **Table 13**. Apart from them, it was also tested to adjust the pH of the reactant solution before going through the solvothermal synthesis. It was noted that the solution containing only yttrium and urea presented a pH of 5.6, but it dropped to 3.6 ~3.8 when aluminum was included. So, conditions 7 and 8 of **Table 13** were applied in another round with the pH adjustment to 6.0 ~7.2, by adding an aqueous solution of NH_3.

Table 13. Conditions tested to synthesize YAM through the two-step urea-based process.

Condition	**Urea (mol.L^{-1})**	**$Y(NO_3)_3.6H_2O$ (mmol.L^{-1})**	**$Al(NO_3)_3.6H_2O$ (mmol.L^{-1})**	**Reaction temperature (°C)**	**1,4-butanediol (% vol.)**
1	0.05	7.50	3.75	70	30
2	0.10	2.50	1.25	80	80
3	0.20	2.50	1.25	80	80
4	0.20	7.50	3.75	70	50
5	0.20	7.50	3.75	80	0
6	0.20	7.50	3.75	80	50
7	0.20	7.50	3.75	85	50
8	0.20	7.50	3.75	85	80
9	0.50	7.50	3.75	85	80

Despite all the modifications of the experimental conditions, the as-obtained product always exhibited an amorphous nature. Taking condition 9 of **Table 13** as an example, this is confirmed by the XRD shown in **Figure 69.(a)**. Moreover, the morphology resembling a continuous and interconnected network of NPs was also observed for all as-obtained samples. Note that this morphology is quite distinct from the amorphous as-obtained product for yttria case ($Y(OH)CO_3.H_2O$), as depicted in **Figure 47.(b)** in **Chapter III**. However, the primary particle of a few nanometers in size appears less interconnected when 50% in volume of 1,4-butanediol is added to the reactant solution while the other synthesis parameters are kept constant. One finds the FE-SEM image for 0% (condition 5 in **Table 13**) and 50% vol. of 1,4-butanediol (condition 6 in **Table 13**) in **Figure 69.(b)** and **(c)**, respectively. This change comes from the ligand effect and the high viscosity of 1,4-butanediol as previously discussed in **section 3.3.3.1** in **Chapter III** for yttria synthesis. By introducing more 1,4-butanediol (80% in volume), using more precursor quantities, and conducting the solvothermal synthesis at 85°C (condition 9 in **Table 13**), the morphology of the as-obtained sample presents even less agglomerated primary particles among all samples (**Figure 69.(d)**). Hence, in the continuity of this study, the condition 9 was adopted for doping with 0.83% mol of Nd^{3+} — the concentration that provided the highest PL emission based on the modified Pechini synthesis — and posterior heat treatment at 1000°C for 1 hour under O_2 flux for YAM crystallization.

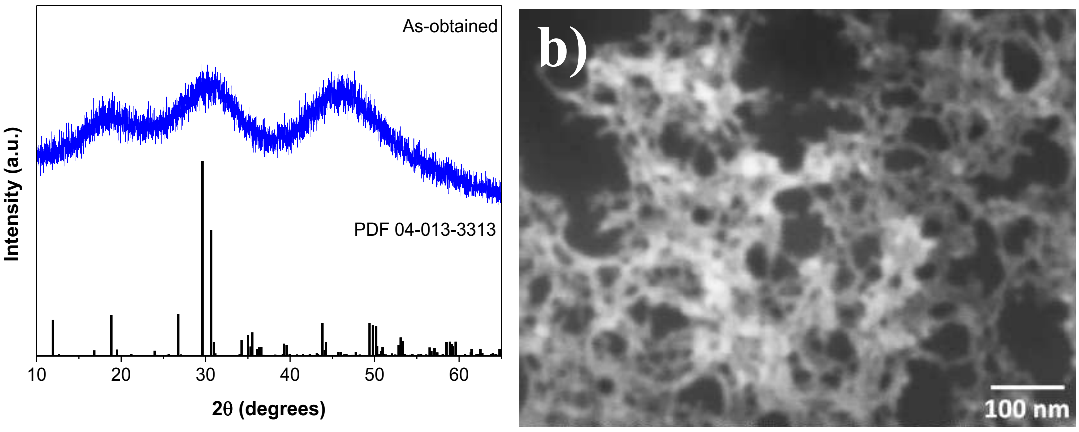

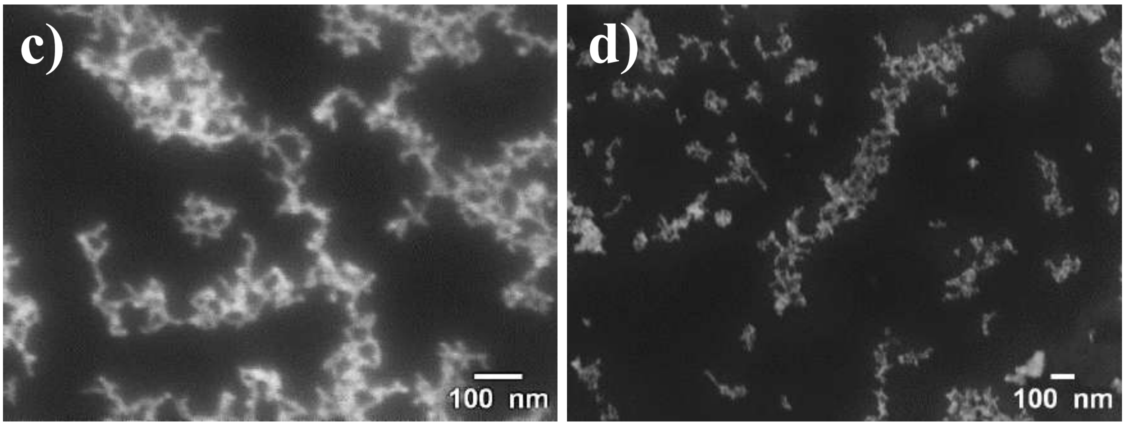

Figure 69. (a) XRD, and FE-SEM images of the amorphous as-obtained product for **(b)** 0, **(c)** 50, and **(d)** 80% in vol. of 1,4-butanediol as co-solvent.

According to the indexation of HR-XRD to the reference PDF 04-013-3313, pure YAM was yielded after calcining the as-obtained amorphous sample (condition 9) at 1000°C/1h, without any traces of secondary phases (**Figure 70.(a)**). The cell parameters along with the coherence length were estimated through the Le Bail Fit on the HR-XRD and are tabulated in **Table 14**. The values corresponding to the cell parameters are comparable to the ones calculated for YAM synthesized by the modified Pechini method with the same doping content (see **Table S2** in **Appendix**).

Figure 70.(b) presents the TEM image of YAM: Nd^{3+}, revealing NCs, but with some degree of agglomeration owing to the high-temperature heat treatment. The size, estimated from over 130 particles across different TEM images, averages 38 ± 10 nm, which closely aligns with Lc = 36 ± 1 nm (**Figure 70.(c)**). In addition, the HR-TEM highlights the sample's excellent crystallinity, showcasing the (122) crystallographic planes corresponding to the most intense peak at 29.62° in the X-ray diffraction pattern. These findings clearly demonstrate the high crystal quality of YAM NCs synthesized via the two-step urea-based route.

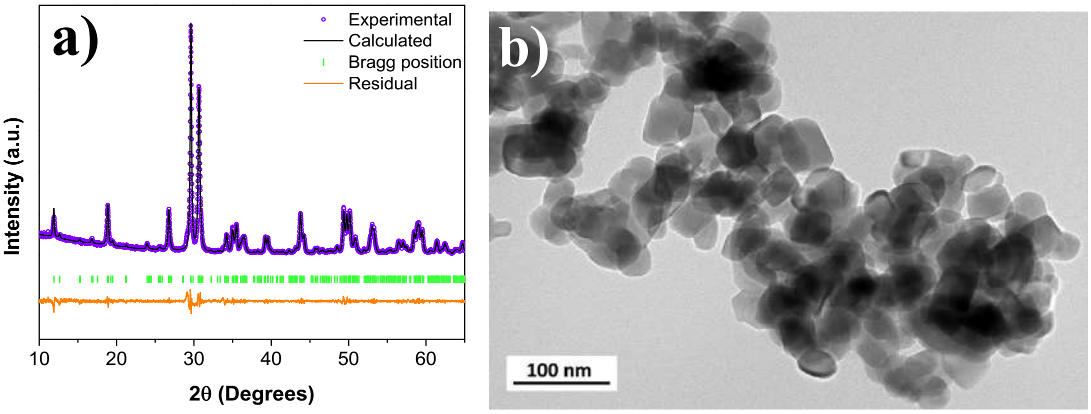

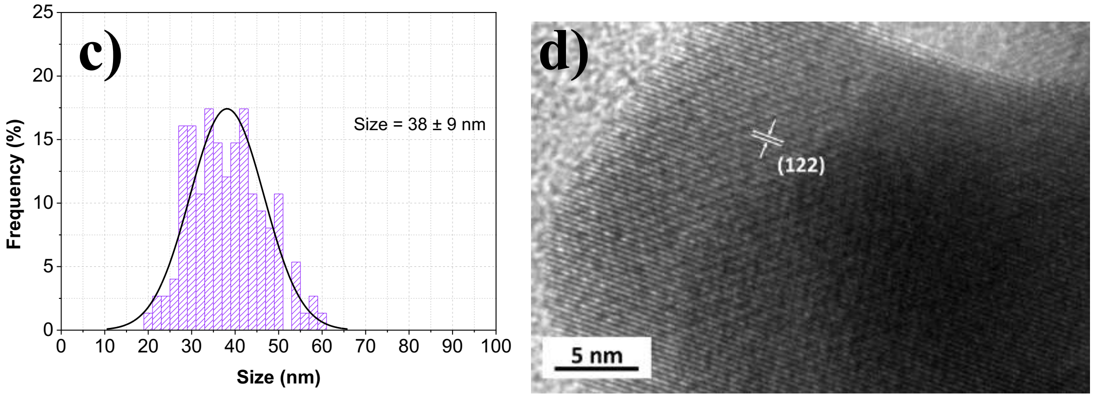

Figure 70.(a) HR-XRD, **(b)** TEM, **(c)** size distribution of NCs based on TEM, and **(d)** HR-TEM of YAM: 0.83% mol Nd^{3+} synthesized by the two-step urea-based route.

Table 14. Cell parameters and coherence length estimated through the Le Bail fit of HR-XRD of YAM: 0.83% mol Nd^{3+} synthesized by the two-step urea-based route.

Material	***a* (Å)**	***b* (Å)**	***c* (Å)**	**Volume (Å³)**	**Lc (nm)**	**χ^2**	**Rp (%)**	**Rwp (%)**
YAM: 0.83% mol Nd^{3+}	7.394	10.467	11.117	814.12	36 ± 1	2.06	9.95	119
Ref.[246]	7.375	10.462	11.110	812.59	-	-	-	-

The FTIR analysis was performed on the samples before and after the annealing, and the associated spectra are found in **Figure 71**. The as-obtained material exhibits characteristic bands related to deformation vibrations (670 – 850 cm^{-1}), symmetric (985 – 1200 cm^{-1}) and asymmetric stretching (1350 – 1530 cm^{-1}) of C-O linkages, as well as the stretching mode of C-H linkages (2873 and 2946 cm^{-1}) and hydroxyl groups (above 3000 cm^{-1}) [89,187,188]. After the heat treatment at 1000°C, the peaks related to Y-O at 513, 559, and 715 cm^{-1} and Al-O bonds at 607 and 792 – 902 cm^{-1} emerged whereas the asymmetric stretching mode of C-O did not disappear completely [147,235,245]. The OH band is still present, but at lower intensity, due to the moisture absorption on the nanopowder. Although crystalline NCs were obtained with the calcination at 1000°C/1h, the complete removal of organic residues could be done by prolonging thermal treatment.

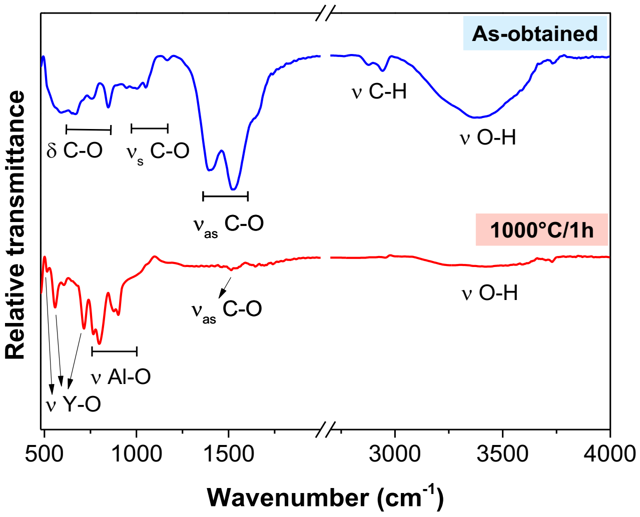

Figure 71. FTIR spectra of as-obtained sample (blue curve) and after calcination at 1000°C/1h (red curve).

Lastly, the PL emission spectrum was recorded under excitation at 808 nm and is shown as a blue curve in **Figure 72**. Upon this excitation, Nd^{3+} ions are promoted from the ground state $^4I_{9/2}$ to the excited states $^4F_{5/2}$, $^2H_{9/2}$. After a fast non-radiative transition, the excited level $^4F_{3/2}$ is then populated. Then, the radiative transitions $^4F_{3/2} \rightarrow {}^4I_{9/2}$ and $^4F_{3/2} \rightarrow {}^4I_{11/2}$ occur in the wavelength ranges of 860 - 950 nm and 1020 - 1140 nm, respectively. Notably, the PL intensity is 3.6-fold less intense when compared to that of YAM: 0.83% Nd^{3+} obtained via the modified Pechini method (orange curve). Possibly, this occurred due to the presence of OH groups, remaining organics, and surface defects. More optimization of the two-step urea-based route to produce YAM NCs is certainly needed, but exploring it paved the way for an alternative method to obtain this phase.

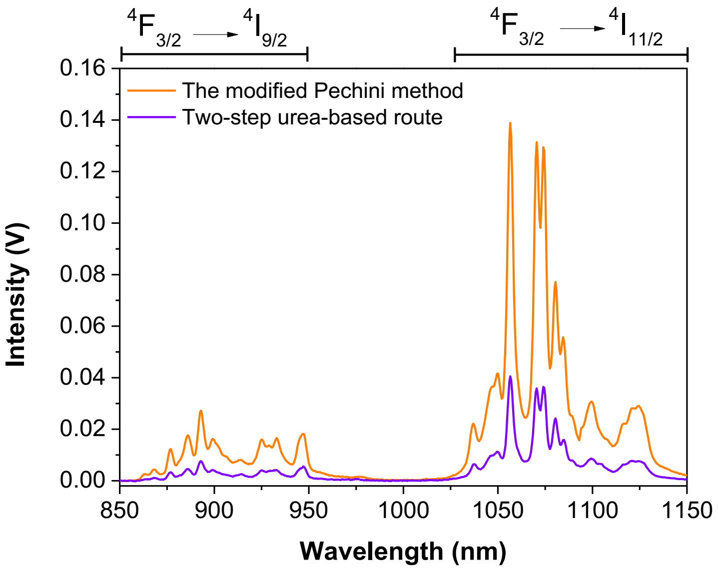

Figure 72. PL emission spectra of YAM: 0.83% mol Nd^{3+} synthesized by the modified Pechini method compared to the one obtained through the two-step urea-based route.

4.4 General remarks and perspectives

In recap, the objective of this chapter was to present an overview of YAM NCs doped with Nd^{3+} and co-doped with Nd^{3+} and Yb^{3+} for nanothermometry. The study initiated with the modified Pechini syntheses of YAM NCs single doped with different concentrations of Nd^{3+}, and a detailed investigation of the structural and optical properties as a function of doping amount was carried out. It was also determined that the optimal doping concentration that yielded the highest PL emission was 0.83% mol. When Nd^{3+} ions are inserted into the YAM crystal structure, they exhibit TCLs that follow Boltzmann's law, allowing temperature monitoring with luminescence emissions. From the LIR technique involving radiative peaks at 1049 nm and 1080 nm, a maximum Sr of 0.54%. K^{-1} is achieved at room temperature, with δT around 0.2 ~ 0.5 K and repeatability of 97.1%. The study advanced with the introduction of Yb^{3+} in different concentrations alongside 0.83% mol Nd^{3+}. By selecting the lowest concentration of 0.17% mol of Yb^{3+}, the material presented Sr of 0.48%. K^{-1} at ambient temperature, and δT varying between 0.3 and 0.4 K. Hence, the co-doping with Yb^{3+} did not enhance the Sr, as it occurred for other oxide matrices reported in the literature [57].

Finally, a new method for producing YAM NCs of around 40 nm was presented. It was used a similar protocol of the two-step urea-based route for yttrium oxide. Some parameters regarding precursor concentration, reaction temperature and pH were tested, and the structural and optical characterization of YAM obtained by this route was depicted.

For future works, some suggestions can be brought up in view of enhancing YAM properties for nanothermometry. First, to perform co-doping engineering, that is, try out different concentrations of both Nd^{3+} and Yb^{3+} simultaneously. This is an interesting test that can tailor the features of YAM: Nd^{3+} - Yb^{3+}, including both the PL intensity and thermal performance. On account of the outcomes attained here, the concentration ranges should be 0.50 to 1.00% mol for Nd^{3+}, and 0.17 to 1.00% mol for Yb^{3+}.

Second, regarding the two-step urea-based method for YAM, more experiments are required to achieve better cost-effectiveness of the synthesis and to attempt to avoid NC agglomeration. Some propositions are to test the reaction time, other types of organic co-solvents (e.g. DEG), and different calcination conditions (temperature, rate, duration, intermediate heat treatment at lower temperature). It is also worth checking the thermal dependence of PL spectrum of YAM: 0.83% mol Nd^{3+}, so that it can be compared with the sample produced by the modified Pechni method. Consequently, this would provide an evaluation of the effect of the synthesis route on the figures of merit in nanothermometry — Sr, δT, and repeatability — for YAM: 0.83% mol Nd^{3+}.

Third, the PL lifetime approach should be tested for thermal sensing. With this method, the PL lifetime decay of a single peak is monitored according to its dependence on temperature. YAM doped with Nd^{3+} and co-doped with Nd^{3+} and Yb^{3+} displayed several emission peaks that evolve well with temperature, including a very high and narrow emission intensity at 1055 nm, whose LIR formed with any other peak did not provide a calibration curve based on the LIR approach. Therefore, the lifetime approach might yield more insightful results compared to the LIR method [14,16].

Lastly, embedding other rare-earth ions in YAM should be definitely explored, aiming at nanothermometry applications other than in biological field. Owing to its crystalline structure, YAM offers numerous possibilities for Ln^{3+} accommodation, which permits diverse combinations that can culminate in promising technological utilities. The literature about the temperature dependence of Ln^{3+}-YAM is still quite scarce, so there is room for further investigation.

Conclusions & Future outlooks

This thesis elucidated the advancements in the development of luminescent nanothermometers based on the inorganic oxide matrices YAG, Y_2O_3, and YAM co-doped with Nd^{3+} and Yb^{3+}. It targeted the synthesis of thermal probes that attended three major requirements towards an accurate temperature measurement, with adequate features for posterior applications in the biological domain: 1) intense PL emission, 2) nanometric dimension, with narrow size distribution and good dispersion, and 3) efficient performance in gauging the temperature (high Sr and excellent δT). The strategies to achieve these goals brought in the appropriate selection of both Nd^{3+} and Yb^{3+} concentrations (co-doping engineering), and the synthesis from solution with particle size control and crystallinity enhancement.

Concerning the ability of emitting intense photoluminescence, **Figure 73** shows how YAG stands out relative to Y_2O_3, when each is co-doped with the concentrations of Nd^{3+} and Yb^{3+} that provides their optimal PL emissions from the study of the modified Pechini syntheses (0.75% mol Nd^{3+} and 0.50% mol Yb^{3+} for YAG and 1.00% mol Nd^{3+} and 0.50% mol Yb^{3+} for Y_2O_3). Although both hosts present cubic structure, YAG exhibits a single Y^{3+} site with D_2 symmetry whereas Y_2O_3 has two different ones (C_2 and C_{3i} symmetries). This feature presumably favors a more uniform distribution of the Ln^{3+} in YAG than in Y_2O_3, lowering the probability of non-radiative processes of Nd^{3+} and enhancing the energy transfer $Nd^{3+} \rightarrow Yb^{3+}$. On the other hand, YAM: Nd^{3+}-Yb^{3+} presented the lowest PL emission among the three oxides in this study when 0.83% mol Nd^{3+} and 0.17% mol Yb^{3+} are used, but it should be adopted the same strategy of co-doping engineering of YAG and Y_2O_3 for YAM for a fairer comparison. Even so, YAM: Nd^{3+}-Yb^{3+} exhibited broader PL emission spectrum due to the strong crystal field strength that led to a greater perturbation of the electronic states, causing a larger splitting of the energy levels. Besides, YAM has four Y^{3+} sites with very low symmetry (C_1), and it is known that Yb^{3+} ions can occupy all of them, but further study is required to understand how Nd^{3+} ions accommodate in YAM structure. In this regard, Nd^{3+}-Yb^{3+} co-doped YAG has an advantage, as it not only presents the highest PL emission, but also more distinguishable (better resolved) PL peaks, which is essential for accurate nanothermometry analysis.

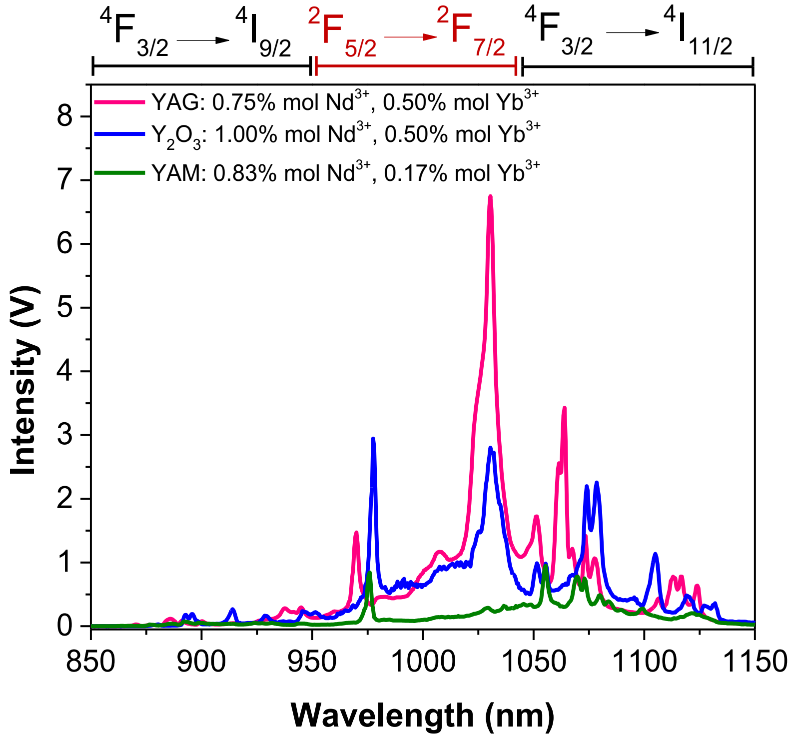

Figure 73. PL emission spectra of YAG: 0.75% mol Nd^{3+}, 0.50% mol Yb^{3+}, Y_2O_3: 1.00% mol Nd^{3+}, 0.50% mol Yb^{3+}, and YAM: 0.83% mol Nd^{3+}, 0.17% mol Yb^{3+}. All three oxides were synthesized via the modified Pechini method, and the corresponding spectra were acquired under the same conditions.

The intensity of the PL emission was also crucial in tailoring the size of the NCs. The optimization of solvothermal synthesis with the addition of only 0.50% in volume of DEG provided NCs of YAG: 0.75% mol Nd^{3+}, 0.50% mol Yb^{3+} as small as 23 ± 10 nm with narrow size distribution (PDI = 0.05). By coating them with a silica layer of 17± 10 nm, a protected annealing at 850°C for 1 hour promoted the removal of organic moieties without causing the coalescence of the NCs, which allowed the enhancement of PL emissions in 5.2-fold of Nd^{3+} and 21-fold of Yb^{3+}. Optimizations regarding the experiments of silica-coating are still needed before moving to the functionalization step (e.g. PEGylation) and experimental assays in biology. This includes inducing a porosity-free shell, with thinner thickness, and avoiding multiple NC cores being involved by the same layer in order to modulate the final NP size and eliminate completely the interaction of OH groups with the luminescent centers. Adjustments in the biphasic procedure can be tested, such as the quantity of silica precursor and NCs to be coated, but also growing undoped YAG layer as protective shell around YAG: Nd^{3+}, Yb^{3+} NCs by the solvothermal method should not be discarded.

The two-step urea-based route enabled the synthesis of Y_2O_3: 1.00% mol Nd^{3+}, 0.50% mol Yb^{3+} NCs with dimensions of 22 ± 10 nm, owing to the groundbreaking use of 1,4-butanediol as an organic co-solvent in the precursor solution and the calcination step with NaCl as a separating media. Pure yttria NCs were obtained, but some pitfalls still prevailed: incomplete crystallization, partial removal of organic moieties, and some degree of agglomeration — though it reduced compared to when no NaCl-matrix is applied during the heat treatment. It resulted in less intense PL emission in comparison with a sample obtained through the modified Pechini method with the same composition of dopants. The calcination of the two-step urea-based route needs a few modifications to prevent agglomeration and allow the complete crystallization of Y_2O_3: Nd^{3+}, Yb^{3+} NCs, so that the PL emissions of Nd^{3+} and Yb^{3+} can be improved. This can be done by either trying excess of NaCl or changing to another type of separating media with a higher melting point, such as K_2SO_4. Still regarding the two-step urea-based route, this provided pure YAM NCs successfully by just including an aluminum source in respect of the procedure applied for Y_2O_3. Differences in morphology were observed when compared to Y_2O_3 NCs, and agglomerated YAM NCs were also obtained, but the primary results of this study open up perspectives for a new method of synthesizing this aluminate oxide.

The synthesis methods of both Nd^{3+}-Yb^{3+} co-activated YAG and Y_2O_3 NCs did not affect their thermal performance. Moreover, YAG: 0.75% mol Nd^{3+}, 0.50% mol Yb^{3+} NCs demonstrated once again to be a more promising luminescent nanothermometer with Sr of 0.60%.K^{-1} and an excellent δT of 0.2 K at physiological temperature (around 309 K) when the LIR approach is employed with PL peaks at 1030 nm (Yb^{3+}) and 1063 nm (Nd^{3+}). In contrast, Y_2O_3: 1.00% mol Nd^{3+}, 0.50% mol Yb^{3+} exhibited a comparable sensitivity to thermal changes for LIR between PL peaks at 1030 nm (Yb^{3+}) and 1055 nm (Nd^{3+}), with Sr of 0.52%. K^{-1}, but a much worse thermal resolution of 0.4 K, considering the body temperature too. The simple crystalline structure combined with the high signal-to-noise ratio of PL emission intensity led YAG: Nd^{3+}-Yb^{3+} NCs to possess an efficient performance in light of the nanothermometry. However, these results are based on powdered samples. When conducting nanothermometry tests in aqueous solution, YAG: 0.75% mol Nd^{3+}, 0.50% mol Yb^{3+} NCs kept showing a similar Sr (0.51%. K^{-1}), but their ability to detect small temperatures increased from 0.2 to 0.6 K at physiological temperature. The OH groups from the aqueous solution lodged inside the pores of the silica shell and caused the PL quenching of the luminescent ions, which made the PL signal noisier and hence, worsened the thermal resolution. This issue can be mitigated by modifying the core-shell procedure as previously described.

YAM: 0.83% mol Nd^{3+}, 0.17% mol Yb^{3+} NCs presented Sr of 0.38%.K^{-1} and a δT no lower than 0.28 K at body temperature, for LIR formed by PL peaks at 1049 nm (Nd^{3+}) and 1029 nm (Yb^{3+}). These values are improved if Yb^{3+} emission at 979 nm, which is outside the BWs, is considered instead: Sr = 0.48%. K^{-1} and δT = 0.3 K at physiological temperature. Nevertheless, by single-doping YAM with 0.83% mol Nd^{3+}, δT remains practically the same at 0.3 K, but a better Sr of 0.50%. K^{-1} is accomplished at 309 K for LIR between the TCLs at 1049 nm and 1080 nm. Even if the effect of Yb^{3+} in YAM did not favor its thermal sensing performance, YAM has good covalent nature of its metal-oxygen bonds, that benefits the energy separation of TCLs when single-doped with Nd^{3+}, thereby influencing positively the Sr. Lastly, due to the scarce quantity of works on YAM in the literature, it would be interesting to explore this host matrix with other rare-earth ions.

Therefore, the outcomes from both syntheses and nanothermometry tests showed Nd^{3+}-Yb^{3+} co-doped YAG has a more prospective potential for posterior applications in the biological field among the host matrices studied herein: the synthesis method for individual NCs is at a more advanced stage, the PL emission is more intense, and the thermal sensing properties are better. Besides, this thesis demonstrated that not only individual NCs must be produced, but it is crucial they are also shielded from the interaction with typical PL quenchers, such as organic and OH molecules. Finally, it is of utmost importance that the experimental conditions of nanothermometry analysis are always defined carefully, since instrumental interferences, especially readout artifacts, can give rise to biased results, and compromise reproducibility of the thermal measurements.

In the continuity of this work, a few suggestions can be made aside from those presented throughout this text. First, to perform an elemental chemical mapping analysis under high-angle annular dark-field-scanning transmission electron microscopy (HAAD-STEM) to ensure accurate determination of the distribution of the elements in the NCs. Also, lifetime measurements, which was not possible in this thesis due to the lack of suitable equipment. This type of analysis would certainly bring a clearer insight about the dynamics of the doping Ln^{3+}, for example to calculate the efficiency of the energy transfer

$Nd^{3+} \rightarrow Yb^{3+}$ and mainly, to determine the existence or not of back energy transfer $Yb^{3+} \rightarrow Nd^{3+}$ for a specific chemical composition and induced by changes of temperature. The lifetime as a function of the temperature would not only provide a deeper understanding about the thermal dependency of the PL peaks but also enable to employ the lifetime-based nanothermometry to obtain the calibration curve and calculate the figures of merit: Sr, δT, and repeatability. Then, evaluate whether better results are achieved with this technique or with LIR approach, especially of Y_2O_3 and YAM co-doped with Nd^{3+} and Yb^{3+}. Although the lifetime nanothermometry requires more sophisticated instrument than those used for LIR nanothermometry, it allows the monitoring of a single PL emission without the need of recording the full PL spectrum, sensitive lifetime-based nanothermometers with Nd^{3+} and Yb^{3+} have already been reported, and reliable *in vivo* thermal measurements can be accomplished with this technique [14,16,18,26].

Second, to conduct experiments of core-shell engineering. Such procedure allows to construct NPs with several layers, which can be inert or active. The luminescent ions can be confined in different volumes to protect them from surface defects, interaction with OH groups, ligands, and solvent molecules, leading to the enhancement of the PL quantum yield. Additionally, combining this core-shell architecture with the lifetime nanothermometry can provide more sensitive nanothermometers to temperature changes. Namely, Hamraoui and co-workers[247] succeeded in improving the Sr of α-$NaYF_4$@$NaYF_4$: Nd^{3+} - Yb^{3+} from 0.25%.°C^{-1} to 1.11%.°C^{-1} by coating the NPs with another layer of CaF_2.

Third, to explore the multiple doping with other Ln^{3+} along with Nd^{3+} and Yb^{3+} ions. Testing Nd^{3+} and Yb^{3+} with other rare-earth ions, such as Er^{3+}, Ho^{3+} and Tm^{3+}, allows to explore the PL emissions in different BWs for nanothermometry [15,20]. In triple-doped system, Yb^{3+} can act as energy-transfer intermediary between Nd^{3+} (energy harvester under 808-nm excitation) and Er^{3+}, Ho^{3+} and Tm^{3+}(acceptors) [36,248]. The additional doping ions can also play the role of overcoming some issues, such as eliminating the back energy transfer $Yb^{3+} \rightarrow Nd^{3+}$, and allowing the increase of the thermal sensitivity, as was the case of SrF_2 co-doped with Nd^{3+}, Yb^{3+}, Er^{3+} and Tm^{3+} reported by Cortelletti and co-workers [249]. However, the inclusion of other elements can cause the local symmetry distortion and consequently, tune the luminescence properties of the activated luminescent centers, for example with the replacement of some Y^{3+} by Gd^{3+} ions[250,251]. In any case, it is noteworthy to mention that the engineering of both core-shell architecture (e.g. insert different doping ions in the layers) and co-doping composition is crucial when working with several types of doping ions, as it is necessary to play on the distances among them to tailor their paths of energy transfer.

Fourth, to assess the thermal sensing performance and extract the calibration curves of the nanoprobe in solutions, especially in physiological medium, with mimicking conditions of the destined environment it will be used. It is important to provide an efficient set-up that isolates the solution from the environment to avoid the influence of external factors and ascertain a refined control of the temperature for stable PL(T) measurements.

Lastly, to perform the tests in the biological context, such as *ex vivo*, *in vitro* and *in vivo*, to evaluate the potential of the Nd^{3+} - Yb^{3+} co-doped YAG nanothermometers under real conditions. The work of Bednarkiewicz et al.[16] serves as a good guideline for both *in vitro* and *in vivo* tests. Particularly, cytotoxicity *in vitro* assays are important to be conducted to evaluate the risks of toxicity associated with the size of the NPs. Smaller particles tend to produce more Reactive Oxygen Species (ROS) per unit surface area, leading to oxidative stress and subsequent cellular damage and death [102].

Although the journey towards the final application is still a long one, each stage of the development of a nanothermometer requires meticulous attention from the outset — a critical point emphasized throughout this thesis.

Bibliography

1. Vallerini Barbosa I. *Nanocristaux Oxydes Luminescents Pour Le Développement de Nanosondes de Température in Vivo*. Université Grenoble Alpes et Universidade federal de Goiás; 2023. http://www.theses.fr/2023GRALI125/document

2. Cantarano A. *Nanocristaux de Grenat Pour l'éclairage Blanc Par LED et Pour La Nanothermométrie*. Université Grenoble Alpes. Accessed September 4, 2023. https://theses.hal.science/tel-03412252

3. Pereira Guimarães BM, da Silva Fernandes CM, Amaral de Figueiredo D, Correia Pereira da Silva FS, Macedo Miranda MG. Cutting temperature measurement and prediction in machining processes: comprehensive review and future perspectives. *International Journal of Advanced Manufacturing Technology*. 2022;120(5-6):2849-2878. doi:10.1007/s00170-022-08957-z

4. Merlone A. Thermal metrology for climate: A review of projects, activities and open issues. *Meas Sci Technol*. 2021;32(10). doi:10.1088/1361-6501/abf375

5. Gowen AA, Tiwari BK, Cullen PJ, McDonnell K, O'Donnell CP. Applications of thermal imaging in food quality and safety assessment. *Trends Food Sci Technol*. 2010;21(4):190-200. doi:10.1016/j.tifs.2009.12.002

6. Hymczak H, Gołąb A, Mendrala K, et al. Core temperature measurement—principles of correct measurement, problems, and complications. *Int J Environ Res Public Health*. 2021;18(20). doi:10.3390/ijerph182010606

7. Wartzek T, Jens M, Imhoff M. Temperature measurement. *Biomedizinische Technik*. 2011;56(5):241-257. doi:10.1515/BMT.2011.108

8. Mashekova A, Zhao Y, Ng EYK, Zarikas V, Fok SC, Mukhmetov O. Early detection of the breast cancer using infrared technology – A comprehensive review. *Thermal Science and Engineering Progress*. 2022;27. doi:10.1016/j.tsep.2021.101142

9. Wang H, Wang B, Normoyle KP, et al. Brain temperature and its fundamental properties: A review for clinical neuroscientists. *Front Neurosci*. 2014;8(SEP). doi:10.3389/fnins.2014.00307

10. Gavriloaia G V., Hurduc A, Ghimigean AM, Fumarel R. Spatial-temperature high-resolution map for early cancer diagnosis. In: *Multimodal Biomedical Imaging IV*. Vol 7171. SPIE; 2009:71710W. doi:10.1117/12.809185

11. Toutouzas K, Drakopoulou M, Markou V, et al. *Increased Coronary Sinus Blood Temperature: Correlation with Systemic Inflammation*. Vol 36.; 2006.

12. Całkosiński I, Dobrzyński M, Rosińczuk J, et al. The use of infrared thermography as a rapid, quantitative, and noninvasive method for evaluation of inflammation response in different anatomical regions of rats. *Biomed Res Int*. 2015;2015. doi:10.1155/2015/972535

13. Wust P, Hildebrandt B, Sreenivasa G, et al. Hyperthermia in cancer treatment. *Lancet Oncol*. 2002;3(8):487-497. doi:https://doi.org/10.1016/S1470-2045(02)00818-5

14. Brites CDS, Millán A, Carlos LD. Lanthanides in Luminescent Thermometry. In: *Handbook on the Physics and Chemistry of Rare Earths*. Vol 49. Elsevier B.V.; 2016:339-427. doi:10.1016/bs.hpcre.2016.03.005

15. Nexha A, Carvajal JJ, Pujol MC, Díaz F, Aguiló M. Lanthanide doped luminescence nanothermometers in the biological windows: Strategies and applications. *Nanoscale*. 2021;13(17):7913-7987. doi:10.1039/d0nr09150b

16. Bednarkiewicz A, Marciniak L, Carlos LD, Jaque D. Standardizing luminescence nanothermometry for biomedical applications. *Nanoscale*. 2020;12(27):14405-14421. doi:10.1039/d0nr03568h

17. Jaque D, Vetrone F. Luminescence nanothermometry. *Nanoscale*. 2012;4(15):4301-4326. doi:10.1039/c2nr30764b

18. Brites CDS, Marin R, Suta M, et al. Spotlight on Luminescence Thermometry: Basics, Challenges, and Cutting-Edge Applications. *Advanced Materials*. 2023;35(36). doi:10.1002/adma.202302749

19. Marciniak L, Kniec K, Elżbieciak-Piecka K, Trejgis K, Stefanska J, Dramićanin M. Luminescence thermometry with transition metal ions. A review. *Coord Chem Rev*. 2022;469. doi:10.1016/j.ccr.2022.214671

20. Đačanin Far L, Dramićanin MD. Luminescence Thermometry with Nanoparticles: A Review. *Nanomaterials*. 2023;13(21). doi:10.3390/nano13212904

21. Harrington B, Ye Z, Signor L, Pickel AD. Luminescence Thermometry Beyond the Biological Realm. *ACS Nanoscience Au*. 2024;4(1):30-61. doi:10.1021/acsnanoscienceau.3c00051

22. Puccini A, Liu N, Hemmer E. Lanthanide-based nanomaterials for temperature sensing in the near-infrared spectral region: illuminating progress and challenges. *Nanoscale*. 2024;16(23):10975-10993. doi:10.1039/d4nr00307a

23. Van Uitert LG, Johnson LF. Energy transfer between rare-earth ions. *J Chem Phys*. 1966;44(9):3514-3522. doi:10.1063/1.1727258

24. Bettineli M. Non-Resonant Energy Transfer between Inorganic Ions in Solids. In: Flint C, ed. *Vibronic Processes in Inorganic Chemistry*. Kluwer Academic Publishers; 1989:347-369.

25. Jia M, Fu Z, Liu G, et al. NIR-II/III Luminescence Ratiometric Nanothermometry with Phonon-Tuned Sensitivity. *Adv Opt Mater*. 2020;8(6). doi:10.1002/adom.201901173

26. Maciejewska K, Bednarkiewicz A, Marciniak L. NIR luminescence lifetime nanothermometry based on phonon assisted Yb3+-Nd3+energy transfer. *Nanoscale Adv*. 2021;3(17):4918-4925. doi:10.1039/d1na00285f

27. Marciniak L, Bednarkiewicz A, Stefanski M, Tomala R, Hreniak D, Strek W. Near infrared absorbing near infrared emitting highly-sensitive luminescent nanothermometer based on Nd3+ to Yb3+ energy transfer. *Physical Chemistry Chemical Physics*. 2015;17(37):24315-24321. doi:10.1039/c5cp03861h

28. Rivera-López F, Babu P, Basavapoornima C, Jayasankar CK, Lavín V. Efficient Nd3+→Yb3+ energy transfer processes in high phonon energy phosphate glasses for 1.0 µm Yb3+ laser. *J Appl Phys*. 2011;109(12). doi:10.1063/1.3580475

29. Campora S, Ghersi G. Recent developments and applications of smart nanoparticles in biomedicine. *Nanotechnol Rev*. 2022;11(1):2595-2631. doi:10.1515/ntrev-2022-0148

30. Dolai J, Mandal K, Jana NR. Nanoparticle Size Effects in Biomedical Applications. *ACS Appl Nano Mater*. 2021;4(7):6471-6496. doi:10.1021/acsanm.1c00987

31. Elsabahy M, Wooley KL. Design of polymeric nanoparticles for biomedical delivery applications. *Chem Soc Rev*. 2012;41(7):2545-2561. doi:10.1039/c2cs15327k

32. Abbasi R, Shineh G, Mobaraki M, Doughty S, Tayebi L. Structural parameters of nanoparticles affecting their toxicity for biomedical applications: a review. *Journal of Nanoparticle Research*. 2023;25(3). doi:10.1007/s11051-023-05690-w

33. Liu Y, Tan J, Thomas A, Ou-Yang D, Muzykantov VR. *The Shape of Things to Come: Importance of Design in Nanotechnology for Drug Delivery*. Vol 3.; 2012.

34. Pominova D V., Romanishkin ID, Proydakova VY, et al. Optimization of upconversion luminescence excitation mode for deeper in vivo bioimaging without contrast loss or overheating. *Methods Appl Fluoresc*. 2020;8(2). doi:10.1088/2050-6120/ab7782

35. Hemmer E, Benayas A, Légaré F, Vetrone F. Exploiting the biological windows: Current perspectives on fluorescent bioprobes emitting above 1000 nm. *Nanoscale Horiz*. 2016;1(3):168-184. doi:10.1039/c5nh00073d

36. Matulionyte M, Skripka A, Ramos-Guerra A, Benayas A, Vetrone F. The Coming of Age of Neodymium: Redefining Its Role in Rare Earth Doped Nanoparticles. *Chem Rev*. 2023;123(1):515-554. doi:10.1021/acs.chemrev.2c00419

37. Shen Y, Lifante J, Fernández N, Jaque D, Ximendes E. In Vivo Spectral Distortions of Infrared Luminescent Nanothermometers Compromise Their Reliability. *ACS Nano*. 2020;14(4):4122-4133. doi:10.1021/acsnano.9b08824

38. Del Rosal B, Villa I, Jaque D, Sanz-Rodríguez F. In vivo autofluorescence in the biological windows: the role of pigmentation. *J Biophotonics*. 2016;9(10):1059-1067. doi:10.1002/jbio.201500271

39. del Rosal B, Rocha U, Ximendes EC, Martín Rodríguez E, Jaque D, Solé JG. Nd3+ ions in nanomedicine: Perspectives and applications. *Opt Mater (Amst)*. 2017;63:185-196. doi:10.1016/j.optmat.2016.06.004

40. Dantelle G, Matulionyte M, Testemale D, Cantarano A, Ibanez A, Vetrone F. Nd3+ doped Gd3Sc2Al3O12 nanoparticles: Towards efficient nanoprobes for temperature sensing. *Physical Chemistry Chemical Physics*. 2019;21(21):11132-11141. doi:10.1039/c9cp01808e

41. Skripka A, Morinvil A, Matulionyte M, Cheng T, Vetrone F. Advancing neodymium single-band nanothermometry. *Nanoscale*. 2019;11(23):11322-11330. doi:10.1039/c9nr02801c

42. Kaczkan M, Malinowski M, Suchocki A, Turczyński S. Cooperative luminescence of Yb3+ ions in multisite YAM crystal. *J Lumin*. 2024;265. doi:10.1016/j.jlumin.2023.120162

43. Weber MJ. Optical properties of Yb3+ and Nd3+-Yb3+ energy transfer in YAlO3. *Phys Rev B*. 1971;4(9):3153-3159. doi:10.1103/PhysRevB.4.3153

44. Kaczkan M, Malinowski M, Suchocki A, Pawlak DA, Turczyński S. Temperature and concentration dependent luminescence of Yb3+ centers in YAM. In: *Journal of Alloys and Compounds*. Vol 842. Elsevier Ltd; 2020. doi:10.1016/j.jallcom.2020.155893

45. Runowski M, Shyichuk A, Tymiński A, Grzyb T, Lavín V, Lis S. Multifunctional Optical Sensors for Nanomanometry and Nanothermometry: High-Pressure and High-Temperature Upconversion Luminescence of Lanthanide-Doped Phosphates - LaPO4/YPO4:Yb3+-Tm3+. *ACS Appl Mater Interfaces*. 2018;10(20):17269-17279. doi:10.1021/acsami.8b02853

46. Kaczmarek AM, Suta M, Rijckaert H, et al. High temperature (nano)thermometers based on LiLuF4:Er3+,Yb3+nano- And microcrystals. Confounded results for core-shell nanocrystals. *J Mater Chem C Mater*. 2021;9(10):3589-3600. doi:10.1039/d0tc05865c

47. Perrella RV, De Sousa Filho PC. High-sensitivity dual UV/NIR-excited luminescence thermometry by rare earth vanadate nanoparticles. *Dalton Transactions*. 2020;49(3):911-922. doi:10.1039/c9dt04308j

48. de Oliveira Lima K, dos Santos LF, Galvão R, Tedesco AC, de Souza Menezes L, Gonçalves RR. Single Er3+, Yb3+: KGd3F10 Nanoparticles for Nanothermometry. *Front Chem*. 2021;9. doi:10.3389/fchem.2021.712659

49. Shang F, Hu C, Xu W, et al. Near-infrared emitting Nd3+-Yb3+ codoped Y2O3 nanocrystals for highly sensitive optical thermometry. *J Alloys Compd*. 2021;858. doi:10.1016/j.jallcom.2020.157637

50. Dibaba ST, Xiaoqian Ge, Ren W, Sun L. Recent progress of energy transfer and luminescence intensity boosting mechanism in Nd3+-sensitized upconversion nanoparticles. *Journal of Rare Earths*. 2019;37(8):791-805. doi:10.1016/j.jre.2019.02.001

51. Zhan Q, Qian J, Liang H, et al. Using 915 nm laser excited Tm3+/Er3+/Ho 3+-doped NaYbF4 upconversion nanoparticles for in vitro and deeper in vivo bioimaging without overheating irradiation. *ACS Nano*. 2011;5(5):3744-3757. doi:10.1021/nn200110j

52. Maia LJQ, Faria Filho FM, Jerez V, Moura AL, De Araújo CB. Structural and luminescence properties of Nd3+/Yb3+ codoped Al4B2O9 nanocrystalline powders. *J Mater Chem C Mater*. 2015;3(44):11689-11696. doi:10.1039/c5tc01696g

53. Naresh V, Lee N. NIR luminescence and energy transfer kinetics in Nd3+/Yb3+ co-doped sodium aluminium bismuth fluoro-borosilicate glasses. *Ceram Int*. 2019;45(17):22649-22659. doi:10.1016/j.ceramint.2019.07.298

54. De Sousa DF, Batalioto F, Bell MJV, Oliveira SL, Nunes LAO. Spectroscopy of Nd3+ and Yb3+ codoped fluoroindogallate glasses. *J Appl Phys*. 2001;90(7):3308-3313. doi:10.1063/1.1397289

55. Sontakke AD, Biswas K, Sen R, Annapurna K. *Efficient Non-Resonant Energy Transfer in Nd 3+-Yb 3+ Codoped Ba-Al-Metaphosphate Glasses*. Vol 160.; 2010. doi:10.1364/JOSAB.27.002750

56. Steinkemper H, Fischer S, Hermle M, Goldschmidt JC. Stark level analysis of the spectral line shape of electronic transitions in rare earth ions embedded in host crystals. *New J Phys*. 2013;15. doi:10.1088/1367-2630/15/5/053033

57. Barbosa I V., Maciel CVT, Moura AL, Maia LJQ, Ibanez A, Dantelle G. Impact of the nature of oxide host matrices on the thermometric luminescence properties of Nd3+- Yb3+ codoped nanocrystals. *Opt Mater (Amst)*. 2024;150. doi:10.1016/j.optmat.2024.115143

58. Jiang X, Sun Y, Wang X, Hu L, Chen S, Yang Q. Temperature dependence of spectroscopic properties and energy transfer in Nd3+/Yb3+ co-doped silicate glass. *J Lumin*. 2022;251. doi:10.1016/j.jlumin.2022.119146

59. Jaque D, Ramirez O, Bausá E, et al. Nd3+→Yb3+ energy transfer in the YAl3(BO3)4 nonlinear laser crystal. *Phys Rev B Condens Matter Mater Phys*. 2003;68(11). doi:10.1103/PhysRevB.68.035118

60. Kalinichev AA, Kurochkin MA, Golyeva E V., et al. Near-infrared emitting YVO4:Nd3+ nanoparticles for high sensitive fluorescence thermometry. *J Lumin*. 2018;195:61-66. doi:10.1016/j.jlumin.2017.11.024

61. Kolesnikov IE, Kalinichev AA, Kurochkin MA, et al. Y2O3:Nd3+ nanocrystals as ratiometric luminescence thermal sensors operating in the optical windows of biological tissues. *J Lumin*. 2018;204:506-512. doi:10.1016/j.jlumin.2018.08.050

62. Balabhadra S, Debasu ML, Brites CDS, et al. Boosting the sensitivity of Nd3+-based luminescent nanothermometers. *Nanoscale*. 2015;7(41):17261-17267. doi:10.1039/c5nr05631d

63. Hernández-Rodríguez MA, Lozano-Gorrín AD, Martín IR, Rodríguez-Mendoza UR, Lavín V. Comparison of the sensitivity as optical temperature sensor of nano-perovskite doped with Nd3+ ions in the first and second biological windows. *Sens Actuators B Chem*. 2018;255:970-976. doi:10.1016/j.snb.2017.08.140

64. Barbosa I V., Dantelle G, Ibanez A, Maia LJQ. Nd3+ doped oxide thermal probes based on luminescence intensity ratio within BW-II and excitation in BW-I. *J Lumin*. 2024;266. doi:10.1016/j.jlumin.2023.120299

65. Wawrzynczyk D, Bednarkiewicz A, Nyk M, Strek W, Samoc M. Neodymium(iii) doped fluoride nanoparticles as non-contact optical temperature sensors. *Nanoscale*. 2012;4(22):6959-6961. doi:10.1039/c2nr32203j

66. Benayas A, Del Rosal B, Pérez-Delgado A, et al. Nd:YAG Near-Infrared Luminescent Nanothermometers. *Adv Opt Mater*. 2015;3(5):687-694. doi:10.1002/adom.201400484

67. Quintanilla M, Zhang Y, Liz-Marzán LM. Subtissue Plasmonic Heating Monitored with CaF2:Nd3+,Y3+ Nanothermometers in the Second Biological Window.

Chemistry of Materials. 2018;30(8):2819-2828. doi:10.1021/acs.chemmater.8b00806

68. Carrasco E, Del Rosal B, Sanz-Rodríguez F, et al. Intratumoral thermal reading during photo-thermal therapy by multifunctional fluorescent nanoparticles. *Adv Funct Mater*. 2015;25(4):615-626. doi:10.1002/adfm.201403653

69. Gomes MA, Carvalho IS, Domingos LFA, et al. Temperature-sensitive luminescence of Y2O3:Nd3+ nanocrystals produced by an eco-friendly route. *Opt Mater (Amst)*. 2019;89:536-542. doi:10.1016/j.optmat.2019.01.064

70. Ximendes EC, Santos WQ, Rocha U, et al. Unveiling in Vivo Subcutaneous Thermal Dynamics by Infrared Luminescent Nanothermometers. *Nano Lett*. 2016;16(3):1695-1703. doi:10.1021/acs.nanolett.5b04611

71. Pudovkin MS, Ginkel AK, Lukinova E V. Temperature sensitivity of Nd3+, Yb3+:YF3 ratiometric luminescent thermometers at different Yb3+ concentration. *Opt Mater (Amst)*. 2021;119. doi:10.1016/j.optmat.2021.111328

72. Marciniak L, Bednarkiewicz A, Trejgis K, Maciejewska K, Elzbieciak K, Ledwa K. Enhancing the sensitivity of a Nd3+,Yb3+:YVO4 nanocrystalline luminescent thermometer by host sensitization. *Physical Chemistry Chemical Physics*. 2019;21(20):10532-10539. doi:10.1039/c9cp01806a

73. Kolesnikov IE, Afanaseva E V., Kurochkin MA, Vaishlia EI, Kolesnikov EY, Lahderanta E. Dual-center co-doped and mixed ratiometric LuVO4:Nd3+/Yb3+nanothermometers. *Nanotechnology*. 2022;33(16). doi:10.1088/1361-6528/ac49c3

74. Ferreira LHAR, Dantelle G, Ibanez A, Maia LJQ. Thermal sensitivity of the Nd3+/Yb3+ co-doped β-BaB2O4 nanoparticles for luminescence nanothermometry. *Physica B Condens Matter*. 2022;644. doi:10.1016/j.physb.2022.414193

75. Ferreira LHAR, Maia LJQ. Synthesis, structural and temperature-sensing properties of nanosized Y2Ba3B4O12: Nd3+/Yb3+ phosphors. *Physica B Condens Matter*. 2023;657. doi:10.1016/j.physb.2023.414825

76. Ximendes EC, Rocha U, Kumar KU, Jacinto C, Jaque D. LaF3 core/shell nanoparticles for subcutaneous heating and thermal sensing in the second biological-window. *Appl Phys Lett*. 2016;108(25). doi:10.1063/1.4954170

77. Gulzar A, Xu J, Yang P, He F, Xu L. Upconversion processes: Versatile biological applications and biosafety. *Nanoscale*. 2017;9(34):12248-12282. doi:10.1039/c7nr01836c

78. Suo H, Guo C, Zheng J, et al. Sensitivity Modulation of Upconverting Thermometry through Engineering Phonon Energy of a Matrix. *ACS Appl Mater Interfaces*. 2016;8(44):30312-30319. doi:10.1021/acsami.6b12176

79. Premcheska S, Lederer M, Kaczmarek AM. The importance, status, and perspectives of hybrid lanthanide-doped upconversion nanothermometers for theranostics. *Chemical Communications*. 2022;58(27):4288-4307. doi:10.1039/d1cc07164e

80. Li C, Lin J. Rare earth fluoride nano-/microcrystals: Synthesis, surface modification and application. *J Mater Chem*. 2010;20(33):6831-6847. doi:10.1039/c0jm00031k

81. Suo H, Zhao X, Zhang Z, et al. Local symmetric distortion boosted photon up-conversion and thermometric sensitivity in lanthanum oxide nanospheres. *Nanoscale*. 2018;10(19):9245-9251. doi:10.1039/c8nr01734d

82. Jahanbazi F, Mao Y. Recent advances on metal oxide-based luminescence thermometry. *J Mater Chem C Mater*. 2021;9(46):16410-16439. doi:10.1039/d1tc03455c

83. Dantelle G, Testemale D, Homeyer E, et al. A new solvothermal method for the synthesis of size-controlled YAG:Ce single-nanocrystals. *RSC Adv*. 2018;8(47):26857-26870. doi:10.1039/c8ra05914d

84. Gomes PF, Silva TC, Maia LJQ, Carvalho JF. Synthesis and visible down- and up-conversion emissions from Yb3+/Ho3+/Tm3+ Co-Doped Y4Al2O9 (YAM) nanocrystalline particles. *J Lumin*. 2020;227. doi:10.1016/j.jlumin.2020.117554

85. Boruc Z, Kaczkan M, Fetlinski B, Turczynski S, Malinowski M. Blue emissions in Dy3+ doped Y4Al2O9 crystals for temperature sensing. *Opt Lett*. 2012;37(24). http://in3.dem.ist.utl.pt/

86. Gasparotto G, Tavares LS, Silva TC, Maia LJQ, Carvalho JF. Structural and spectroscopic properties of Eu3+ doped Y4Al2O9 compounds through a soft chemical process. *J Lumin*. 2018;204:513-519. doi:10.1016/j.jlumin.2018.08.055

87. Kumar P, Singh D, Gupta I, Singh S, Nehra S, Kumar R. A study of phase evolution, crystallographic and down-conversion luminescent behaviour of monoclinic Y4Al2O9:Dy3+ nanophosphors for white light applications. *Opt Mater (Amst)*. 2023;138. doi:10.1016/j.optmat.2023.113677

88. Lupei V, Lupei A, Gheorghe C, Hau S, Ikesue A. Efficient sensitization of Yb3+ emission by Nd3+ in Y2O3 transparent ceramics and the prospect for high-energy Yb lasers. *Opt Lett*. 2009;34(14):2141.

89. Malek Khachatourian A, Golestani-Fard F, Sarpoolaky H, Vogt C, Toprak MS. Microwave assisted synthesis of monodispersed Y2O3 and Y2O3:Eu3+ particles. *Ceram Int*. 2015;41(2):2006-2014. doi:10.1016/j.ceramint.2014.09.105

90. Sanità G, Carrese B, Lamberti A. Nanoparticle Surface Functionalization: How to Improve Biocompatibility and Cellular Internalization. *Front Mol Biosci*. 2020;7. doi:10.3389/fmolb.2020.587012

91. Yao . J, Maslov K, Hu S, Wang L V. *Photoacoustic Imaging; (170.3880) Medical and Biological Imaging; (160.4236) Nanomaterials. Nanotube-Enhanced Non-Invasive Photoacoustic Mapping of the Sentinel Lymph Node*. Vol 54.; 2009.

92. Crucho CIC. Silica coatings: From nanostructures to biological entities. *Appl Mater Today*. 2024;38. doi:10.1016/j.apmt.2024.102179

93. Maurin I, Dantelle G, Boilot JP, Gacoin T. A protected annealing process for the production of high quality colloidal oxide nanoparticles with optimized physical properties. *J Mater Chem C Mater*. 2013;1(1):13-22. doi:10.1039/c2tc00127f

94. Croissant JG, Butler KS, Zink JI, Brinker CJ. Synthetic amorphous silica nanoparticles: toxicity, biomedical and environmental implications. *Nat Rev Mater*. 2020;5(12):886-909. doi:10.1038/s41578-020-0230-0

95. Mukhopadhyay L, Rai VK. Colloidal stability and optical thermometry in mesoporous silica coated phosphate based upconverting nanoparticles. *J Alloys Compd*. 2021;878. doi:10.1016/j.jallcom.2021.160351

96. Savchuk OA, Carvajal JJ, Cascales C, Aguiló M, Díaz F. Benefits of Silica Core-Shell Structures on the Temperature Sensing Properties of Er,Yb:GdVO4 Up-Conversion Nanoparticles. *ACS Appl Mater Interfaces*. 2016;8(11):7266-7273. doi:10.1021/acsami.6b01371

97. Kolesnikov IE, Kurochkin MA, Kalinichev AA, et al. Effect of silica coating on luminescence and temperature sensing properties of Nd3+ doped nanoparticles. *J Alloys Compd*. 2018;734:136-143. doi:10.1016/j.jallcom.2017.11.048

98. Savchuk O, Marti JJC, Cascales C, et al. Bifunctional tm3+,yb3+:Gdvo4@sio2 core-shell nanoparticles in hela cells: Upconversion luminescence nanothermometry in the first biological window and biolabelling in the visible. *Nanomaterials*. 2020;10(5). doi:10.3390/nano10050993

99. Geitenbeek RG, Prins PT, Albrecht W, Van Blaaderen A, Weckhuysen BM, Meijerink A. NaYF4:Er3+,Yb3+/SiO2 Core/Shell Upconverting Nanocrystals for Luminescence Thermometry up to 900 K. *Journal of Physical Chemistry C*. 2017;121(6):3503-3510. doi:10.1021/acs.jpcc.6b10279

100. Quintanilla M, Henriksen-Lacey M, Renero-Lecuna C, Liz-Marzán LM. Challenges for optical nanothermometry in biological environments. *Chem Soc Rev*. 2022;51(11):4223-4242. doi:10.1039/d2cs00069e

101. Zhu GH, Gray ABC, Patra HK. Nanomedicine: controlling nanoparticle clearance for translational success. *Trends Pharmacol Sci*. 2022;43(9):709-711. doi:10.1016/j.tips.2022.05.001

102. Nikzamir M, Akbarzadeh A, Panahi Y. An overview on nanoparticles used in biomedicine and their cytotoxicity. *J Drug Deliv Sci Technol*. 2021;61. doi:10.1016/j.jddst.2020.102316

103. Shenoi-Perdoor S. *Fluorescent Organic@silicate Core-Shell Nanoparticles for in Vivo Vascular Imaging*. Université Grenoble Alpes; 2018. Accessed September 9, 2023. https://theses.hal.science/tel-02489142

104. Suk JS, Xu Q, Kim N, Hanes J, Ensign LM. PEGylation as a strategy for improving nanoparticle-based drug and gene delivery. *Adv Drug Deliv Rev*. 2016;99:28-51. doi:10.1016/j.addr.2015.09.012

105. Shi D, Beasock D, Fessler A, et al. To PEGylate or not to PEGylate: Immunological properties of nanomedicine's most popular component, polyethylene glycol and its alternatives. *Adv Drug Deliv Rev*. 2022;180. doi:10.1016/j.addr.2021.114079

106. Nikam A V., Prasad BLV, Kulkarni AA. Wet chemical synthesis of metal oxide nanoparticles: A review. *CrystEngComm*. 2018;20(35):5091-5107. doi:10.1039/C8CE00487K

107. Pechini MP. Method of Preparing Lead and Alkaline Earth Titanates and Niobates and Coating Method Using the Same to Form a Capacitor. Published online 1967.

108. Olav T, Sunde L, Grande T, Einarsrud MA. Modified Pechini Synthesis of Oxide Powders and Thin Films. In: *Handbook of Sol-Gel Science and Technology*. Springer International Publishing; 2016:1-30.

109. Erson P′, Neves P, Maia LJQ, et al. Synthesis and Characterization of the β-BaB 2 O 4 Phase Obtained by the Polymeric Precursor Method. *J Solgel Sci Technol*. 2004;29:89-96. doi:10.1023/B:JSST.0000023010.79540.6f

110. Tomala R, Marciniak L, Li J, et al. Comprehensive study of photoluminescence and cathodoluminescence of YAG:Eu3+ nano- and microceramics. *Opt Mater (Amst)*. 2015;50:59-64. doi:10.1016/j.optmat.2015.06.042

111. Marin R, Sponchia G, Riello P, Sulcis R, Enrichi F. Photoluminescence properties of YAG:Ce3+,Pr3+ phosphors synthesized via the Pechini method for white LEDs. *Journal of Nanoparticle Research*. 2012;14(6). doi:10.1007/s11051-012-0886-5

112. Lamer VK, Dinegar RH. *Theory, Production and Mechanism of Formation of Monodispersed Hydrosols*.

113. Nguyen TD. From formation mechanisms to synthetic methods toward shape-controlled oxide nanoparticles. *Nanoscale*. 2013;5(20):9455-9482. doi:10.1039/c3nr01810e

114. Chang J, Waclawik ER. Colloidal semiconductor nanocrystals: Controlled synthesis and surface chemistry in organic media. *RSC Adv*. 2014;4(45):23505-23527. doi:10.1039/c4ra02684e

115. Varanda LC, De Souza CGS, Perecin CJ, et al. Inorganic and organic-inorganic composite nanoparticles with potential biomedical applications: Synthesis challenges for enhanced performance. In: *Materials for Biomedical Engineering: Bioactive Materials, Properties, and Applications*. Elsevier; 2019:47-99. doi:10.1016/B978-0-12-818431-8.00004-0

116. Mudalige T, Qu H, Van Haute D, Ansar SM, Paredes A, Ingle T. Characterization of Nanomaterials: Tools and Challenges. In: *Nanomaterials for Food Applications*. Elsevier; 2018:313-353. doi:10.1016/B978-0-12-814130-4.00011-7

117. Guerrero-Martínez A, Pérez-Juste J, Liz-Marzán LM. Recent progress on silica coating of nanoparticles and related nanomaterials. *Advanced Materials*. 2010;22(11):1182-1195. doi:10.1002/adma.200901263

118. Cichos J, Karbowiak M. A general and versatile procedure for coating of hydrophobic nanocrystals with a thin silica layer enabling facile biofunctionalization and dye incorporation. *J Mater Chem B*. 2014;2(5):556-568. doi:10.1039/c3tb21442g

119. Wiercigroch-Walkosz K, Cichos J, Karbowiak M. Growth of silica shell on hydrophobic upconverting nanocrystals – Mechanism and control of porosity. *Colloids Surf A Physicochem Eng Asp*. 2019;572:1-9. doi:10.1016/j.colsurfa.2019.03.083

120. Cantarano A, Yao J, Matulionyte M, et al. Autofluorescence-Free in Vivo Imaging Using Polymer-Stabilized Nd3+-Doped YAG Nanocrystals. *ACS Appl Mater Interfaces*. 2020;12(46):51273-51284. doi:10.1021/acsami.0c15514

121. Marciniak L, Bednarkiewicz A, Drabik J, Trejgis K, Strek W. Optimization of highly sensitive YAG:Cr3+,Nd3+ nanocrystal-based luminescent thermometer operating in an optical window of biological tissues. *Physical Chemistry Chemical Physics*. 2017;19(10):7343-7351. doi:10.1039/c6cp07213e

122. Periša J, Ristić Z, Piotrowski W, Antić Ž, Marciniak L, Dramićanin MD. All near-infrared multiparametric luminescence thermometry using Er3+, Yb3+-doped

YAG nanoparticles. *RSC Adv*. 2021;11(26):15933-15942. doi:10.1039/d1ra01647d

123. Jain A, Sengar P, Hirata GA. Rare-earth-doped Y3Al5O12 (YAG) nanophosphors: Synthesis, surface functionalization, and applications in thermoluminescence dosimetry and nanomedicine. *J Phys D Appl Phys*. 2018;51(30). doi:10.1088/1361-6463/aaca49

124. Berends AC, Van De Haar MA, Krames MR. YAG:Ce3+Phosphor: From Micron-Sized Workhorse for General Lighting to a Bright Future on the Nanoscale. *Chem Rev*. 2020;120(24):13461-13479. doi:10.1021/acs.chemrev.0c00618

125. Odziomek M, Chaput F, Lerouge F, Sitarz M, Parola S. Highly luminescent YAG:Ce ultra-small nanocrystals, from stable dispersions to thin films. *J Mater Chem C Mater*. 2017;5(47):12561-12570. doi:10.1039/c7tc03504g

126. Revaux A, Dantelle G, George N, Seshadri R, Gacoin T, Boilot JP. A protected annealing strategy to enhanced light emission and photostability of YAG:Ce nanoparticle-based films. *Nanoscale*. 2011;3(5):2015-2022. doi:10.1039/c0nr01000f

127. Inoue M, Otsu H, Kominami H, Inui T. *Glycothermal Synthesis of Rare Earth Aluminium Garnets*. Vol 226.; 1995.

128. Shannon RD. Revised Effective Ionic Radii and Systematic Studies of Interatomic Distances in Halides and Chalcogenides. *Acta Crytallographica*. 1976;32:757-767. https://www.researchgate.net/publication/306153198

129. Loiko P, Basyrova L, Maksimov R, et al. Comparative Study of Ho:Y2O3 and Ho:Y3Al5O12 Transparent Ceramics Produced from Laser-Ablated Nanoparticles. *J Lumin*. 2021;240(118460). doi:10.1016/j.jlumin.2021.118460

130. Meijer JM, Aarts L, Van Der Ende BM, Vlugt TJH, Meijerink A. Downconversion for solar cells in YF3: Nd3+, Yb 3+. *Phys Rev B Condens Matter Mater Phys*. 2010;81(3). doi:10.1103/PhysRevB.81.035107

131. Martins GM, Siqueira KPF, Fantini C, Moreira RL, Dias A. New insight on the use of diffuse reflectance spectroscopy for the optical characterization of

Ln2Ge2O7 (Ln = lanthanides) pyrogermanates. *J Lumin*. 2021;238. doi:10.1016/j.jlumin.2021.118312

132. Sontakke AD, Biswas K, Mandal AK, Annapurna K. Time resolved fluorescence and energy transfer analysis of Nd 3+-Yb 3+-Er 3+ triply-doped Ba-Al-metaphosphate glasses for an eye safe emission (1.54 μm). *J Fluoresc*. 2010;20(1):425-434. doi:10.1007/s10895-009-0562-z

133. Makuła P, Pacia M, Macyk W. How To Correctly Determine the Band Gap Energy of Modified Semiconductor Photocatalysts Based on UV-Vis Spectra. *Journal of Physical Chemistry Letters*. 2018;9(23):6814-6817. doi:10.1021/acs.jpclett.8b02892

134. Torrent J, Barrón V. Diffuse reflectance spectroscopy. In: *Methods of Soil Analysis, Part 5: Mineralogical Methods*. Vol 5. wiley; 2015:367-385. doi:10.2136/sssabookser5.5.c13

135. Som S, Sharma SK. Eu 3+/Tb 3+-codoped Y 2O 3 nanophosphors: Rietveld refinement, bandgap and photoluminescence optimization. *J Phys D Appl Phys*. 2012;45(41). doi:10.1088/0022-3727/45/41/415102

136. Wan Y, Li M, Xie E, Xu S, Huang Y, Deng W. Luminescent properties and first-principles calculations of (Cr,Ca):YAG crystals. In: *International Journal of Modern Physics B*. Vol 31. World Scientific Publishing Co. Pte Ltd; 2017. doi:10.1142/S0217979217440702

137. Winarski D, Persson C, Selim FA. Hydrogen in insulating oxide Y3Al5O12 strongly narrows the band gap. *Appl Phys Lett*. 2014;105(22). doi:10.1063/1.4903343

138. Lupei V, Lupei A, Ikesue A, Gheorghe C, Hau S. Sensitization of Yb3+ Emission in Laser Oxide Ceramics. *Rom Rep Phys*. 2010;62(3):429-443.

139. Walsh BM, McMahon JM, Edwards WC, Barnes NP, Equall RW, Hutcheson RL. Spectroscopic characterization of Nd:Y2O3: application toward a differential absorption lidar system for remote sensing of ozone. *Journal of the Optical Society of America B*. 2002;19(12):2893. doi:10.1364/josab.19.002893

140. Brown DC, Vitali VA. Yb:YAG kinetics model including saturation and power conservation. *IEEE J Quantum Electron*. 2011;47(1):3-12. doi:10.1109/JQE.2010.2063417

141. Balda R, Fernández J, Iparraguirre I, Al-Saleh M. Spectroscopic study of Nd3+/Yb3+ in disordered potassium bismuth molybdate laser crystals. *Opt Mater (Amst)*. 2006;28(11):1247-1252. doi:10.1016/j.optmat.2006.01.027

142. Balda R, Ignacio Peña J, Angeles Arriandiaga M, et al. *Spectroscopic Properties of Er 3+ and Nd 3+ Doped Glasses with the 0.8CaSiO3-0.2Ca3(PO4)2 Eutectic Composition*. Vol 51.; 2006.

143. Caldiño U, Jaque D, Martín-Rodríguez E, et al. Nd3+ → Yb3+ resonant energy transfer in the ferroelectric Sr0.6 Ba0.4 Nb2 O6 laser crystal. *Phys Rev B Condens Matter Mater Phys*. 2008;77(7). doi:10.1103/PhysRevB.77.075121

144. Song YJ, Liu QQ, Zong N, et al. Spectroscopic properties and energy transfer in Nd3+/Yb3+co-doped yttrium aluminum garnet. *Laser Phys*. 2021;31(6). doi:10.1088/1555-6611/abf9a1

145. Bednarkiewicz A, Hreniak D, Stręk W. Cooperative processes in Nd3+/Yb3+ co-doped YAG nanocrystallites. *Radiation Effects and Defects in Solids*. 2003;158(1-6):31-37. doi:10.1080/1042015021000052665

146. Hosokawa S, Tanaka Y, Iwamoto S, Inoue M. Defect structure of rare earth aluminium garnets obtained by the glycothermal method. *J Alloys Compd*. 2008;451(1-2):309-313. doi:10.1016/j.jallcom.2007.04.063

147. Asakura R, Isobe T, Kurokawa K, Aizawa H, Ohkubo M. Tagging of avidin immobilized beads with biotinylated YAG:Ce3+ nanocrystal phosphor. *Anal Bioanal Chem*. 2006;386(6):1641-1647. doi:10.1007/s00216-006-0814-6

148. Vorsthove M, Kynast U. Efficiency issues in Ce3+ doped YAG nanocrystals. *Mater Res Bull*. 2011;46(11):1761-1765. doi:10.1016/j.materresbull.2011.08.007

149. Ma Z, Ji H, Tan D, et al. Porous YAG:Nd 3+ fibers with excitation and emission in the human "nIR optical window" as luminescent drug carriers. *Chemistry - A European Journal*. 2012;18(9):2609-2616. doi:10.1002/chem.201101262

150. Aboulaich A, Deschamps J, Deloncle R, et al. Rapid synthesis of Ce3+-doped YAG nanoparticles by a solvothermal method using metal carbonates as precursors. *New Journal of Chemistry*. 2012;36(12):2493-2500. doi:10.1039/c2nj40429j

151. Emrie DB. Sol-Gel Synthesis of Nanostructured Mesoporous Silica Powder and Thin Films. *J Nanomater*. 2024;2024. doi:10.1155/2024/6109770

152. Hahm E, Jo A, Kang EJ, et al. Ultra-fine control of silica shell thickness on silver nanoparticle-assembled structures. *Int J Mol Sci*. 2021;22(21). doi:10.3390/ijms222111983

153. Kang X, Cheng Z, Li C, et al. Core-shell structured up-conversion luminescent and mesoporous NaYF 4:Yb3+/Er3+@ n SiO2@ m SiO 2 nanospheres as carriers for drug delivery. *Journal of Physical Chemistry C*. 2011;115(32):15801-15811. doi:10.1021/jp203039t

154. Wang L, Zhao F, Yang X, Pan C, Huang H. Property of YAG:Ce3+ nanophosphors prepared by solvothermal method using triethylene-tetramine as a reaction solvent. *RSC Adv*. 2015;5(33):26339-26345. doi:10.1039/c5ra00580a

155. Inoue M, Kimura M. Alkyl derivatives of boehmite having the second stage structure. *Molecular Crystals and Liquid Crystals Science and Technology Section A: Molecular Crystals and Liquid Crystals*. 2000;341:431-436. doi:10.1080/10587250008026177

156. Thiruchitrambalam M, Palkar VR, Gopinathan V. Hydrolysis of aluminium metal and sol-gel processing of nano alumina. *Mater Lett*. 2004;58(24):3063-3066. doi:10.1016/j.matlet.2004.05.043

157. Singh AK. *Study on The Effect of Different Sols on High Alumina Castable Refractory.*; 2017. https://www.researchgate.net/publication/318122611

158. Inoue M, Nishikawa T, Inui T. Reactions of rare earth acetates with aluminum isopropoxide in ethylene glycol: Synthesis of the garnet and monoclinic phases of rare earth aluminates. *J Mater Sci*. 1998;33:5835-5841. doi:10.1023/A:1004466402877

159. Suárez M, Fernández A, Menéndez JL, Torrecillas R. Transparent yttrium aluminium garnet obtained by spark plasma sintering of lyophilized gels. *J Nanomater*. 2009;2009. doi:10.1155/2009/138490

160. Zhu Q, Zhong L, Yang L, Xu X. Synthesis of the High Performance YAG:Ce Phosphor by a Sol-Gel Method. *ECS Journal of Solid State Science and Technology*. 2012;1(4):R119-R122. doi:10.1149/2.017204jss

161. Guerbous L, Boukerika A. Nanomaterial host bands effect on the photoluminescence properties of Ce-doped YAG nanophosphor synthesized by sol-gel method. *J Nanomater*. 2015;2015. doi:10.1155/2015/617130

162. Xie T, Zhang L, Wang J, Xie T, Zhu Q, Zhang X. Co-precipitation synthesis, structural characterization and fluorescent analysis of Nd 3+ doped Y 3 Al 5 O 12 and Yb 3 Al 5 O 12 nanocrystallines. *Journal of Materials Science: Materials in Electronics*. 2019;30(3):2299-2308. doi:10.1007/s10854-018-0502-2

163. Zhang S, Tie S, Zhang F. Cristobalite formation from the thermal treatment of amorphous silica fume recovered from the metallurgical silicon industry. *Micro Nano Lett*. 2018;13(10):1465-1468. doi:10.1049/mnl.2018.5167

164. Fidalgo A, Ilharco LM. The defect structure of sol-gel-derived silica/polytetrahydrofuran hybrid films by FTIR. *J Non Cryst Solids*. 2001;283(1-3):144-154. doi:10.1016/S0022-3093(01)00418-5

165. Gu G, Ong PP, Chu C. *Thermal Stability of Mesoporous Silica Molecular Sieve*.

166. Shahrokh Abadi MH, Delbari A, Fakoor Z, Baedi J. Effects of annealing temperature on infrared spectra of SiO2 extracted from rice husk. *Journal of Ceramic Science and Technology*. 2015;6(1):41-45. doi:10.4416/JCST2014-00028

167. Nien YT, Chen KM, Chen IG. Improved photoluminescence of Y3Al5O12:Ce nanoparticles by silica coating. *Journal of the American Ceramic Society*. 2010;93(6):1688-1691. doi:10.1111/j.1551-2916.2010.03624.x

168. Yu S, Wong TKS, Hu X, Goh TK. Effect of processing temperature on the properties of sol-gel-derived mesoporous silica films. *Thin Solid Films*. 2004;462-463(SPEC. ISS.):306-310. doi:10.1016/j.tsf.2004.05.022

169. Waseem M, Mustafa S, Naeem A, Shah K. *Synthesis and Characterization of Silica by Sol-Gel Method.*; 2009. https://www.researchgate.net/publication/285105909

170. Piotrowski WM, Szymczak M, Rodríguez EM, et al. Step by step optimization of luminescence thermometry in MgTiO3:Cr3+, Nd3+@SiO2 nanoparticles towards bioapplications. *Mater Chem Phys*. 2024;312. doi:10.1016/j.matchemphys.2023.128623

171. Zou R, Huang J, Shi J, et al. Silica shell-assisted synthetic route for mono-disperse persistent nanophosphors with enhanced in vivo recharged near-infrared persistent luminescence. *Nano Res*. 2017;10(6):2070-2082. doi:10.1007/s12274-016-1396-z

172. Rabouw FT, Prins PT, Villanueva-Delgado P, Castelijns M, Geitenbeek RG, Meijerink A. Quenching Pathways in NaYF4:Er3+,Yb3+ Upconversion Nanocrystals. *ACS Nano*. 2018;12(5):4812-4823. doi:10.1021/acsnano.8b01545

173. Samsonova E V., Popov A V., Vanetsev AS, et al. An energy transfer kinetic probe for OH-quenchers in the Nd3+: YPO4 nanocrystals suitable for imaging in the biological tissue transparency window. *Physical Chemistry Chemical Physics*. 2014;16(48):26806-26815. doi:10.1039/c4cp03774j

174. Rajakumar G, Mao L, Bao T, et al. Yttrium Oxide Nanoparticle Synthesis: An Overview of Methods of Preparation and Biomedical Applications. *Appl Sci*. Published online 2021:11. doi:10.3390/app

175. Du P, Luo L, Yue Q, Li W. The simultaneous realization of high- and low-temperature thermometry in Er3+/Yb3+-codoped Y2O3 nanoparticles. *Mater Lett*. 2015;143:209-211. doi:10.1016/j.matlet.2014.12.123

176. Galvão R, Santos LF dos, Gonçalves RR, Menezes L de S. Fluorescence Intensity Ratio-based temperature sensor with single Nd 3 + :Y 2 O 3 nanoparticles: Experiment and theoretical modeling . *Nano Select*. 2021;2(2):346-356. doi:10.1002/nano.202000148

177. Dos Santos LF, Martins JC, Lima KO, et al. In vitro assays and nanothermometry studies of infrared-to-visible upconversion of nanocrystalline Er3+,Yb3+ co-doped Y2O3 nanoparticles for theranostic applications. *Physica B Condens Matter*. 2022;624. doi:10.1016/j.physb.2021.413447

178. Nexha A, Pujol MC, Díaz F, Aguiló M, Carvajal JJ. Luminescence nanothermometry using self-assembled Er3+, Yb3+ doped Y2O3 nanodiscs: Might the upconversion mechanism condition their use as primary thermometers? *Opt Mater (Amst)*. 2022;134. doi:10.1016/j.optmat.2022.113216

179. Geitenbeek RG, Salzmann BBV, Nieuwelink AE, Meijerink A, Weckhuysen BM. Chemically and thermally stable lanthanide-doped Y 2 O 3 nanoparticles for remote temperature sensing in catalytic environments. *Chem Eng Sci*. 2019;198:235-240. doi:10.1016/j.ces.2018.10.004

180. Boukerika A, Guerbous L. Annealing effects on structural and luminescence properties of red Eu 3+-doped Y2O3 nanophosphors prepared by sol-gel method. *J Lumin*. 2014;145:148-153. doi:10.1016/j.jlumin.2013.07.037

181. Brandão-Silva AC, Gomes MA, Macedo ZS, Avila JFM, Rodrigues JJ, Alencar MARC. Multiwavelength Fluorescence Intensity Ratio Nanothermometry: High Sensitivity over a Broad Temperature Range. *Journal of Physical Chemistry C*. 2018;122(35):20459-20468. doi:10.1021/acs.jpcc.8b05345

182. Laia AS, Gomes MA, Brandão-Silva AC, et al. Nd 3+ doped Y 2 O 3 micro-and nanoparticles: A comparative study on temperature sensing and optical heating performance within the 1 st biological window. *Opt Mater (Amst)*. 2023;142. https://ssrn.com/abstract=4452447

183. Kumar D, Sharma M, Pandey OP. Morphology controlled Y2O3:Eu3+ nanophosphors with enhanced photoluminescence properties. *J Lumin*. 2015;158:268-274. doi:10.1016/j.jlumin.2014.09.046

184. Wang J, Jia C. Synthesis and Luminescence of Y2O3:Eu3+ Nanoparticles by the Coprecipitation. *Ferroelectrics*. 2015;482(1):129-135. doi:10.1080/00150193.2015.1057089

185. Bilir G, Özen G, Di Bartolo B. Synthesis and spectral characterization of yttrium oxide nano-powders doped with Nd3+ ions with a large range of concentrations. *Opt Mater (Amst)*. 2015;42:281-286. doi:10.1016/j.optmat.2014.12.047

186. Li N, Yanagisawa K. Controlling the morphology of yttrium oxide through different precursors synthesized by hydrothermal method. *J Solid State Chem*. 2008;181(8):1738-1743. doi:10.1016/j.jssc.2008.03.031

187. Pazura Y, Baumer VN, Deyneka TG, Vovk OM, Yavetskiy RP. Synthesis of Y2O3 and Y2O3:Nd 3+ monodisperse crystalline nanospheres by homogenous precipitation. *Functional Materials17*. 2010;17(1):107-113.

188. Yan T, Zhang D, Shi L, Yang H, Mai H, Fang J. Reflux synthesis, formation mechanism, and photoluminescence performance of monodisperse Y2O3:Eu3+ nanospheres. *Mater Chem Phys*. 2009;117(1):234-243. doi:10.1016/j.matchemphys.2009.05.047

189. Sung JM, Lin SE, Wei WCJ. Synthesis and reaction kinetics for monodispersive Y2O3:Tb3+ spherical phosphor particles. *J Eur Ceram Soc*. 2007;27(7):2605-2611. doi:10.1016/j.jeurceramsoc.2006.11.065

190. De Oliveira Lima K, Rocha Gonçalves R, Giaume D, Ferrier A, Goldner P. Influence of defects on sub-Å optical linewidths in Eu3+: Y2O3 particles. *J Lumin*. 2015;168:276-282. doi:10.1016/j.jlumin.2015.08.012

191. Liu S, Fossati A, Serrano D, Tallaire A, Ferrier A, Goldner P. Defect Engineering for Quantum Grade Rare-Earth Nanocrystals. *ACS Nano*. 2020;14(8):9953-9962. doi:10.1021/acsnano.0c02971

192. Mills SJ, Kartashov PM, Ma C, et al. Yttriaite-(Y): The natural occurrence of Y2O3 from the Bol'shaya Pol'ya River, Subpolar Urals, Russia. *American Mineralogist*. 2011;96(7):1166-1170. doi:10.2138/am.2011.3740

193. Mudavakkat VH, Atuchin V V., Kruchinin VN, Kayani A, Ramana C V. Structure, morphology and optical properties of nanocrystalline yttrium oxide (Y2O3) thin films. *Opt Mater (Amst)*. 2012;34(5):893-900. doi:10.1016/j.optmat.2011.11.027

194. Wang XJ, Zhang LD, Zhang JP, He G, Liu M, Zhu LQ. Effects of post-deposition annealing on the structure and optical properties of Y2O3 thin films. *Mater Lett*. 2008;62(26):4235-4237. doi:10.1016/j.matlet.2008.07.003

195. Lü Q, Wu Y, Ding L, et al. Visible upconversion luminescence of Tb3+ ions in Y2O3 nanoparticles induced by a near-infrared femtosecond laser. *J Alloys Compd*. 2010;496(1-2):488-493. doi:10.1016/j.jallcom.2010.02.085

196. Lupei A, Lupei V, Ikesue A, Gheorghe C, Hau S. Nd → Yb energy transfer in (Nd, Yb):Y2O3 transparent ceramics. *Opt Mater (Amst)*. 2010;32(10):1333-1336. doi:10.1016/j.optmat.2010.04.017

197. Sohn S, Kwon Y, Kim Y, Kim D. Synthesis and characterization of near-monodisperse yttria particles by homogeneous precipitation method. *Powder Technol*. 2004;142(2-3):136-153. doi:10.1016/j.powtec.2004.03.013

198. Li JG, Zhu Q, Li X, Sun X, Sakka Y. Colloidal processing of Gd2O3:Eu3+ red phosphor monospheres of tunable sizes: Solvent effects on precipitation kinetics and photoluminescence properties of the oxides. *Acta Mater*. 2011;59(9):3688-3696. doi:10.1016/j.actamat.2011.03.004

199. Yoo HS, Jang HS, Im W Bin, Kang JH, Jeon DY. Particle size control of a monodisperse spherical Y2O3: Eu3+ phosphor and its photoluminescence properties. *J Mater Res*. 2007;22(7):2017-2024. doi:10.1557/jmr.2007.0257

200. Ghanadzadeh Gilani A, Ghanadzadeh Gilani H, Ansari M. A thermodynamic study of solute-solvent interactions through dielectric properties of the mixtures consisting of 1,4-butanediol, 1-octanol, and 1,4-dioxane at different temperatures. *Journal of Chemical Thermodynamics*. 2012;55:203-212. doi:10.1016/j.jct.2012.05.032

201. Zhuravlev VI. Dielectric properties of multiatomic alcohols: 1,4-butanediol. *Russian Journal of Physical Chemistry A*. 2015;89(12):2213-2221. doi:10.1134/S0036024415120353

202. Sun L, Dlgulllo RM, Tela’ AS. Densities and Viscosities of Four Butanediols between 293 and 463 K. *J Chem Eng Data*. 1092:246-240.

203. Kong L, Li B, Zhao L, Zhang R, Wang C. Density, viscosity, surface tension, excess property and alkyl chain length for 1,4-butanediol (1) + 1,2-propanediamine (2) mixtures. *J Mol Liq*. 2021;326. doi:10.1016/j.molliq.2020.115107

204. Pang FM, Seng CE, Teng TT, Ibrahim MH. Densities and viscosities of aqueous solutions of 1-propanol and 2-propanol at temperatures from 293.15 K to 333.15 K. *J Mol Liq*. 2007;136(1-2):71-78. doi:10.1016/j.molliq.2007.01.003

205. Faria MAF, Martins RJ, Cardoso MJEM, Barcia OE. Density and viscosity of the binary systems ethanol + butan-1-ol, + pentan-1-ol, + heptan-1-ol, + octan-1-ol, nonan-1-ol, + decan-1-ol at 0.1 mpa and temperatures from 283.15 K to 313.15 K. *J Chem Eng Data*. 2013;58(12):3405-3419. doi:10.1021/je400630f

206. Rong CB, Poudyal N, Chaubey GS, et al. High thermal stability of carbon-coated L10-FePt nanoparticles prepared by salt-matrix annealing. *J Appl Phys*. 2008;103(7). doi:10.1063/1.2832506

207. Anwar J, Frenkel D, Noro MG. Calculation of the melting point of NaCl by molecular simulation. *Journal of Chemical Physics*. 2003;118(2):728-735. doi:10.1063/1.1522375

208. Guzik M, Alombert-Goget G, Guyot Y, et al. Spectroscopy of C3i and C2 sites of Nd3+-doped Lu2O3 sesquioxide either as ceramics or crystal. *J Lumin*. 2016;169:606-611. doi:10.1016/j.jlumin.2014.12.063

209. Song L, Dong Y, Shao Q, Jiang J. Preparation of Y3Al5O12:Ce nanophosphors using salt microemulsion method and their luminescent properties. *J Mater Sci*. 2018;53(21):15196-15203. doi:10.1007/s10853-018-2623-7

210. Das A, Saha S, Panigrahi K, et al. Morphology control and photoluminescence properties of Eu3+-activated Y4Al2O9 nanophosphors for solid state lighting applications. *CrystEngComm*. 2018;20(18):2540-2552. doi:10.1039/c8ce00289d

211. Talik E, Guzik A, Zajdel P, Lipińska L, Baran M, Szubka M. Structural, electronic and magnetic properties of Y4Al2O9 sol-gel powders with Tb3+ and Yb3+ co-doping. *Mater Res Bull*. 2016;83:56-64. doi:10.1016/j.materresbull.2016.05.018

212. Rabinovitch Y, Moune OK, Tétard D, Faucher MD. Synthesis, optical absorption, and site-selective excitation of the 3P0 levels in Y4Al2O 9:Pr3+. *Journal of Physical Chemistry A*. 2004;108(40):8244-8255. doi:10.1021/jp048123j

213. You W, Lai F, Jiang H, Liao J. The up-conversion properties of Yb 3+ and Er 3+ doped Y4Al2O9 phosphors. *Physica B Condens Matter*. 2012;407(7):1094-1098. doi:10.1016/j.physb.2012.01.077

214. Kaczkan M, Boruc Z, Turczyński S, Malinowski M. Effect of temperature on the luminescence of Sm3+ ions in YAM crystals. *J Alloys Compd*. 2014;612:149-153. doi:10.1016/j.jallcom.2014.05.186

215. Kaczkan M, Turczyński S, Malinowski M. Spectroscopic properties and Judd–Ofelt analysis of Eu3+ in Y4Al2O9 crystals. *J Lumin*. 2018;196:111-115. doi:10.1016/j.jlumin.2017.12.027

216. Kumar P, Singh D, Gupta I, Singh S, Nehra S, Kumar R. Realization of warm reddish-orange light emitter single phase Y4Al2O9:Sm3+ nanophosphors for indoor lighting applications. *J Lumin*. 2023;257. doi:10.1016/j.jlumin.2023.119703

217. Liu C, Pokhrel S, Tessarek C, et al. Rare-Earth-Doped Y4Al2O9 Nanoparticles for Stable Light-Converting Phosphors. *ACS Appl Nano Mater*. 2020;3(1):699-710. doi:10.1021/acsanm.9b02231

218. Okada G, Akatsuka M, Kimura H, et al. Characterizations of Ce-doped Y4Al2O9 crystals for scintillator applications. *Sensors and Materials*. 2018;30(7):1547-1554. doi:10.18494/SAM.2018.1919

219. Kumar P, Singh D, Gupta I, Singh S, Nehra S, Kumar R. Er3+-doped Y4Al2O9 nanophosphors for advance display applications: Synthesis, crystal chemistry and down conversion photoluminescent investigation. *Mater Chem Phys*. 2023;301. doi:10.1016/j.matchemphys.2023.127610

220. Lian Y shu, Wang Y, Li J fu, et al. Structural and fluorescence features of Dy3+:Y4Al2O9 phosphors for yellow color emitting displays. *Vacuum*. 2020;173. doi:10.1016/j.vacuum.2020.109165

221. Liu B, Liu Y, Zhu C, et al. Advances on strategies for searching for next generation thermal barrier coating materials. *J Mater Sci Technol*. 2019;35(5):833-851. doi:10.1016/j.jmst.2018.11.016

222. Zhou X, Xu Z, Fan X, Zhao S, Cao X, He L. Y4Al2O9 ceramics as a novel thermal barrier coating material for high-temperature applications. *Mater Lett*. 2014;134:146-148. doi:10.1016/j.matlet.2014.07.027

223. Yu J, Wang C, Yu Y, Yuan Q, Tan Y, Feng Z. Hot corrosion behavior of Y4Al2O9 ceramics for thermal barrier coatings exposed to calcium-magnesium-alumina-silicate at 1250 °C. *J Eur Ceram Soc*. 2019;39(4):1487-1495. doi:10.1016/j.jeurceramsoc.2018.10.034

224. Das A, Saha S, Panigrahi K, Ghorai UK, Chattopadhyay KK. Enhanced Photoluminescence Properties of Low-Dimensional Eu3+-Activated Y4Al2O9 Phosphor Compared to Bulk for Solid-State Lighting Applications and Latent Fingerprint Detection-Based Forensic Applications. *Microscopy and Microanalysis*. 2019;25(6):1422-1430. doi:10.1017/S143192761900028X

225. Boruc Z, Fetlinski B, Kaczkan M, Turczynski S, Pawlak D, Malinowski M. Temperature and concentration quenching of Tb3+ emissions in Y4Al 2O9 crystals. *J Alloys Compd*. 2012;532:92-97. doi:10.1016/j.jallcom.2012.04.017

226. Ryba-Romanowski W, Lisiecki R, Rzepka A, Lipińska L, Pajaczkowska A. Luminescence and excitation energy transfer in rare earth-doped Y4Al2O9 nanocrystals. *Opt Mater (Amst)*. 2009;31(8):1155-1162. doi:10.1016/j.optmat.2008.12.006

227. Ah R', Azis S, Hashim M, Hassan J. The Formation of Yttrium Aluminium Monoclinic (Y4Al2O9) by Sol-Gel Synthesis at Low Heating Temperature. Published online 2014. https://www.researchgate.net/publication/263389975

228. Xia G, Zhou S, Zhang J, Wang S, Wang H, Xu J. Sol-gel combustion synthesis and luminescence of Y4Al 2O9:Eu3+ nanocrystal. *J Non Cryst Solids*. 2005;351(37-39):2979-2982. doi:10.1016/j.jnoncrysol.2005.07.007

229. Yadav R, Khan AF, Yadav A, et al. Intense red-emitting Y4Al2O9 :Eu 3+ phosphor with short decay time and high color purity for advanced plasma display panel. *J Solid State Chem*. 2006;179(5):477-480.

230. Dubey V, Kaur J, Parganiha Y, Suryanarayana NS, Murthy KVR. Study of formation of deep trapping mechanism by UV, beta and gamma irradiated Eu3+ activated SrY2O4 and Y4Al2O9 phosphors. *Applied Radiation and Isotopes*. 2016;110:16-27. doi:10.1016/j.apradiso.2015.12.047

231. Ma J, Yu Z, Zhang D, et al. The molten salt synthesis of (Y1-xEux)4Al2O9 solid solution powders and their pl properties. *Journal of the American Ceramic Society*. 2014;98(2):370-373. doi:10.1111/jace.13393

232. Xu JS, Zhu YJ. Y4Al2O9 hierarchically nanostructured microspheres assembled with nanosheets: Microwave-solvothermal synthesis combined with thermal treatment and photocatalytic property. *Mater Lett*. 2011;65(17-18):2793-2796. doi:10.1016/j.matlet.2010.12.045

233. Kostić S, Lazarević Z, Radojević V, et al. Study of structural and optical properties of YAG and Nd:YAG single crystals. *Mater Res Bull*. 2015;63:80-87. doi:10.1016/j.materresbull.2014.11.033

234. Lemański K, Michalska M, Ptak M, Małecka M, Szysiak A. Surface modification using silver nanoparticles for Y4Al2O9:Nd – Synthesis and their selected studies. *J Mol Struct*. 2020;1202. doi:10.1016/j.molstruc.2019.127363

235. Wang C, Wang Y. A study of phase evolution and crystal growth for nano-sized monoclinic Y4Al2O9 as a novel thermal barrier coatings. *Ceram Int*. 2019;45(16):19679-19683. doi:10.1016/j.ceramint.2019.06.217

236. Martins JC, Bastos ARN, Ferreira RAS, Wang X, Chen G, Carlos LD. Primary Luminescent Nanothermometers for Temperature Measurements Reliability Assessment. *Adv Photonics Res*. 2021;2(5). doi:10.1002/adpr.202000169

237. Zhou Y, Xiang H, Lu X, Feng Z, Li Z. Theoretical prediction on mechanical and thermal properties of a promising thermal barrier material: Y4Al2O9. *Journal of Advanced Ceramics*. 2015;4(2):83-93. doi:10.1007/s40145-015-0140-6

238. Wang Y, Hrubiak R, Turczyński S, et al. Spectroscopic properties and martensitic phase transition of Y4Al2O9:Ce single crystals under high pressure. *Acta Mater*. 2019;165:346-361. doi:10.1016/j.actamat.2018.11.057

239. Giorgetti M, Berrettoni M, Saladino ML, Caponetti E. Evidence for a double doping regime in Nd:YAG nanopowders. *J Mater Sci*. 2009;44(6):1572-1579. doi:10.1007/s10853-009-3322-1

240. Poulos M, Giaremis S, Kioseoglou J, et al. Lattice Dynamics and Thermodynamic Properties of Y3Al5O12 (YAG). *Journal of Physics and Chemistry of Solids*. 2021;162. https://www.sciencedirect.com/science/article/pii/S0022369721005783

241. Maciejewska K, Bednarkiewicz A, Meijerink A, Marciniak L. Correlation between the Covalency and the Thermometric Properties of Yb3+/Er3+Codoped Nanocrystalline Orthophosphates. *Journal of Physical Chemistry C*. 2021;125(4):2659-2665. doi:10.1021/acs.jpcc.0c09532

242. Netzsch P, Hämmer M, Turgunbajew E, et al. Beyond the Energy Gap Law: The Influence of Selection Rules and Host Compound Effects on Nonradiative Transition Rates in Boltzmann Thermometers. *Adv Opt Mater*. 2022;10(11). doi:10.1002/adom.202200059

243. Monteseguro V, Rathaiah M, Linganna K, et al. Chemical pressure effects on the spectroscopic properties of Nd3+-doped gallium nano-garnets. *Opt Mater Express*. 2015;5(8):1661. doi:10.1364/ome.5.001661

244. Suta M, Meijerink A. A Theoretical Framework for Ratiometric Single Ion Luminescent Thermometers—Thermodynamic and Kinetic Guidelines for Optimized Performance. *Adv Theory Simul*. 2020;3(12). doi:10.1002/adts.202000176

245. Ah R', Azis S, Hashim M, Hassan J. *The Formation of Yttrium Aluminium Monoclinic (Y4Al2O9) by Sol-Gel Synthesis at Low Heating Temperature.*; 2014. https://www.researchgate.net/publication/263389975

246. Yamane H, Omori M, Hirai T. Thermogravimetry and Rietveld analysis for the high-temperature X-ray powder diffraction pattern of Y4Al2O9. *J Mater Sci Lett*. 1995;14:470-473. doi:10.1007/BF00665905

247. Hamraoui K, Torres-Vera VA, Zabala Gutierrez I, et al. Exploring the Origin of the Thermal Sensitivity of Near-Infrared-II Emitting Rare Earth Nanoparticles. *ACS Appl Mater Interfaces*. 2023;15(27):32667-32677. doi:10.1021/acsami.3c04125

248. Zhang X, Zhao Z, Zhang X, et al. Magnetic and optical properties of NaGdF4:Nd3+, Yb3+, Tm3+ nanocrystals with upconversion/downconversion

luminescence from visible to the near-infrared second window. *Nano Res*. 2015;8(2):636-648. doi:10.1007/s12274-014-0548-2

249. Cortelletti P, Skripka A, Facciotti C, et al. Tuning the sensitivity of lanthanide-activated NIR nanothermometers in the biological windows. *Nanoscale*. 2018;10(5):2568-2576. doi:10.1039/c7nr06141b

250. Singh S, Kachhap S, Sharma M, Singh SK. Enhancing the temperature sensing property of a Ca0.79−xBixEr0.01Yb0.2MoO4 phosphor via local symmetry distortion and reduction in non-radiative channels. *RSC Adv*. 2023;13(22):14991-15000. doi:10.1039/d3ra02929h

251. Li M, Zhou J, Lei R, Wang H, Deng D, Xu S. An effective way to improve near-infrared-II luminescence and optical thermometry performance via Gd3+ incorporation in Er3+, Yb3+: ZrO2 nanocrystals. *Opt Commun*. 2021;496. doi:10.1016/j.optcom.2021.127111

Appendix: Supplementary Information

Chapter II

- HR-XRD with Le Bail fit of YAG: 0.75% mol Nd^{3+}, 0.50% mol Yb^{3+} NCs versus % volume DEG (Solvothermal method).

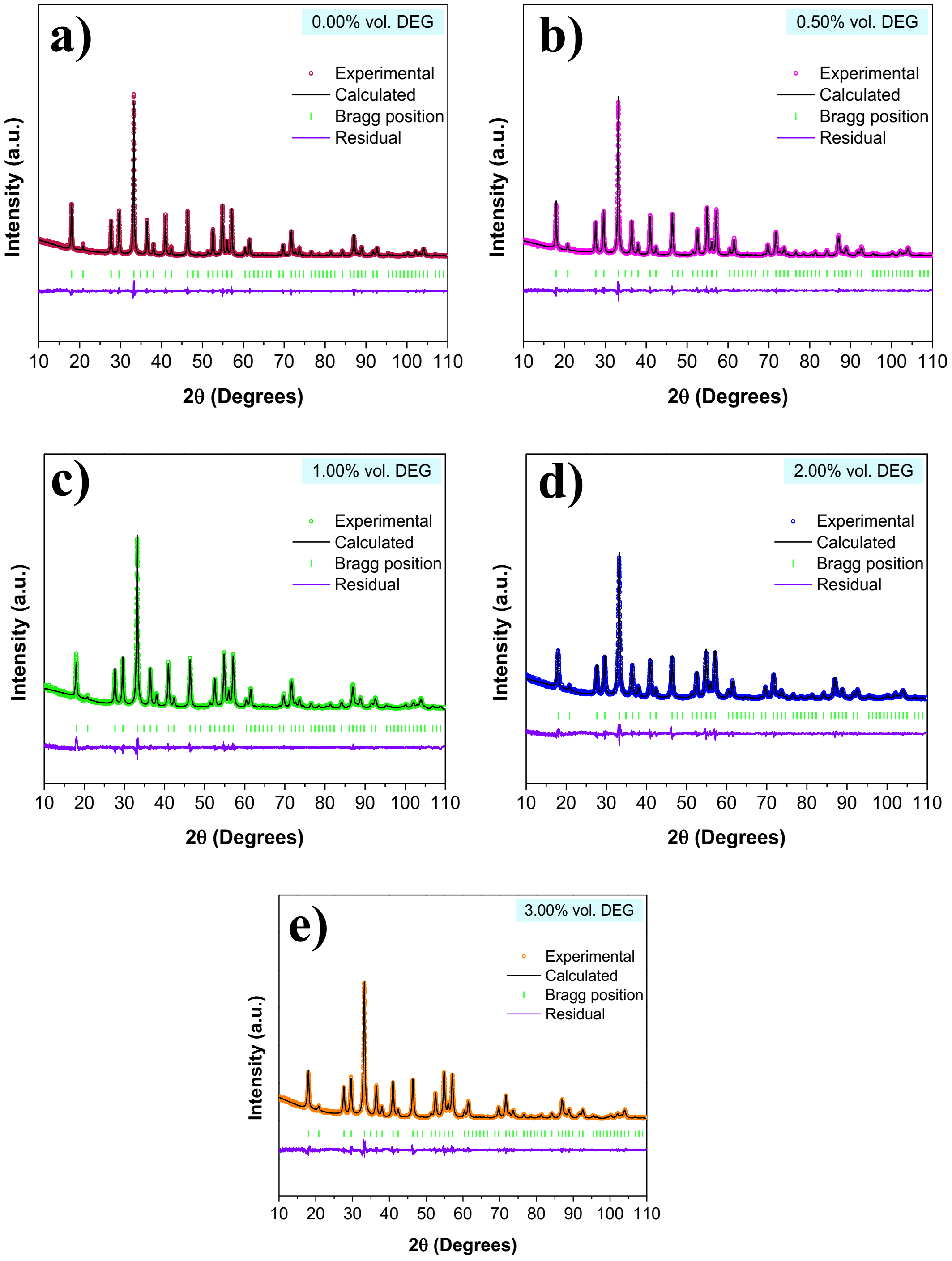

Figure S1. HR-XRD patterns with Le Bail fit of YAG NCs synthesized via the solvothermal method using **(a)** 0.00, **(b)** 0.50, **(c)** 1.00, **(d)** 2.00, and **(e)** 3.00% vol. DEG.

- Size distribution of YAG: 0.75% mol Nd^{3+}, 0.50% mol Yb^{3+} NCs versus % volume DEG (Solvothermal method).

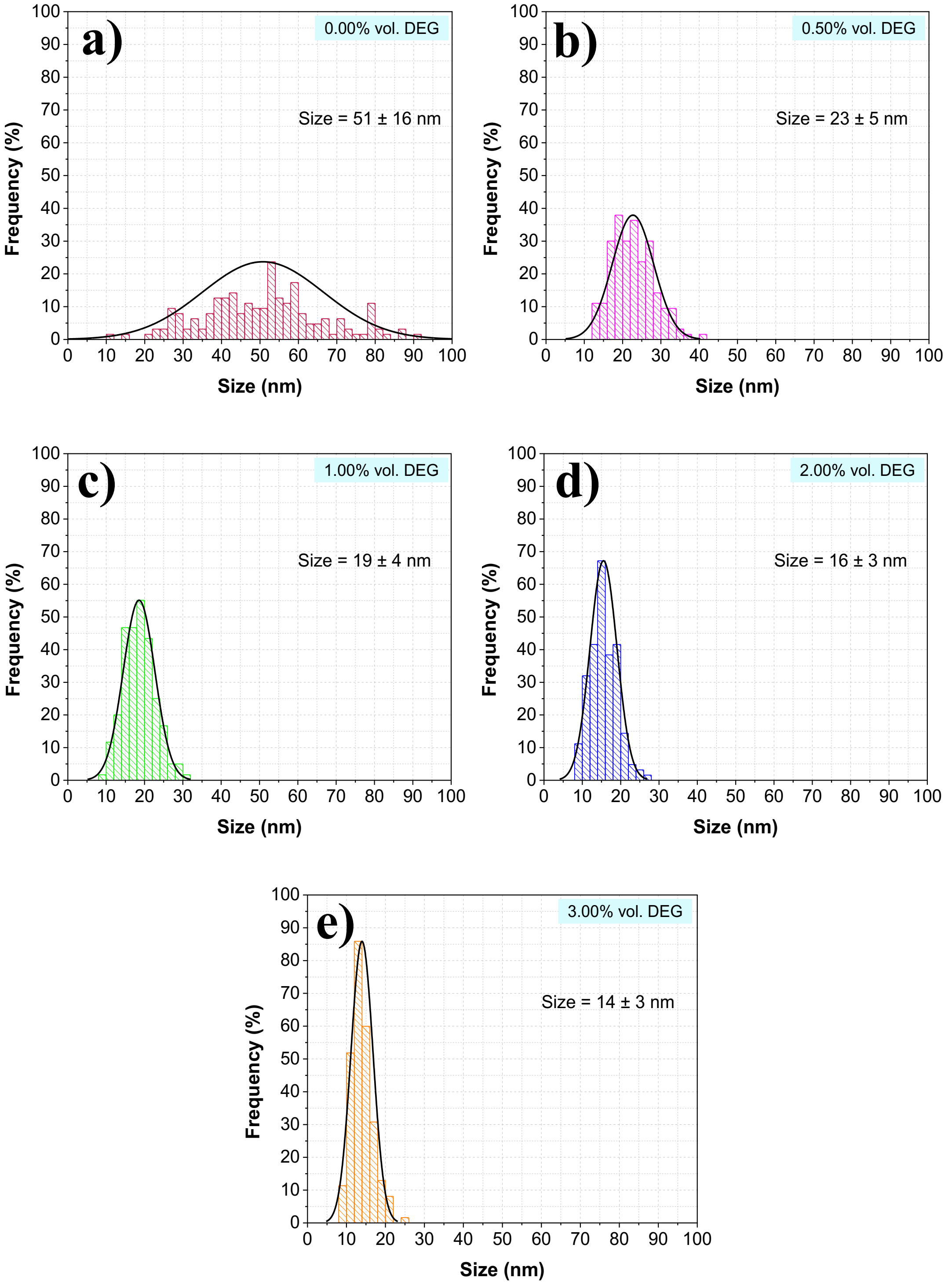

Figure S2. Size distribution of YAG NCs synthesized via the solvothermal method using **(a)** 0.00, **(b)** 0.50, **(c)** 1.00, **(d)** 2.00, and **(e)** 3.00% vol. DEG. This calculation was performed considering above 150 NCs from different TEM images.

- HR-XRD of YAG: 0.75% mol Nd^{3+}, 0.50% mol Yb^{3+} NCs (Solvothermal method) before and after annealing at 850°C.

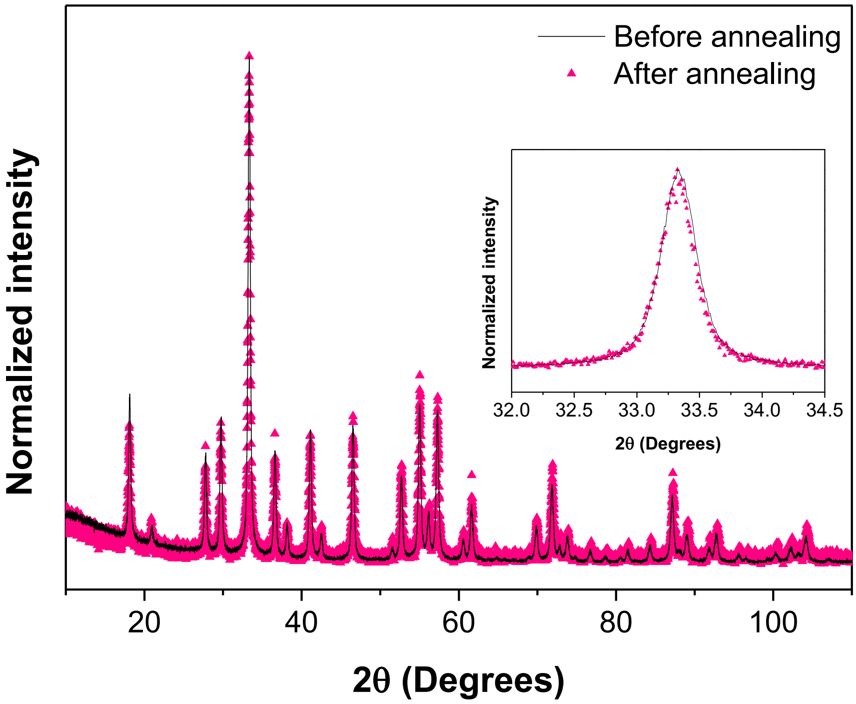

Figure S3. HR-XRD of YAG: 0.75% mol Nd^{3+}, 0.50% mol Yb^{3+} synthesized via the solvothermal method before and after annealing.

Table S1. Cell parameters and coherence length of YAG: 0.75% mol Nd^{3+}, 0.50% mol Yb^{3+} synthesized via the solvothermal method before and after annealing.

Sample		***a*** **(Å)**	***b*** **(Å)**	***c*** **(Å)**	**Volume ($Å^3$)**	**Coherence length - Lc (nm)**	χ^2	**Rp (%)**	**Rwp (%)**
YAG: 0.75% mol Nd^{3+}, 0.50% mol Yb^{3+}	Before annealing	12.048	12.048	12.048	1748.88	22 ± 1	1.50	10.9	12.1
	After annealing	12.021	12.021	12.021	1737.30	21 ± 1	1.81	17.3	25.4
	Ref.[129]	12.016	12.016	12.016	1732.32	-	-	-	-

Chapter IV

- Le Bail fit results of YAM: Nd^{3+} synthesized by the modified Pechini method.

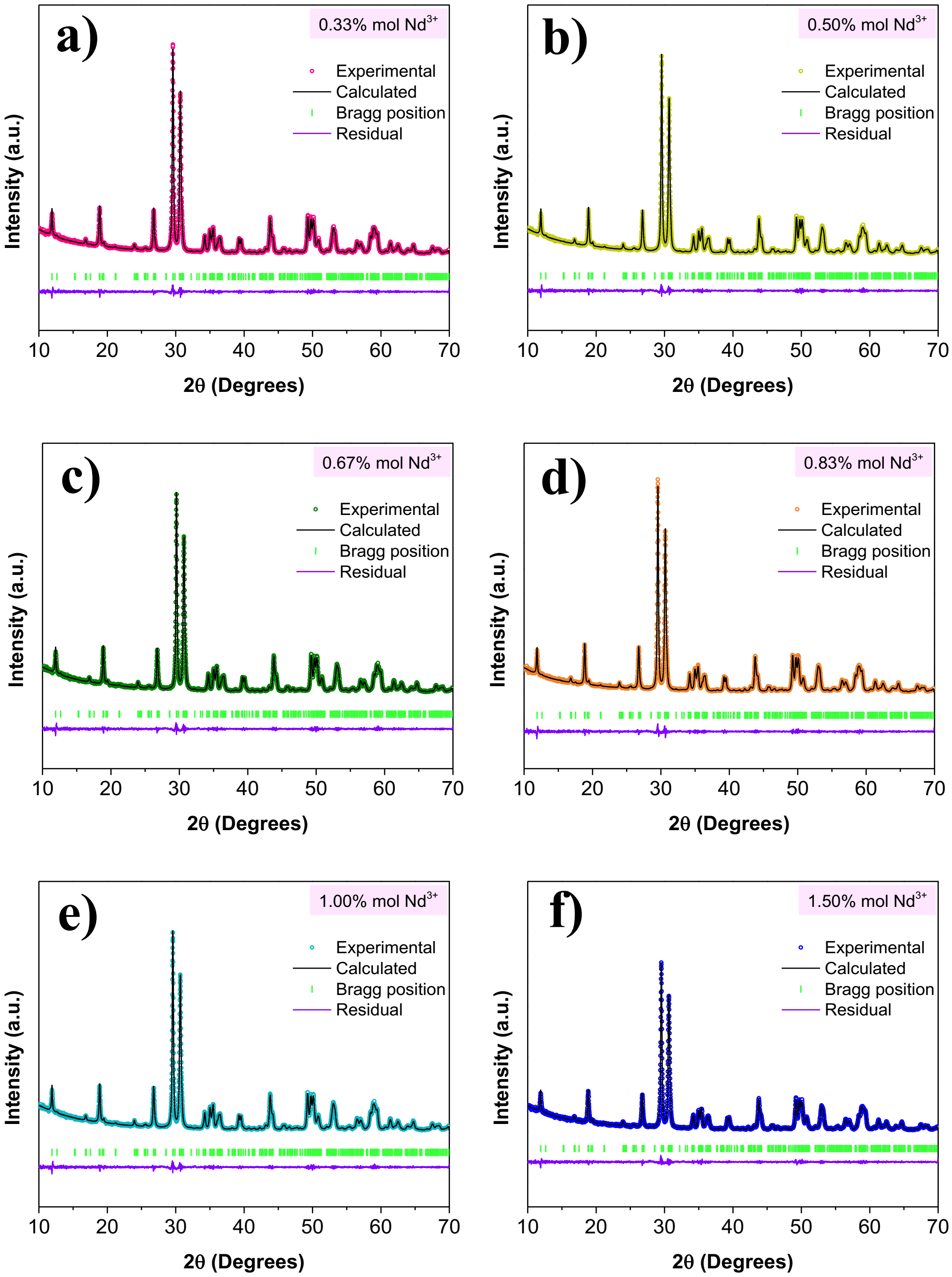

Figure S4. HR-XRD patterns with calculated Le Bail fit of YAM when doped with **(a)** 0.33, **(b)** 0.50, **(c)** 0.67, **(d)** 0.83, **(e)** 1.00, and **(f)** 1.50% mol Nd^{3+}.

Table S2. Cell parameters and coherence length of YAM doped with different concentrations of Nd^{3+}.

Nd^{3+} concentration	***a* (Å)**	***b* (Å)**	***c* (Å)**	**Volume (Å³)**	**Lc (nm)**	**χ^2**	**Rp (%)**	**Rwp (%)**
0.33% mol Nd^{3+}	7.386	10.466	11.110	813.80	42 ± 1	1.31	7.25	8.18
0.50% mol Nd^{3+}	7.388	10.467	11.113	814.33	46 ± 1	1.41	7.58	8.53
0.67% mol Nd^{3+}	7.390	10.469	11.115	814.97	45 ± 1	1.35	7.53	8.43
0.83% mol Nd^{3+}	7.391	10.472	11.117	815.50	48 ± 2	1.34	7.29	8.28
1.00% mol Nd^{3+}	7.393	10.472	11.119	815.80	44 ± 1	1.27	7.26	8.10
1.50% mol Nd^{3+}	7.398	10.473	11.126	816.54	44 ± 2	1.33	7.93	8.87
Ref.[246]	7.375	10.462	11.110	812.59	-	-	-	-

- Le Bail fit results of YAM: Nd^{3+} - Yb^{3+} synthesized by the modified Pechini method.

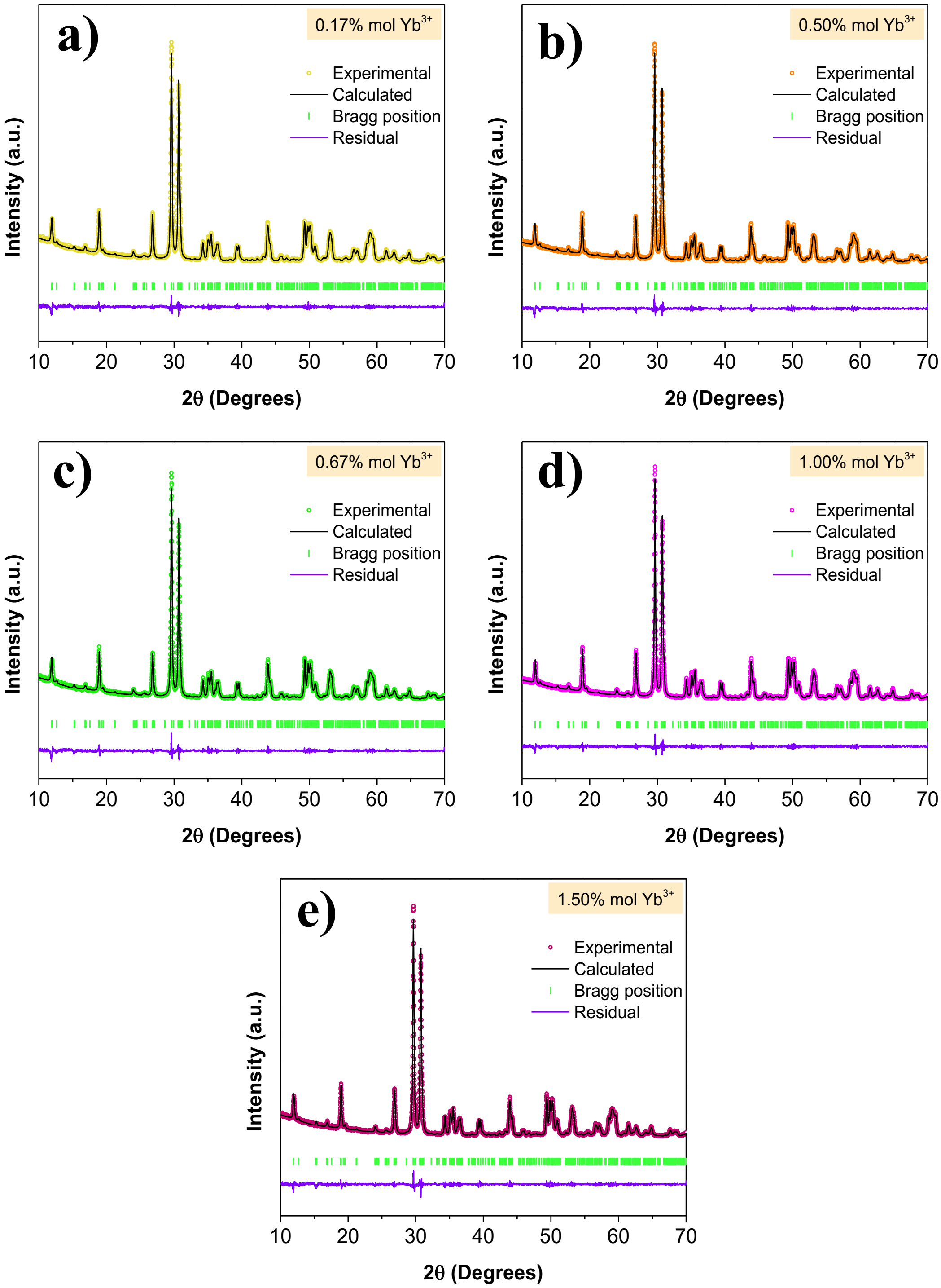

Figure S5. HR-XRD patterns with calculated Le Bail fit of YAM when doped with 0.83% mol $Nd^{3+}$and **(a)** 0.17, **(b)** 0.50, **(c)** 0.67, **(d)** 1.00, and **(e)** 1.50% mol Yb^{3+}.

Table S3. Cell parameters and coherence length of YAM doped with 0.83% mol Nd^{3+} and different concentrations of Yb^{3+}.

Yb^{3+} concentration	***a* (Å)**	***b* (Å)**	***c* (Å)**	**Volume (Å^3)**	**Lc (nm)**	**χ^2**	**Rp (%)**	**Rwp (%)**
0.17% mol Yb^{3+}	7.388	10.466	11.112	814.38	49± 3	1.68	7.96	8.93
0.50% mol Yb^{3+}	7.383	10.457	11.110	812.99	46± 3	1.80	8.22	9.34
0.67% mol Yb^{3+}	7.380	10.457	11.107	812.56	46± 3	1.94	8.87	9.91
1.00% mol Yb^{3+}	7.375	10.453	11.102	811.08	53± 3	1.62	8.10	8.98
1.50% mol Yb^{3+}	7.373	10.451	11.098	810.50	48± 3	1.88	8.95	9.84
Ref.[246]	7.375	10.462	11.110	812.59	-	-	-	-